Mechanics of Phase Transformation in NiTi Shape Memory Alloys at The Atomistic Scale

Fatemeh Yazdandoost

Dissertation submitted to the faculty of the Virginia Polytechnic Institute and State University in partial fulfillment of the requirements for the degree of

Doctor of Philosophy
In
Mechanical Engineering

Reza Mirzaeifar, Chair
Mehdi Ahmadian
Mitsuhiro Murayama
Pablo Tarazaga
Ling Li

December 10th 2018
Blacksburg, VA

Keywords: Nickel-Titanium, Shape Memory Alloy, Dislocation, Grain Boundary, Phase Transformation, Energy Dissipation, Stress Shock Wave, Molecular Dynamics, Graphene, Niobium.

Mechanics of Phase Transformation in NiTi Shape Memory Alloys at The Atomistic Scale

Fatemeh Yazdandoost

ABSTRACT

During the past decade, Shape Memory Alloys (SMAs), particularly Nickel-Titanium (NiTi) alloys, have received increasing attention mainly because of their promising role to be integrated into multifunctional systems for actuation, morphing, and sensory capabilities in a broad variety of applications including biomedical, aerospace and seismological engineering. The unique performance of all the novel devices developed by SMAs relies on either the shape memory effect or pseudoelasticity, the two distinctive properties of SMAs. Both these unique properties are based on the inherent capability of SMAs to have two stable lattice structures at different stress or temperature conditions, and the ability of changing their crystallographic structure by a displacive phase transformation between a high-symmetry austenite phase and a low-symmetry martensite phase, in response to either mechanical or thermal loading. These properties make them a superior candidate for using as damping materials under high-strain-rate loading conditions in different engineering fields. SMA materials used in the most applications are polycrystalline in nature. In polycrystalline SMAs at the bulk-level, in addition to the phase transformation at the lattice-level, the thermomechanical response is also highly sensitive to the microstructural properties. In this work, the microstructure, as well as defects, such as dislocations and the stacking faults, are studied in the NiTi crystalline structure. In addition, the performance of NiTi under shock wave loading and vibrations, and their energy dissipation capabilities are examined using computational modeling, globally and locally. The effect of graphitic and metal structures, as reinforcements, on the performance of NiTi matrix composites under static and shock stress wave loading conditions is also investigated at the atomistic scale.

Mechanics of Phase Transformation in NiTi Shape Memory Alloys at The Atomistic Scale

Fatemeh Yazdandoost

GENERAL AUDIENCE ABSTRACT

During the past decade, Shape Memory Alloys (SMAs), particularly Nickel-Titanium (NiTi) alloys, have received increasing attention mainly because of their promising role to be integrated into multifunctional systems for actuation, morphing, and sensory capabilities in a broad variety of applications including biomedical, aerospace and seismological engineering. The unique performance of all the novel devices developed by SMAs relies on their ability of changing their crystallographic structure by a displacive phase transformation between a high-symmetry austenite phase and a low-symmetry martensite phase, in response to either mechanical or thermal loading. These properties make them a superior candidate for using as damping materials in different engineering fields. In this work, the microstructure, as well as defects are studied in the NiTi crystalline structure. In addition, the performance of NiTi under shock wave loading and vibrations, and their energy dissipation capabilities are examined using computational modeling, globally and locally. The effect of graphitic and metal structures, as reinforcements, on the performance of NiTi matrix composites under static and shock stress wave loading conditions is also investigated at the atomistic scale.

Acknowledgments

I would like to thank my advisor, Dr. Reza Mirzaeifar, who trusted me and gave me the opportunity to work in his group. I am very thankful for his great guidance and support over the past years. I am really grateful and proud to have worked under his supervision. He set a great example for me to be a good researcher, a creative thinker, and a patient mentor.

I would like to thank my committee members: Dr. Ahmadian, Dr. Murayama, Dr. Tarazaga and Dr. Li for their valuable insight, comments and support. I would also like to thank Dr. Taheri and Dr. Shahab for their support and kindness over my graduate career. In addition, I would acknowledge Advanced Research Computing at Virginia Tech for providing computational resources and technical support that have contributed to the results reported within this work.

I would like to thank my parents, my brothers, my sisters-in-law and my lovely nephew for their endless love, support and encouragement. I wish we lived in a better world where they would be able to attend my graduation ceremony.

Last but not the least, I would like to thank my best friend and my husband, Ayoub, for all his caring, kindness, encouragement, sacrifices and patience.

Dedicated

to

My Best Friend, Ayoub,

&

My Adorable Cats

Table of Contents

List of Figures

List of Tables

Chapter 1. Introduction

During the past decade, Shape Memory Alloys (SMAs), particularly the near-equiatomic Nickel-Titanium (NiTi) alloys, have received increasing attention mainly because of their promising role to be integrated into multifunctional systems for actuation, morphing, and sensory capabilities in a broad variety of applications including biomedical [1], aerospace [2] and seismological engineering [3]. The unique performance of all the novel devices developed by SMAs relies on either the shape memory effect or pseudoelasticity, the two distinctive properties of SMAs. Both these unique properties are based on the inherent capability of SMAs to have two stable lattice structures at different stress or temperature conditions, and the ability of changing their crystallographic structure by a displacive phase transformation between a high-symmetry austenite phase and a low-symmetry martensite phase, in response to either mechanical or thermal loading.

1.1 Microstructure of NiTi Shape Memory Alloys

SMA materials used in the most applications are polycrystalline in nature. In polycrystalline SMAs at the bulk-level, in addition to the phase transformation at the lattice-level, the thermomechanical response is also highly sensitive to the microstructural properties such as grain sizes, orientation distributions and grain boundaries (GBs) [4-8]. Among these, grain boundaries are significant microstructural features of polycrystalline materials with a strong impact on the bulk properties [9].

The microstructural properties of grain boundaries have a significant influence on many physical and mechanical properties of bulk polycrystalline materials, including the strength, ductility, fracture toughness, and corrosion resistance. The influence of grain boundaries on all of these properties is largely defined by GB structure and the excess free energy per unit area that exists in the system due to the presence of the grain boundaries. Although both the energy and structure of grain boundaries in various metals has been the subject of extensive theoretical, computational and experimental studies, there have been very few studies on the grain boundaries in polycrystalline shape memory materials.

The concept of grain boundary design, defined as controlling the grain boundary characteristics to alleviate the adverse effects of GBs and boost their advantageous effects within the bulk

polycrystalline materials was presented by Watanabe [10] for the first time. Since this pioneering work on grain boundary design, manipulating the grain boundary features using thermomechanical processing methods to reach specified bulk polycrystalline properties, known as grain boundary engineering (GBE), has been extensively studied as an efficient method for improving predefined material properties in polycrystalline materials [9]. Several experimental and computational studies have been performed on utilizing GBE to improve a broad range of material properties including stress-corrosion resistance [11], intergranular fracture [12] and high-temperature fracture resistance [13]. More recent efforts in GBE focus on characterizing the GBs in polycrystalline materials based on their coincidence site lattice (CSL), increasing the distribution of Σ3 GBs in low stacking fault energy (SFE) materials [14], and considering the role of grain boundary planes [9, 15-20].

The distribution of different grain boundary types in a polycrystalline highly affects the material properties at the bulk level. This distribution inversely correlates with the excess free energy per unit area of each grain boundary. During past decades, a significant number of experimental and computational studies have been performed on grain boundary energy of various metals, ceramics and alloys including MgO, Y_2O_3, Ni, Ni-based alloys, Al, Au, Cu, ferritic steel and austenite steel [21-32]. Despite vast number of computational simulations of grain boundary energies of metals, there have been few studies on GBs of body centered cubic metals (BCC) [33-37], while most of the researches are focused on face centered cubic (FCC) metals.

NiTi alloys are the most widely used SMAs, mainly due to their superior mechanical properties compared to the other discovered alloys with shape memory effect. In spite of extensive computational and experimental efforts on studying NiTi martensitic phase transformation in the past two decades [38-45], our fundamental understanding of phase transformation at the vicinity of grain boundaries and the GB characteristics in NiTi alloys is still in infancy due to our limited understanding of complex morphology and structures at the grain boundaries in these alloys. The only reported works on the interaction between GBs and the mechanical properties in polycrystalline NiTi alloys are limited to some experimental studies, which mostly focus on the overall response of polycrystalline SMAs, not the local effects of microstructural features such as GBs. Among these, several investigations have been reported on evolution of microstructure and crystallographic texture [46], fracture properties and fatigue in polycrystalline samples [47], the

effect of heterogeneous precipitate on the mechanical response of NiTi alloys [48], and the effect of grain size on phase transition stress [49] and on rate-dependent thermomechanical response [50] in polycrystalline NiTi. In a pioneering work on studying the effect of microstructural features on the phase transformation, Brinson *et al.* [51] studied the correlation between the microstructure of grains/variants and the mechanical behavior of polycrystalline NiTi using in-situ optical microscopy. In some recent experiments, the interfaces in the microstructure of shape memory alloys have been studied by considering the grain boundaries in oligocrystalline or bicrystal samples. Some examples are the works by Ueland *et al*. [52] and Ueland and Schuh [4] on studying Oligocrystalline shape memory alloys (oSMAs) and the effect of grain constraints on martensitic transformation in Cu-Zn-Al oSMA, and also the phase transformation at the vicinity of the interface in a bicrystal wire. Despite these studies on the interfaces in shape memory alloys, there is still a gap of knowledge, and obvious need for a systematic analysis of grain boundary characteristics, including the energy and structure, in NiTi shape memory alloys.

In chapter 2, we utilize MD simulations and density functional theory (DFT) calculations to investigate the structure of symmetric tilt grain boundaries and the energy of both symmetric and asymmetric tilt grain boundaries in NiTi alloys. The good agreement reported between the experiment and atomistic-level simulation results reveals the fact that both methods are reliable if they have been applied properly. MD and DFT are the most appropriate computational techniques to simulate and calculate the grain boundary energies and structures accurately [53-60]. MD is a powerful tool to study adequately large simulations containing a huge number of atoms (up to a couple of hundred million), and DFT calculations are able to shed light into many unknown fundamental properties of materials at the atomistic level by studying small systems (up to a couple of hundred atoms). In this study, symmetric and asymmetric tilt grain boundaries are considered in NiTi austenite, and the energy of each grain boundary is computed in the atomistic model with a many-body interatomic potential for NiTi binary alloys. The energies of symmetric and asymmetric grain boundaries are reported as functions of the misorientation and inclination angle, respectively. The symmetric grain boundary structures are studied and the structural units are identified for the GBs. Low angle grain boundary energies are compared with the Read-Shockley model, and it is shown that this simplified model can predict the energies in this intermetallic system with an acceptable accuracy. Two representative grain boundaries are selected and their structure and energies are studied using DFT calculation. The results of MD simulations are

validated by the DFT calculations. The electron density distributions in the grain boundaries are also studied and bonding strength between Ni and Ti atoms at the interface, and at the vicinity of dislocations in the grain boundary is investigated.

1.2 Defects in NiTi Shape Memory Alloys

Despite extensive researches that have been reported in recent years on various aspects of the thermomechanical response of NiTi SMAs, our fundamental understanding of dislocation mechanisms in these alloys is still highly limited. The few works performed on studying dislocations in NiTi, are mostly focused on formation of defects and dislocations in martensite phase, mainly because these alloys experience plastic deformation in mechanical loading after completion of austenite to martensite stress-induced phase transformation. However, some recent experimental observations has uncovered the complicated mechanisms of phase transformation, particularly in polycrystalline SMAs, and evidently the observed nonrecoverable strain accumulated in cyclic loading of SMAs (which happens even at deformations bellow the strains corresponding to the completion of phase transformation) is directly related to the formation of dislocations in austenite phase of NiTi alloys [61-64]. This phenomenon motivates us to study the structure, energy, and stress distributions of dislocations in austenite NiTi alloys. Such an investigation will also highly benefit our fundamental understanding of grain boundaries in NiTi SMAs, which has a substantial effect on the thermomechanical properties of these alloys [65, 66].

All crystalline materials contain imperfections and defects, which have significant effects on their electrical, optical, and mechanical properties. These defects can be as point defects (vacancy, impurity, and self-interstitials atom), stacking faults, grain boundaries, twin boundaries, volume defects, or dislocations [67]. Among all these defects, dislocations and stacking faults have attracted attention from many researchers over the past years, as they are the most important defects influencing the mechanical properties and the main cause of plasticity [68]. In spite of extensive experimental and computational efforts on studying dislocations in many crystalline materials [68-77], there have been a few studies on dislocations in NiTi binary alloys [69, 78]. Moreover, predicting the dislocation slip planes and mobility of dislocations are very important subjects for the materials researchers, and SFE curves are the primary factors in predicting these microstructural properties. Studying the SFE curves, is a proper method for determining the mobility of dislocations [79], and predicting the dislocation slip [80]. Although there have been

extensive researches on studying the stacking fault in different alloys and metals computationally and experimentally [20, 81-88], research on stacking fault of NiTi is still at early stages of development. Recently, a few investigations have been reported on studying SFE in NiTi alloys computationally and experimentally [6, 80].

Among different computational methods which are capable of studying defect-related phenomena in metals and alloys, MD has been proven to be one of the most accurate and efficient methods. Various aspects of the thermomechanical response, and martensitic phase transformation of NiTi shape memory alloys at the atomistic level have been intensively studied in recent years using the embedded atom method (EAM), and modified embedded atom method (MEAM) in MD framework. Among these successful attempts, some examples are modeling stress- and temperature-induced structural phase transitions using EAM potentials [89, 90] and MEAM potential [91], modeling the shape memory effect [92], studying the pseudoelasticity and shape memory in NiTi nanopillars [40], investigating the energy and structure of twins in martensite phase [93], analyzing the shape recovery of NiTi nanowires under torsion [94], structural phase transformations in NiTi nanowires [95], investigating the grain boundaries energy and structure in NiTi alloys [96], and modeling NiTi superelasticity in presence of nanoprecipitates [97-99]. Many of these works have used experimental observations or DFT calculations to validate the accuracy of their MD results.

Although accurate prediction of a broad range of properties confirms the validity of using MD and these potentials to study the microstructural properties of NiTi systems, utilizing this framework to study defects/dislocations in NiTi systems has to be accompanied with special caution. There are two major technical challenges that have to be considered carefully before studying any defect related phenomena in NiTi using any of these EAM or MEAM potentials. Firstly, none of these potentials has been particularly trained for prediction of defect properties in NiTi. The second concern relates to the conflict between the assumptions of central force many body potentials and the asymmetries in the crystal structure at the vicinity of dislocations. In the formation of dislocations there are some regions with a structure far from the ideal lattice. For transition metals and their alloys, including NiTi, directional bonding might have a significant effect on the response of material, and this effect is more severe in the case of having a non-perfect lattice. By this, implementing the accuracy of an EAM potential has to be accompanied with extra caution.

In this study we investigate the applicability of MD simulations to study various aspects of the stacking fault energies, dislocation dissociation, and also the structure, energy and stress distribution of edge dislocations in austenite NiTi. We consider three different potentials, which are commonly used in the literature to study the thermomechanical response of NiTi, and through several case studies examine the accuracy of each of these potentials to predict the dislocation properties. The theory of elasticity, and DFT calculations are used to validate the results of MD simulations.

1.3 NiTi Shape Memory Alloys as Shock Wave Energy Dissipative Materials

As mentioned in the previous section, the shape memory effect and the pseudoelastic response of NiTi alloys is due to their ability of changing their crystallographic structure by a displacive phase transformation between a high symmetry austenite phase and a low-symmetry martensite phase [96, 98]. The pseudoelastic response of NiTi is hysteretic [97, 100, 101]. This phenomenon is associated with a reversible displacive solid-solid phase transformation in NiTi alloys. The reversible phase transformation provides an energy dissipation in both the direct and reverse phase transformations. This forward and reverse phase transformations make NiTi a superior candidate for designing and fabricating energy absorbing devices to be used in high-strain-rate loading conditions such as shock loading [102]. A unique property of SMAs is their ability to dissipate the energy by two complementary mechanisms: (a) through deformation-induced phase transformations in the device caused by the structural vibrations, and (b) through the phase transformation caused by the stress wave propagation.

In chapter 4, we investigate the phase transformation and the associated energy dissipation in NiTi alloys, when the material is subjected to shock loadings. A set of computational studies, using Finite Element Method (FEM), is performed to study the fundamental aspects of phase transformation and energy dissipation during structural vibrations in NiTi alloys then in order to study the effect of coating the surface of the structure with a NiTi layer to improve its resistance to shock loads, we have considered two identical aluminum substrates, and have bonded two thin layers of NiTi and aluminum with the same thickness on these substrates. The responses of the structures are compared, and the efficiency of NiTi layer in damping the energy of shock loads is investigated. In the next step of this study, we focus on dynamic response and behavior of NiTi alloys under shock loading at the atomistic scale.

The dynamic response of various metals and alloys subjected to shock loading through MD method are extensively investigated [103-112] while the investigations on the NiTi alloys are limited to two studies. Lagoudas *et al*. [113] studied the wave propagation problem in a cylindrical polycrystalline NiTi rod induced by an impact loading through finite element method. Yin *et al*. [107] investigated phase transformation of NiTi nano pillar subjected to shock loading. Therefore, in this work, the energy dissipation and the phase transformation caused by the stress wave propagation in single crystal and polycrystalline austenite NiTi alloys under shock wave loadings are investigated. MD simulations are utilized as a superior method to study the effect of microstructures such as lattice orientations, grain sizes and grain boundaries on the patterns of stress wave and phase transformation initiation and propagation at the atomistic level in NiTi alloys. A criterion based on equivalent shear strains is used to detect the inelastic deformation in the NiTi structures. This parameter is used to detect the regions with martensitic phase transformation and plastic deformation. Regions with phase transformation and plastic deformation in the structures are distinguished by implementing two proposed methods. Due to the high-strain-rate loading condition, it is expected to observe the inelastic deformation in NiTi structures being caused by both phase transformation and plastic deformation. In order to study this assumption, the total energy dissipated during the stress wave propagation in NiTi alloys is calculated, and the contributions of phase transformation and plastic deformation in the dissipated energy are investigated and compared. Moreover, in order to show the superiority of NiTi alloys in dissipating energy under shock loading, the dynamic behavior of NiTi alloys and Al are compared at the atomistic scale. Besides, the dissipated energy due to plastic deformation and phase transformation are calculated for both materials.

1.4 Graphitic Structures as Reinforcing Material in NiTi Shape Memory Alloys

Carbon based nanomaterials such as carbon nanotubes (CNTs) and graphene exhibit excellent properties including high electrical and thermal conductivity, low mass density, high flexibility, and extremely high tensile moduli/strengths [114-117]. While individual CNTs are known as one of the strongest fibers ever known, even the strongest fabricated macroscale CNT yarns and fibers are still significantly weaker than individual nanotubes. The loss in mechanical properties is mainly because the deformation mechanism of CNT fibers is highly governed by the weak shear strength corresponding to sliding of nanotubes on each other. Adding polymer coating to the

bundles, and twisting the CNT yarns to enhance the intertube interactions are both efficient methods to improve the mechanical properties of macroscale yarns. Here, we perform MD simulations to unravel the unknown deformation mechanism in the intertube polymer chains and also local deformations of the CNTs at the atomistic scale. Our results show that the lateral pressure can have both beneficial and adverse effects on shear strength of polymer coated CNTs, depending on the local deformations at the atomistic scale.

Carbon based nanomaterials, such as CNTs and graphene, due to their excellent characteristics, have recently drawn researchers' extensive attention for their potential application in designing and fabricating new generations of composite materials with superior mechanical and multifunctional performance. Particularly, CNTs have been widely used as reinforcing materials in various metal matrix composites (MMCs) [118-125]. Although there are reports on reduction in mechanical performance of MMCs [118] due to insufficient CNTs dispersion using simple mechanical mixing approaches, improvements in the mechanical properties of the MMCs have been achieved via utilizing more complicated fabrication methods such as molecular level mixing [119, 120], electrochemical co-deposition [123] and CNT-functionalization associated with hydrophilic metal flake coatings [125]. Strengthening effects of well-dispersed CNTs into the MMCs can be attributed to the outstanding load-bearing capability of the CNTs and their stress transfer proficiency due to the extensive filler/matrix interface area provided by the high aspect ratio of CNTs. Like CNTs, graphene nanoplatelets (GNPs) or nanosheets (GNSs) have been used to fabricate MMCs based on aluminum [124, 126-128], copper [129-132], magnesium [133], and nickel [134]. Compared to the CNTs and due to their two-dimensional (2D) geometry, GNSs are more difficult to disperse into the metal matrices. Therefore, utilizing mechanical alloying techniques to incorporate GNSs into MMCs resulted in either deterioration [124, 128], or moderate improvements [127, 129] in the mechanical performance of the MMCs. However, through more complicated fabrication techniques, such as using hydrophilic metal flake coatings [126], electro co-deposition [134], molecular level mixing [130], pulse reversed electro deposition [131], hybridizing GNS with metal nanoparticles [132], and liquid state dispersion into metal melt associated with solid state friction stirring [133], higher volume fractions of GNSs could be dispersed into the metal matrices resulting in better improvements in the mechanical properties.

In addition to their great mechanical properties, the unique 2D geometry of GNSs has encouraged their application in a recently new type of MMCs, metal nanolayered composites [135]. Metal nanolayered composites with high density interlayers have been shown to be capable of interlocking dislocations resulting in various exceptional properties, such as ultra-high strength and self-healing [135-138]. It is shown that the presence of single layer graphene in between single crystal metal nanolayers could result in ultrahigh strength metal nanopillars [135]. In recent years, atomistic simulations of metal single crystals in interaction with graphene nanosheets have been used to reveal the mechanisms behind strengthening effects of GNSs on single crystal metal nanolayered composites [135, 139, 140]. However, to the best of our knowledge, there are no atomistic simulations so far reporting the effect of graphene sheets in polycrystalline metals.

In the present work, we introduce a new nickel-graphene nanolayered composite system in which instead of putting the large individual graphene sheets that cover all the interlayer area, monolayer graphene flakes are spread inside the interlayers so that only a fraction of the interlayer area (13%-30%) is covered. Compared to the previous similar composite systems [135], the introduced graphene-metal nanolayered composite is easier and more cost-effective to fabricate in large scales. At the first steps of this study, a systematic investigation on the effect of various graphene reinforcement configurations on the nickel-graphene systems performance is done by utilizing a series of atomistic simulations. The molecular dynamics simulations of various nanocrystalline nickel-graphene systems are performed, for the first time, under both compression and nanoindentation loadings to reveal the effect of graphene nanosheets on hindering the dislocation propagation inside the metallic systems. As the result, the best applicable nickel-graphene nanolayered systems are identified, fabricated and examined in the experiments.

In order to fabricate the composites, electron beam evaporation technique is utilized for depositing the metal layers. As a result, a nanocrystalline structure for the nickel layers is obtained. It is well established that in polycrystalline metals there is a so-called Hall-Petch relation [141, 142] between the strength and the average grain size in which the strength increases as the grain size decreases. However, it is also observed that at nanocrystalline metals with few-nanometer average grain sizes, as the grain size decreases the material experiences softening showing a reverse Hall-Petch effect [143-146]. Hence, there is an average grain size range in which a nanocrystalline metal has the maximum possible strength [147, 148]. In the composite systems introduced in this study,

the nickel layers possess a nanocrystalline structure with an average grain size very close to this optimum size. Therefore, this material system benefits from both the nanocrystallinity of the metal as well as the strengthening effects of the graphene interlayers at the same time.

Based on these obtained results, in the next step of this study, we use GNPs and NiTi alloys to make a MMC capable of interlocking dislocations and preventing the propagation of plastic deformations. As mentioned in Section 4.3, the dissipated energy in NiTi alloys under shock loading condition is due to both plastic deformation and phase transformation. The plastic deformation is an undesired phenomenon even though it contributes as a small portion of the dissipated energy. Therefore, in order to prevent the propagation of plastic deformation in NiTi alloys under loading, a new nanocrystalline NiTi-graphene composite is proposed in the current work. In addition, the strengthening mechanism in graphene reinforced NiTi alloys are explained and the interaction of the graphene particles with plastic deformation propagation are studied at the atomistic scale. In order to complete this study, the interaction of these graphene particles and shock stress wave in single crystalline NiTi-graphene composites is investigated through molecular dynamics method. Moreover, the dynamic behavior of three NiTi-graphene composites with different graphene particles arrangements are investigated and compared in order to reveal the effect of graphene particles orientations and arrangements on the composites' response under shock wave loadings.

1.5 NiTi-Nb Composite as a Superelastic and High Hysteresis Material

NiTi shape memory alloys due to their two unique properties, shape memory effect and superelasticity, are widely used as damping materials in various devices in order to absorb vibrations [149-153]. In passive control devices for example, NiTi alloys can be used as either martensitic or austenitic material. In martensitic and austenitic NiTi alloys, the damping capability comes from martensite variations reorientation and stress-induced martensitic phase transformation, respectively. The martensitic NiTi alloys have a higher damping capabilities compared to the austenitic alloys due to the dissipation of energy during twinning-detwinning transformations [154, 155]. But they have no strain recovery capability like the austenitic NiTi materials. In addition, NiTi shape memory alloys in martensite phase possess very low yield strength and can be easily deformed into other shapes [153]. This is due to the reorientation of martensite variants or occurrence of detwinning in the deformation process [149, 153]. This

disadvantage would limit the application of NiTi alloys as a high strength damping material in engineering applications [156]. Therefore, it is necessary to develop a new material which has high yield strength and high damping capability. Accordingly, there have been several experimental studies on various metal-NiTi alloys in order to develop a new NiTi based alloys which have both high yield strength and high damping capability [157-161]. Among these investigations, there have been some studies on the NiTi-Nb composite [150, 156, 157, 162-164]. It has been shown that Nb is a superior candidate to be used as reinforcement in NiTi alloys. Due to the compatibility between the microstructures of NiTi and Nb, they make a perfect composite with high damping capability and high yield strength [163, 164]. In this work, NiTi-Nb composite is investigated computationally and at the atomistic scale for the first time. Moreover, the mechanism behind these improvements are studied and the results of our simulations are in good agreement with the reported experimental results.

1.6 Dissertation Objectives and Structure

The following chapters of this dissertation address the objectives as follows. Second chapter is devoted to investigate the NiTi microstructure. Particularly, it studies the energy and structure of symmetric and asymmetric tilt grain boundaries of austenite NiTi crystalline structure. Third chapter investigates the dislocation energy and structure, as well as the stacking fault energy. Finite element method is used in the first section of the forth chapter to examine the energy dissipation capabilities of NiTi plates during vibrational loading. The second section of this chapter specifically studies the effect of grain size and crystal orientations on the NiTi behavior under shock stress wave loading condition at the atomistic level. The last section of this chapter calculates the dissipated energy due to phase transformation and plastic deformation inside the NiTi bulk and nanopillar structures. In chapter 5, initially the effect of lateral pressure on the performance of CNT bundles and yarns is investigated using multiscale modeling. Next, the enhancing performance of graphene nanoparticles in a Ni-graphene composites is studied experimentally and numerically. At the third section of this chapter, NiTi-graphene nanolayered composites are studied under tensile loading and in the last section their performance under shockwave stress loading is investigated. In chapter 6, Nb is used as the reinforcing material in a NiTi-Nb composite material and the performance of both the superelastic and the shape memory NiTi-Nb composites

material systems is examined via MD simulations. The last chapter is devoted to the conclusion and contributions.

Chapter two of this work includes a published paper in **Computational Materials Science journal**. The title of work is: **Tilt grain boundaries energy and structure in NiTi alloys**. The author acknowledges the publisher of the work, **Elsevier** for giving the right to include the article in this dissertation which is not provided to be published commercially.

Chapter 2. Microstructure of NiTi Shape Memory Alloys

2.1 Overview

In this chapter energy and structure of tilt grain boundaries are studied in Nickel-Titanium (NiTi) alloys. Molecular dynamics (MD) simulations are utilized to investigate the excess energy of symmetric and asymmetric tilt grain boundaries as a function of the misorientation and inclination angles. Structural units of different symmetric grain boundaries are identified and the correlation between the structure and energy is investigated. It is shown that the Read-Shokley model can accurately predict the energy of low angle symmetric tilt grain boundaries in austenite NiTi alloy. Density functional theory (DFT) calculations are used to study two representative symmetric grain boundaries. Comparing to DFT calculations, it is shown that the MD results can predict the GB potential energies accurately. The Electron charge density distributions are studied and the bonding strength between atoms, and low/high charge density regions are investigated, and accosted with the structural units in the grain boundaries. It shown that a symmetric arrangement of Ni and Ti atoms at the GB improved the uniformity of bonding and charge density distribution.

2.2 Methods

Molecular Dynamics Simulations

A many-body interatomic potential for the NiTi binary alloy is used. The embedded atom potential (EAM) of NiTi was originally developed by Lai and Liu [165] and has been modified by Zhong *et al*. [93]. They modified the potential function with cubic polynomial interpolations to smooth the discontinuities near the cut-off radius. It was demonstrated that the MD calculated lattice constants and energies of various phases of NiTi are in a good agreement with the results of experiments and *ab initio* calculations [40, 93]. This modified potential has been widely used to study different aspects of the thermomechanical response of NiTi alloys at the atomistic level [40, 93, 95, 166]. Conjugate gradient method in three dimensional periodic computational cells has been used to minimize the structural energy to investigate phase transformation mechanisms at the grain boundaries in Section 2.2. All the molecular dynamics simulations to calculate the grain boundary energies (Section 2.4) have been performed using three dimensional periodic computational cells, at the finite temperature T=400 K using time integration on Nose-Hoover

style non-Hamiltonian equations of motion in isothermal-isobaric (*npt*) ensembles. Large-scale Atomic/Molecular Massively Parallel Simulator (LAMMPS) [167] is used for performing the simulations and Ovito [168] visualization tool has been used for post-processing the results of MD simulations.

Density Functional Theory Calculations

Two sets of calculations with GGA, Ultrasoft and PAW pseudopotentials has been performed based on the DFT method as implemented in Quantum Espresso (QE) code [169]. For the calculations with Ultrasoft pseudopotential, Vanderbilt Ultrasoft with Perdew-Burke-Ernzerhof (PBE) pseudopotential have been used for titanium and Rappe Rabe Kaxiars Joannopoulos with Perdew-Burke-Ernzerhof (PBE) pseudopotential have been utilized for nickel. For the calculations with PAW pseudopotential Projector Augmented-Wave [170] with Perdew-Burke-Ernzerhof (PBE) have been used for both nickel and titanium. Monkhorst-Pack [171] *K-point* meshes are used for Brillouin zone integration. One *K-point* for each 50 Angstrom has been considered in all simulations in order to get the accurate calculations and convergence.

2.3 Temperature induced phase transformation at the grain boundaries

Molecular statics simulations using Conjugate Gradient (CG) energy minimizations at T = 0 K have been extensively utilized for calculating the grain boundary energy of several BCC and FCC materials [9, 15, 16, 172-174]. However, calculating the GB energy in austenite NiTi using energy minimization is a challenge, since austenite is not the stable phase at T = 0 K. It is worth noting that several MD works have been reported on utilizing energy minimization for analyzing the potential energy of austenite phase in NiTi [89, 98, 99, 175]. These calculations are all valid since the austenite phase is at a local minimum in energy landscape of NiTi, and a perfect B2 austenite structure will remain stable at T = 0 K during energy minimization. However, the grain boundaries are planar defects containing dislocations, point defects and possible precipitates. As we will show in this section, these defects will trigger the phase transformation at the vicinity of grain boundaries either at low temperatures in a molecular dynamics simulation or during energy minimization in molecular statics studies. Here we present two sample cases on the austenite phase instability at the vicinity of grain boundaries, both at low temperatures and during energy minimization as shown in Figure 2-1.

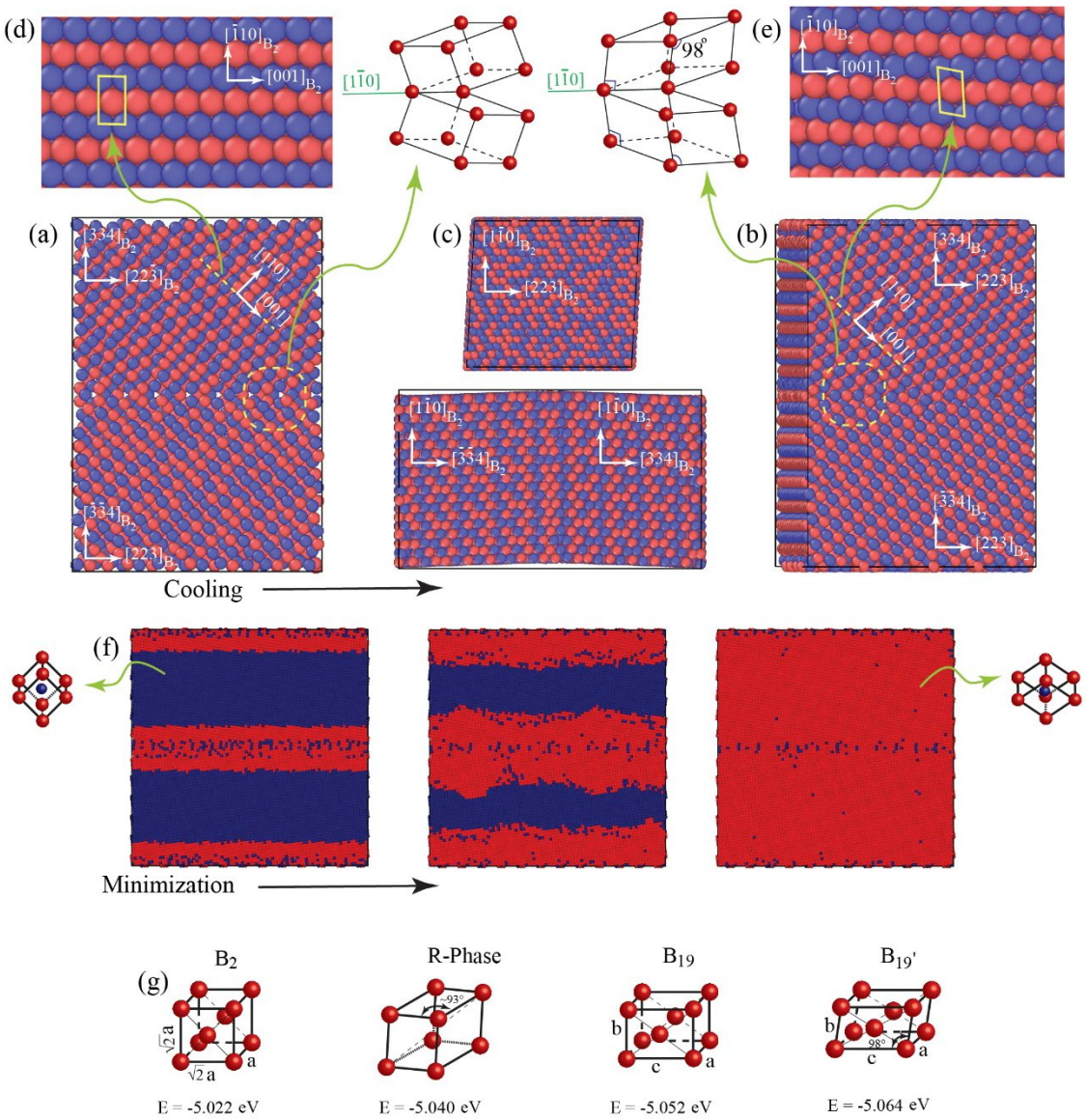

Figure 2-1. (a) A symmetric tilt Σ17 (334)[1$\bar{1}$0] grain boundary equilibrated at T= 400 K, and (b) cooling the structure to T= 1 K with the rate of 0.5 K per picosecond. (c) The (223) and (334) views of the transformed structure with (d and e) the [110] view of the top grain before and after the phase transformation, at high and low temperatures. Blue and red represent Ni and Ti atoms, respectively in (a-e). (f) A symmetric tilt Σ25 (710)[001] grain boundary minimized at T=0 K using the CG method. Blue and red represent the atoms with energies close to austenite and martensite. (g) Cohesive energies of various NiTi phases. Blue color in (f) corresponds to B2 and the other phases are marked with red.

A symmetric tilt Σ17 (334)[1$\bar{1}$0] grain boundary equilibrated at T = 400 K is shown in Figure 2-1(a). After the equilibration at high temperature, the structure is cooled down to T = 1 K with the rate of 0.5 K per picosecond as shown in Figure 2-1(b). Phase transformation happens in the structure when the system is cooled down below the martensite finish transformation temperature

($M_f \approx 300\ K$), and two symmetric martensite variants are formed with the grain boundary acting as the symmetry plane. A schematic of the crystal orientations before and after the phase transformation is also shown in Figure 2-1. The (223) and (334) views of transformed structure are shown in Figure 2-1(c), where the tilt in the structure during phase transformation is obviously seen. The [110] views of the top grain before and after the phase transformation, at high and low temperatures, clearly show the B2 austenite and B19' martensite structures as shown in Figure 2-1(d) and (e), respectively. Comparing the atoms positions in (110) planes demonstrates the change of angle from 90 to ~98 degrees in austenite to martensite phase transformation [41]. A future communication by the authors will study the details of temperature induced phase transformation mechanisms at the vicinity of grain boundaries in NiTi. However, the above-considered case study clearly shows that the structure and energy of grain boundaries in austenite cannot be studied at low temperatures.

Instability of austenite phase at low temperatures might also lead to erroneous results if the energy minimization is used for calculating the structure and energy of grain boundaries in austenite NiTi. As an example, consider a symmetric tilt Σ25 (710)[001] grain boundary minimized at T = 0 K using the CG method as shown in Figure 2-1(f). During the energy minimization, phase transformation is triggered at the vicinity of the grain boundary and martensite phase initiates and grows through the structure. In this figure, cohesive energies of various NiTi phases, shown in Figure 2-1(g), are used to color code the atoms at different phases. The region with blue color represents the austenite phase, while the red color shows atoms with energies close to one of the other phases. Tracking the energy of atoms in the system during minimization confirms the phase transformation from austenite to either R-Phase or B19/B19' martensite caused by the atom displacements during energy minimization.

To overcome this challenge, we will use a novel method for calculating the grain boundary energies and structures. In all of the following MD simulations, we equilibrate GBs at T = 400 K (which is above the NiTi transformation temperature predicted by the EAM potential [93, 95]) to guaranty the stability of austenite, and the potential energy component of the total energy is used to calculate the GB energies.

2.4 Structure and energy of tilt GBs in NiTi

MD simulations are performed to calculate the grain boundary energies of both symmetric and asymmetric tilt grain boundaries. The grain boundaries are equilibrated at T = 400 K with the EAM interatomic potentials. In-plane rigid body translations and atoms deletion criteria are used to reach the minimum grain boundary energy of the structures with a method similar to what has been implemented in [15]. In this method, one of the grains is moved in the plane of the grain boundary in a loop with several different positions, and at each position a range of different overlap values is considered for deleting the extra atoms at the grain boundary after moving one of the grains. At each position and selected overlap, the grain boundary energy is calculated and recorded to find the structure corresponding to the minimum possible potential energy for a grain boundary. The equilibrated structures are created using three dimensional periodic cells consisting two grains with approximately 240×240×30 Å in x, y and z directions (size slightly changes from different directions to satisfy the periodicity). The three dimensional periodic computational cells are large enough to eliminate any interactions between the two grain boundaries during the equilibrating simulation [15, 176]. The grain boundary excess energies are calculated by subtracting the potential energy of a perfect structure with the same number of atoms from the potential energy of equilibrated bicrystal structures. The energies are reported per unit grain boundary area in the sequel.

2.4.1 Energy of symmetric tilt GBs

Grain boundary energies as a function of misorientation angle (θ) are calculated and shown in Figure 2-2 and 3, for two GBs with <001> and <110> tilt axis, respectively. Low order coincidence site lattice (CSL) systems are also shown in these figures. The energy in <001> GBs slightly changes by varying θ, while the <110> grain boundary energies strongly vary by changing the misorientation angle. Σ5 (210)[001] symmetric tilt grain boundary is the deepest cusp for the <001> tilt axis, while Σ3 (112)[$1\bar{1}0$], Σ9 (114)[$1\bar{1}0$] and Σ11 (332)[$1\bar{1}0$] are the three deepest cusps for the <110> tilt axis. It is worth noting that for the <001> tilt axis, there is no coherent twin boundary and it only shows a minor cusp at Σ5 (210)[001]. While, for the <110> tilt axis, Σ3 (112)[$1\bar{1}0$] is a coherent twin boundary and the other two grain boundaries (Σ9 and Σ11) are minor cusps.

Comparing the GB energies of NiTi, Al, Cu [15], Mo [173], BCC and FCC Fe [177] shows that the overall trend of energy distributions in NiTi alloy is similar to the mentioned metals. Among these, Al is a high stacking fault energy (HSFE) metal while Cu, Mo, and Fe (in both phases) are all low stacking fault energy (LSFE) metals. The calculated GB energy distributions of NiTi are closer to energy distributions of LSFE materials. Comparing the NiTi GB energies with BCC Fe confirms that the trend of GB energy distributions in NiTi and Fe are similar, which is expected considering both having body center cubic structures. The GB energies in BCC Fe [177] are, on average, two times greater than the calculated values for NiTi in this chapter. This ratio is also compatible with the ratio between the stacking fault energies of NiTi and Fe, as γ_{us} for (001)[010] system of NiTi and Fe are $(800\ \mathrm{mJ\ m^{-2}})$ [6] and $(1200\ \mathrm{mJ\ m^{-2}})$ [82], respectively. Also γ_{us} values for (011)[100] system of NiTi and Fe are $(140\ \mathrm{mJ\ m^{-2}})$ [6] and $(470\ \mathrm{mJ\ m^{-2}})$ [82], respectively.

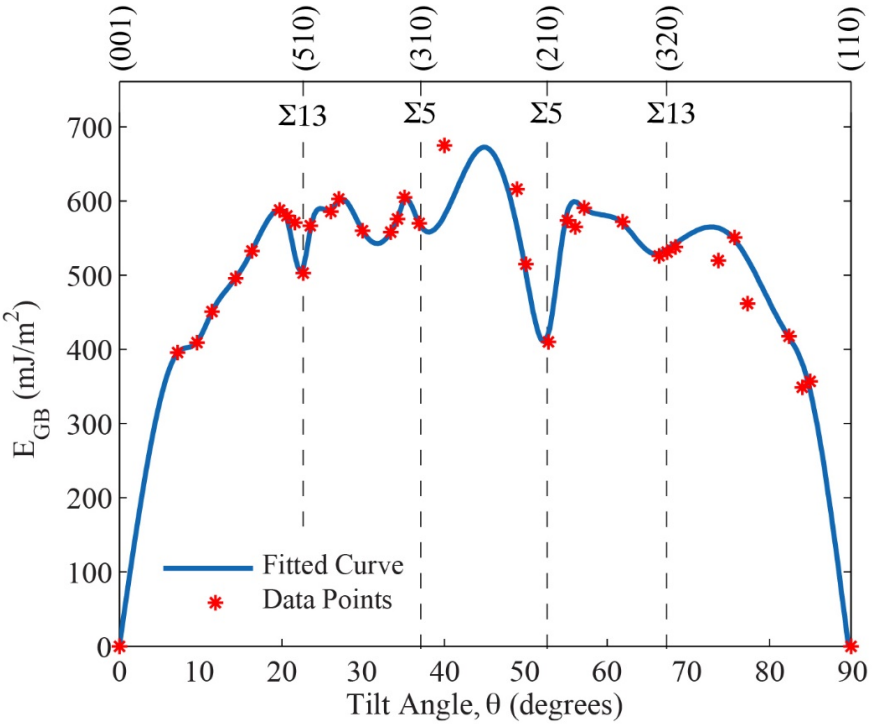

Figure 2-2. Grain boundary energies as a function of misorientation angle (θ) with <001> tilt axis.

Coherent twin boundary energies of NiTi, Mo and BCC Fe are greater than the coherent twin boundary energies in Al, Cu and FCC Fe. This is expected as BCC (112) planes are not closed-packed in contrast with the FCC system. The Σ3 (112)[$1\bar{1}0$] twin boundary in BCC system consists of a stacking disorders of the nonclosed packed face [177], while FCC twin boundary Σ3

(111)[$1\bar{1}0$] has a closed-packed face, and consequently a lower energy compared to the BCC system. The unstable SFE, γ_{us}, of NiTi, Al and Cu for (011)[100] system are $600, 153$ and 49 mJ m^{-2}, respectively and coherent twin boundary energies for NiTi, Al and Cu are $216, 75$ and 22 mJ m^{-2} [15]. The ratios of GB energies are following the same trend as the stacking fault energies, as expected, which confirm the validity of our results. In order to validate the calculated energies, we also will compare the results for two representative GBs in NiTi with DFT calculations in the following sections.

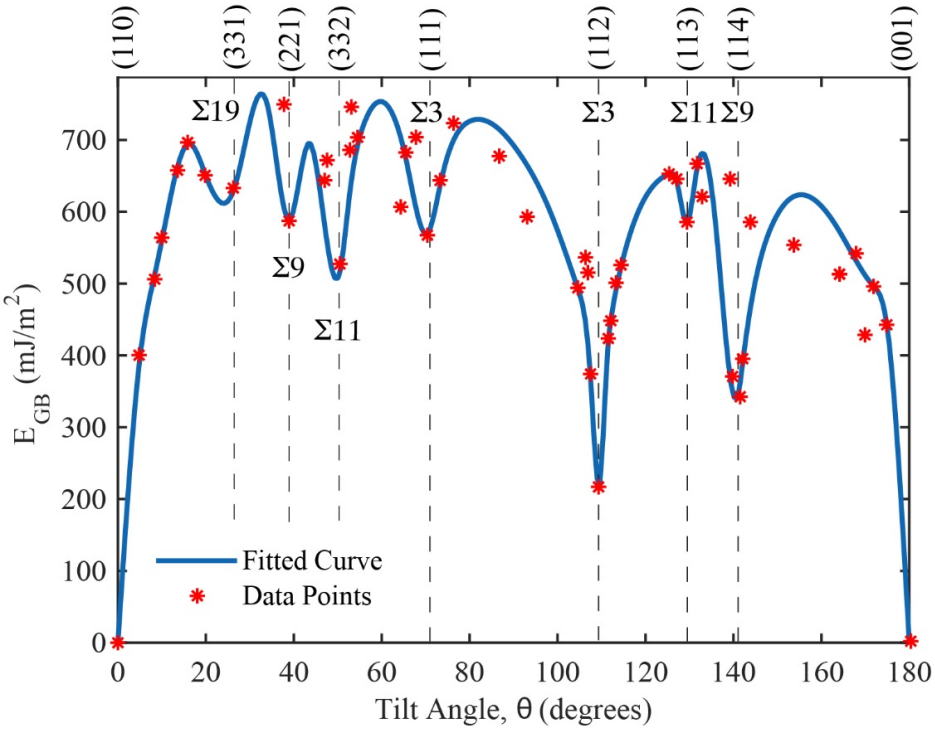

Figure 2-3. Grain boundary energies as a function of misorientation angle (θ) with <110> tilt axis.

Comparing both curves with similar distributions for other metals (either BCC or FCC) reveals that the fluctuations of GB energies with changing the misorientation angle in NiTi are much more compared to the other metals. This phenomenon can be a result of possible local phase transformations near dislocations at the vicinity of grain boundaries due to the stress concentrations originated by the dislocation on the boundary. It is worth noting that although the considered temperature is above A_f, which is the austenite finish temperature at zero stress, an austenite to martensite phase transformation is still possible at a nonzero stress [178]. A high stress concentrated locally at the vicinity of dislocations on the grain boundary might trigger the phase

transformation by tilting a thin layer of atoms from B2 to B19' structure, and alter the energy distribution. More details of local phase transformation mechanisms around the dislocations and at the vicinity or grain boundaries and triple junctions will be the topic of a future communication by the authors.

2.4.2 Energy of Σ3 asymmetric tilt GBs

The inclination angle (ϕ) is defined as the angle of rotation of grain boundary plane about the axis perpendicular to the tilt axis from the symmetric tilt grain boundary plane. The asymmetric grain boundaries studied in this section are created by rotating a Σ3 (112)[$1\bar{1}0$] symmetric grain boundary about the tilt axis [$1\bar{1}0$] [15]. The asymmetric grain boundary energies as a function of the inclination angle are shown in Figure 2-4. The energies are depicted for grain boundaries with inclination angles ranging from $\phi = 0$ (corresponding to Σ3 (112)[$1\bar{1}0$] GB) to $\phi = 90$ (Σ3 (111)[$1\bar{1}0$] GB) in NiTi.

Asymmetric grain boundary energies can be approximated by combining the corresponding symmetric grain boundary energies. For the studied Σ3 asymmetric tilt grain boundary (ATGB), the energy can be defined as a function of inclination angle ϕ:

$$\gamma_{\phi} = \gamma_{CTB}\, cos\, \phi + \gamma_{SITB}\, sin\, \phi, \qquad (2\text{-}1)$$

where γ_{CTB} (216 mJ m^{-2}) and γ_{SITB} (570 mJ m^{-2}) are the Σ3 (112) coherent twin boundary and Σ3 (111) symmetric incoherent twin boundary energies, respectively [15].

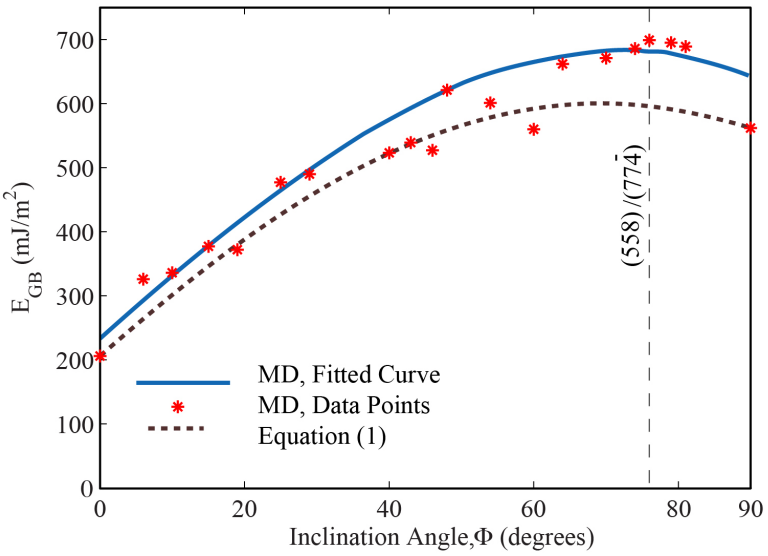

Figure 2-4. Σ3 Asymmetric tilt grain boundary energies as a function of inclination angle (Φ).

The calculated symmetric grain boundary energies of NiTi are implemented in (2-1) and the approximate energy is shown along with the MD results in Figure 2-4. The overall trend is following the MD results, with the approximate values slightly lower than the MD calculations. The observed difference between the MD simulations and the approximation in Equation (2-1) is attributed to the discrete nature of molecular dynamics simulations, which are associated with local arrangements of the atoms at the grain boundaries, particularly close to the dislocations. This difference can be highly affected by the selection of different interatomic potentials in the MD simulations.

2.4.3 Structure of (100) and (110) symmetric tilt GBs

Some selected representative grain boundaries with [001] and $[1\bar{1}0]$ tilt axes are studied in order to investigate the correlation between GB energies and structures. To obtain the structural units (SUs) of GBs, a simple procedure is used so that a line is drawn in the grain boundary which devides the structure into two adjoining grains. The atomic positions at the vicinity of grain boundaries are then investigated and structural units of the grain boundaries are found and shown in Figure 2-5 and 6. The relationship between the GB energies and structures is directly connected to coincidence-site lattice model as well. This correlation is based on the assumption that the grain boundary energy is lower when the number of bonds that are broken at the grain boundary is smaller [179]. When the coincidence of atomic positions in both adjacent grains is high, then the number of broken bonds at the grain boundary is small, and the energy of this type of GB is

relatively low. CSL grain boundaries with lower Σ values are also constructed with smaller and simpler structural units, which represent more atoms being in the perfect structure, and causes smaller excess energy for the grain boundary.

The NiTi GB structures equilibrated at T = 400 K for [001] and $[1\bar{1}0]$ tilt axes are shown in Figure 2-5 and 6, respectively. Figure 2-5(a), (e), (f) and (h) show the basic structural units (the SUs which cannot be decomposed to simpler units) for the symmetric grain boundaries with [001] tilt axis. Grain boundary of Σ1 (100)[001] and Σ1 (110)[001] systems consist of A and A′ single structural units. The GBs of Σ5 (310)[001] and Σ5 (210)[001] systems consist of B and C basic SUs, respectively. All the other representative GB structural units can be defined as a combination of these basic SUs.

Figure 2-5(b) shows the SUs for a (10,1,0) grain boundary which consists of seven periods of Σ1 (100)[001] system and one period of Σ5 (310)[001] system, and can be represented by the reaction: $a_0[10\ 1\ 0] = 7a_0[100] + a_0[310]$.

The structural units of Σ25 (710)[001] and Σ13 (510)[001] systems shown in Figure 2-5(c) and (d) are given by the reactions: $a_0[710] = 4a_0[100] + a_0[310]$ and $a_0[510] = 2a_0[100] + a_0[310]$, respectively. The Σ13 (320)[001] system shown in Figure 2-5(g) is a combination of C and A′ SUs: $a_0[320] = a_0[210] + a_0[110]$. Figure 2-5(d), (e), (f) and (g) have the lowest CSL which corresponds to the deepest cusps in the energy landscape and have simpler SUs compared to the structures with higher CSLs.

Figure 2-6(a), (h) and (d), (g) show the single SUs and basic SUs of NiTi GBs structures with $[1\bar{1}0]$ tilt axis. Figure 2-6(b) and (c) show the SUs of Σ9 (221)$[1\bar{1}0]$ and Σ11 (332)$[1\bar{1}0]$ correspond to $a_0[221] = a_0[111] + a_0[110]$ and $a_0[332] = 2a_0[111] + a_0[110]$ reactions. Structural units of Σ17 (334)$[1\bar{1}0]$ and Σ17 (223)$[1\bar{1}0]$ shown in Figure 2-6(e) and (f) are consist of B and C basic structural units. The combination can be represented by the reactions: $a_0[334] = 2a_0[111] + a_0[112]$ and $a_0[223] = a_0[111] + a_0[112]$, respectively. These representative GBs correspond to the lowest CSLs Σ3, Σ9 and Σ11, with the simple structures also have deepest cusps in energy landscape as shown in Section 2.4.1.

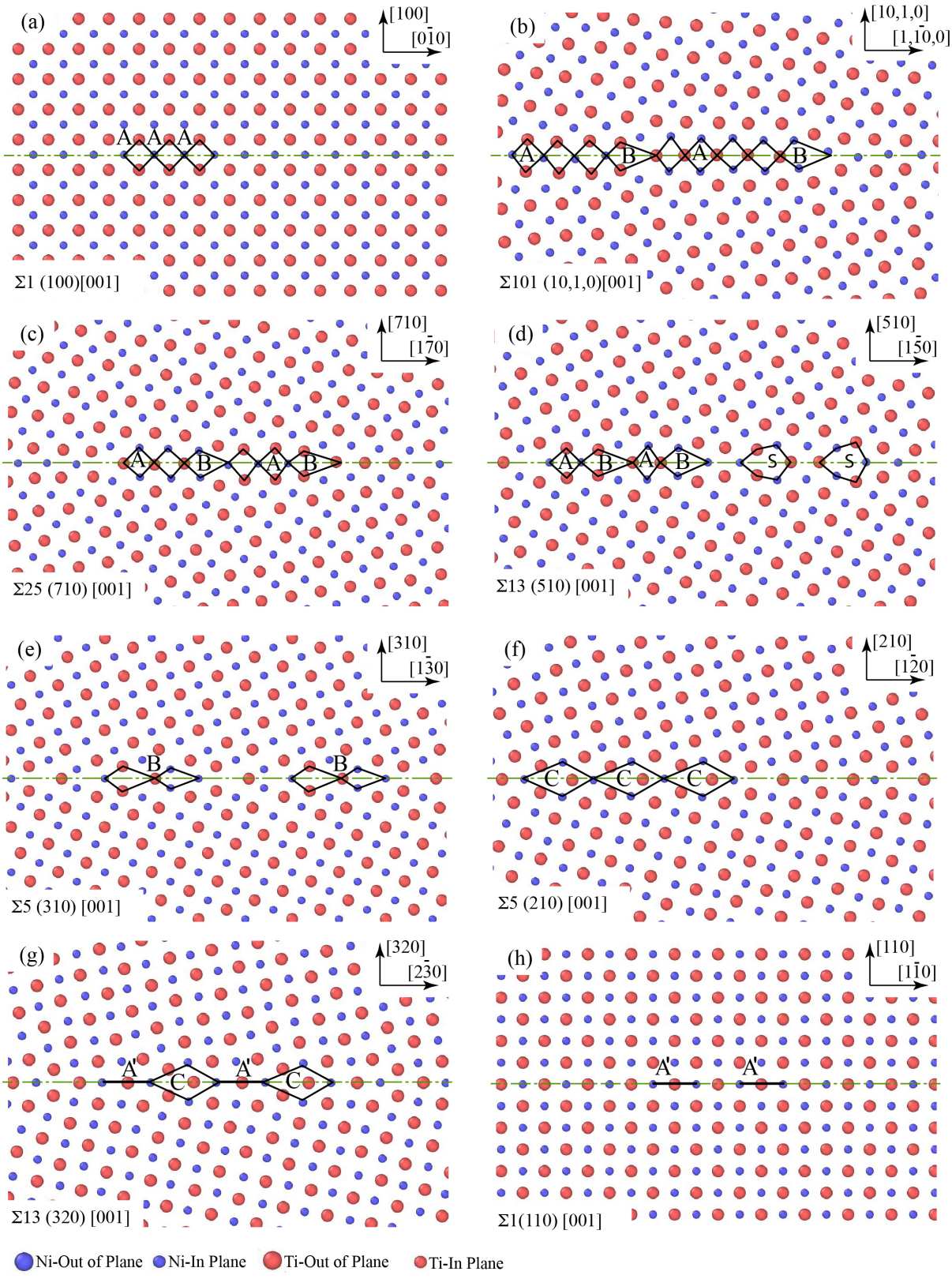

Figure 2-5. Structural units of NiTi GBs equilibrated at T=400 K for [001] tilt axis.

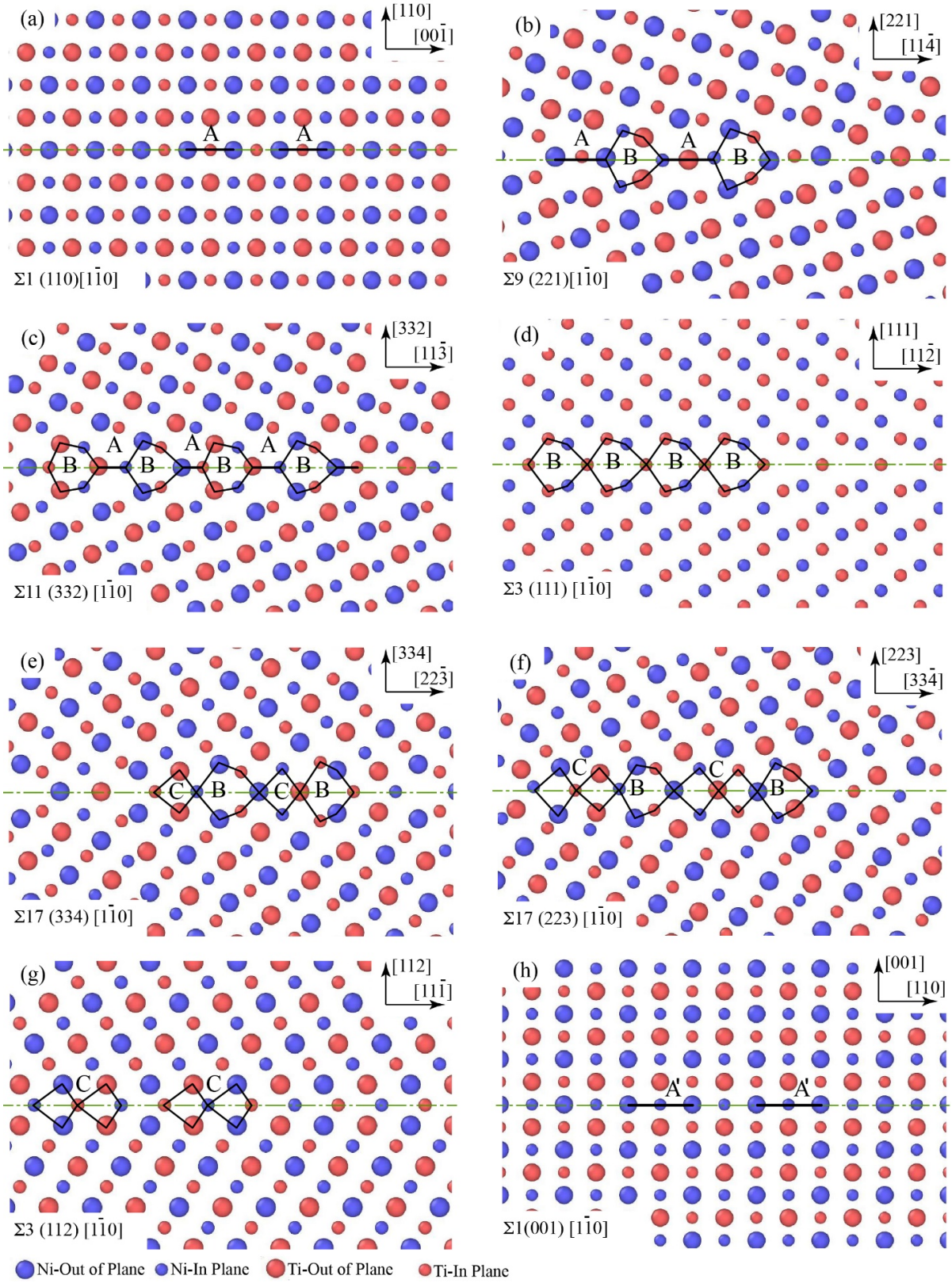

Figure 2-6. Structural units of NiTi GBs equilibrated at T=400 K for [1$\bar{1}$0] tilt axis.

2.4.4 Read-Shockley model for low angle tilt GBs in NiTi

The energy of a low angle grain boundary can be approximated as a summation of all the dislocation energies on the GB. The density of the dislocations on the GBs is a function of the misorientation angle θ and inclination angle ϕ. Having the density and the energy of a single dislocation, the GB energy E_{GB} has been calculated as a function of θ and ϕ by Read and Shockley [180]. For a symmetric grain boundary ($\phi = 0$) the energy per unit length is expressed as:

$$E_{\mathrm{GB}} = \frac{\theta}{b}\left\{\frac{Gb^2}{4\pi(1-\nu)}\ln\left(\frac{r}{r_0}\right) + \frac{Gb^2}{4\pi(1-\nu)}\left[1 + \ln\left(\frac{b}{2\pi r_0}\right)\right]\right\}, \tag{2-2}$$

where θ is the misorientation angle, G and ν are the shear modulus and Poisson ratio, respectively. Parameter r indicates the outer radius of a cylinder around each dislocation for calculating the energy, which is set to half the distance between two adjacent dislocations. The radius of dislocation core is shown by r_0. For symmetric tilt grain boundaries ($\phi = 0$) with [001] tilt axes, the grain boundary can be considered as an array of edge dislocations in $(100)[0\bar{1}0]$ system, with (100) and $[0\bar{1}0]$ being the glide plane and the burger vector, respectively. The symmetric tilt grain boundary with $[1\bar{1}0]$ tilt axes be considered as an array of edge dislocations in $(001)[110]$ system, where (001) is the glide plane and $[110]$ is the edge dislocation burger vector. For these two systems, the Read-Shokley model is used by considering the burger vectors $b = a$ and $b = \sqrt{2}a$, where a is the lattice constant (3.008 Å for NiTi). This model has been used to calculate the grain boundary energy of various materials including silicon ferrite [180], ice [181] and nickel-based super alloys [182].

In this section, we study the validity of considering the Read-Shockley model to calculate the GB energies for low angle grain boundaries in NiTi, compared to the GB energies calculated from MD simulations. This comparison for GBs with [001] and $[1\bar{1}0]$ tilt axes are shown in Figure 2-7(a) and (b), respectively.

As it is shown in Figure 2-7, the data points from MD simulations for both the tilt axes follow the Read-Shockley curve. As expected, for the low angle grain boundaries $0 \leq \theta \leq 15°\sim20°$ the data from MD simulations and theory are in a very good agreement while the difference increases for the higher misorientation angles. For obtaining the results shown in Figure 2-7 the dislocation core radii for [001] and $[1\bar{1}0]$ tilt axis are considered as $r_0 = b/3$ and $r_0 = 0.4b$ to find the best match

between the MD and Read-Shockley model results. This selection indicates that the dislocation cores shrink to a same radius in GBs with [001] tilt axes. This phenomenon has to be studied in more detail with the DFT calculations to investigate the differences in the dislocations of both grain boundaries in NiTi.

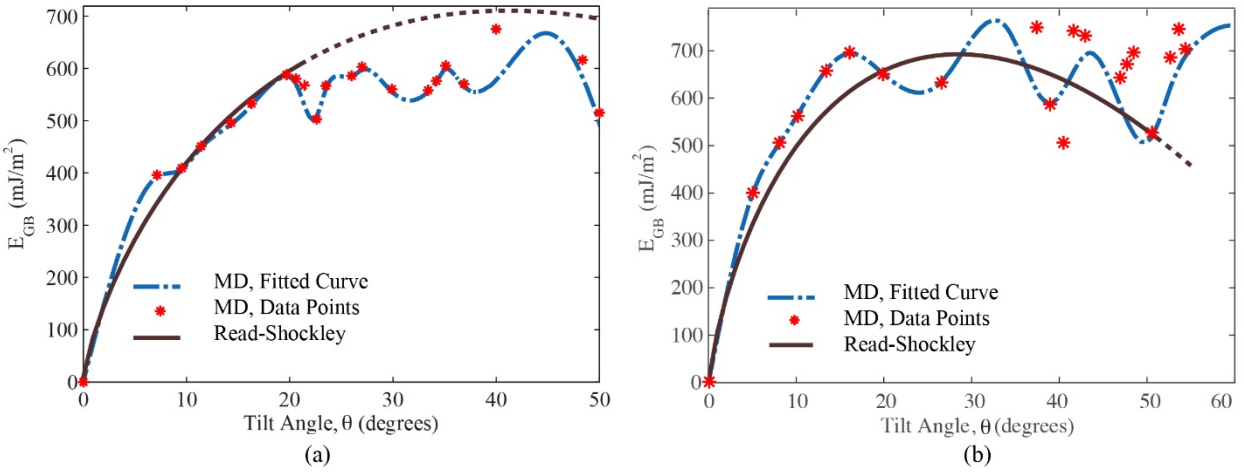

Figure 2-7. Comparison of grain boundary energies obtained from MD simulations and the Read-Shockley model for symmetric tilt grain boundaries with (a) [001] and (b) $[1\bar{1}0]$ tilt axis and the burger vectors $b = a$ and $b = \sqrt{2}a$, respectively.

2.5 Density functional theory calculations for GBs in NiTi

Two representative grain boundaries are studied in this section, and DFT calculations are used to investigate the energy, atomic relaxations, and also the electron charge density distributions at the vicinity of GB in NiTi austenite.

2.5.1 Grain boundary energy

While validating the results of empirical potentials in MD simulations against the experiments is the superior option, experimental difficulties in measuring the grain boundary energies in NiTi alloys, motivates us to use *ab-initio* calculations as an accurate alternative for experiments. Several microscopic features such as grain boundary energies, atomic forces, equilibrium structures, electron densities and band structures can be calculated accurately by density functional theory [183-187].

Two representative grain boundaries, Σ3 (112)$[1\bar{1}0]$ and Σ13 (510)[001], are selected and DFT calculations are performed to measure the GB energies. In each case, two pseudopotentials (PAW and Ultrasoft) have been used to perform *relax* and *scf* calculations. Two sets of calculations are

performed for each GB; once with the positions of atoms being fixed and in the other calculation the positions are relaxed. The change of potential energy in the system is tracked during the relaxation of atomic positions, and the solution is continued until the convergence is achieved in the potential energy. To perform a comprehensive comparison between the MD and DFT calculations for the grain boundary energies, three sets of MD simulations are considered; once with the structures minimized but the atomic position being constrained to move no more than 0.025 Å at each minimizing increment, once with minimizing when the atoms are free to move and being relaxed, and also the MD simulations at high temperature T=400 K. The grain boundary excess energies are calculated in each case by subtracting the potential energy of a perfect structure with the same number of atoms from the potential energy of equilibrated bicrystal structures. The calculated energies by different MD setting and DFT calculations are compared in Table 1 and 2. It is worth noting that both the selected representative GBs, have an ordered structure with minimal defects, since one of them is a coherent twin and the other one is a low number CSL. The ordered structures in the grain boundary enable us to perform energy minimizations at T = 0 K without triggering phase transformation to calculate the GB potential energy (see Section 2.3).

Table 2-1. Calculated energies of Σ3 (112)[1$\bar{1}$0] grain Boundary by different MD setting and DFT calculations.

Density Functional Theory (Quantum Espresso)				**Molecular Dynamic Simulation (Lammps)**		
PAW Pseudopotential		**Ultrasoft Pseudopotential**		**EAM Potential**		**EAM Potential**
Relaxed	Not Relaxed	Relaxed	Not Relaxed	Minimized	Not Minimized	T=400
362.159	488.730	331	447.336	357.065	380.510	216

Table 2-2. Calculated energies of Σ13 (510)[001] grain Boundary by different MD setting and DFT calculations.

Density Functional Theory (Quantum Espresso)				**Molecular Dynamic Simulation (Lammps)**		
PAW Pseudopotential		**Ultrasoft Pseudopotential**		**EAM Potential**		**EAM Potential**
Relaxed	Not Relaxed	Relaxed	Not Relaxed	Minimized	Not Minimized	T=400
751.288	1183.79	490.282	904.600	505.248	515.255	503

For both the selected grain boundaries, comparing the energies calculated by either PAW or Ultrasoft pseudopotentials before and after relaxations show that the relaxation of atomic positions significantly decreases the GB energies. Displacement fields of atoms during relaxations are shown in Figure 2-8(a) and(b) for (510) and (112) GBs, respectively. Arrows show the displacement trajectory of each atom during relaxation. The atoms in Figure 2-8(b), which corresponds to a coherent GB, are less displaced compared to the atoms in the (510) GB shown in Figure 2-8 (a). The atoms displacement field is directly associated with the structural units shown in Figure 2-5(d) and Figure 2-6(g). Also, the change of energy during relaxation, as shown in Tables 1 and 2, confirms the larger atomic displacements in the non-coherent grain boundary. In the next section, we will study how these relaxations at the grain boundary will affect the electron charge density distribution at the vicinity of GBs and dislocations.

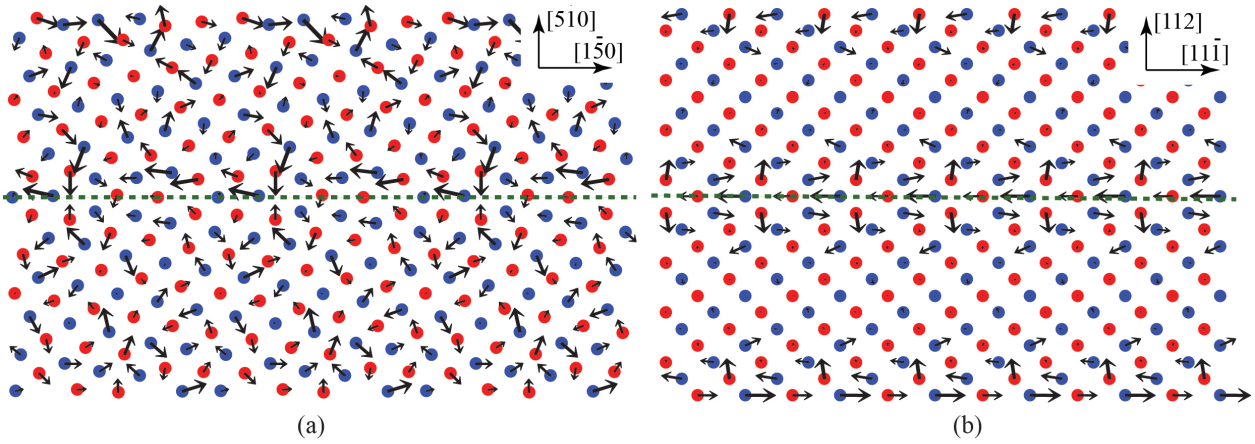

Figure 2-8. Displacement fields of atoms during relaxations for (a) (510) and (b) (112) GBs, calculated by DFT. Arrows show the displacement trajectory of each atom during relaxation.

Comparing the MD and DFT results shows that the GB energy of (112) relaxed structure calculated by the MD simulations agrees with the energies obtained from both the PAW and Ultrasoft pseudopotentials with an acceptable accuracy (with 1.3% and 7.8% errors, respectively). For the (510) GB relaxed structure, MD simulation results are closer to the Ultrasoft pseudopotential DFT calculations.

Comparing the results obtained by three different assumptions in MD simulations shows that for (510) GB, both the potential energies from minimization at T = 0 K are close to the energy obtained from equilibration at T = 400 K, while the potential energy at high temperature is slightly lower than the energy from minimization.

For the (112) coherent GB, the difference is larger and the energy calculated at T = 400 K is remarkably lower than the GB energies from minimization at T = 0 K. This phenomenon is because the atomic positions are free to relax at high temperature in austenite phase, and the movements of one of the grains (See Section 2.4.1) guaranties finding the minimum possible energy for the GBs at high temperatures. It is worth noting that for the (510) GB, the atoms require to move substantially from their initial positions to relax the structure at the grain boundary. Although the DFT calculations are predicting a correct trajectory of atomic displacements to relax the structure, the amount of final displacement predicted by DFT is still smaller than MD simulations, particularly those obtained at a high temperature. This is considered as the main reason behind the observed difference between the MD and DFT calculations for the GB energy.

2.5.2 Electron charge density distributions

Investigating the electron density distributions at GBs will facilitate better understanding how the bonding at the vicinity of a GB differs from the bulk material, which provides useful information about arrangement of dislocations at GBs, and also the diffusion along the grain boundaries. Charge density distributions for the two selected representative GBs, Σ3 (112)[$1\bar{1}0$] and Σ13 (510)[001], are shown in Figure 2-9. The charge density distributions are shown on two planes perpendicular to the tilt axis, one through the atomic plane (z = 0, where z is the coordinate in the direction of tilt axes) and another plane through the layer between the two atomic planes (z=a/2) for both GBs. The insets on each figure show the charge density distribution on two horizontal lines passing through the grain boundary (solid black line), and passing through the bulk region (dashed red line). Figure 2-9(a) shows the density distribution on the z = 0 plane passing through the atoms, which contains both Ni and Ti atoms, for the (112) coherent twin boundary. Electron densities around Ni atoms are greater compared to the Ti atoms in this configuration. Figure 2-9(b) shows the electron distribution on the layer between the atomic planes. In this layer, at the vicinity of the grain boundary line, the structural units which contain three Ni and one Ti atoms (see Section 2.4.3) have lower charge densities inside the structural unit compared to those having three Ni and one Ti atoms. Comparing the distributions between the GB and bulk regions (see the insets) shows a slight decrease in the charge densities near the grain boundary on both z = 0 and a/2 planes which corresponds to the bond weakening on the grain boundary. The large areas with low charge density in the structural units observed in Figure 2-9(b) might act as the initiation sites for the temperature- or stress-induced phase transformation due to the weak bonding between the atoms. Figure 2-9(c)

shows the electron distributions of (510) GB on the $z = 0$ plane, which only contains Ti atoms. A homogenous electron distribution is observed since all the atoms are of the same type. The inset shows more peaks in the charge density distribution on the grain boundary compared to the bulk region, due to the arrangement of the atoms to create the mirror plane on the GB. Charge density on the $z = a/2$ plane is shown in Figure 2-9(d). The distribution on the grain boundary line is compared with the bulk region in the inset. The maximum value of the charge density is lower at the grain boundary compared to bulk material, but the distribution is more uniform and multiple frequent peaks are added to the distribution. This phenomenon can be expressed by considering the arrangement of Ni and Ti atoms at this GB (see Figure 2-5(d)). While the (510) GB consists of repeated SUs A and B, an alternative structural unit can be considered for this GB (shown with S on both Figure 2-9(d) and Figure 2-5(d). Each of these structural units S contains three Ni and three Ti atoms. Compared to a structural unit with non-equal number of Ni and Ti atoms (i.e. see C units in Figure 2-9(b) with Three Ni and one Ti atoms), the S units have a more uniform distribution of electrons inside the structural unit, mainly because the non-uniformity in the electrons distribution originates from the difference of Ni and Ti atoms in attracting the electrons. A more uniform charge density distribution on the grain boundary is associated with a uniform distribution of bond strengths. Since the bond strengths are distributed uniformly in the bulk material, having a more uniform distribution of bonds in the grain boundary will be associated with a smaller difference between the stress distributions in the grain boundary and the bulk material when the system is subjected to an external load [187]. In this case, reduction of the stress concentration at the grain boundaries will improve the mechanical properties in a polycrystalline material. This phenomenon makes any of the grain boundaries with more uniform structural units (and consequently more uniform distribution of charge densities), i.e. the Σ13 (510)[001] or Σ5 (210)[001] GBs, a good candidate in a grain boundary engineering optimization. It is worth noting that investigating a comprehensive list of grain boundaries with a uniform charge density distribution in NiTi systems requires several DFT calculations of various GBs, and the selected studies in this section are only two representative samples.

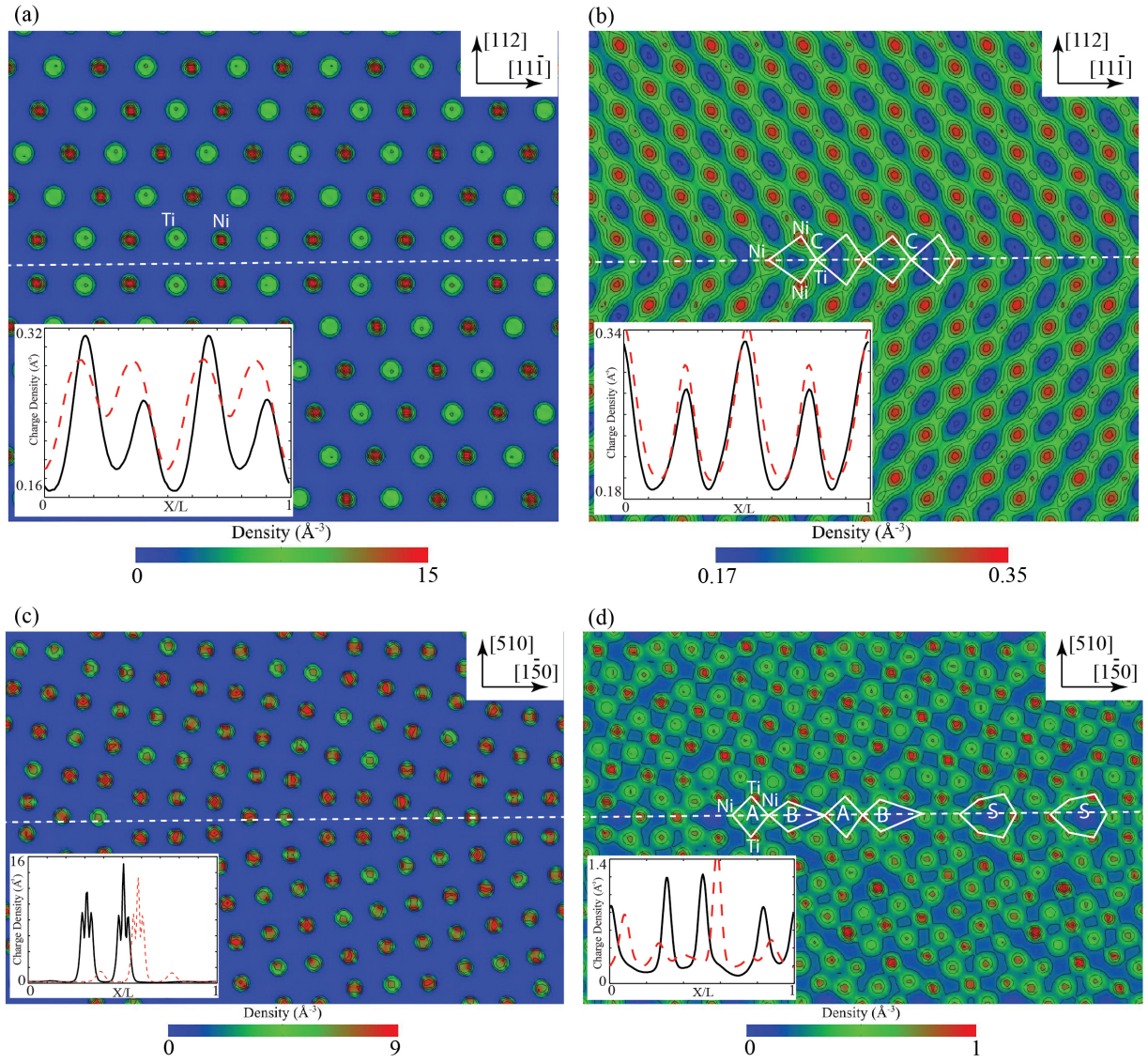

Figure 2-9. Charge density distributions for the two selected representative GBs, Σ3 (112)[1$\bar{1}$0] and Σ13 (510)[001]. (a) The density distribution on the z=0 plane passing through the atoms, which contains both Ni and Ti atoms, for the (112) coherent twin boundary and (b) the electron distribution on the layer between the atomic planes for the (112) coherent twin boundary. (c) The electron distribution of (510) GB on the z=0 plane, which only contains Ti atoms and (d) charge density of (510) GB on the z=a/2 plane. Insets show the charge density distribution on a line passing through the GB (solid black lines) and a line parallel to the GB in the bulk material (dashed red lines).

2.6 Conclusions

Molecular dynamics (MD) simulations and density functional theory (DFT) calculations are utilized to investigate the energy and structure of symmetric and asymmetric tilt grain boundaries (GBs) in austenite NiTi shape memory alloys. The grain boundaries excess energies are calculated as a function of the inclination and misorientation angles. The structural units at the grain boundary

are identified and the correlation between the structure and grain boundary energy is studied. It is shown that the Read-Shokley model can predict the energy of low angle tilt grain boundaries in NiTi with an acceptable accuracy by considering appropriate dislocation core radii at different orientations. Two representative symmetric GBs are studied by DFT calculations. The MD results are validated against DFT, and the electron charge density distribution at the grain boundaries are compared with the bulk material to study the bonding strengths at the grain boundaries.

Chapter three of this work includes a published paper in **Journal of Alloys and Compounds journal**. The title of work is: **Generalized stacking fault energy and dislocation properties in NiTi shape memory alloys**. The author acknowledges the publisher of the work, **Elsevier** for giving the right to include the article in this dissertation which is not provided to be published commercially.

Chapter 3. Defects in NiTi Shape Memory Alloys

3.1 Overview

Dislocations in the austenite phase of Nickel-Titanium (NiTi) shape memory alloys (SMAs) are of critical importance mainly due to their connection to the unrecoverable strains accumulated in SMAs during cyclic loadings, and also the key role of dislocations in the structure and energy of grain boundaries in these alloys. In this chapter, we investigate the energy and structure of dislocations, and also the generalized stacking fault energies in NiTi austenite by implementing molecular dynamics (MD) simulations. Through our results the validity and accuracy of three different potentials, two EAM potentials with different cutoff radii and one 2NN MEAM potential, for studying defect related properties of NiTi alloys is investigated. It is shown that while none of these potentials are particularly trained for predicting defect properties in NiTi systems, they can be efficiently utilized to study the stacking fault energies, the energy and structure of edge dislocations, stress distributions at the vicinity of edge dislocations, and even the details of dislocation dissociation in NiTi austenite phase. Particularly our results can be used as a tool to select the appropriate potential for studying any problem related to a specific aspect of defects in austenite NiTi SMAs.

3.2 Materials and Methods

3.2.1 Potentials

In this chapter, the accuracy and capability of three different potentials in studying defect-related phenomena in NiTi alloys are studied. For this purpose, we consider two commonly used EAM potentials, and also a recently developed 2NN MEAM potential. In the following sections, SFE and the energies of various dislocations for different crystal orientations in NiTi alloys are studied using these three potentials in MD simulations. Results are compared and validated against theoretical and DFT calculations.

EAM Potential with cutoff radius $r_c = 4.2$ Å

One of the most widely used many-body interatomic potentials for NiTi binary alloys is the EAM potential which was originally developed and evaluated by Lai and Liu [165]. This potential was later improved with a smooth cutoff behavior to avoid the diverging forces in simulations

involving large atomic displacements [93]. This Finnis-Sinclair potential computes pairwise interactions for the alloy using a generalized form of EAM potentials. The total energy of the system is expressed as [93]:

$$E = \sum_i \left\{ \sum_{j \neq i} A_{\alpha\beta} \exp\left[-p_{\alpha\beta} \left(\frac{r_{ij}}{d_{\alpha\beta}} - 1 \right) \right] - \sqrt{\sum_{j \neq i} F(r_{ij})} \right\}, \tag{3-1}$$

where, the first term in the curly bracket describes the pair interaction, the second term represents the many-body effect, and

$$F(r_{ij}) = \xi_{\alpha\beta}^2 \exp\left[2q_{\alpha\beta} \left(\frac{r_{ij}}{d_{\alpha\beta}} - 1 \right) \right]. \tag{3-2}$$

Parameters α and β represent the element types (here Ni and Ti) of atoms *i* and *j*. The distance between atoms *i* and *j* is denoted by r_{ij}. The parameters in this potential for describing a NiTi alloy (i.e. values for Ni-Ni, Ti-Ti, and Ni-Ti interaction) are fitted to the properties of a cubic NiTi system at 0 K [165]. Since the function $F(r_{ij})$ and its derivative with respect to r_{ij} are nonzero at the cutoff radius, in order to smooth the interatomic forces and energies in the molecular dynamics model we use the following modification on this function [93]:

$$F(r_{ij}) = \begin{cases} \xi_{\alpha\beta}^2 exp\left[2q_{\alpha\beta} \left(\frac{r_{ij}}{d_{\alpha\beta}} - 1 \right) \right], & r_{ij} \leq r_1, \\ c_{3,\alpha\beta}(r_{ij} - r_1)^3 + c_{2,\alpha\beta}(r_{ij} - r_1)^2 + c_{1,\alpha\beta}(r_{ij} - r_1) + c_{0,\alpha\beta}. & r_1 < r_{ij} \leq r_c, \end{cases} \tag{3-3}$$

where the four coefficients $c_{i,\alpha\beta}$, *i*=1,2,3,4 are determined by imposing the continuity conditions on $F(r_{ij})$ and its first derivative at r_1 and r_c. The coefficients for this potential have been calculated and reported by Zhong *et al*. [93] for a cutoff radius $r_c = 4.2$ Å.

EAM Potential with cutoff radius $r_c = 5.2$ Å

Another many-body interatomic potential for NiTi binary alloy is embedded atom potential which was originally developed by Ren and Sehitoglu [99]. This recently introduced potential is also Finnis–Sinclair type expressing the total potential energy as:

$$E = \sum_{i=1}^{N-1} \sum_{j=i+1}^{N} \phi_{t_i t_j} r_{ij} + \sum_{i=1}^{N} F_{t_i}(\bar{\rho}_i), \tag{3-4}$$

where,

$$\bar{\rho}_i = \sum_{j} \rho_{t_i t_j}(r_{ij}). \tag{3-5}$$

The element types of atoms i and j are denoted by t_i and t_j, respectively. The distance between atoms i and j are expressed as r_{ij}. The pair interaction between atoms i and j is denoted by $\phi_{t_i t_j} r_{ij}$, and $F_{t_i}(\bar{\rho}_i)$ is the embedding energy function which is a function of host electron density $\bar{\rho}_i$, inducing by all the other atoms. Both $\phi_{NiTi}(r)$ and $\rho_{NiTi}(r)$ are constructed to match the properties of NiTi alloy using the cubic spline form:

$$f(r) = \sum_{i=1}^{N_i} a_i (r_i - r)^3 H(r_i - r), \tag{3-6}$$

in which $H(r)$ is the Heaviside step function definde as:

$$H(x) = \begin{cases} 1 & for\ x \geq 0 \\ 0 & for\ x < 0. \end{cases} \tag{3-7}$$

The coefficients a_i and r_i for this potential are calculated and reported by Ren and Sehitoglu [99] for a cutoff radius $r_c = 5.2$ Å. Increasing the cutoff radius from 4.2 Å to 5.2 Å incorporates forth nearest neighbors in B2 NiTi lattice, which can significantly improve the potential accuracy.

2NN MEAM Potential with cutoff radius $r_c = 5.0$ Å

The MEAM potential was originally developed and proposed by Baskes [188] as a modified form of EAM potential by considering additionally angular dependent terms. This potential was later improved by Lee and Baskes [189] by introducing 2NN MEAM potentials. In order to overcome some critical weaknesses of the original MEAM approach, they partially considered 2NN interactions in MEAM description. Recently, Ko *et al*. [190] have developed a 2NN MEAM potential for NiTi binary system. In this potential the total energy of the system is expressed as:

$$E = \sum_i \left[F_i(\bar{\rho}_i) + \frac{1}{2} \sum_{j(\neq i)} S_{ij} \phi_{ij}(R_{ij}) \right], \quad (3\text{-}8)$$

where R_{ij} is the distance between atoms i and j. The screening function and the pair interaction between atoms i and j as a function of R_{ij} are denoted by S_{ij} and ϕ_{ij}, respectively.

The functional form of the background electron density $\bar{\rho}_i$ needs to be defined in order to calculate the embedding energy. Since additional angular terms are considered for the directional character of bonding in MEAM approach, the background electron density is computed by combining several partial electron density terms for different angular contributions with weighting factors $t^{(h)}(h = 1 - 3)$. Each partial electron density is a function of atomic configuration and atomic electron density. The atomic electron density $\rho^{a(h)}(h = 0 - 4)$ is expressed as:

$$\rho^{a(h)}(R) = \rho_0 \, exp\left[-\beta^{(h)} \left(\frac{R}{r_e} - 1 \right) \right], \quad (3\text{-}9)$$

where r_e is the nearest-neighbor distance in the equilibrium reference structure. The adjustable parameters ρ_0 and $\beta^{(h)}$ are atomic electron density scaling factor and the decay lengths, respectively. The coefficients of this potential for NiTi system are calculated and reported by Ko *et al.* [190] for a cutoff radius $r_c = 5.0$ Å.

It is worth noting that among the three selected potentials in this study, the first two EAM potentials are both ignoring any angular dependency. Some technical difficulties have been observed in the application of a many body central force potentials to defect related problems, mainly because in the formation of dislocations, and also at the vicinity of defects such as grain boundaries there are some regions with a structure far from the ideal lattice. For transition metals and their alloys, directional bonding might have a significant effect on the response of material, and this effect is more severe in the case of having a non-perfect lattice. By this, implementing a Finnis-Sinclair potential for studying the NiTi system has to be accompanied with special caution. The third potential selected here has the angular dependency, which is presumably more accurately for studying defects in NiTi system. However, since none of these potentials has been specifically trained for studying defects in NiTi system, our results in the following sections will show in most

cases the central force EAM potentials are even more accurate. Although in some cases the MEAM potentials is more accurate compared to the EAM potentials.

3.2.2 Molecular Dynamics Simulations

Large-scale Atomic/Molecular Massively Parallel Simulator (LAMMPS) [167] is utilized for performing the simulations, and Ovito [168] visualization tool is used for post-processing the results of MD simulations. Two EAM and one 2NN MEAM potentials (Section 3.2.1) for the NiTi binary alloy are used to compute dislocation energy and SFE. Conjugate gradient method in three dimensional computational cells is used to minimize the structural energy. The boundary condition used for computing SFE is periodic, periodic and free surface in the x (glide direction), y (in the glide plane), and z (perpendicular to the glide plane) directions, respectively. For calculating the dislocation energy, the three dimensional periodic computational cells are used. All the molecular dynamics simulations to calculate the SFE (Section 3.3) and dislocation energy (Sections 3.4 and 3.5) are performed at the temperature T = 0 K. More details of the simulations are given in each section.

3.3 Stacking Fault Energy

A perfect crystal is made of stack of atom layers, which are arranged in a regular sequence. A stacking fault is a planar defect which interrupts the regular stacking sequence in the crystal [67]. Hence, stacking fault terminates the perfect stacking sequence in the crystal. The energy per unit area associated with this planar defect is called stacking fault energy [67]. In this section, stacking faults are created in a perfect NiTi structure, and the subsequent fault energies are investigated. Two blocks of atoms are used in two sets of MD simulations in which the top half of the crystal is rigidly displaced, while the lower half remains fixed. The displacement is applied along the x direction (glide direction) for $(011)[100]$, $(011)[1\bar{1}1]$, $(011)[0\bar{1}1]$, and $(001)[100]$ systems. Two different configurations are considered and before applying the displacement in one set of simulations the crystal is relaxed in three directions (relaxed structure), while in the other set the crystal is only allowed to relax in z direction (unrelaxed structure). The cell sizes in these systems are $\sim 46 \times 46 \times 44$ Å. After each incremental displacement in the x direction, the crystal is allowed to relax in the z direction, and then the stacking fault energy is calculated. The results obtained from the three selected potentials in MD simulations are compared to the DFT results provided by Ezaz *et. al* [6]. In their study, DFT calculations are performed to examine the

generalized stacking fault energy curves for $\{001\}$, $\{\bar{2}11\}$, and $\{001\}$ planes. The slip directions considered in DFT calculations are $\langle 100\rangle$, $\langle 111\rangle$, and $\langle 011\rangle$. It has also been shown that the DFT results are consistent with the experimental observations of dislocation slip [6].

The stacking fault energy curves for the relaxed structures and unrelaxed structures are shown in Figure 3-1 and 2, respectively. The horizontal axis shows gliding distance, and the vertical axis denotes stacking fault energy per unit area, mJ/m^2. The SFE curves exhibit a semi-sinusoidal shape as expected and predicted by DFT calculations [6]. For the relaxed structures of (011) $[100]$, (011) $[1\bar{1}1]$, (011) $[0\bar{1}1]$, and (001) $[100]$ systems, the SFE curves obtained from each potential are shown in Figure 3-1(a), (b), (c) and (d), respectively.

For $(011)[100]$ system, the stacking fault energy, γ_{sf}, predicted by DFT is $142\ mJ/m^2$. Comparing the SFE results of the three considered potentials, all the MD simulations predict a higher energy, although the EAM with $r_c = 4.2$ Å predicts a closer value to the DFT calculations. However, for $(011)[1\bar{1}1]$ system, the stable stacking fault energy, γ_{sf}, computed by all the three MD simulations is approximately $515\ mJ/m^2$ which is identical to the calculated energy from DFT. The resulted unstable stacking fault energy, γ_{us}, of DFT for this system is $660\ mJ/m^2$. The unstable stacking fault energy computed by 2NN for this system is remarkably higher ($\sim 1300\ mJ/m^2$), while both the EAM potentials predict an energy very close to the DFT calculations. For both (011) $[0\bar{1}1]$ and (001) $[100]$ systems shown in Figure 3-1(c) and (d), the EAM potential with the smaller cutoff radius underestimates the SFE while the 2NN potential overestimates the energy. The EAM potential with $r_c = 5.2\ A°$ predicts almost the same value as DFT calculations in the former system, yet, it overestimates the energy in the latter.

In the SFE curves of the unrelaxed structure shown in Figure 3-2, both the 2NN potential and the EAM potential with smaller cutoff radius, overestimate the SFE. The EAM potential with the larger cutoff radius predicts the SFEs of (011) $[1\bar{1}1]$, (011) $[0\bar{1}1]$ systems (Figure 3-2(b) and (c)) very close to the DFT calculations, while it still overestimates the energy for (011) $[100]$ and (001) $[100]$ systems (Figure 3-2(a) and (d)).

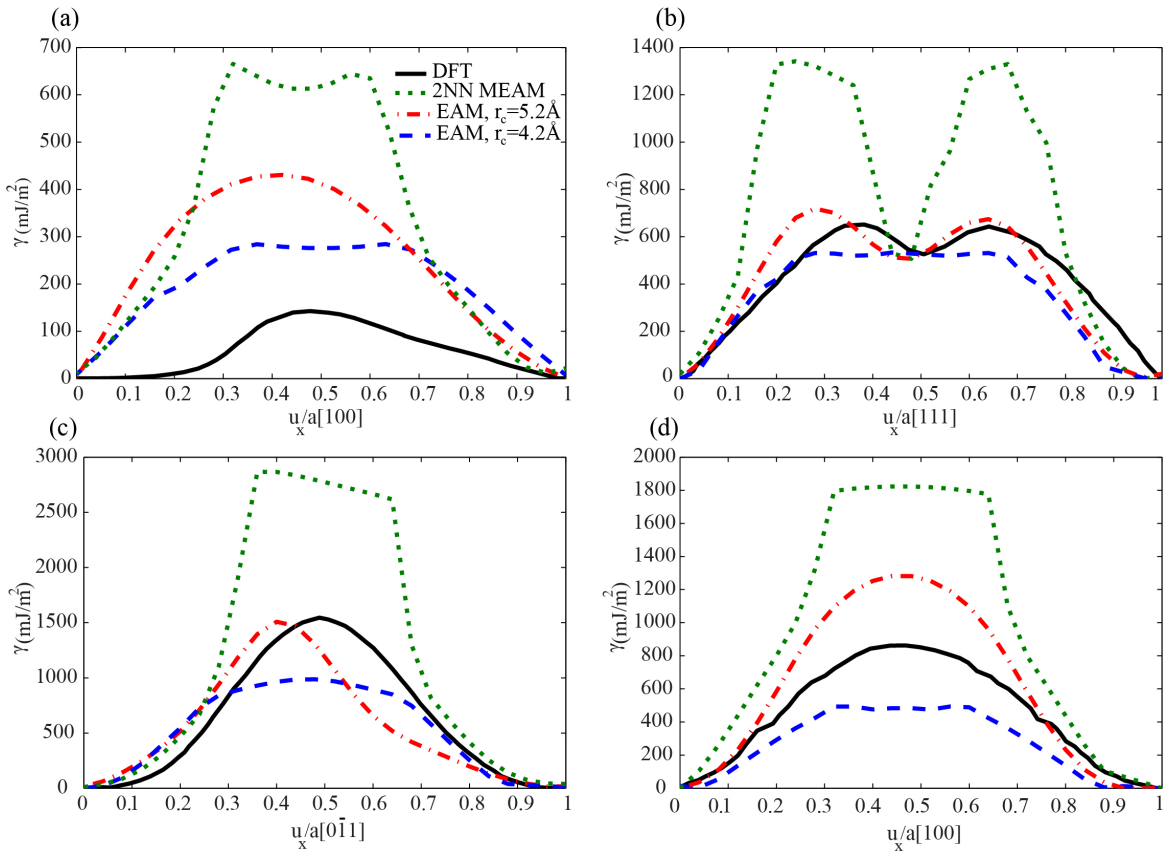

Figure 3-1. Stacking Fault Energy curves obtained from DFT calculations and MD simulations for NiTi relaxed structure with three different potentials: EAM with $r_c = 4.2$ Å, EAM with $r_c = 5.2$ Å, and 2NN MEAM with $r_c = 5$ Å. Four systems are considered to compute the SFE with the three different potentials: (a) System (011) [100], (b) System (011) [1$\bar{1}$1], (c) System (011) [0$\bar{1}$1], and (d) System (001) [100].

As observed, the 2NN potential overestimates the energy in all the simulations and except for the stable stacking fault energy in (011) [1$\bar{1}$1] system, all the other predictions are not in a good agreement with the DFT calculations. This is highly affected by the training set of the potential, and by considering more defects related parameters in the training set, the accuracy of this MEAM potential can be significantly improved. In contrast, both the EAM potentials compute consistent results with the DFT calculations. Moreover, as expected, the EAM potential with the larger cutoff radius results in energies slightly closer to the DFT, compared to the EAM with the smaller cutoff radius. Considering the considerable computational cost associated with adding extra neighbors in the potential with a large cutoff, and the small differences between the results of the two EAM potentials, the EAM potential with the smaller cutoff radius can be considered as an efficient and accurate choice. Considering the stacking fault energy, and a comprehensive set of defect related

parameters in the training procedure of any of these potentials could significantly improve the predicted values for SFEs. This is the topic of a future communication by the authors.

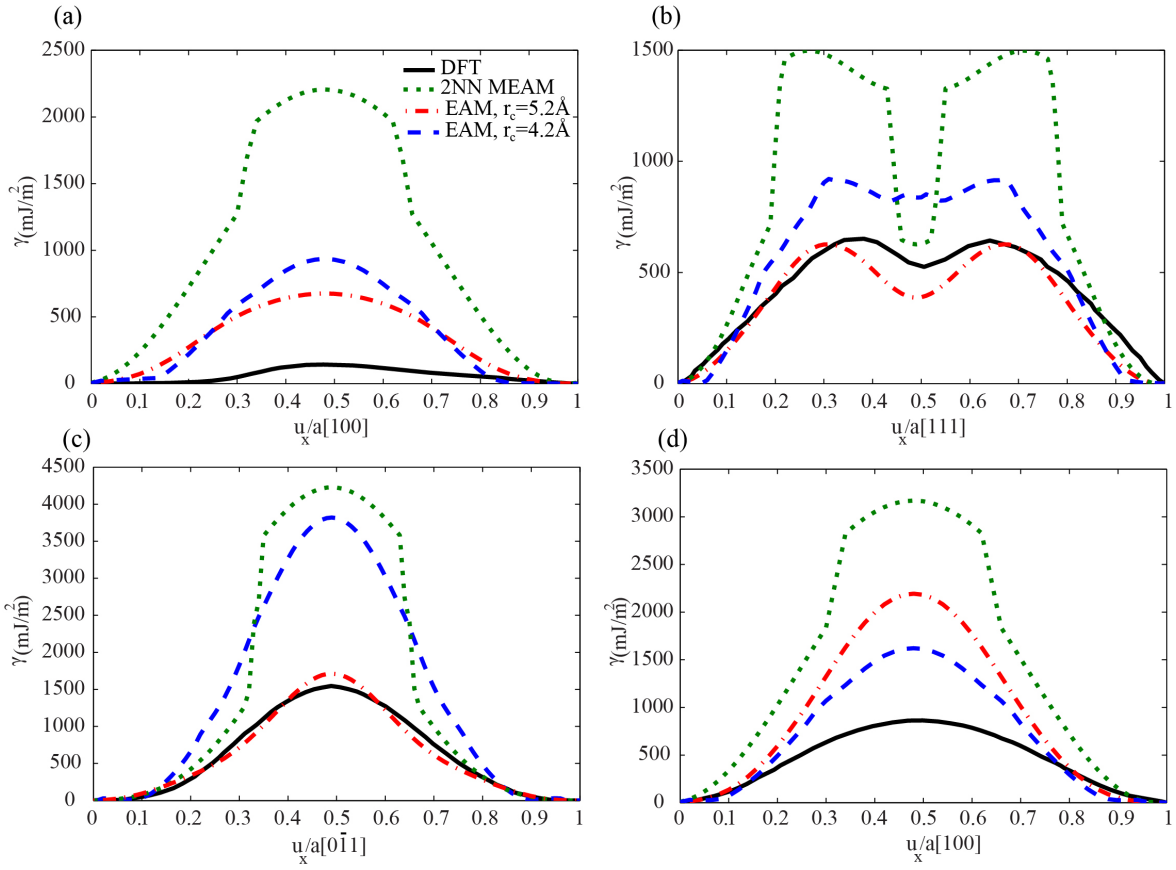

Figure 3-2. Stacking Fault Energy curves obtained from DFT calculations and MD simulations for NiTi unrelaxed structure with three different potentials: EAM with $r_c = 4.2$ Å, EAM with $r_c = 5.2$ Å, and 2NN MEAM with $r_c = 5$ Å. Four systems are considered to compute the SFE with the three different potentials: (a) System (011) [100], (b) System (011) [1$\bar{1}$1], (c) System (011) [0$\bar{1}$1], and (d) System (001) [100].

3.4 Dislocations Structure and Energy

The generalized SFE curves are primary factors in predicting the microstructural properties of materials. For instance, the SFE curves are responsible for determining the core width, stacking fault width, and mobility of dislocations [79]. Moreover, they can be used to predict the dislocation slip [80]. The maximum shear stress required to rigidly move one plane of atoms on the adjacent plane, which is called theoretical critical shear strength, can be obtained by taking the maximum slope of the SFE curves [67, 80]. In this section, several possible dislocation slip systems are

investigated and the dislocation energy of these systems are computed by the three potentials described in Section 3.2. Then, the calculated energies are validated against theory of elasticity.

There are two main issues associated with MD simulation of dislocation structures. First, the minimum number of dislocations in a fully periodic simulation cell should be two, *i.e.* a dislocation dipole should be considered. This way, the net burger vector in the periodic simulation cell will be zero and the periodicity can be applied to the boundaries. Second, it should be considered that the two dislocations in a dipole not only interact with each other but also interact with their periodic images. Hence, extra calculations of strain, forces, and energy should be considered. Cai and Bulatov [191] have developed a code (MD++) in order to simulate dislocation dipoles by considering both these issues. They have established a mathematically consistent and numerically efficient procedure for regularization of the lattice sums and the corresponding image fields [192]. This code has been used to construct the initial structure of all the dislocations in the present work, while all the energy calculations are performed by LAMMPs with the details given in Section 3.2.

The dislocation dipole structure is created in an atomistic simulation cell with full 3D periodic boundary conditions. As the first step in simulating a dipole containing two edge dislocations, a rectangular atomic cell with an orthogonal box is created. Then, a layer of atoms is removed and all other atoms are displaced according to the linear elastic displacement field of a dislocation dipole in a periodic cell [67, 193]. The displacement field of an infinite edge dislocation in an isotopic elastic medium is represented as [193]:

$$u_x(x,y) = \frac{b}{2\pi}\left[\theta(x,y) + \frac{xy}{2(1-\upsilon)(x^2+y^2)}\right], \tag{3-10}$$

$$u_y(x,y) = -\frac{b}{2\pi}\left[\frac{1-2\upsilon}{4(1-\upsilon)}ln(x^2+y^2) + \frac{(x^2-y^2)}{4(1-\upsilon)(x^2+y^2)}\right], \tag{3-11}$$

$$u_z(x,y) = 0, \tag{3-12}$$

where b is the burger vector (in x direction). Poisson's ratio and the angle between x axis and the vector connecting the origin to point $(x, y, 0)$ are denoted by υ and θ, respectively. After applying the displacement field, the structure is exported to LAMMPS. Then, the structure is relaxed using the conjugate gradient relaxation method and the energy of the dislocation dipole is calculated. It

is worth noting that in all cases, the energy of a system with defects is compared against a perfect system with the same number of atoms to calculate the excess energy of the defects.

The energies of dislocation dipoles as a function of separation distance are shown in Figure 3-3 for $(01\bar{1})[100]$, $(010)[100]$, and $(011)[0\bar{1}1]$ systems. The results from MD simulations are compared and validated against calculations from elasticity theory. The energy of one dislocation based on theory of elasticity is expressed as [67]:

$$E_{el}(edge) = \frac{Gb^2}{4\pi(1-\upsilon)} ln\left(\frac{R}{r_0}\right), \tag{3-13}$$

where b, G, υ, R, and r_0 are burger vector, shear modulus, Poisson's ratio, crystal radius, and core radius, respectively. The crystal radius in each dipole, is considered as half of the separation distance, i.e. the distance between two dislocations. The core radius depends on the burger's vector. We consider the values of $b/3$ for $(01\bar{1})[100]$ and $(010)[100]$ systems, and $4b/10$ for $(011)[0\bar{1}1]$ system for the core radius, and use the following expression from theory of elasticity to calculate the core energy [67, 180]:

$$E_{core}(edge) = \frac{Gb^2}{4\pi(1-\upsilon)}\left[1 + ln\left(\frac{b}{2\pi r_0}\right)\right]. \tag{3-14}$$

By the selecting the above mentioned values for the core radius, in all the systems the calculated core energies are ~10% of the dislocation energy, which is constant with the expected value from theory and experiments [194]. The dislocation energies calculated from MD simulations and the theoretical expression for different separation distances of $(01\bar{1})[100]$, $(010)[100]$, and $(011)[0\bar{1}1]$ systems are shown in Figure 3-3(a), (b) and (c), and the corresponding structures (around one of the dislocations in the dipole) are shown in Figure 3-3(d), (e) and (f). The 2NN potential in all the three systems, significantly overestimates the dislocation energy. In the $(01\bar{1})[100]$ system, the two EAM potentials predict almost same values of energy, yet slightly higher than the elasticity results. However, in $(010)[100]$ system, the results of the EAM potential with $r_c = 5.2$ Å are in a good agreement with the elasticity results, but the EAM potential with the lower cutoff radius still overestimates the energy.

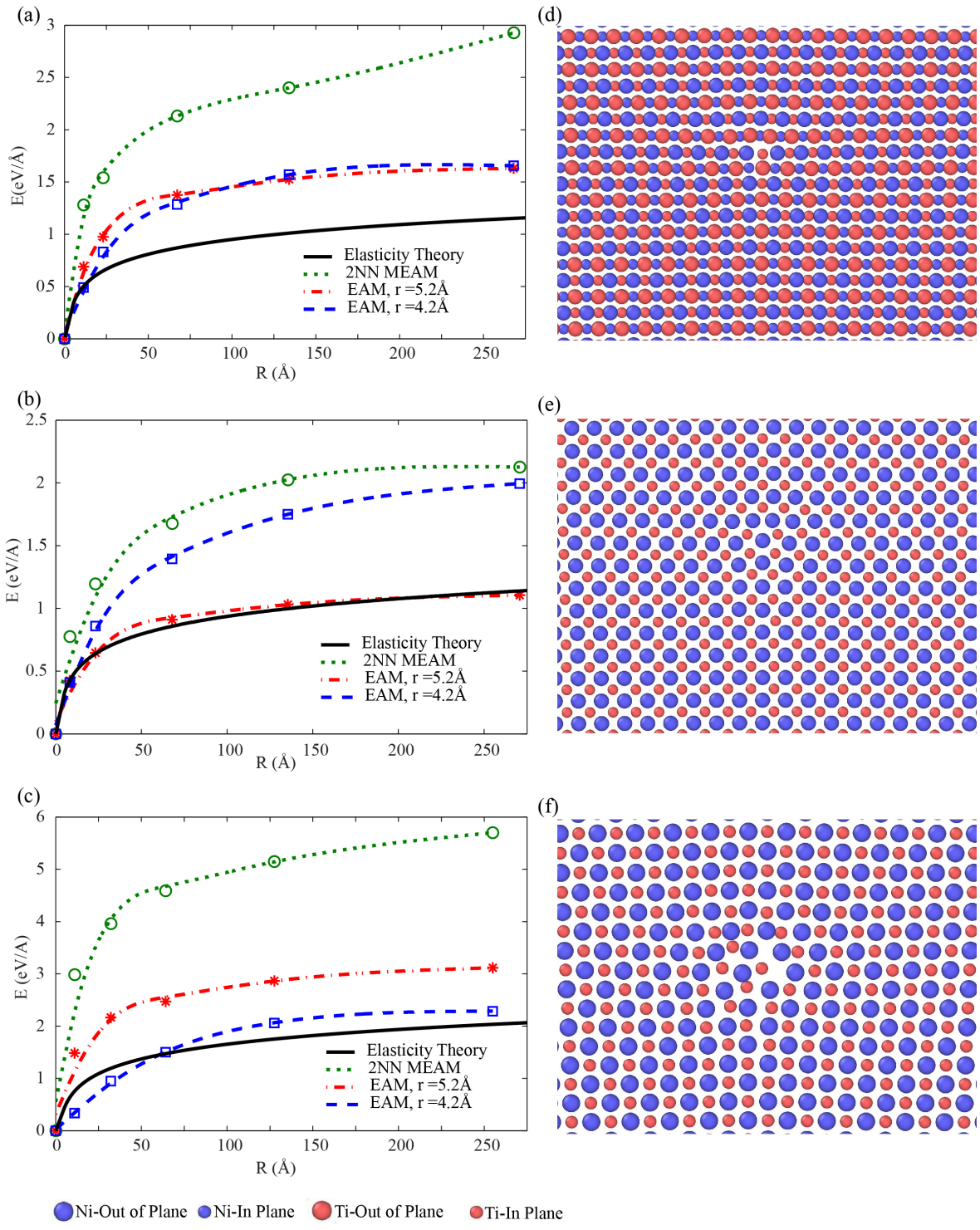

Figure 3-3. The energy of edge dislocations in a dipole as a function of separation distances (R is half of the distance between two dislocations in a dipole) for (a) $(01\bar{1})[100]$, (b) $(010)[100]$, and (c) $(011)[0\bar{1}1]$ systems computed by EAM with $r_c = 4.2$ Å, EAM with $r_c = 5.2$ Å, and 2NN MEAM with $r_c = 5$ Å potentials. The relaxed dislocation structures are shown for (d) $(01\bar{1})[100]$, (e) $(010)[100]$, and (f) $(011)[0\bar{1}1]$ systems.

In contrary, for $(011)[0\bar{1}1]$ system, the EAM potential with $r_c = 4.2$ Å predicts the same results as elasticity theory while the other EAM potential overestimates the energy. We will focus on the two EAM potentials in the rest of this study.

In this section, three relatively low energy dislocation systems in B2 NiTi alloy were discussed. In some dislocation systems with higher energies dislocation can dissociate into partials. Through dissociation, the dislocation splits into partial dislocations with a stable equilibrium distance and comprising smaller burger vectors. In the next section dislocation dissociation for $(0\bar{1}1)[111]$ system will be discussed.

3.5 Dislocation Dissociation

Dislocations may decompose into perfect dislocations with smaller burger vectors, and a stable equilibrium distance. This procedure happens in order to reduce the total energy of the system. It has been shown through DFT calculations that dissociation is energetically favorable in $(0\bar{1}1)[111]$ systems [6]. The burger vector dissociation in this system is expressed as:

$$a\langle 111\rangle \rightarrow a\langle 100\rangle + a\langle 011\rangle. \tag{3-15}$$

During the splitting procedure, two main energies interact with each other. The first energy is due to the repulsing interaction between the two partial dislocations. This energy changes approximately proportional to $1/d$, where d is the distance between the partial dislocations. Moreover, as a result of the splitting procedure, a stacking fault appears between the two partial dislocations with energy proportional to d. The partial dislocations tend to reduce the distance d to minimize the stacking fault energy, while having a larger distance will minimize the replacing energy. Hence, there is an equilibrium distance between the partial dislocations, which corresponds to the minimum total energy. In this study, in addition to studying the structure and energy of dislocation dissociation in NiTi, we also perform MD simulations with two EAM potentials to find the equilibrium distance between the partial dislocations in the above mentioned system. A series of MD simulations are performed with each potential, and the energy is calculated as a function of the distance between partials to obtain the equilibrium distance resulting in the minimum structural energy. The selected trial distance varies between 5.5 Å and 10.5 Å to find the lowest energy configuration. The energy as a function of the partials distance is shown in Figure 3-4(a), and the equilibrium distance is obtained at $d = 7.95$ Å for both the potentials.

The dissociated dislocation is created with the distance of 7.95 Å between the two partials in the $(0\bar{1}1)[111]$ system. It is worth nothing that although the initial dislocation is from edge type, the two partials are both mixed with edge and screw components. In order to apply the elastic theory displacement field on the structure, MD++ code is once utilized to create each partial dislocation, and the displacement of all the atoms are calculated. Then the displacements on all the atoms resulting from each of the two partial dislocations are superposed to obtain the structure with the displacement field corresponding to both the partials. This structure is exported to LAMMPS, and relaxed using the conjugate gradient relaxation method. The final structure of relaxed dissociated dislocation is shown in Figure 3-4(b).

Two sets of MD simulations are performed using the two EAM potentials. As a result, after energy minimization the disregistry and density curves are obtained and shown in Figure 3-4(c) and (d), respectively. The disregistry curve shows that both the potentials predict very close values for the distribution of disregistry. The density curves in Figure 3-4(d) illustrate two peaks revealing that the dislocation is split into two partial dislocations. The distance between the two peaks are 7.4 Å and 8.09 Å for the EAM potentials with $r_c = 5.2$ Å and $r_c = 4.2$ Å, respectively, which are very close to the pre-considered equilibrium distance 7.95 Å.

3.6 Dislocation Stresses

In this section, the stress distributions around the dislocations in the dipoles calculated by MD simulations are studied. A representative core structure close to one of the two edge dislocations in a dipole, as well as the selected path of atoms for plotting the normal stress σ_{11} data along y direction, are shown in Figure 3-5(a). The obtained normal stress distributions are shown in Figure 3-5(b-d). The normal stress is computed using the two EAM potentials, and compared against the stress field from the theory of elasticity for three different systems in this figure.

Based on the theory of elasticity, the stress field around an infinite long straight dislocation can be expressed as [67]:

$$\sigma_{11} = -\frac{Gb}{2\pi(1-\upsilon)}\, y\, \frac{(3x^2+y^2)}{(x^2+y^2)^2}, \tag{3-16}$$

$$\sigma_{22} = \frac{Gb}{2\pi(1-\upsilon)}\, y\, \frac{(x^2-y^2)}{(x^2+y^2)^2}, \tag{3-17}$$

$$\sigma_{12} = \frac{Gb}{2\pi(1-\upsilon)}\, x\, \frac{(x^2-y^2)}{(x^2+y^2)^2}, \tag{3-18}$$

$$\sigma_{33} = \upsilon(\sigma_{11}+\sigma_{22}) = -\frac{Gb\upsilon}{\pi(1-\upsilon)}\, \frac{y}{(x^2+y^2)}. \tag{3-19}$$

For an edge dislocation, all the displacements and strains in z direction are zero, representing a plane strain deformation.

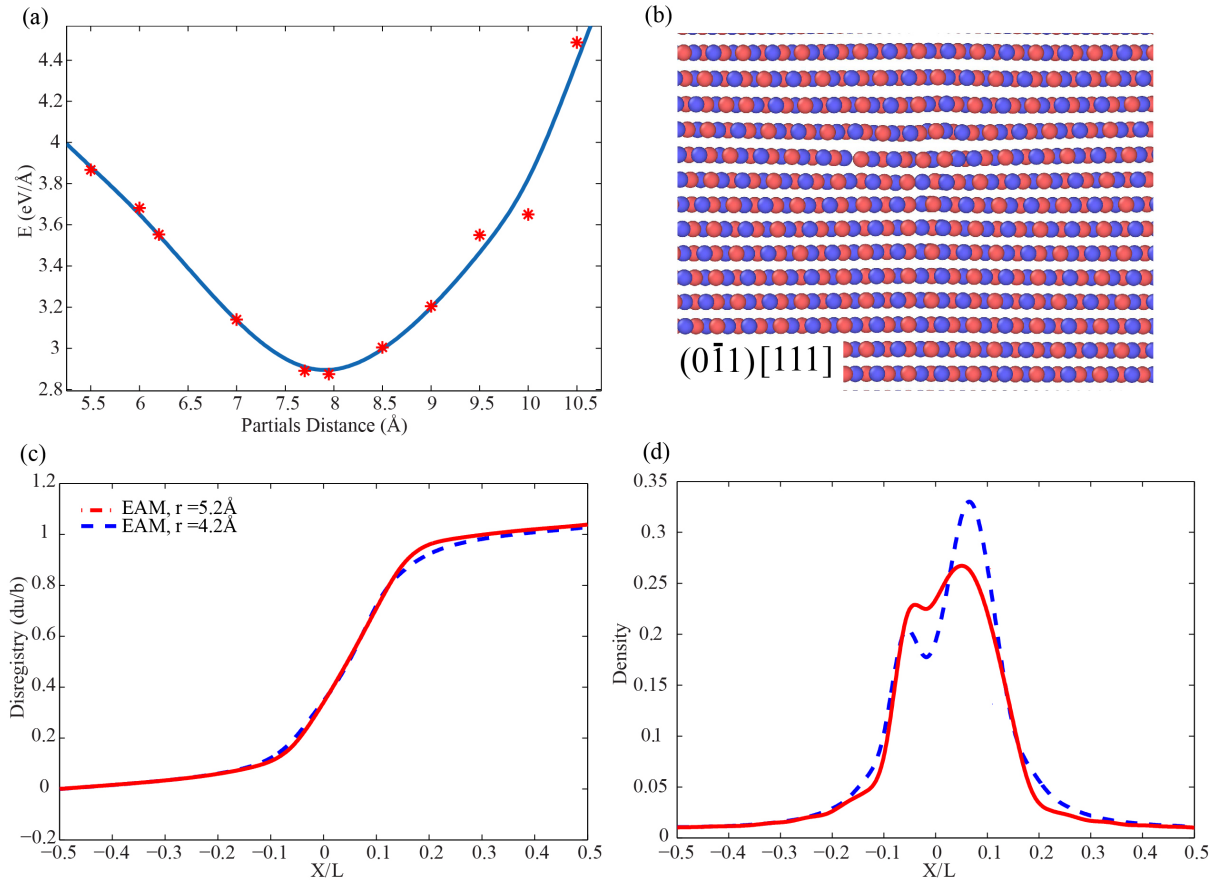

Figure 3-4. (a) The energy configuration results for the trial MD simulations to find the equilibrium distance between the two partial dislocations, (b) the relaxed dissociated dislocation structure, (c) disregistry and (d) density vs. scaled distance curves obtained from EAM potentials with $r_c = 5.2$ Å and $r_c = 4.2$ Å.

Among the normal stress components, the largest one is σ_{11} which acts parallel to the slip vector. The slip plane is defined as $y = 0$.

The maximum compressive stress, and the maximum tensile stress act above and below the slip plane, respectively [67]. Figure 3-5(b-d) show the variations of normal stress in austenite NiTi at the vicinity of different edge dislocations along the y direction. Predicted by the MD simulations, the stress distribution in all the cases approaches to zero correctly when the distance from the core increases. In $(01\bar{1})[100]$ and $(010)[100]$ systems, the EAM potential with $r_c = 4.2$ Å slightly overestimates the stress while the other potential predicts almost identical stress curves to the elasticity theory results. However, in the $(011)[0\bar{1}1]$ system, both the potentials predict the stresses very close to the theory of elasticity.

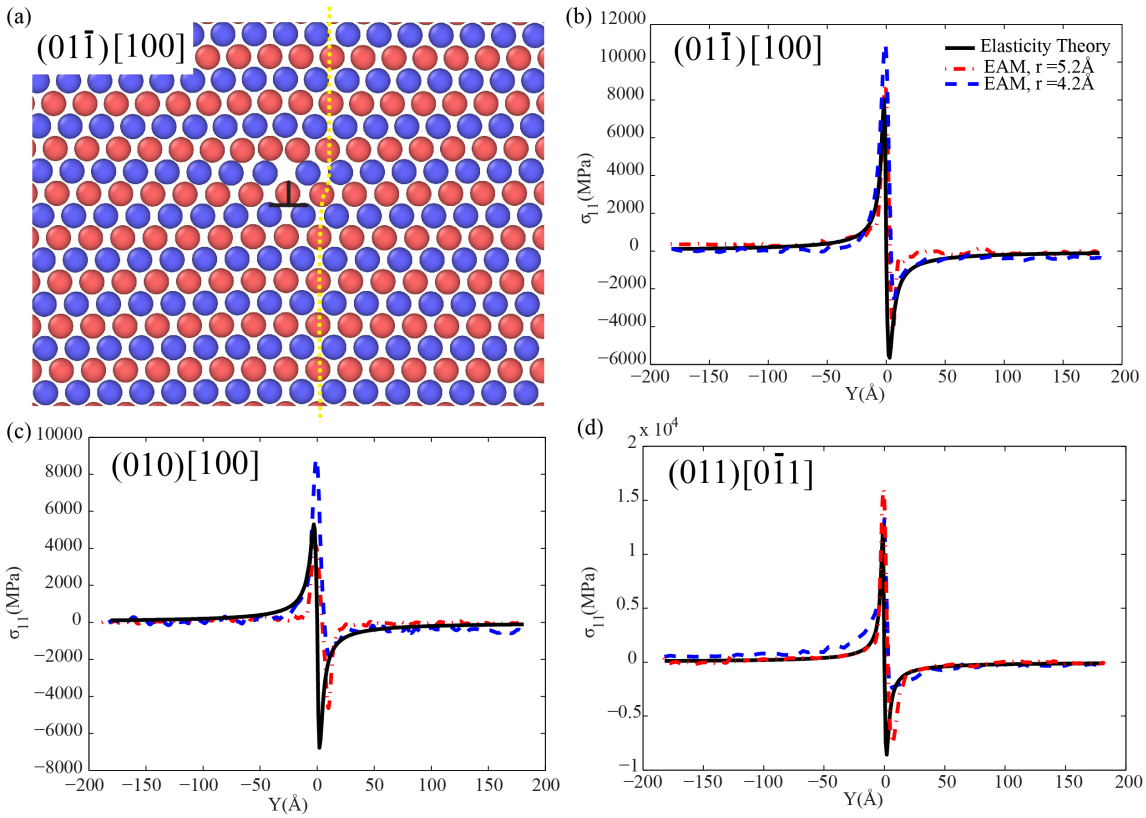

Figure 3-5. (a) The core structure and the selected path for reading the normal stress σ_{11} data along y direction, and the normal stress distribution along the vertical path from the simulations using EAM potentials with $r_c = 5.2$ Å and $r_c = 4.2$ Å compared to the elasticity solution for $(01\bar{1})[100]$ (b), $(010)[100]$ (c), and $(011)[0\bar{1}1]$ (d) systems.

The contour plots of σ_{11} and σ_{12} around the dislocations in a dipole structure for the selected three systems are shown in Figure 3-6. The contour plots obtained by the two EAM potentials are very similar, and for the sake of brevity only those obtained from the EAM potential with smaller cutoff radius are presented here. MD simulations are clearly predicting the expected shape of stress

distributions, and the change of signs around the dislocation tips in all the systems for both the normal and shear components.

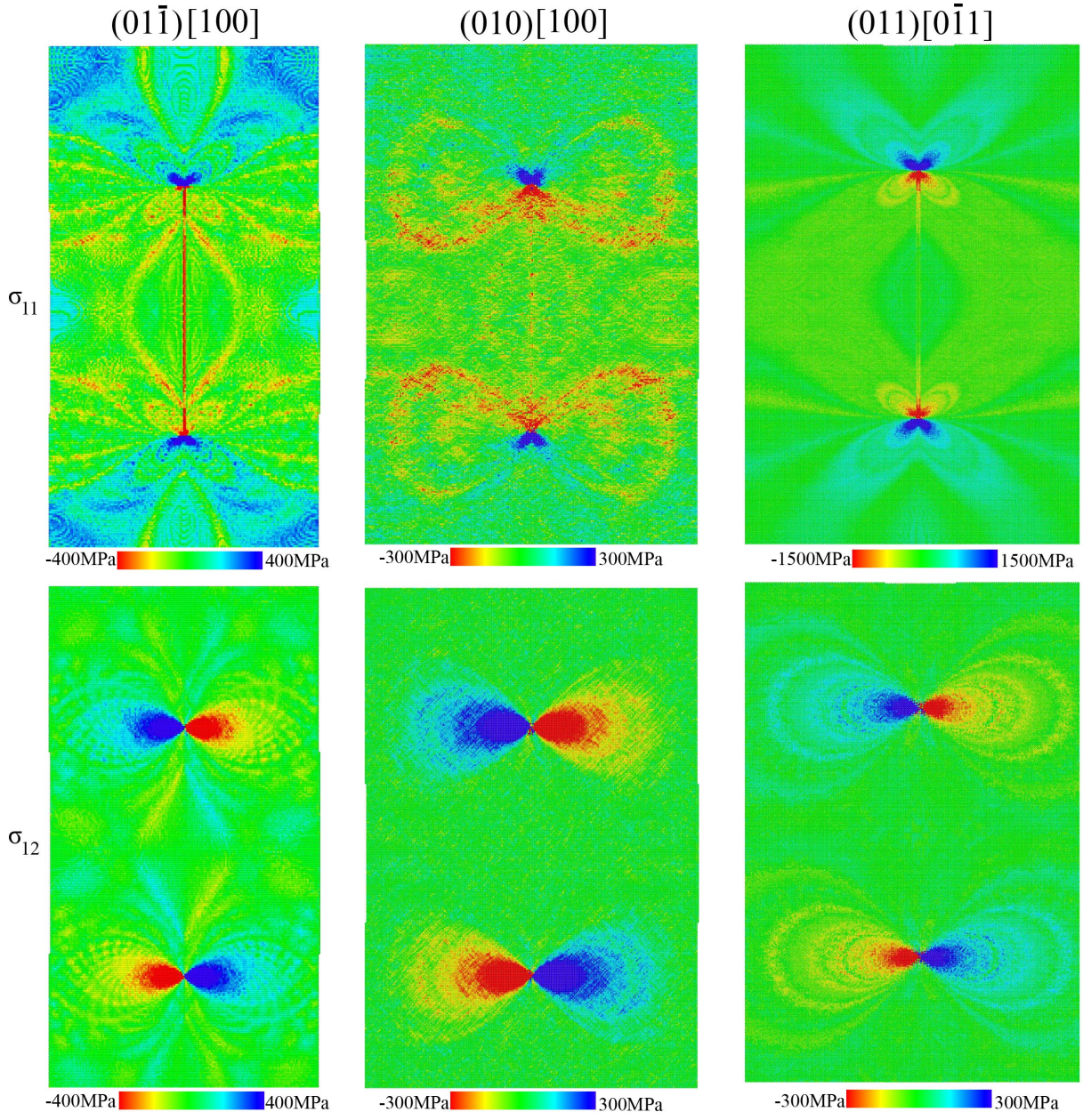

Figure 3-6. Contour plots of σ_{11} and σ_{12} at the vicinity of edge dislocations in three dipole systems: $(01\bar{1})[100]$, $(010)[100]$, and $(011)[0\bar{1}1]$.

The results shown in Figure 3-5 and Figure 3-6, clearly show the accuracy of both the EAM potentials for predicting the stress distributions at the vicinity of edge dislocations in NiTi austenite phase. Also the observed match between MD results and the theoretical calculations shows the

applicability of predictions by the theory of elasticity in calculating the energy and stress of edge dislocations in NiTi.

3.7 Conclusions

Molecular dynamics (MD) simulations are utilized to study the defects in austenite NiTi alloys. Three different potentials, two EAM with different cutoff radii and one 2NN MEAM, are selected and the accuracy of each potential is investigated by studying the stacking fault energies, and also the energy, structure and stress distribution of edge dislocation in austenite NiTi. A high-energy dislocation is also considered and the dislocation dissociation is modeled with the MD simulations. In each case, the results of each potential are compared against the elasticity theory and the density functional theory calculations at the atomistic level. Our results shed light into some unknown aspects of defects in austenite NiTi, which will benefit studying the origins of unrecoverable strains accumulated in NiTi during cyclic loading, and also help us better understand the grain boundaries in SMAs. Through our results, it is shown that although none of the selected potentials are particularly trained for studying defects in NiTi, they are accurate in predicting defect-related properties, although for some properties one of the potentials might be preferred and more precise compared to the others.

Chapter four of this work includes two published papers. One work with the title of **Dissipation of cavitation-induced shock waves energy through phase transformation in NiTi alloys** is published in **International Journal of Mechanical Sciences journal** and the other work with the title of **Stress Wave and Phase Transformation Propagation at the Atomistic Scale in NiTi Shape Memory Alloys Subjected to Shock Loadings** is published in **Shape Memory and Superelasticity journal**. The author acknowledges the co-authors of the first work, **Dr. Shima Shahab, Omidreza Sadeghi, Marjan Bakhtiari-Nejad**. In addition, the author acknowledges the publishers of these articles, **Elsevier** and **Springer** for giving the right to include the articles in this dissertation which is not provided to be published commercially.

Chapter 4. NiTi Shape Memory Alloys as Shock Wave Energy Dissipative Materials

4.1 Energy Dissipation and Phase Transformation Caused by the Structural Vibrations in NiTi Alloys

4.1.1 Overview

Energy dissipation in aluminum plates coated with a thin layer of Nickel-Titanium (NiTi) alloy subjected to a shock loading is studied in this chapter. Finite element simulations are performed to investigate the energy dissipation capability of aluminum plates coated with a NiTi layer, when the structure vibrates by exerting and removing a concentrated transverse force at the center. When the energy of incident shock waves caused by cavitation bubbles is strong enough, the energy dissipation due to global structural vibrations can complement the energy dissipation due to the phase transformation. The computational results show that the observed energy dissipation in the experiments (performed in collaboration with MInDS group from department of biomedical engineering and mechanics at Virginia Tech) is exclusively caused by the shock wave propagation, not the transverse vibrations, and also investigate the details of energy dissipation for both NiTi and Al-NiTi composite plates subjected to a cyclic transverse load at the center [195].

4.1.2 Material Modeling

For analyzing the SMA and aluminum plates coated with a thin SMA layer, finite element simulations are used. Three-dimensional constitutive relations are utilized and an appropriate user subroutine (UMAT) is written in the commercially available finite element program ABAQUS that enables this code to model SMA structures using solid elements and some two-dimensional elements. The details of implementing the constitutive equations in a displacement based finite element formulation are given in [196], and many case studies for validating the model are presented in [197-199]. The model is briefly reviewed in the following.

The phenomenological macroscopic SMA constitutive model is based on postulating the total Gibbs free energy (G) of a polycrystalline SMA as [200]:

$$G\left(\boldsymbol{\sigma},T,\boldsymbol{\varepsilon}^t,\xi\right)=-\frac{1}{2\rho}\boldsymbol{\sigma}:S:\boldsymbol{\sigma}-\frac{1}{\rho}\boldsymbol{\sigma}:\left[\boldsymbol{\alpha}\left(T-T_0\right)+\boldsymbol{\varepsilon}^t\right]+ c\left[\left(T-T_0\right)-T\ln\left(\frac{T}{T_0}\right)\right]-s_0T+u_0+f(\xi) \tag{4-1}$$

where, σ, T, T_0, ε^t, ξ and $f(\xi)$ are the Cauchy stress tensor, temperature, reference temperature, transformation strain, martensite volume fraction, and hardening function, respectively. The parameters S, α, c, ρ, s_0 and u_0 are defined as effective compliance tensor, effective thermal expansion coefficient tensor, effective specific heat, density, effective specific entropy and effective specific internal energy at the reference state, respectively. Any effective material properties P is defined as: $P=P^A+\xi(\Delta P)$ where $\boldsymbol{P^A}$ is the same property in austenite phase and $\Delta P=P^M-P^A$ is the difference in that property between martensite and austenite phases. The hardening function is defined as:

$$f\left(\xi\right)=\begin{cases}\frac{1}{2}\rho b^M\xi^2+\left(\mu_1+\mu_2\right)\xi, & \dot{\xi}>0\\ \frac{1}{2}\rho b^A\xi^2+\left(\mu_1-\mu_2\right)\xi, & \dot{\xi}<0\end{cases} \tag{4-2}$$

where, ρb^A, ρb^M, μ_1 and μ_2 are material constants for transformation strain hardening. The upper condition in the equation represents the phase transformation from austenite to martensite and the lower case stands for reverse phase transformation. The constitutive relation of shape memory material can be obtained by using the total Gibbs free energy as $\boldsymbol{\varepsilon}=-\rho\,\partial G/\partial\boldsymbol{\sigma}=S:\boldsymbol{\sigma}+\boldsymbol{\alpha}\left(T-T_0\right)+\boldsymbol{\varepsilon}^t$ and the evolution of the transformation strain tensor is related to the evolution of the martensitic volume fraction as $\dot{\boldsymbol{\varepsilon}}^t=\boldsymbol{\Gamma}\dot{\xi}$. Transformation tensor related to the deviatoric stress is defined as:

$$\boldsymbol{\Gamma}=\begin{cases}\frac{3}{2}H\frac{\boldsymbol{\sigma}'}{\bar{\sigma}}, & \dot{\xi}>0\\ H\frac{\boldsymbol{\varepsilon}^{tr}}{\bar{\varepsilon}^{tr}}, & \dot{\xi}<0\end{cases} \tag{4-3}$$

where, H, $\boldsymbol{\varepsilon}^{tr}$, $\boldsymbol{\sigma}'$, $\bar{\sigma}$ and $\bar{\varepsilon}^{tr}$ are the maximum uniaxial transformation strain, the value of transformation strain at the reverse phase transformation, the deviatoric stress tensor, the second deviatoric stress invariant and second deviatoric transformation strain invariant, respectively.

The transformation function which controls the onset of direct and reverse phase transformations can be defined as:

$$\Phi = \begin{cases} \pi - Y, & \dot{\xi} > 0 \\ -\pi - Y, & \dot{\xi} < 0 \end{cases} \tag{4-4}$$

where Y is the measure of internal dissipation due to microstructural changes during phase transformation and the thermodynamic force, π, is obtained by using the second law of thermodynamics on the local entropy production as:

$$\begin{aligned} \pi = {} & \boldsymbol{\sigma} : \boldsymbol{\Gamma} + \frac{1}{2}\boldsymbol{\sigma} : \Delta S : \boldsymbol{\sigma} + \Delta\boldsymbol{\alpha} : \boldsymbol{\sigma}\left(T - T_0\right) \\ & + \rho\Delta c\left[\left(T - T_0\right) - T\ln\left(\frac{T}{T_0}\right)\right] + \rho\Delta s_0 T - \frac{\partial f}{\partial \xi} - \rho\Delta u_0 \end{aligned} \tag{4-5}$$

The transformation function denotes the elastic domain in the stress-temperature state which means when $\Phi < 0$, the material response is elastic and the martensitic volume fraction is not changing ($\dot{\xi} = 0$). During the forward phase transformation from austenite to martensite ($\dot{\xi} > 0$) and the reverse phase transformation from martensite to austenite ($\dot{\xi} < 0$), the state of stress, temperature and martensitic volume fraction should remain on the transformation surface which is characterized by $\Phi = 0$. The transformation surface in the stress-temperature state is represented by two separate faces which are related to $\xi = 0$, and $\xi = 1$. For developing an incremental displacement based finite element formulation, the tangent stiffness and thermal moduli tensors are required. In order to obtain these tensors, the constitutive model of SMA material should be linearized and represented as the following incremental form:

$$d\boldsymbol{\sigma} = \Im : d\boldsymbol{\varepsilon} + \Re dT \tag{4-6}$$

In addition, rewriting the constitutive equation in the differential form and applying the evolution equation leads to:

$$d\boldsymbol{\varepsilon} = S : d\boldsymbol{\sigma} + \boldsymbol{\alpha}\, dT + \left[\Delta S : \boldsymbol{\sigma} + \Delta\boldsymbol{\alpha}\left(T - T_0\right) + \boldsymbol{\Gamma}\right] d\xi \tag{4-7}$$

The derivative of the transformation function with respect to stress tensor is:

$$\frac{\partial \Phi}{\partial \boldsymbol{\sigma}} = \begin{cases} \Delta S : \boldsymbol{\sigma} + \Delta\boldsymbol{\alpha}\left(T - T_0\right) + \boldsymbol{\Gamma}, & \dot{\xi} > 0 \\ -\Delta S : \boldsymbol{\sigma} - \Delta\boldsymbol{\alpha}\left(T - T_0\right) - \boldsymbol{\Gamma}, & \dot{\xi} < 0 \end{cases} \tag{4-8}$$

The consistency condition ($\dot{\Phi}=0$) can be written as:

$$d\Phi = \frac{\partial \Phi}{\partial \boldsymbol{\sigma}} : d\boldsymbol{\sigma} + \frac{\partial \Phi}{\partial T} dT + \frac{\partial \Phi}{\partial \xi} d\xi = 0 \tag{4-9}$$

The differential of the martensitic volume fraction, $d\xi$, can be eliminated between Equation (4-7) to (4-9). Rearranging the obtained equation in the form of Equation (4-6) gives the continuum tangent moduli tensors for the forward and reverse phase transformations as:

$$\begin{aligned} \mathfrak{I} &= C - \left(C : \frac{\partial \Phi}{\partial \boldsymbol{\sigma}} \otimes C : \frac{\partial \Phi}{\partial \boldsymbol{\sigma}} \right) \left(\frac{\partial \Phi}{\partial \boldsymbol{\sigma}} : C : \frac{\partial \Phi}{\partial \boldsymbol{\sigma}} \mp \frac{\partial \Phi}{\partial \xi} \right)^{-1} \\ \mathfrak{R} &= -\mathfrak{I} : \boldsymbol{\alpha} - \frac{\partial \Phi}{\partial T} \left(C : \frac{\partial \Phi}{\partial \boldsymbol{\sigma}} \right) \left(\frac{\partial \Phi}{\partial \boldsymbol{\sigma}} : C : \frac{\partial \Phi}{\partial \boldsymbol{\sigma}} \mp \frac{\partial \Phi}{\partial \xi} \right)^{-1} \end{aligned} \tag{4-10}$$

where the symbol $\otimes$ represents the tensor product, $C = S^{-1}$, and parameter $\mp$ stands for (+) in the forward and (-) in the reverse phase transformations.

Details of implementing the calculated Jacobians and the constitutive equations into the user subroutine (UMAT) in the finite element program are given by Qidwai and Lagoudas [196] as a computational step-by-step algorithm. For algorithmic details of the time integration procedure for a rate-independent single-crystal constitutive model for SMAs, readers are referred to [201].

4.1.3 Finite Element Model

In the present study, the FE model simulates the phase transformation and energy dissipation, which occur during vibration-induced deformations in both NiTi and NiTi coated Aluminum plates for comparison purposes. Material properties in the presented constitutive model for $Ni_{50}Ti_{50}$ are calibrated by using the experimental results presented by Jacobus *et al.* [202]. The obtained properties are reported in our previous work [7]. The responses of material in a uniaxial tensile

test obtained from the calibrated model and experiments are compared in Figure 4-1, and it is shown that the model is correctly predicting the critical features in the response, including the transformation strains, hysteretic response, and the transformation strain.

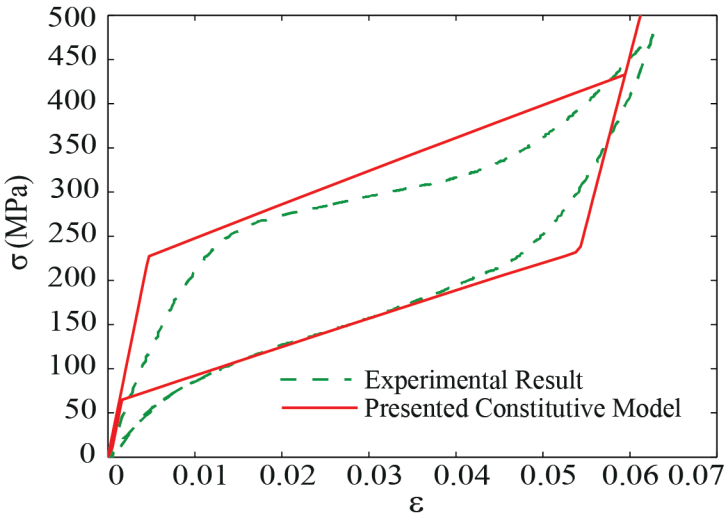

Figure 4-1. The responses of material in a uniaxial tensile test obtained from the calibrated model and experiments [35].

Rectangular plates of $61.4\times42.4\times2$ mm (the same dimensions as the samples used in the experiments) are considered in the finite element model. Two sides of the plates (the 61.4 mm sides) are clamped in all directions, and the other two sides are left free, consistent with the experiments. Three dimensional quadratic brick elements with reduced integration (element C3D20R in ABAQUS) are used in the finite element model of the plates. A convergence analysis is performed for choosing the appropriate number of elements. By refining the mesh, the stress and force in the force-displacement responses are tracked to find the appropriate mesh. The stress distribution and force values are considered to be converged when the maximum differences by refining the mesh are smaller than 0.1 MPa and 10 N, respectively. The convergence is achieved by using ~10000 elements in the model, which has been used in all the finite element simulations in this study.

4.1.4 Energy dissipation in a vibrating SMA plate

Simulating the shock wave propagation in SMA materials is practically difficult since the constitutive equations developed for SMA material are based on the quasi-static behavior. However, a quasi-static simulation can be used to investigate if the observed energy dissipation in the experiments is originating from the structural vibrations or the stress wave propagation in the

NiTi alloy. As the first step, a NiTi plate with the dimensions and boundary conditions given in Section 4.1.3 is considered, and a central force is applied to the plate. The central force is simulating the pressure applied by the water jet in the experiments, with the difference that the force is applies with a remarkably lower rate in the simulations to study the structural vibrations caused by that force. The load is applied in multiple cycles of loading-unloading and the force versus transverse deflection of the plate center is calculated, as shown in Figure 4-2(a).The dissipated energy in each cycle can be measured by calculating the area inside the hysteresis graphs. The energy dissipations are found to be 0.0405, 0.2880, 0.8340, 1.4704 and 2.2421 J for 0.5, 1, 1.5, 2 and 2.5 mm transverse displacements, respectively. As expected, the hysteresis area grows when the transverse displacement at the center increases (see Figure 4-2(b)). This can be justified, as more regions of the plate will contribute to the energy dissipation caused by the phase transformation. The observed trend of the decrease in the dissipated energy with decreasing the central deflection clearly shows that for the case of having a transverse deflection in the order of micrometers, the energy dissipation caused by the global deflections of the plate and structural vibrations will be zero. Recorded transverse deflections in the experiments (in the order of $4-6\ \mu\text{m}$) clearly proves that the observed energy dissipation in the experiments is exclusively caused by the phase transformation cycles activated through shock wave propagation in the material. It is worth noting that in the experiments, if the energy of the incident shock is remarkably larger, or the plate geometry allows larger deflection (i.e. the plate side to the thickness ratio is smaller), the vibration-induced energy dissipation will also be activated besides the shock wave energy dissipation. Another question that can be answered by the computational simulations is that how efficient the system will be if instead of using a plate made of NiTi, a plate made of elasto-plastic material coated with a thin layer of NiTi is used.

This design, as used in the experiments in this chapter, will be remarkably cost effective, particularly if the energy dissipation efficiency is retained by an acceptable amount. The efficiency of a system made of a plate coated with a NiTi layer can be predicted by studying the phase transformation distribution in the NiTi plate as shown in Figure 4-2(c). As expected, the phase transformation is activated at the center of the plate (due to the maximum displacements) and the clamped area (due to the stress concentration, as shown in Figure 4-2(d)). Tracking the phase transformation and stress distributions in the cross-section (Figure 4-2(e) and (f)) demonstrates

that the upper and lower layers of the plate have the most significant contributions in the energy dissipation, and the phase transformation is highly concentrated in these areas. Therefore, we have also considered an Al plate coated by NiTi layers in order to investigate the behavior of the plate under the same loading conditions. In the next section the energy dissipation when a thin NiTi layer is coated on the surface of an aluminum plate is studied computationally, and the efficiency is compared with the case of having the whole thickness made of NiTi.

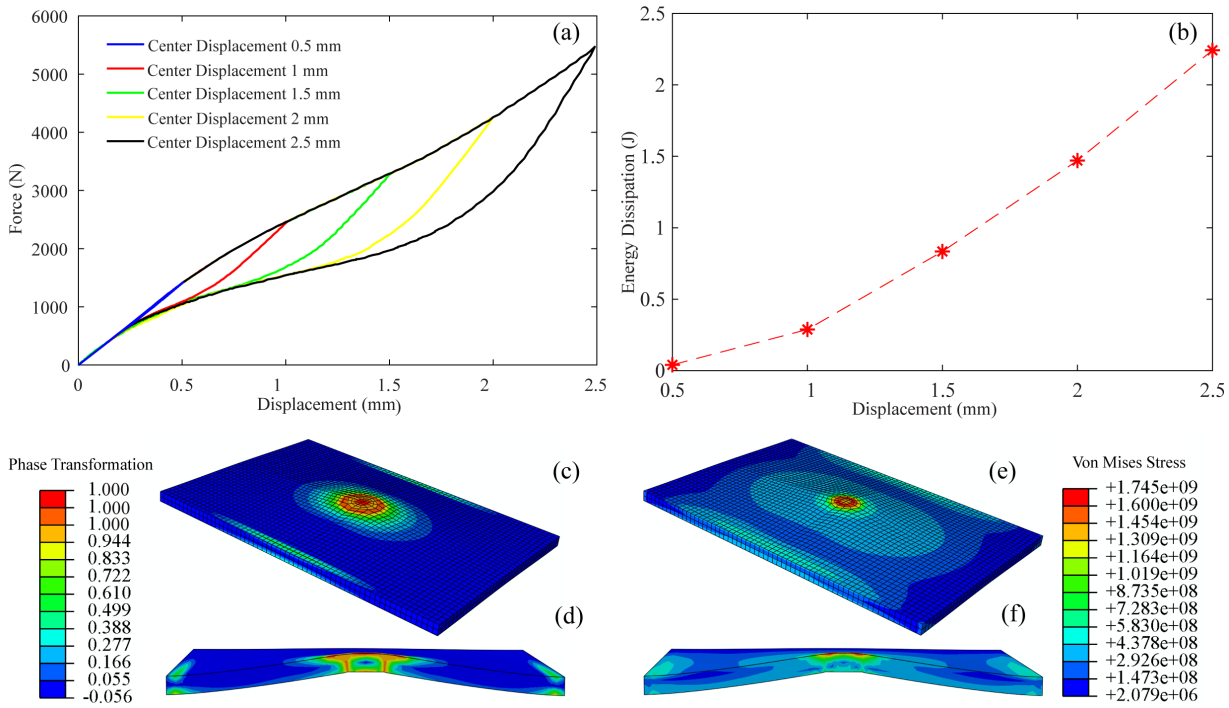

Figure 4-2. (a) Force versus deflection for center transverse displacements of 0.5, 1, 1.5, 2, and 2.5 mm in the NiTi plate, and (b) energy dissipation for different center displacements in the NiTi plate. The energy dissipation for each displacement is obtained by calculating the area inside the corresponding hysteresis force-deflection graphs. (c) Contour plot of phase transformation and (d) Von Mises stress distributions in the NiTi plate. (e) Distribution of the phase transformation and (f) Von Misses stress in the cross-section of the plate. All the contours are plotted for the center transverse deflection of 2.5 mm.

4.1.5 Energy dissipation in a vibrating SMA composite plate

A composite plate, with exactly same boundary conditions and dimensions as the plate simulated in Section 4-1-4 is considered, while 75% of the thickness is made of aluminum and the remaining 25% is NiTi. Aluminum layer is modeled using an elastic-perfectly plastic material with yield strength $\sigma_y = 234$ MPa. The plate is subjected to the same cyclic loadings as the plate of Section 4.1.4 and the force-deflection at the center of composite plate is shown in Figure 4-3(a). The areas under the force-displacement curves are calculated for center displacements of 0.5, 1, 1.5, 2 and

2.5 mm , and the corresponding energy dissipation values for these displacements are obtained as 0.0776, 0.6980, 1.7500, 3.1000 and 4.8000 J, respectively. As shown in Figure 4-3(a), in all the cycles, after unloading the structure, some residual deflection is remained at the center of the plate, which is caused by the plastic deformation in the aluminum layer. It can be concluded that the portion of the calculated energy dissipation for each displacement is the contribution of the plastic deformation in the Al layer. To study the contribution of phase transformation in dissipating the energy, we consider three plates with the same total thickness, while one of them is made of NiTi, one is made of elasto-plastic Al with 25% of its thickness being replaced by NiTi, and the third one is a composite plate with 25% of the thickness made of NiTi and the rest of thickness made of an elastic aluminum in which any plastic deformation is ignored in it. The force deflection curves for these plates are shown in Figure 4-3(b) for a center lateral deflection of 1 mm applied to all of them. The energy dissipated for the elastic Al plate coated with NiTi layer is 0.110 J , while the values for the NiTi plate and elasto-plastic Al plate coated with NiTi are 0.2880 and 0.6980 J , respectively. Comparing the elasto-plastic and elastic Al plates coated with a NiTi thin layer, shows that the amount of dissipated energy is reduced from 0.6980 J to 0.110 J when the plastic deformation energy dissipation is eliminated by ignoring the plastic deformations in the Al layer. This result shows that most of the energy dissipation in Al-NiTi composites is due to the plastic deformation in the Al layer. In addition, comparing the results for the case of the whole thickness made of NiTi and the elastic Al-NiTi plates, shows that approximately 38% of the energy dissipation capability is retained when only $1/4$ of the thickness is made of NiTi. Considering the significant cost efficiency in using NiTi layers instead of plates made of NiTi, these results confirm using composite plates with NiTi coatings as being a promising method to design efficient energy dissipating devices.

Figure 4-3(c) shows the comparison between the energy dissipation of the same three plates as those studied in Figure 4-3(b), by applying a larger deflection on the plates. Shown in this figure, for the center displacement of 2.5 mm , the energy dissipation values are 2.2421 , 4.8000 and 4.6900 J for the NiTi, elasto-plastic Al-NiTi and Al plates, respectively. Similar to the case of 1 mm central deflection, the elasto-plastic Al-NiTi plate is the most efficient system for dissipating the energy, while the residual deflections after unloading the structure remain a significant disadvantage for this system.

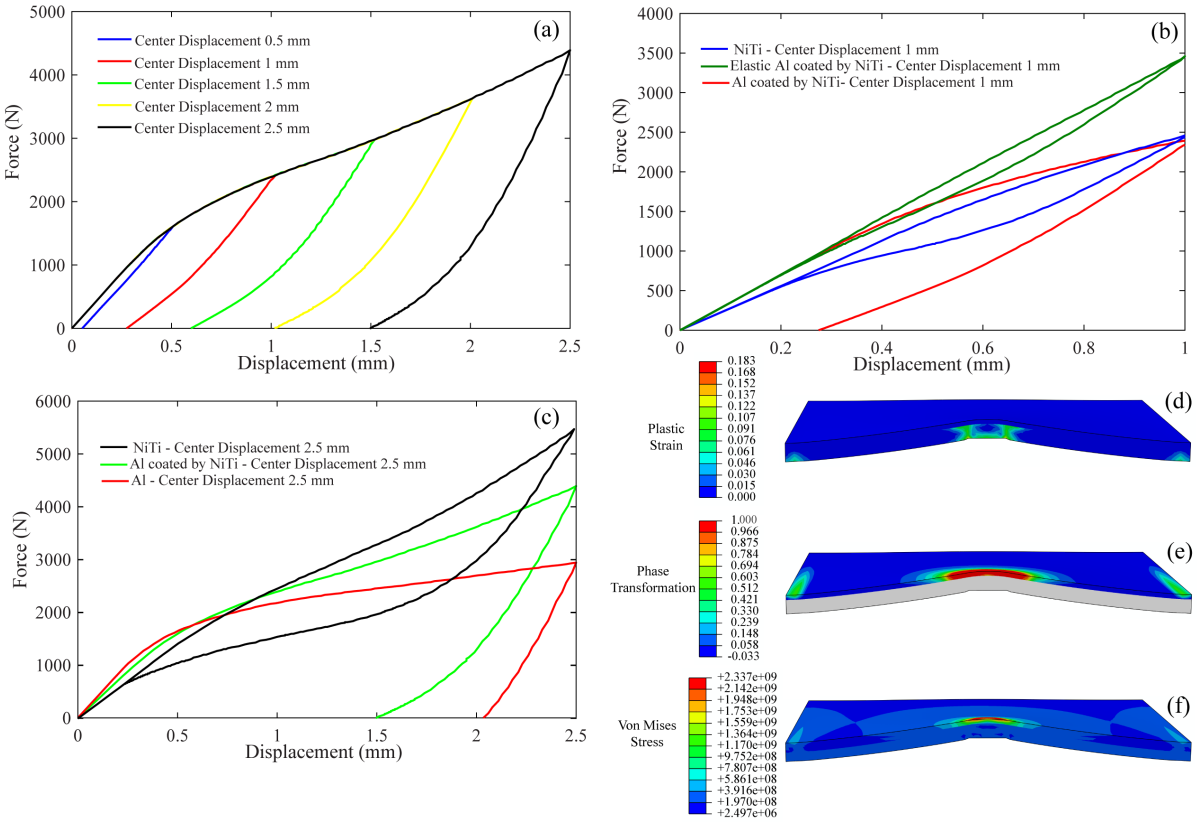

Figure 4-3. (a) Force-deflection for Al-NiTi plates subjected to center transverse displacements of 0.5, 1, 1.5, 2, 2.5 mm. (b, c) Comparison between the Force-deflection curves for a NiTi, an elasto-plastic Al-NiTi, and an elastic Al-NiTi plate subjected to the 1 and 2.5 mm center transverse deflections. (d-f) Distributions of the plastic strain, phase transformation, and Von Misses stress in the cross-section of elasto-plastic-NiTi plates subjected to the 2.5 mm transverse deflection at the center of the plate.

The plastic strain, phase transformation and Von Misses stress distributions in the cross-section of an elasto-plastic Al plate coated with a NiTi layer are shown in Figure 4-3(d-f) for the center deflection of 2.5 mm. As expected, the plastic deformation concentrated in the Al layer and the phase transformation in the top NiTi coating layer show the contribution of this layer in the observed energy dissipation.

4.1.6 Conclusions

The unique property of SMAs in dissipating the energy of shock loadings is investigated using complementary experimental and computational frameworks. An experimental setup is designed and implemented for generating spark-generated collapsing bubbles near a plate surface under water and producing a water jet; where the jet leads to a shock loading applied to the geometric center of the plate. Two different composite plates are considered in the experiments; one made by bonding a NiTi thin layer to an aluminum plate and another one with bonding an aluminum

thin layer, with the same length, width and thickness, to a separate but identical aluminum plate. These two composites are subjected to almost identical cavitation-induced shock loads and their responses are compared. The effects of energy dissipation through the phase transformation in NiTi-bonded plate on damping the transverse deflections and in-plane strains are investigated. A high-speed camera, a hydrophone, a laser Doppler vibrometer and multiple strain gauges are used to characterize the generated bubbles and the mechanical response of plates. The experimental results clearly show that the NiTi coating layer, even for the thickness of the order of one-tenth of the base structure, can effectively damp the stress shock waves in the structure. Using a set of computational simulations, it is shown that if the incident shock wave is strong enough to cause global vibrations in the structure, the phase transformations originated from the deflections of the structure can also contribute to the energy dissipation and damp the response of the structure. The results provide us a better fundamental understanding about the observed excellent erosion resistance of NiTi alloys and the efficiency of using a thin layer coating of NiTi on various structures to improve their cavitation resistance in different applications.

4.2 Stress Shock Wave Propagation and Energy Dissipation in NiTi Alloys at the Atomistic Scale

4.2.1 Overview

In this section, the energy dissipation and the phase transformation caused by the stress wave propagation in single crystal and polycrystalline NiTi alloys under shock wave loading are investigated through molecular dynamics method (MD). MD method, due to its convenient capture of details at atomic level and reveal of intrinsic deformation mechanisms in materials, is a superior candidate to study the microstructure and dynamic response of materials under shock wave loading. The dynamic response of various metals and alloys subjected to shock loading through MD method are extensively investigated [103-112] while the investigations on the NiTi alloys are limited to two studies. Lagoudas *et al*. [113] studied the wave propagation problem in a cylindrical polycrystalline NiTi rod induced by an impact loading through finite element method. Yin *et al*. [107] investigated phase transformation of NiTi nano pillar subjected to shock loading.

The dynamic response of material is strongly dependent on microstructural properties such as lattice orientation, grain sizes and grain boundaries and to the best of our knowledge, the effects of these microstructures on the stress shock wave propagation in NiTi alloys are not studied yet.

Therefore, in the present research, we also investigate the effects of lattice orientations on the stress shock wave propagation. Moreover, the effect of grain sizes and grain boundaries on the stress shock wave propagation and phase transformation propagation in polycrystalline NiTi under shock loading are investigated.

4.2.2 Methods

A series of molecular dynamics simulations are performed to investigate the effects of nanostructure on the shock-induced stress wave propagation in NiTi alloys using a many body interatomic potential, originally developed by Lai *et al.* [203] and subsequently improved by Zhong *et al.* [93]. The potential function has been modified with cubic polynomial interpolations to smooth the discontinuities near the cut-off radius. Through multiple case studies, it has been demonstrated that the results of MD calculations are in a good agreement with the experimental results and also ab initio calculations [40, 93]. This potential is adopted in our work. The total potential energy of NiTi is expressed as Equation (3-1) and the modified function is shown in Equation (3-3). The coefficients for this potential have been calculated and reported by Zhong *et al.* [93] for cut-off radius $r_c = 4.2$ Å.

In the present work this widely used potential along with large-scale atomic/molecular massively parallel simulator (LAMMPS) [167] is utilized for performing the simulations, and Ovito [168] visualization tool is used for post-processing the results of MD simulations. The MD simulations are performed for six different 3D computational cells with the average size of $500 \times 500 \times 500$ Å which are periodic only in x and y directions. In order to simulate the computational cells, three different single crystals with shock directions aligned with $[001]$, $[1\bar{1}1]$, and $[110]$ crystal orientations, and three polycrystalline structures with average grain sizes of 13.5, 18.4 and 25 nm are considered. The single and polycrystalline structures are stabled in the austenite phase. The polycrystalline cells are created using Vorronoi Tessellation algorithm [204]. After creating the single and polycrystalline bulks, the structural energy is minimized using conjugate gradient method. Then, thermal equilibrium is applied to the system using time integration on Nose-Hoover style non-Hamiltonian equations of motion in canonical (nvt) ensembles to set the temperature at T = 350 K for 100 ps. After temperature equilibrium, the system is set to temperature and pressure free using nve ensemble. In order to simulate the shock loading, in a circular area with diameter of 100 Å, 5 layers of atoms with total thickness of 2.2 nm at the bottom of the bulk system is

subjected to the wall/piston [26] loading condition. The wall/piston loading duration is 3 ps with the speed of 7 Å/ps. Figure 4-4 shows a single crystal and a polycrystalline NiTi bulks subjected to the wall/piston loading condition. Finally, after removing the load, the system is equilibrated for 5 ps to let the stress wave propagates through the structure. The results of stress wave propagation and phase transformation, in different oriented single crystals and polycrystalline structures with different grain sizes are discussed thoroughly in the following sections.

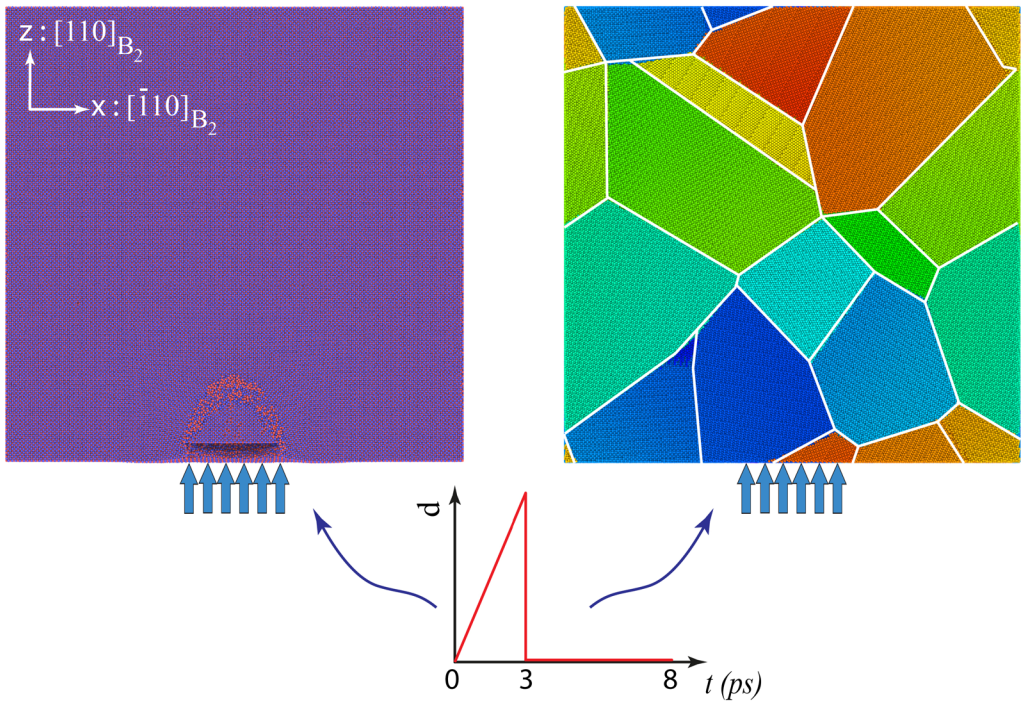

Figure 4-4. Schematic representation of the single crystal and polycrystaline bulks subjected to the shock wave loading.

4.2.3 Stress wave propagation and phase transformation in different crystal orientations

4.2.3.1 Stress wave propagation

In this section, in order to study the effect of lattice orientation on the shock-induced stress wave propagation, three NiTi single crystals with shock loading directions aligned with [110], [1$\bar{1}$1] and [001] crystallographic directions are simulated. The other two orthogonal directions have been taken as [$\bar{1}$10] [001], [21$\bar{1}$] [011] and [100] [010], respectively. The evolution and propagation of the normal and shear stresses in the bulk material are shown in Figure 4-5 and 6, respectively. The first two columns in Figure 4-5 correspond to the normal stress distribution during the loading and the last three columns represent the stress propagation in unloading (when the shock load is

removed as shown schematically in Figure 4-4). For all the three single crystals, two shock wave fronts are detected which start to propagate in almost half-circular patterns. The outer circle corresponds to the elastic shock wave front and the inner one represents the inelastic shock wave front, since the elastic shock wave has higher propagation velocity than the inelastic one [205]. As it will be discussed in Section 5, the inelastic deformation is a combination of permanent plastic deformation and forward austenite to martensite phase transformation. Comparing the three crystal orientations, the elastic wave front which has the magnitude of around -7 GPa is propagated farther in the crystal with the $[1\bar{1}1]$ shock direction. This result was expected since $[1\bar{1}1]$ slip direction contains the greatest number of atoms per length in body-centered-cubic (BCC) structures. It is well stablished that, since elastic material constants in an anisotropic material depend on the direction, elastic wave propagation velocity in an anisotropic material also depends on the direction. That is the reason that the shock wave fronts do not show a hemispherical surface. The elastic material constants of austenite NiTi alloy, which is an anisotropic medium, reported by Brill *et al.* [206], are C_{11} = 144 GPa, C_{12} = 112 GPa, and C_{44} = 22 GPa. The velocity of the normal mode of elastic stress waves through the crystallographic directions of $< 110 >$, $< 1\bar{1}1 >$, and $< 001 >$ can be calculated as [207]:

$$c_{n_{<110>}} = \sqrt{{}^{1}/_{2\rho}\,(C_{11} + C_{12} + 2C_{44})}, \tag{4-11}$$

$$c_{n_{<1\bar{1}1>}} = \sqrt{{}^{1}/_{3\rho}\,(C_{11} + 2C_{12} + 4C_{44})}, \tag{4-12}$$

$$c_{n_{<001>}} = \sqrt{{}^{1}/_{\rho}\,C_{11}}, \tag{4-13}$$

where, ρ and c_n are density and normal mode elastic wave propagation velocity, respectively. The calculated values of c_n for the three directions are 4804, 4836, and 4707 m/s. The maximum calculated velocity belongs to the second direction $< 1\bar{1}1 >$ which is in agreement with the contour plots of Figure 4-5. Right after the onset of unloading, another elastic shock wave initiates and starts to propagate [205]. The unloading wave which is faster than phase transformation wave contributes to the drop in the phase transformation stress peak from -25 GPa to -10 GPa, when it reaches the phase transformation wave front. A portion of the unloading wave reflects back towards the wall when it hits the inelastic wave front, and then it again reflects back towards the loading direction [205].

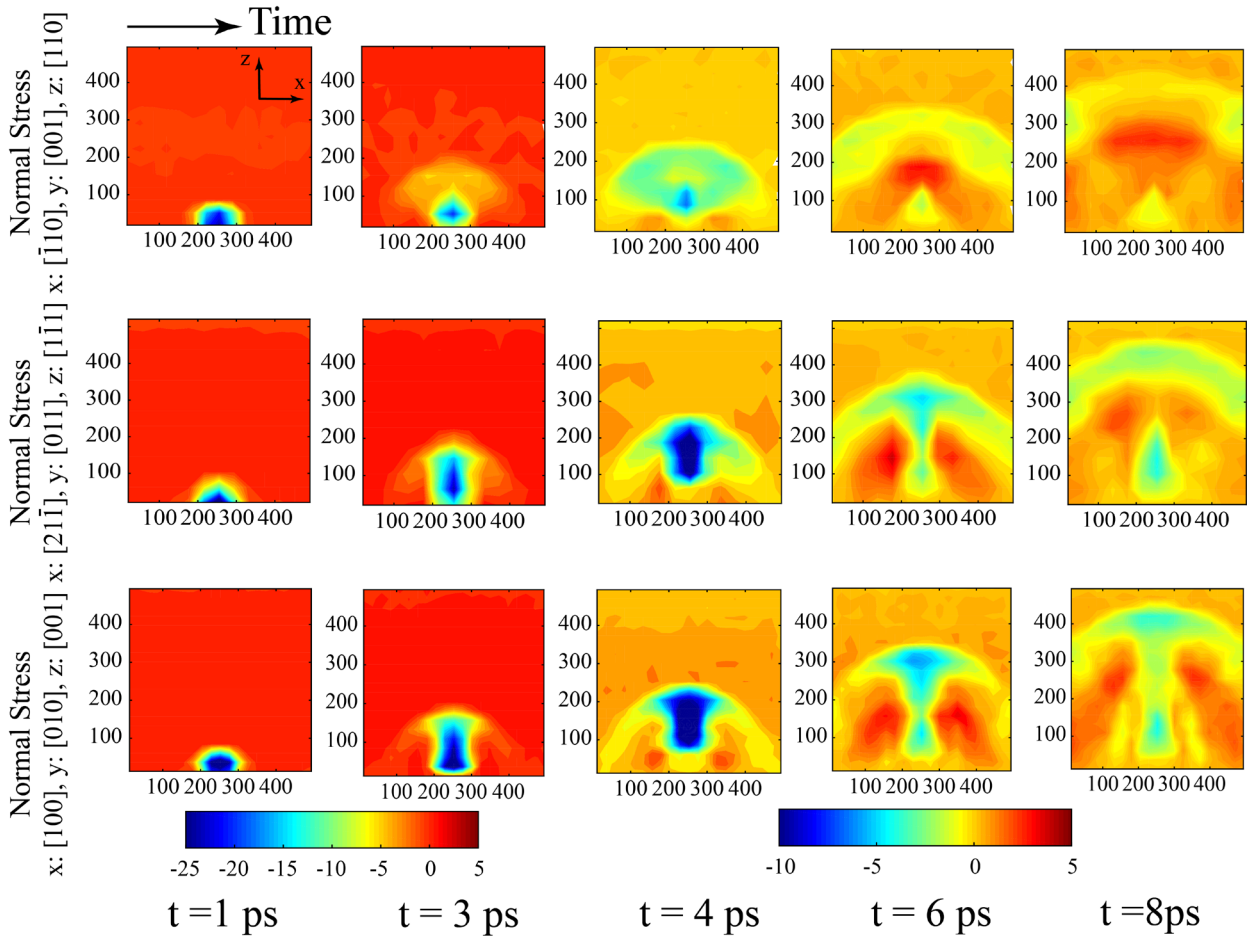

Figure 4-5. Normal stress wave propagation of the three single crystals for shock directions aligned with [110], [1$\bar{1}$1], and [001]. The stress values in color bars are in GPa.

As a result of these several reflections, dark orange area in the contour plots of t = 6 ps and t = 8 ps, where the normal stress is positive, shows the propagation of the unloading elastic wave.

Figure 4-6 shows the propagation of shear stress waves. Unlike the normal stress waves which initiate and propagate from the circle surface, the shear stress waves initiate from the peripheral of the circle. In a 2D view like Figure 4-6, the wave initiation region appears as a pair of points where in one of them the shear stress is positive and in the other one negative. Similar mechanism as in normal stress wave propagation happens for shear stress wave propagation. The first two columns in Figure 4-6 show the initiation steps and the last three columns represent the propagation steps. Due to the different shock source geometries of shear and normal stress waves, the shear stress wave propagation pattern appears to be more complicated than the normal stress.

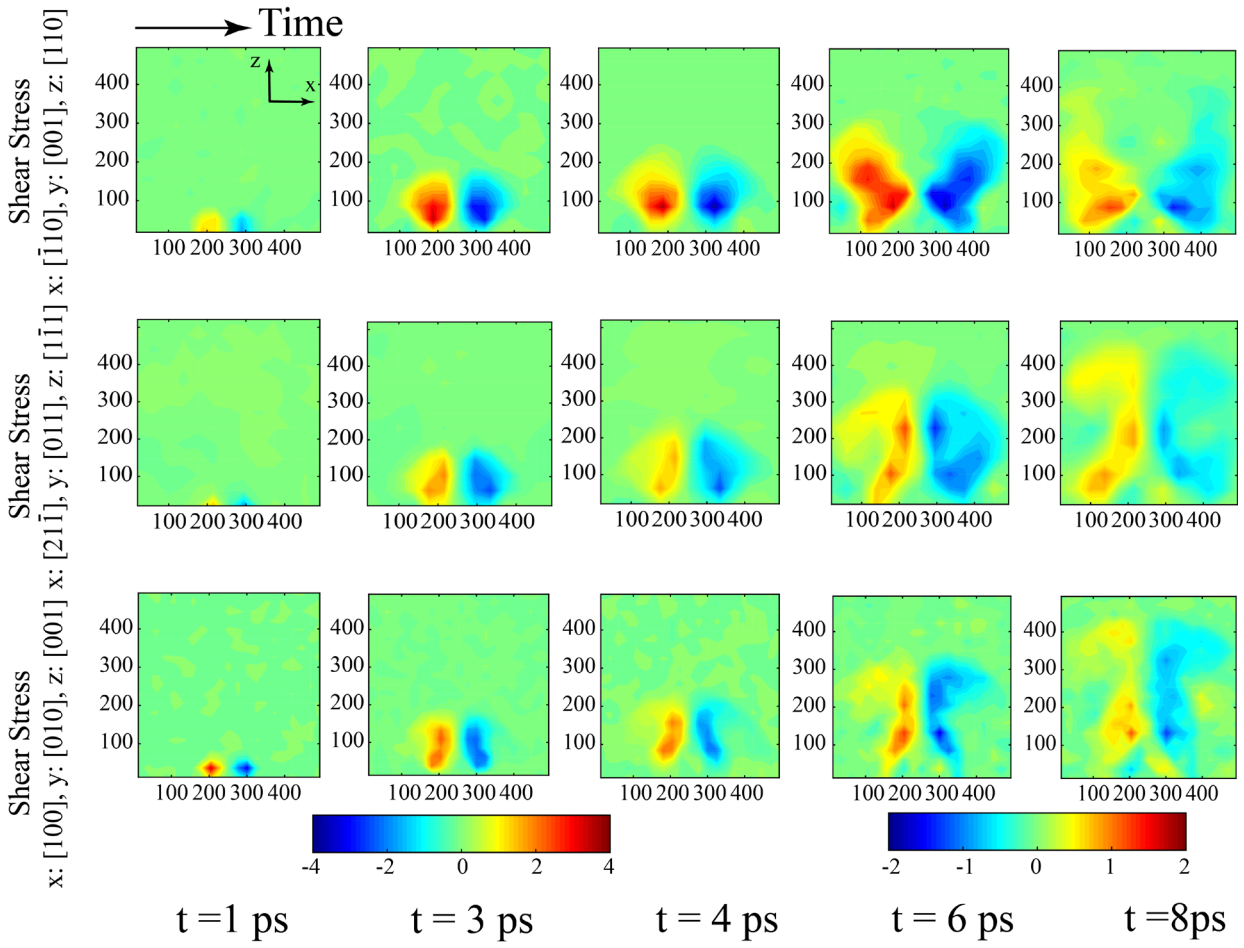

Figure 4-6. Shear stress wave propagation of the three single crystals for shock directions aligned with [110], [1$\bar{1}$1] and [001]. The stress values in color bars are in GPa.

Figure 4-7 shows the normal stress wave propagation (for convenience, the values of the compressive and tensile stresses are shown positive and negative, respectively) over length for different times in the shock direction. Figure 4-7(a) illustrates the evolution of maximum peak stress in the bulk of crystals, for the three orientations, over the time of simulation. The maximum normal stress values for all the crystal orientations show rapid increase shortly after the start of loading. However, for the first orientation, [110], (showing in blue), the maximum stress drops quicker than the other two directions. Right after the end of loading (3 ps) the stress drops at an almost constant rate for all the directions. The curves reach constant values after 6 ps. Figure 4-7(b), (c) and (d) show the distribution of normal stress along the length of the crystals at different times of simulation for the three single crystals with different shock directions [110], [1$\bar{1}$1] and [001], respectively.

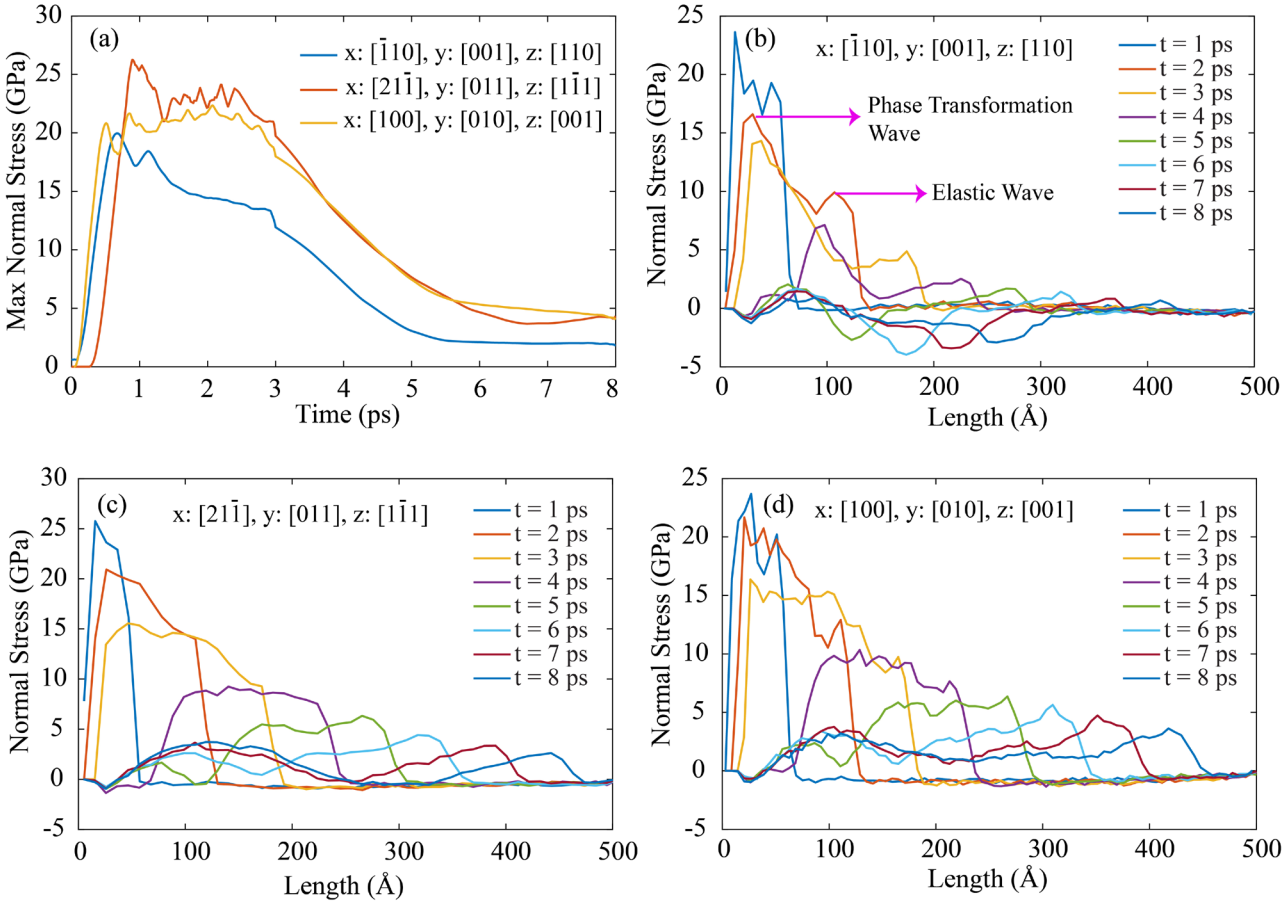

Figure 4-7. (a) Maximum of normal stress wave during loading and propagation time for three different oriented single crystals. (b) Normal stress wave propagation for x: [$\bar{1}$10], y: [001], z: [110] single crystal. (c) Normal stress wave propagation for x: [21$\bar{1}$], y: [011], z: [1$\bar{1}$1] single crystal. (d) Normal stress wave propagation for x: [100], y: [010], z: [001] single crystal.

For the majority of the curves, two distinctive peaks can be observed. The left peak corresponds to the phase transformation shock wave front and the right peak to the elastic shock wave front. As time passes, these two peaks move to the right (the loading direction), but since the elastic wave moves faster than the phase transformation, the two peaks take apart. From the time and locations of these peaks, the shock wave propagation speed for elastic and phase transformation waves can be calculated for the three crystal orientations. The phase transformation shock wave speeds are calculated as 1229.5, 1025 and 568 m/s, and the elastic shock wave speeds calculated as 5563, 5797 and 5241 m/s for the first [110], second [1$\bar{1}$1], and third [001] orientations, respectively. The elastic wave speeds calculated from the MD simulations are in agreement with the values calculated from Equations (4-13), (4-14) and (4-15). The maximum phase transformation speed is

for the shock direction [110], and the maximum elastic wave speed is for the shock direction $[1\bar{1}1]$.

At the first three curves (1-3 ps) the phase transformation peaks are at high levels (above 14 GPa). This high stress level propagates the phase transformation and plastic deformation through the bulks. Although from 1 ps to 3 ps some drop in the peak of stress is observed, which could be due to energy dissipation through phase transformation and plastic deformation. However, as discussed before, at the onset of unloading, another elastic wave with an opposite direction starts to propagate at the elastic wave speed. At the time of ~4 ps, this unloading wave partially reaches the phase transformation peak and therefore, causes a significant drop in the stress level. This is why at the time of 5 ps the phase transformation peak drops below 5 GPa for all the directions. This unloading wave then partially reflects back to the wall and again reflects back towards the loading direction. As a combination of these several interactions of unloading elastic wave with the phase transformation wave, this peak drops even more up to the point that for the first orientation, the compressive normal stress drops below zero. Same observation was reported in [205]. Figure 4-8 shows the maximum recorded stress values correspond to elastic wave front at different times and their corresponding positions over the length of the crystals, for the three considered crystal orientations. The calculated stress values are obtained from averaging over the cross-sections of the middle cylinder along the loading direction. It can be seen that the third orientation shows the highest stress level and the first orientation the lowest. In Figure 4-8, the first crystal shows greater decay in elastic wave front peak compared to the other crystal orientations. To clarify, at the length of 200 Angstrom, the stress in the first orientation drops under 5 GPa, while for the other two directions the stress level is around 10 GPa. Moreover, as shown in Figure 4-7(b) the first crystal also shows greater drop in inelastic wave front peak which causes the shortest phase transformation region along the loading direction and it will be discussed more in the next section.

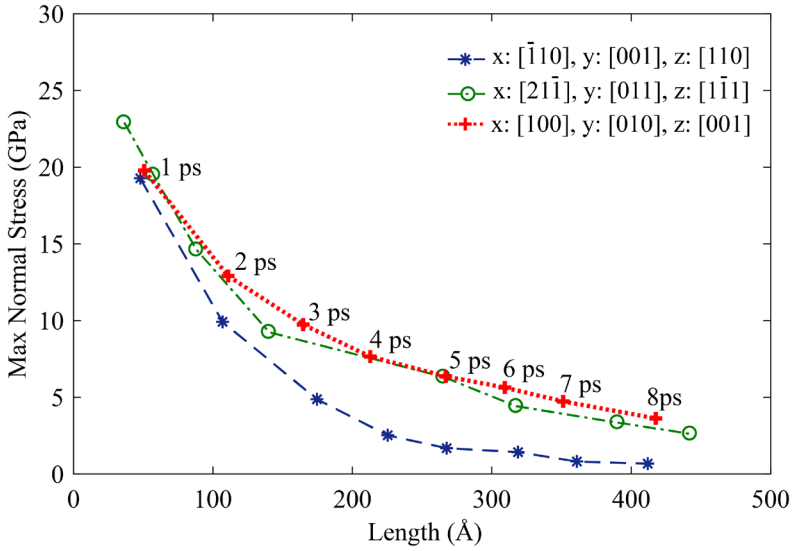

Figure 4-8. Decay of normal stress wave for the three single crystals with shock directions aligned with [110], [1$\bar{1}$1] and [001].

4.2.3.2 Phase transformation propagation

For an austenite NiTi alloy to transform to a B19' martensite phase, a specific strain condition is needed. The deformation matrix which defines the required deformations of phase transformation from austenite phase to martensite phase is called deformation gradient matrix *F*. The deformation gradient matrix is calculated for the martensitic phase transformation from B2 austenite phase to B19' martensite phase of NiTi alloys [41, 93] and using this matrix, the Lagrangian strain matrix can be calculated which gives the required strain components for martensitic phase transformation. The Lagrangian strain matrix of atom *i* is expresses as [208]:

$$\eta_i = \frac{1}{2}\left(F_i F_i^{T} - I\right) \tag{4-14}$$

In order to detect inelastic deformations, Von Mises shear strain definition is utilized. This strain condition which is a good measure of local inelastic deformation can be expressed as [208]:

$$\eta_i^{Mises} = \sqrt{\left(\eta_{yz}^{2} + \eta_{xz}^{2} + \eta_{xy}^{2} + \frac{\left(\eta_{yy} - \eta_{zz}\right)^2 + \left(\eta_{xx} - \eta_{zz}\right)^2 + \left(\eta_{xx} - \eta_{yy}\right)^2}{6}\right)} \tag{4-15}$$

Using the required Lagrangian strain matrix for martensitic phase transformation, the threshold value of η_i^{Mises} is calculated as 0.11, which is also compatible with the reported value in [209]. The regions correspond to this value of Mises shear strain will have a completed phase transformation to martensite, any region with an equivalent shear strain above this threshold, could have a combination of phase transformation and plastic deformation. Von Mises strain distribution

in the three crystal orientations were calculated and shown in the contour plots of Figure 4-9. The green colored regions are just above 0.11 and the red colored areas correspond to the strain levels of 0.2 and above. These regions in the plots show the atoms which have a combination of plastic deformation and phase transformation.

Comparing the contour plots of t=4 ps and t=8 ps, it can be seen that some areas are green first, but they return to blue at the end. These regions are the areas in which the forward phase transformation has propagated with no plastic deformation, and the phase transformation has been reversed back to austenite. The remaining areas, which has not returned back to austenite at the end of t = 8ps, are either martensite regions which need more time to recover to austenite, or the regions in which have experienced a plastic deformation during the stress wave propagation. If the simulation is extended to a very long time, the remaining areas with pure plastic deformation and phase transformations can be distinguished, as the martensite areas will transform back to austenite and the equivalent strain will become zero, while the plastic regions will hold a nonzero strain.

The difference in the contours of the three different orientations is due to the difference in their shear stress wave propagation patterns shown in Figure 4-6. The contour plots of Figure 4-6 are almost coinciding with the contour plots of Figure 4-9, revealing that phase transformation and plastic deformation in NiTi are prominently governed by shear stress, which means when the shear stress in slip planes reaches the critical value, slip happens and those affected regions are permanently deformed. Moreover, when a defect such as plastic deformation is generated in the structure, that can be a trigger for phase transformation propagation. So, we can say that those red colored regions show the plastic deformation due to slippage on slip planes and also they show the phase transformations which happen due to the presence of the defects.

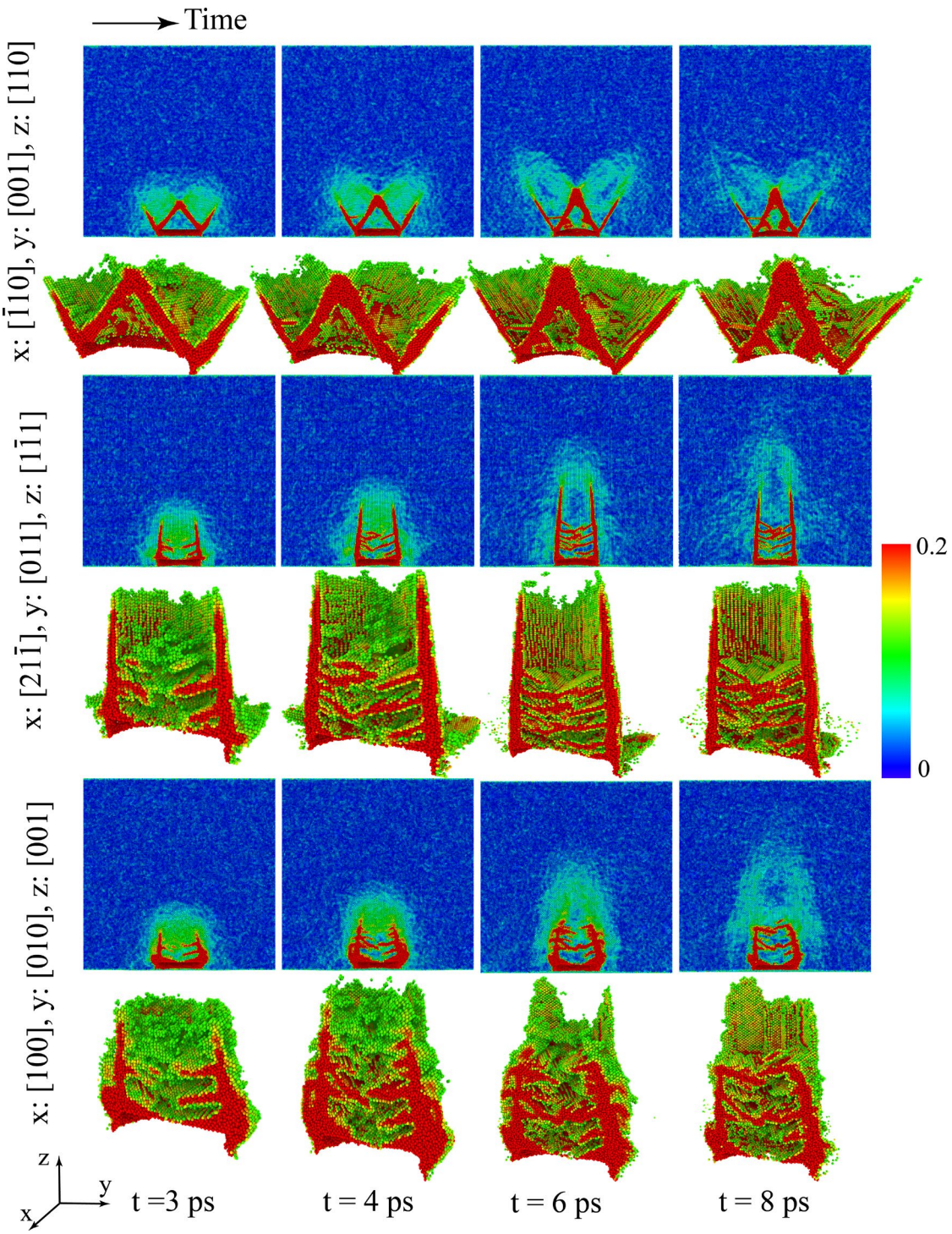

Figure 4-9. Von Mises shear strain parameter which shows phase transformation propagation and plastic deformation in three different oriented single crystals under shock loading. Von Mises shear strain values 0 and 0.11 correspond to regions with austenite and martensite phases, respectively. The values between 0.11 and 0.2 show regions with combined phase transformation and plastic deformation.

That's the reason that we see some of the red colored regions returned to blue at the end of the simulation. In Section 5 we will study the most favorable slip systems of the single crystals with x: [100] y: [010] z: [001] as a representative crystal structure and we will investigate the activated slip systems due to the shock loading. Furthermore, we will propose a method to distinguish the plastic deformation and phase transformation in the structure under shock loading.

4.2.4 Interaction of Stress wave and phase transformation propagation with the grains in polycrystalline NiTi

4.2.4.1 Stress wave propagation

In order to study the effect of grain sizes on the stress wave propagation, three polycrystalline NiTi with different average grain sizes of 13.5 nm, 18.4 nm, and 25 nm are simulated. It is worth noting that the selected size of grains, which actually represent nanocrystalline material, is due to the restrictions in using MD simulations for large systems. However, it is expected that the fundamental findings will be expandable to polycrystalline structures s with larger grain sizes, with an acceptable accuracy.

The evolution and propagation of the normal and shear stresses in the bulks are shown in Figure 4-10 and Figure 4-11, respectively. As it is mentioned in the previous section, the first two columns correspond to the stress distribution during the loading and the last three columns correspond to the stress distribution after removing the shock loading. In Figure 4-10 for all the three polycrystalline structures, two shock wave fronts are initiated and started to propagate in almost half-circular patterns, same as the single crystals. The outer circle corresponds to the elastic wave front and the inner one represents the inelastic shock wave front, since the elastic shock wave has higher propagation velocity than the inelastic one. Right after the removing the shock loading, the unloading elastic shock wave initiates and starts to propagate. The unloading wave which is faster than phase transformation wave contributes to the drop in the phase transformation stress peak from -25 GPa to -10 GPa, when it reaches the phase transformation wave front, dark red area in the contour plots of t = 6 ps and t = 8 ps, where the normal stress is positive, shows the propagation of the unloading elastic wave. Comparing the stress wave propagations in three different polycrystalline structures, it can be seen that the drops of shock wave fronts increases by decreasing the grain sizes.

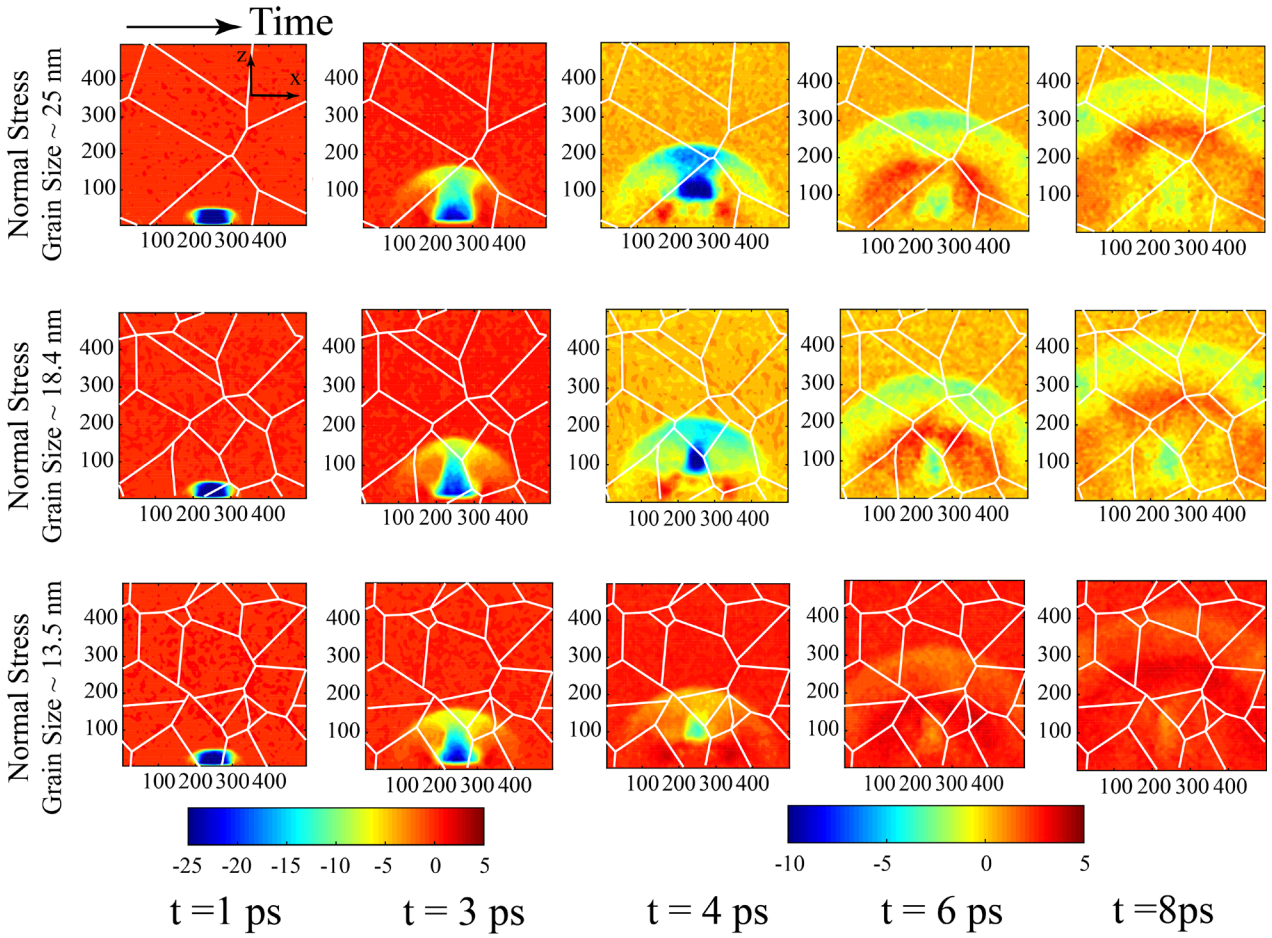

Figure 4-10. Normal stress wave propagation in polycrystalline structures of NiTi for three different grain sizes: 13.5 nm, 18.4 nm, and 25nm. The stress values in color bars are in GPa.

Moreover, by decreasing the grain sizes, the grain boundaries volume fraction in the bulk structures is increased and these grain boundaries not only damp the stress shock wave propagations, but also cause many reflections of shock stress waves. Since, in fine grain sizes the volume fraction of grain boundaries increases, then they can damp the stress waves more compare to the coarse grain sizes.

Figure 4-11 shows the propagation of shear stress. The shear stress wave initiates at the peripheral of the cylinder which is a circle. In a 2D view like Figure 4-10, the wave initiation region appears as a pair of points where in one of them the shear stress is positive and in the other one negative, same as single crystals. It can be seen that the shear stress wave front decreases after t = 4 ps when it reaches the first grain boundary in the shock direction and similar mechanism as normal stress wave propagation happens for the shear stress wave propagation in polyscrstals.

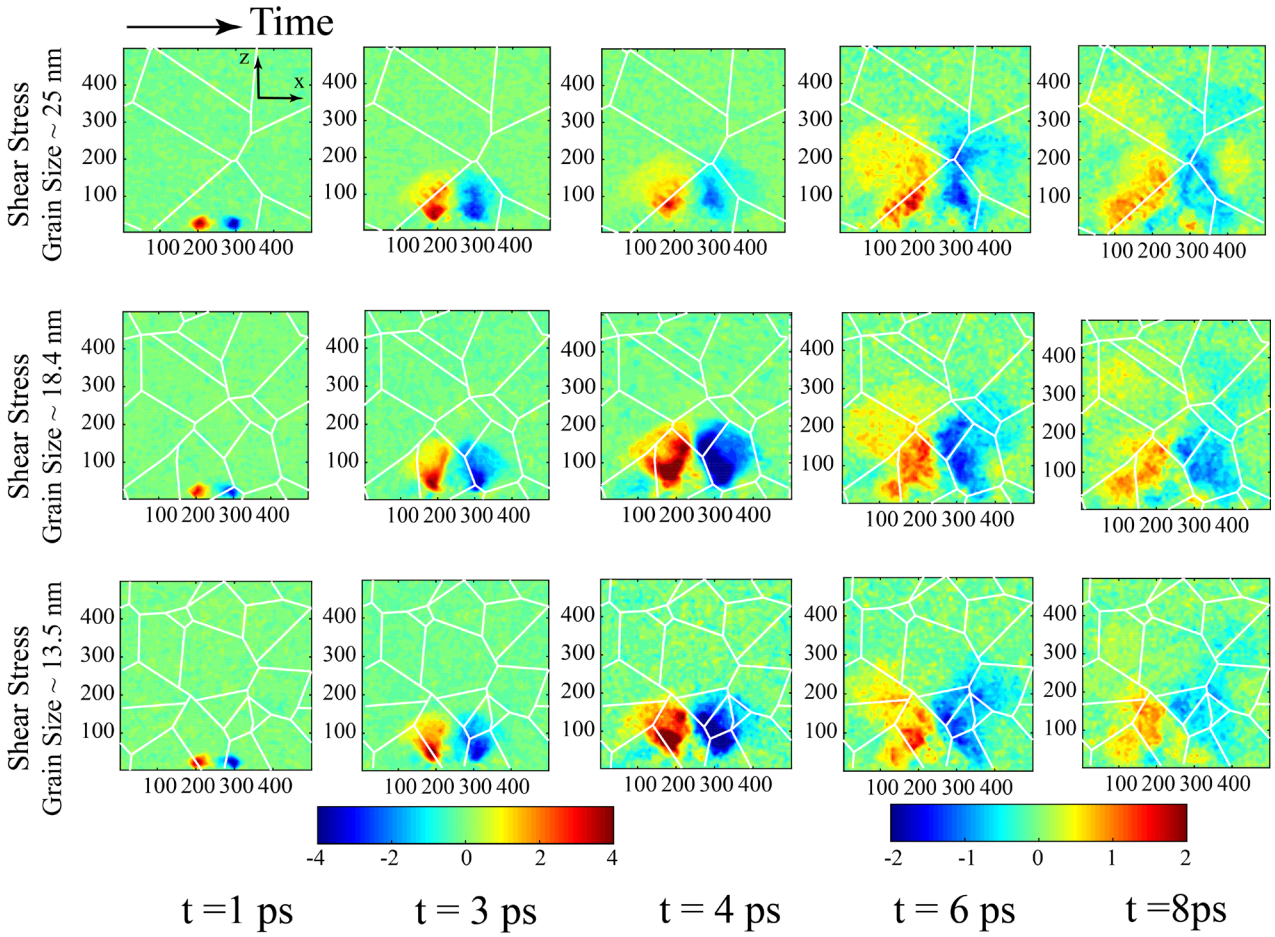

Figure 4-11. Shear stress wave propagation in polycrystalline structures of NiTi for three different grain sizes: 13.5 nm, 18.4 nm, and 25nm. The stress values in color bars are in GPa.

Figure 4-12(a) illustrates the evolution of maximum peak stress in the polycrystalline NiTi, for the three grain sizes, over the time of simulation. The maximum normal stress values for all the grain sizes shows the same trend. However, during the loading it can be seen that the normal stress decrease by decreasing the size of grains. As it is mentioned in the previous section, this can be due to increasing the volume fraction of grain boundaries in the bulk structure and the reflections from grain boundaries. These grain boundaries act like an obstacle for stress wave fronts in the shock direction. Figure 4-12(b), (c) and (d) show the distribution of normal stress along the length of the bulk structures at different times of simulation for the three different grain sizes. At the first three curves (1-3 ps) the phase transformation peaks are at high levels (above 13 GPa). This high stress level propagates the phase transformation and plastic deformation through the bulks. Although from 1 ps to 3 ps some drop in the peak stress is observed, which could be due to energy

dissipation through phase transformation and plastic deformation and also it could be due to presence of grain boundaries which act like an obstacle for shock stress wave. At the time of 4 ps and after that, the peak of elastic wave and phase transformation wave for the coarse grain are greater compared to the other grain sizes.

However, as discussed before, at the onset of unloading, another elastic wave with an opposite direction starts to propagate and at the time of 4 ps, this wave partially reaches the phase transformation peak and therefore, causes a significant drop in the stress level. This is why at the time of 5 ps the phase transformation peak drops below 5 GPa for all the grain sizes.

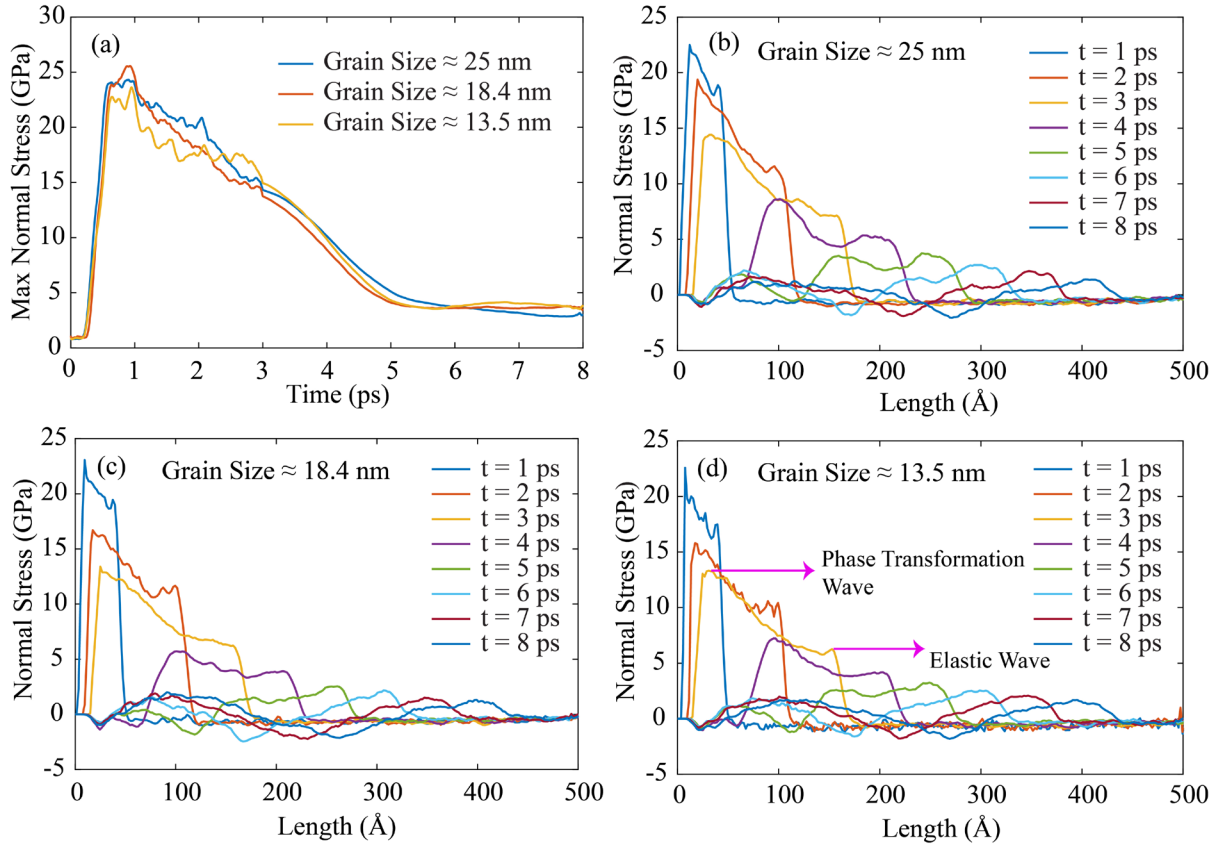

Figure 4-12. (a) Maximum of normal stress wave during loading and propagation time for three polycrystalline structures with three different grain sizes: 13.5nm, 18.4 nm, and 25 nm. (b) Normal stress wave propagation for average grain size of 25 nm (c) Normal stress wave propagation for average grain size of 18.4 nm. (d) Normal stress wave propagation for average grain size of 13.5 nm.

Figure 4-13 shows the maximum recorded stress values correspond to elastic wave front at different times and their corresponding positions over the length of the considered polycrystalline structures. The calculated stress values are obtained from averaging over the cross-sections of the

middle cylinder along the loading direction same as single crystals. It can be seen that the coarse grain size overally shows the highest stress level and the fine grain size the lowest. In Figure 4-13, the grain size 13.5 nm shows more decay in elastic wave front peak compared to the other polycrystalline structures. For instance, at the length of 100 Angstrom from the surface on which the shock loading is applied, the stress in the grain size 13.5 nm drops under 10 GPa, while for the other two polycrystalline structures the stress level is still above 10 GPa. In addition, the grain sizes 13.5 nm and 18.4 nm show greater drop in inelastic wave front peak compared to the 25 nm. In the next section, the phase transformation propagation and plastic deformation in these polycrystalline structures will be discussed.

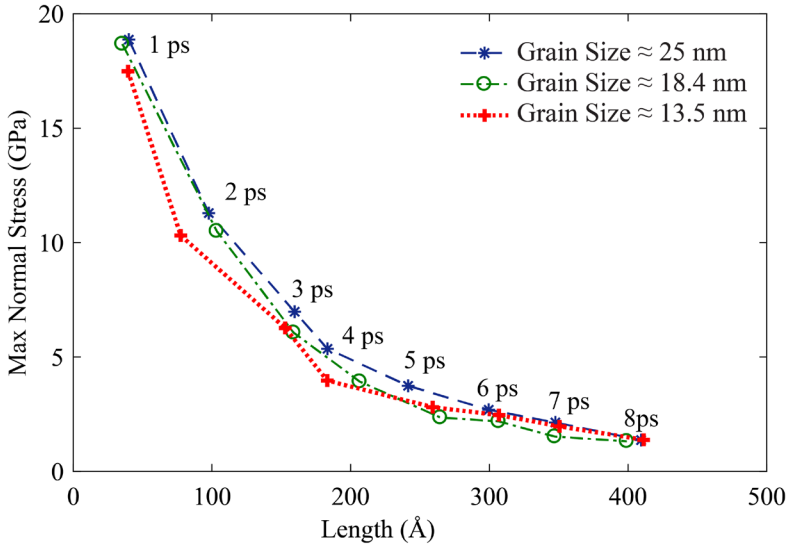

Figure 4-13. Decay of normal stress wave for three polycrystalline structures with three different grain sizes: 13.5nm, 18.4 nm, and 25 nm.

4.2.4.2 Phase transformation propagation

As it is mentioned before for an austenite NiTi to transform to a B19' martensite, there is a threshold in the equivalent Von Mises strain which is equal to 0.11. Above this strain threshold, the state of the material could be a combination of phase transformation and plastic deformation. The Von Mises strain propagation for the three polycrystalline NiTi with different grain sizes are shown in Figure 4-14. This parameter shows both phase transformation and plastic deformation propagation. At the time of 8 ps, which is 5 ps after removing the shock loading, some of the regions with phase transformation are recovered back to austenite. More time is needed to capture all the regions in which all the phase transformation is recovered in the structures. However, but it

is not possible in practice due to the computational restrictions. In order to solve this problem in the next section we propose a method to distinguish the regions with plastic deformation and phase transformation in the single crystal and polycrystalline NiTi alloys. It can be seen in Figure 4-14 that the size of phase transformed regions decrease by reducing the size of grains in polycrystalline structures. As it is expected, grain boundaries volume fraction increases when the grain sizes decrease and these grain boundaries as obstacles prevent the phase transformation propagation in the polycrystalline structures. It can be seen that the phase transformation and plastic deformations initiate at the loading region and they start to propagate but they are stopped when reaching the grain boundaries. Also, the pattern of phase transformation shows that when the phase transformation and plastic deformation reach the grain boundaries they prefer to propagate through the boundaries, over penetrating to the neighbor grain. Since, grain boundaries are kind of defects in the structure and they are a summation of several dislocations, they could trigger the plastic deformation and phase transformation propagation and deploy them to propagate through the boundaries.

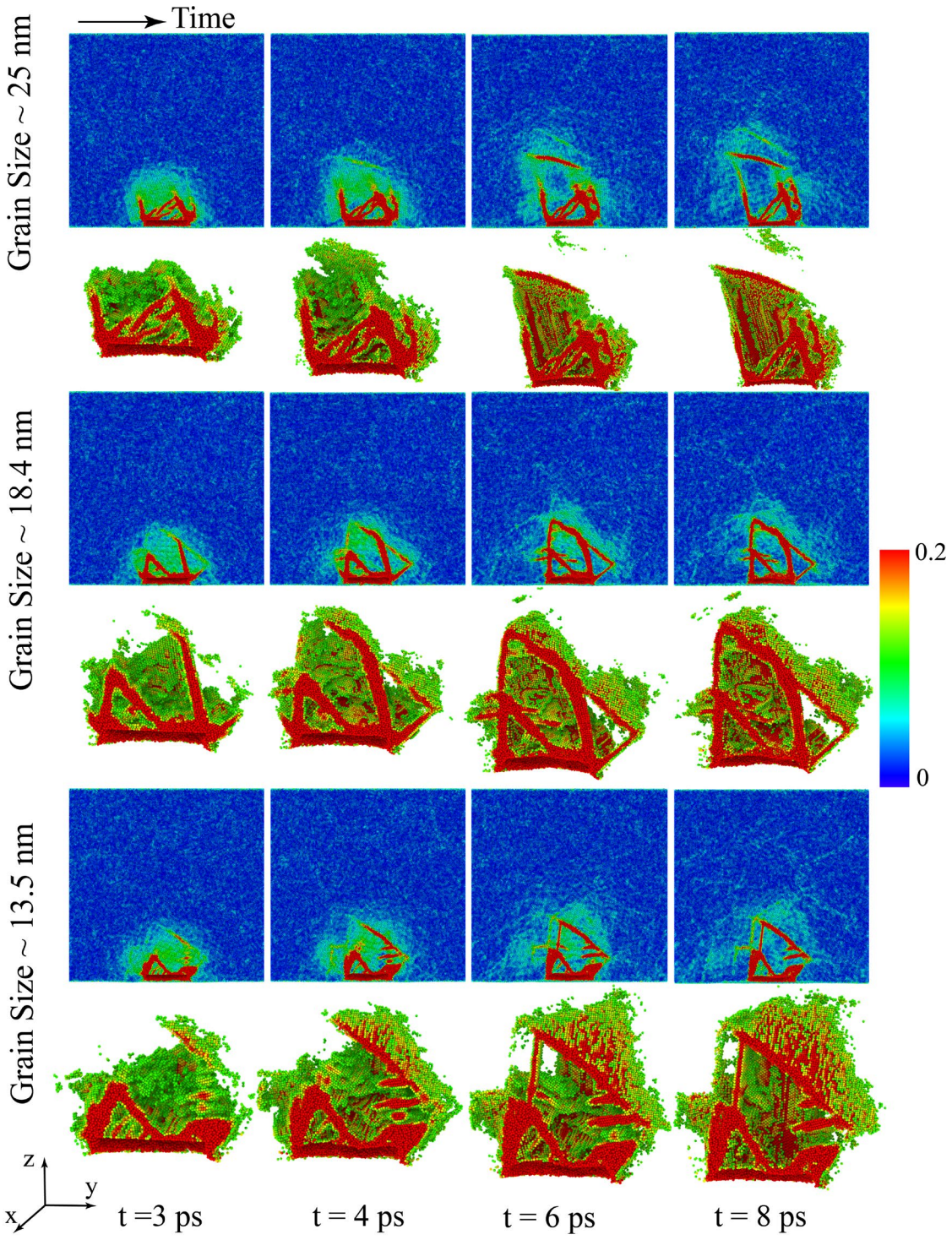

Figure 4-14. Von Mises shear strain parameter which shows phase transformation propagation and plastic deformation in three different polycrystalline structures under shock loading. Von Mises shear strain values 0 and 0.11 correspond to regions with austenite and martensite phases, respectively. The values between 0.11 and 0.2 show regions with combined phase transformation and plastic deformation.

4.2.5 Interaction between plastic deformation and phase transformation

In this section, two methods are used to distinguish the plastic deformation and phase transformation due to shock loading in NiTi single crystal x: [100] y: [010] z: [001], which is selected as a representative direction.

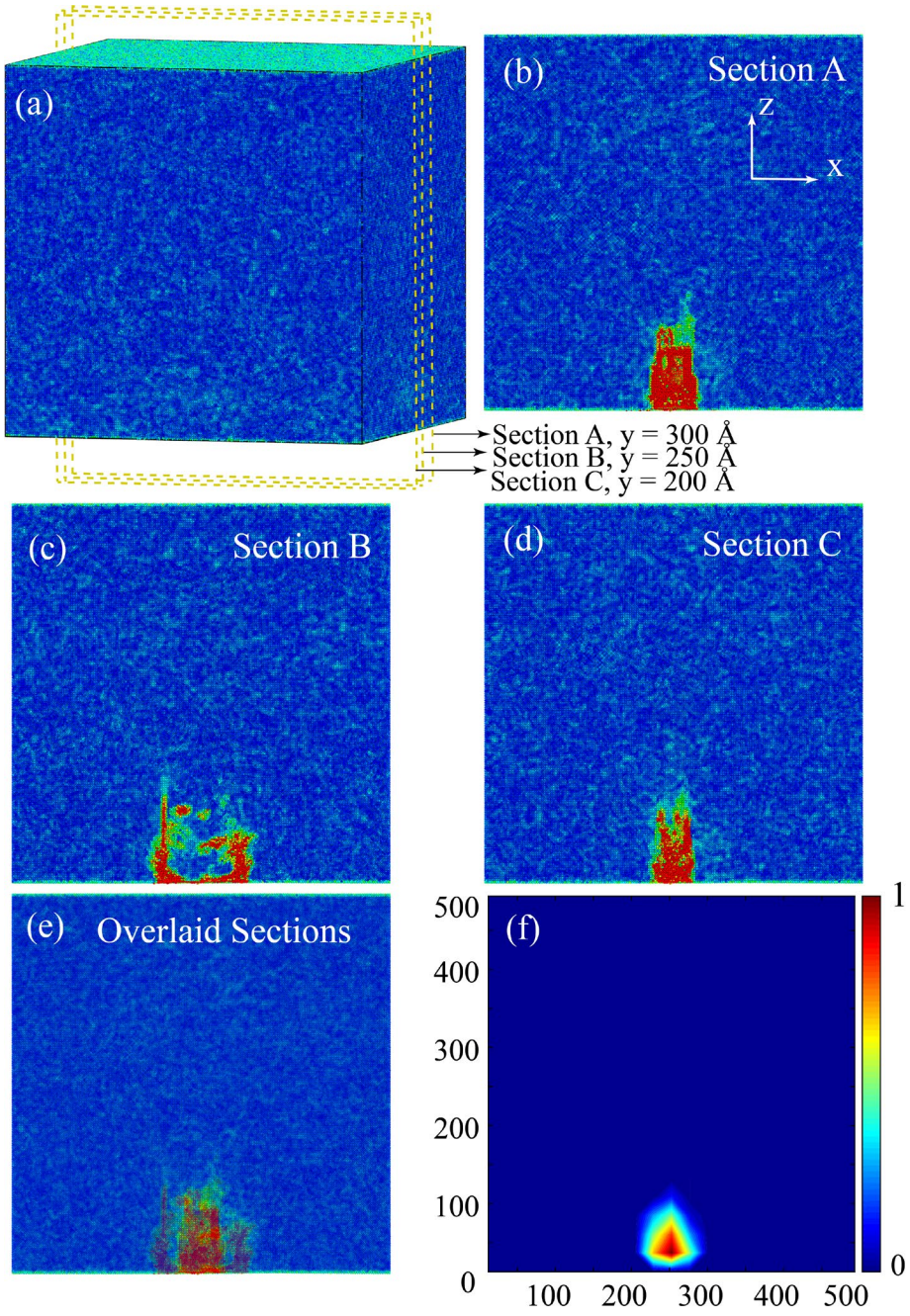

Figure 4-15. (a) Single crystal of NiTi with crystal orientations of [100] [010] [001]. (b-d) Plastically deformed region on x-z planes at y = 200, 250, and 300 Å. (e) Overlaid plastically deformed regions. (f) Plastically deformed region from theory of plasticity.

In the first method, after applying the shock load for 3 ps, the load is removed and we give the structure enough time (200 ps) to relax and let all the martensitic phase transformation returns to austenite phase and only plastic deformations remains in the structure. Figure 4-15(a) shows the single crystal under shock loading. It is worth noting that the load is applied on a circle (with its center at x = y = 250 Å) on the lower surface. Three sections A, B and C are shown in this figure which correspond to the beginning, middle and the end of loading regions. The permanently deformed regions are illustrated at these three sections in Figure 4-15(b), (c) and (d), respectively. The overlaid sections which shows all the permanently deformed regions is shown in Figure 4-15(e). In the second method, we consider the most favorable slip systems of a B2 NiTi alloy structure [6, 80]. These slip systems and the corresponding critical stress values are expressed in [80]:

Table 4-1. Critical shear stress values of B2 NiTi alloys in austenite phase for the (011)[100] and (011)[1$\bar{1}$1] slip systems.

Slip Plane	Slip Direction	$(\tau_{Shear})_{Critical}$ (GPa)
(011)	[100]	0.71
(011)	[1$\bar{1}$1]	1.2

The shear stress in these slip planes are calculated every 0.1 ps for the total time of simulation and in each slip system which shear stress reaches the critical value, slip happens and the corresponding region is assumed to experience a plastic deformation which is permanently deformed. Figure 4-15(f) shows the superposition of those permanently deformed regions. This contour plot also illustrates the intensity of the slippage during the time of simulation which means the red colored areas show those regions that the slip systems were activated more than once during the time of simulations. Comparing Figure 4-15(e) and (f), it can be seen that there is a good agreement between the two methods. We could say that in order to detect and distinguish the plastic deformation and phase transformation in the NiTi structures under shock loading, we could use the second proposed method since it is computationally cost effective.

4.2.6 Conclusions

In this work the energy dissipation and the phase transformation caused by the stress wave propagation in single crystal and polycrystalline austenite NiTi alloys under shock wave loadings

are investigated. Molecular dynamics (MD) simulations are utilized as a superior method to study the effect of microstructures such as lattice orientations, grain sizes and grain boundaries on the patterns of stress wave and phase transformation initiation and propagation at the atomistic level in NiTi alloys. A criterion based on equivalent shear strains is used to detect the inelastic deformation in the NiTi structures. This parameter is used to detect the regions with martensitic phase transformation and plastic deformation. Regions with phase transformation and plastic deformation in the structures are distinguished by implementing two proposed methods. It is expected to observe the dissipated energy in NiTi structures being caused by both phase transformation and plastic deformation.

4.3 Energy Dissipation of Shock Stress Wave through Phase Transformation and Plastic Deformation in NiTi Alloys

4.3.1 Overview

The distinctive performance of seismic and passive control devices developed by NiTi alloys relies on their hysteretic pseudoelastic response [102, 210-212]. NiTi alloys pseudoelastic response is based on their capabilities of changing their crystallographic structure between a low-symmetry martensite phase and a high-symmetry austenite phase in response to either mechanical or thermal loadings. The hysteretic pseudoelastic response of NiTi alloys [97, 100, 101] provides ideal energy dissipation and damping capabilities. Furthermore, NiTi alloys are superior candidates to be used in structures under high-strain-rate and shock wave loadings. In recent years, the dynamic response of various metals and alloys subjected to shock loading, in absence of phase transformation, have been extensively investigated [103-112, 213]. There have been a number of studies on the dynamic behavior of NiTi alloys subjected to high-strain-rate loadings computationally and experimentally [113, 205, 214-223] but the experimental investigations are barely reported due to the limitation of measurement devices to capture the complicated transformation and plastic behavior of NiTi alloys at very high-strain-rates loads. The limitations of experimental researches and also the distinctive ability of Molecular Dynamics (MD) method to capture the fundamental details of intrinsic deformation mechanisms at the atomic level, make it a superior candidate to study the dynamic response of NiTi alloys under shock wave loadings. Among the computational studies, there have been some computational works at the atomistic level. *Yin et al*. [107] investigated the phase transformation of NiTi nano pillars subjected to shock loadings using MD simulations. Also,

we have recently studied the response of single and polycrystalline NiTi alloys subjected to shock loadings using MD simulations at the atomistic scale, and the effects of lattice orientations, grain boundaries and grain sizes on the shock wave propagation and shock-induced phase transformation propagation are investigated [224]. Since shock wave loading is a high-strain-rate loading condition, the dissipated energy in NiTi alloys can be due to both plastic deformation and phase transformation, and in spite of these computational efforts, there is still a need to understand if the major portion of the dissipated energy is due to phase transformation or plastic deformation. Therefore, in this work, the dynamic response and stress wave propagation behavior under shock loading for two different material systems, NiTi alloy and Al, are studied using MD simulations at the atomistic scale. Moreover, the dissipated energy due to plastic deformation and phase transformation are calculated and compared for both materials.

4.3.2 Computational Modeling

A series of molecular dynamics simulations are performed to investigate the dissipated energy caused by plastic deformation and phase transformation in NiTi alloys and Al under the shock-induced stress wave. Two many-body interatomic potentials are used to simulate NiTi and Al structures. The Al potential with cut-off radius $r_c = 6.287$ Å is developed by Mishin *et al.* [225]. The functional form of this potential follows the form of the embedded-atom method (EAM). The method they used for developing this potential was based on experimental data and *ab initio* calculations and improved by rescaling the interatomic distances. They also obtained the optimum parametrization of the potential by alternating the fitting and testing step which included a comparison between the *ab initio* structural energies and those predicted by their potential [225]. The NiTi potential is originally developed by Lai *et al.* [203] and subsequently improved by Zhong *et al.* [93]. The potential function has been modified with cubic polynomial interpolations to smooth the discontinuities near the cut-off radius. Through multiple case studies, it has been demonstrated that the results of MD calculations are in a good agreement with the experimental results and also ab initio calculations [40, 93]. This potential with cut-off radius $r_c = 4.2$ Å is adopted in our work. The more details of total potential energy, pair interaction function and the modified embedding energy function of NiTi alloys are described in [224].

In the present work these two widely used potentials along with large-scale atomic/molecular massively parallel simulator (LAMMPS) [167] are utilized for performing the simulations, and

Ovito [168] visualization tool and MATLAB are used for post-processing the results of MD simulations. Two sets of MD simulations are performed for NiTi and Al. One set includes 3D computational cells of NiTi and Al pillars with the average size of $50 \times 50 \times 1000$ Å. The other set contains 3D computational cells of NiTi and Al bulks with the average size of $400 \times 400 \times 500$ Å. The computational cells for the second set of simulations are periodic only in x: $[\bar{1}10]$ and y: $[001]$ directions and the shock direction is aligned with z: $[110]$ direction.

After creating the single and polycrystalline bulks, the structural energy is minimized using conjugate gradient method. Then, thermal equilibrium is applied to the system using time integration on Nose-Hoover style non-Hamiltonian equations of motion in canonical (nvt) ensembles to set the temperature at T = 350 K for 100 ps. After temperature equilibrium, the system is set to temperature and pressure free using nve ensemble. In order to simulate the shock loading in bulk systems, in a circular area with diameter of 100 Å, 5 layers of atoms at the bottom of the bulk systems are subjected to the wall/piston [26] loading condition. The wall/piston loading duration is 3 ps with the speed of 7 Å/ps. In pillar systems for simulating the shock loading, similar to the bulk systems, 5 layers of atoms at the bottom of the pillars are subjected to the wall/piston [26] loading condition for the loading duration of 3 ps. However, for the pillar systems, different velocities are used. In order to have an equal maximum stress levels for NiTi and Al, the velocity is assumed as 1 Å/ps and 2 Å/ps for NiTi and Al, respectively. Besides, to have an equal input deflection for both systems, the velocity is considered as 3 Å/ps. Figure 4-16(a) and Figure 4-25(a) show a pillar and a single crystal NiTi subjected to the wall/piston loading condition, respectively. Finally, after removing the load, the bulk and pillar systems are equilibrated for 5 ps and 20 ps, respectively to let the stress wave propagates through the structures. The results of shock stress wave propagation through pillar and bulk systems are shown in the following sections. Also, the phase transformation and plastic deformation propagation and the corresponding energy dissipation are discussed thoroughly in the following sections.

4.3.3 Results and Discussions

4.3.3.1 One dimensional shock wave propagation through material nano pillars

Figure 4-16(a) illustrates the NiTi pillar and the wall/piston loading condition. However not shown here, Al system experiences similar loading condition. As expected, the first atomic layers under

the shock loading condition undergo large stress and deformation. Subsequently, the stress wave is guided along the loading direction (z- direction). Figure 4-16(b) shows the propagation of stress wave through the pillar at times 1 ps to 21 ps. The stress wave front can be identified as the areas with higher density of dark blue color, since the normal stress wave is intrinsically compressive.

Besides the linear elastic deformations, the high level of stress propagating along the nano-pillars have the potential to impose inelastic energy dissipating deformations; plastic deformation for Al, and plastic deformation and martensitic phase transformation for NiTi system. For NiTi pillars shown in Figure 4-16, the basic difference between the deformations due to phase transformation and plastic deformation is their stability after removing the stress. Figure 4-16(c) shows a cross-section of the pillar at the place of the peak stress for t = 13 ps, and Figure 4-16(d) is the cross-section at a place along the pillar where the peak stress has passed by. The B19' martensite structures has formed at the cross-section with the peak stress level, confirming that phase transformation propagates along the pillar under propagating shock stress condition. However, the structure of NiTi at the cross-section of Figure 4-16(d) is purely B2 structure, showing that as the stress peak passes by, the structure at that cross-section has undergone the martensitic transformation followed by a revere transformation.

In contrast to phase transformation, the plastic deformation does not disappear as the stress peak leaves. Therefore, at the times quite larger than the loading time, the remaining deformation will be plastic deformation. Figure 4-16(e) shows the propagation of plastic deformation inside the NiTi pillar. To confirm that the deformation is due to plastic behavior, the simulation is extended up to t = 403 ps. The only region that plastic deformation is observed in the NiTi pillar was the first 50 Å close to the loading area. The plastic deformation is along the shear planes shown in Figure 4-16(a).

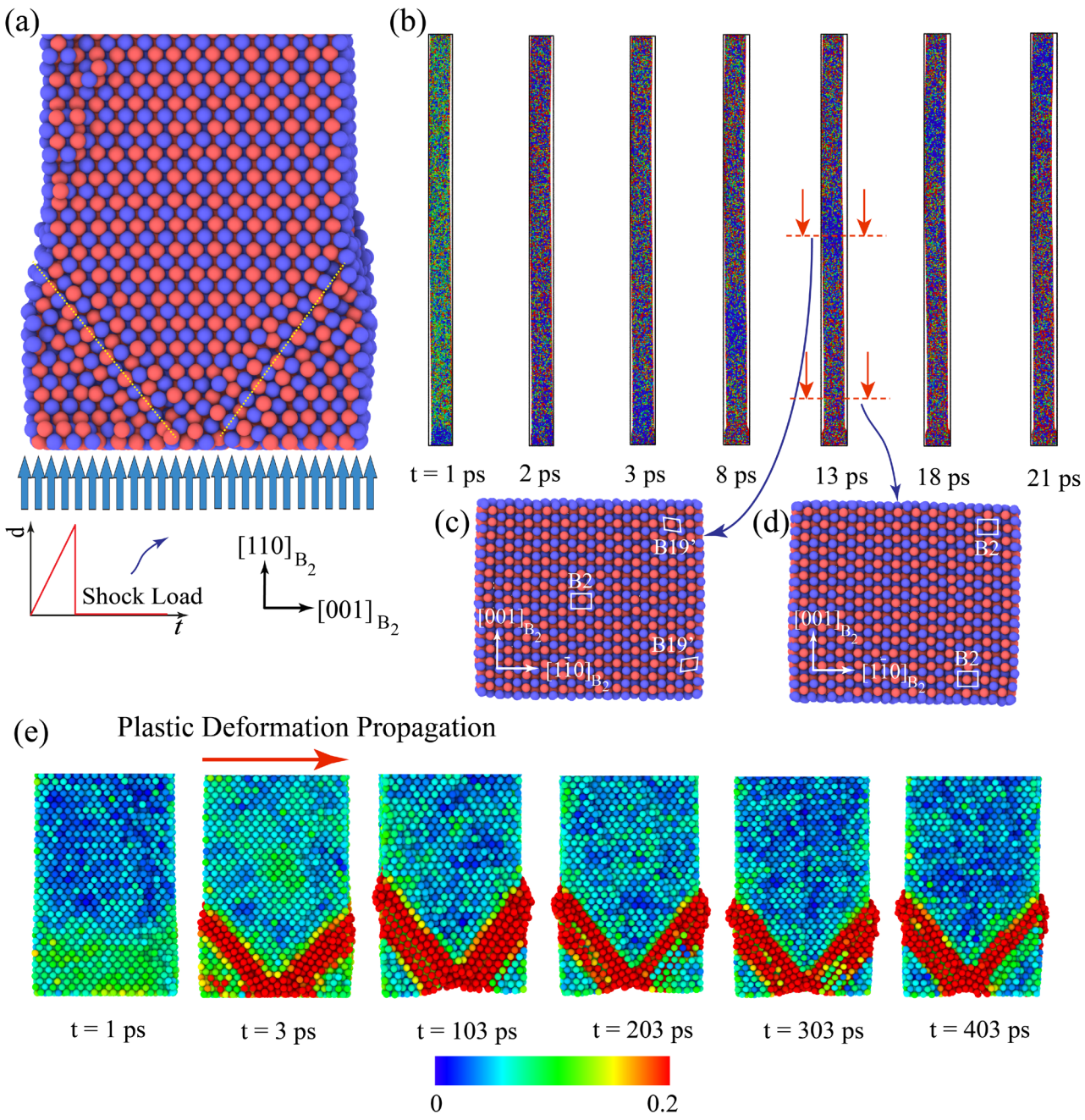

Figure 4-16. (a) Schematic representation of the NiTi pillar subjected to the shock wave loading. (b) Shock stress wave propagation in shock direction during the loading and unloading. (c) Martensitic phase transformation due to shock stress wave propagation in the cross-section at z = 500 Å. (d) The reverse martensitic phase transformation (Austenite phase) in the cross-section at z = 120 Å. (e) Von Mises shear strain parameter which shows the plastic deformation and phase transformation propagation. In this case after enough time of propagation, 400 ps, we still can see the red areas which means these areas represent the plastic deformation in the pillar.

Figure 4-17 shows the shear Von Mises strain propagation which represents the plastic deformation propagation in Al pillar under shock loading. As it is mentioned before, the plastic deformation does not disappear as the stress peak leaves. Therefore, at the times quite larger than the loading time, the remaining deformation will be plastic deformation. Same as NiTi pillar, to confirm that the deformation is due to plastic behavior, the simulation is extended up to t = 403 ps and it can be seen that the remaining deformation (red regions) are plastic deformation.

Figure 4-17. Von Mises shear strain parameter which shows the plastic deformation propagation in Al pillar under shock loading. In this case after enough time of propagation, 400 ps, we still can see the red areas which means these areas represent the plastic deformation in the pillar.

Figure 4-18 shows the normal stress distribution along the pillars for Al and NiTi systems, for the set of simulations with same input loading velocities (3 Å/ps). Figure 4-18(a) shows the average normal stress over time at the first two atomic layers. The peak stress for both material systems occurs around the time of 3 ps, when the input loading drops to zero, and then almost suddenly, the normal stress drops. As shown, the peak stress is higher for NiTi when the loading velocity is the same for both material systems. This was expected, since the density of NiTi is higher than Al's and therefore, the linear momentum of the atoms in the NiTi structure is higher, resulting in developing higher stress inside the NiTi structure. Figure 4-18(b) shows the maximum normal stress traveling through NiTi and Al pillars as a function of time. As mentioned, the maximum stress has a higher value in the NiTi system. However, as time increases, the peak stress drops significantly in the NiTi structure, compared to the Al system. This could be due to the damping effect of phase transformation in the NiTi system. This effect is more evident comparing the graphs of Figure 4-18 (c) and (d). Figure 4-18(c) and (d) show the normal stress distribution along the pillars at different times (from 1 ps to 11 ps) for NiTi and Al, respectively. Besides the significant drop in the stress peak in the NiTi, these figures show that the peak stress travels faster inside Al than inside NiTi, as for example at t = 11 ps, the stress peak is at ~400 Å in the NiTi pillar and at ~600 Å in the Al. This result was also expected, due to the fact that stress in pillars travel at the sound speed. The sound speed is proportional to the square root of elastic modulus over density, and since austenite NiTi and Al have almost the same elastic moduli, higher density of NiTi would lead to slower stress wave propagation.

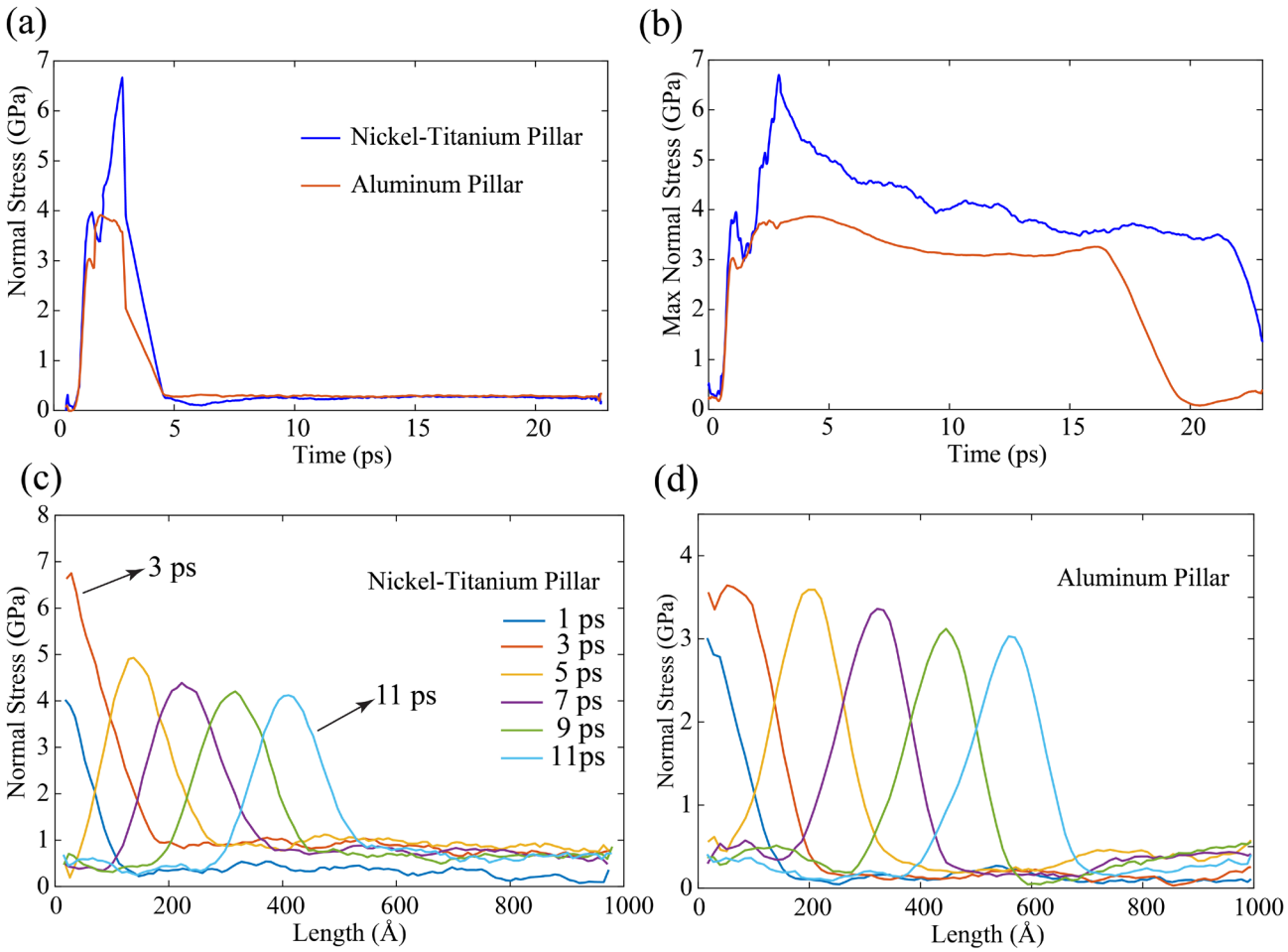

Figure 4-18. The corresponding results represent the stress wave propagation in NiTi and Al pillars when an equal deflection 9 Å is applied to the systems. (a) Normal stress wave during loading and propagation time in the first two atomic layers in NiTi and Al pillars. (b) Maximum normal stress wave propagation during loading and propagation time in NiTi and Al pillars. (c) Normal stress wave propagation over length in different time of simulation for NiTi pillar. (d) Normal stress wave propagation over length in different time of simulation for Al pillar.

In order to provide a better comparison of stress propagation in NiTi and Al systems, another set of simulations are performed where the peak stresses at both NiTi and Al systems are in the same range (~ 3 GPa). Normal stress distributions, as a result of this set of simulations, are shown in Figure 4-19. The input velocities applied to the structures are 2 and 1 Å/ps for Al and NiTi systems, respectively. The significant drop in the peak stress for NiTi is more pronounced in the graphs of Figure 4-19(b) where at the time around 15 ps, the max stress for NiTi has drop to the third of its peak value, while in the Al it has been dropped slightly.

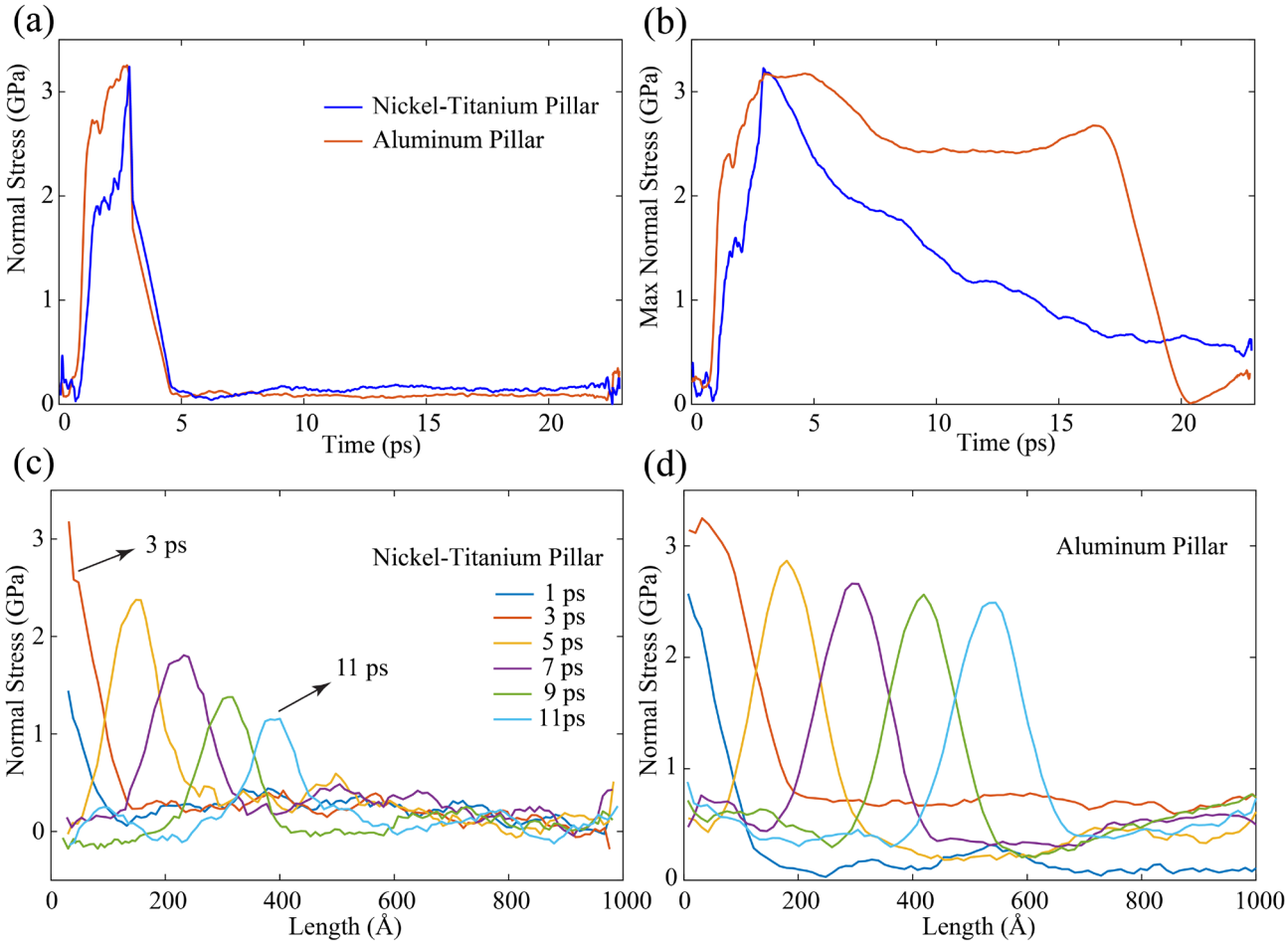

Figure 4-19. The corresponding results represent the stress wave propagation in NiTi and Al pillars when 1 Å and 2 Å deflection is applied to the NiTi and Al systems, respectively. (a) Normal stress wave during loading and propagation time in the first two atomic layers in NiTi and Al pillars. (b) Maximum normal stress wave propagation during loading and propagation time in NiTi and Al pillars. (c) Normal stress wave propagation over length in different time of simulation for NiTi pillar. (d) Normal stress wave propagation over length in different time of simulation for Al pillar.

As a result of wave propagation through the material systems, which is shown in Figure 4-18 and Figure 4-19, the material structures undergo repetitive loadings and unloadings. For austenite NiTi, these repetitive loadings and unloadings will lead to recurring martensitic direct and reverse phase transformations. Considering the stress-strain behavior of the superelastic NiTi, the area of the hysteresis loop between the loading and unloading curves is the amount of energy per unit volume dissipated through a phase transformation cycle. Besides, some strains cannot be recovered during unloading, indicating the energy dissipation due to plastic deformation. As a result, the input energy due to the external force, i.e. work applied by the shock loading, will be transformed into the kinetic energy due to velocity and elastic energy, and some of it will be dissipated through

plastic deformation and phase transformation. The percentage of the energy dissipation can be calculated as [205]:

$$D(\tau) = \frac{P(\tau) - \big(K(\tau) - W(\tau)\big)}{P(\tau)} \tag{4-16}$$

Where P is the external work applied by the shock loading, K is the kinetic energy, and W is the stored elastic energy inside the material. P and K can be calculated using the following equations [205]:

$$P(\tau) = \int_0^{\tau} \sigma(0,t)\, v(0,t)\, dt \tag{4-17}$$

$$K(\tau) = {}^{1}/_{2} \int_0^{L} \rho\, (v(x,\tau))^2\, dx \tag{4-18}$$

And the stored elastic energy in a regular elastic material can be calculated as [205]:

$$W(\tau) = {}^{1}/_{2} \int_0^{L} \sigma(x,\tau)\, \varepsilon^e(x,\tau)\, dx \tag{4-19}$$

Where ε^e is the elastic strain which is ${}^{\sigma}/_{E}$, where σ is stress and E is the elastic modulus. This equation is used for Al pillar, in order to calculate the amount of stored elastic energy. However, in this study, the amount of stored energy in superelastic NiTi is considered as the amount of energy that returns to the system, if the stress is removed. In that case for each stress condition the area underneath the unloading portion of stress-strain curve is considered as the stored energy. The amount of dissipated energy due to phase transformation is also considered to be the area inside the hysteresis loop of the stress-strain curve for the corresponding maximum stress. In the case of the stress beyond the failure stress in NiTi, in addition to the energy dissipated through phase transformation up to that point, the amount of energy dissipation due to plastic deformation is calculated as the area under the loading portion of stress-strain curve minus the hysteresis loop area right before the failure stress, minus the stored elastic energy of martensite NiTi calculated at that specific stress. It should be noted that all the calculated energies, except the external work, are per unit volume of the pillars and in order to have them comparable with the external work they need to be multiplied by the volume of the pillars.

Using the methods described, the external work, elastic energy, kinetic energy and energy dissipation percentage for the NiTi pillar is calculated over time and shown in Figure 4-20(a-d),

respectively. It can be seen that elastic and kinetic energies show sudden increase from zero at the start of loading, and then decrease over time. The energy dissipation ratio however tends to go to 100% as time extends.

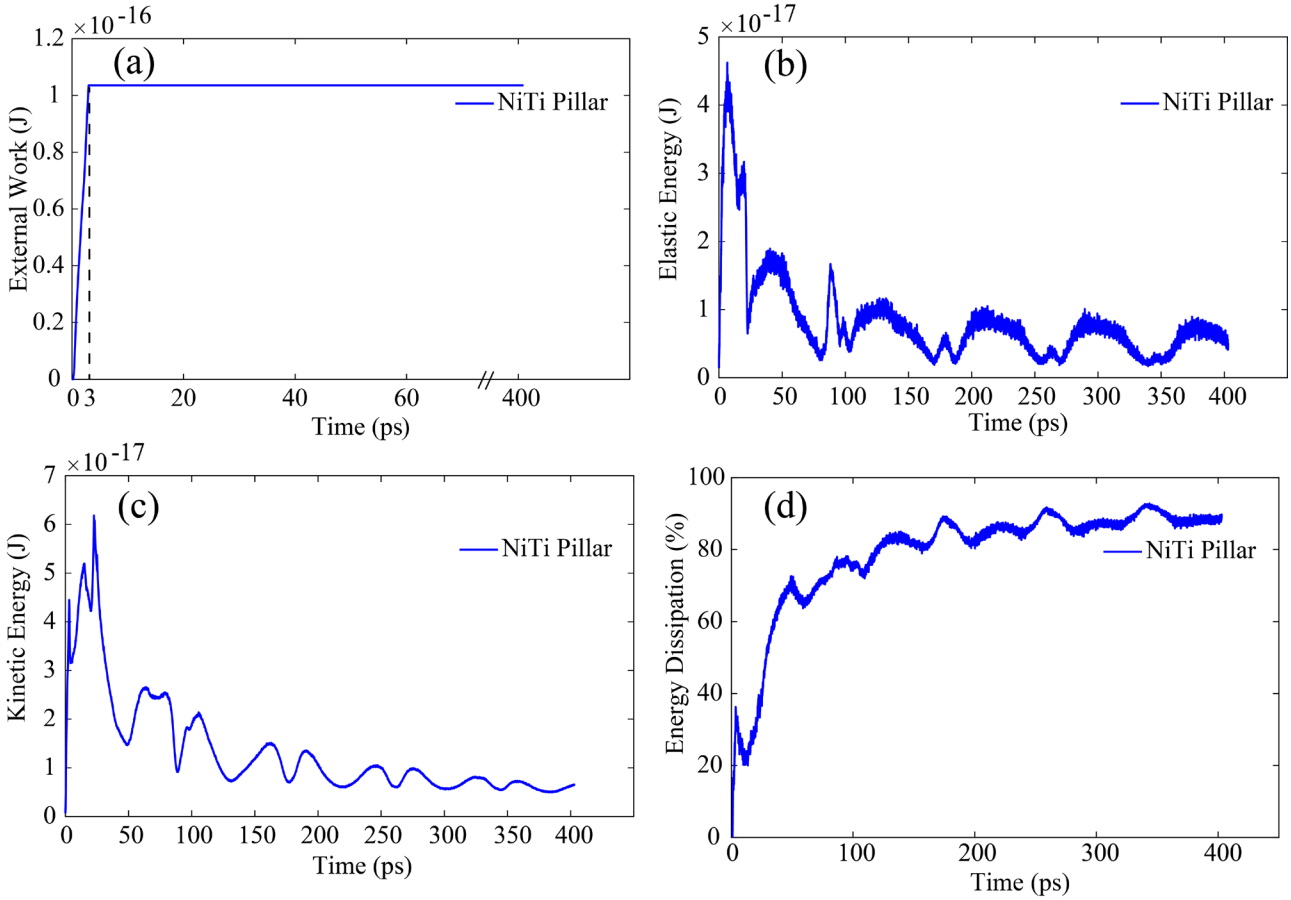

Figure 4-20. (a) Work done by applied force to the NiTi pillar. (b) Stored elastic energy in the NiTi pillar. (c) Kinetic energy in the NiTi pillar. (d) Total shock stress wave dissipated energy in NiTi pillar.

Moreover, the accumulative energy dissipation during different time steps due to phase transformation and plastic deformation is shown in Figure 4-21(a). It can be seen that after first 3 ps of the simulation, almost no energy is dissipated through plastic deformation. Figure 4-21(b) shows that, approximately 80 percent of the total work is dissipated due to phase transformation and plastic deformation both which is in agreement with the result shown in Figure 4-20(d). During the loading (from 0 to 3 ps), the dissipated energy is due to phase transformation and plastic deformation but the plastic deformation has more portion compare to the phase transformation as shown in Figure 4-21(b). After loading and during unloading, the dissipated energy due to plastic deformation is remained constant but the dissipated energy due to the phase transformation is

increased over time because the shock stress wave travels through the pillar and causes phase transformation.

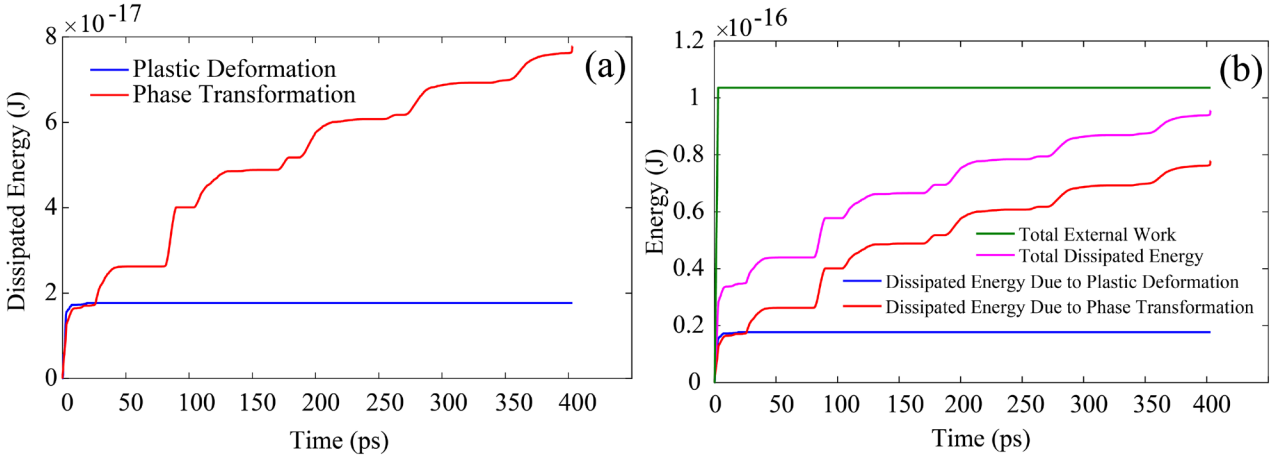

Figure 4-21. (a) Dissipated Energy due to phase transformation and plastic deformation in NiTi pillar. (b) Dissipated Energy due to plastic deformation and phase transformation and total external work in NiTi pillar.

Using the same approach, the external work, elastic energy, kinetic energy and energy dissipation percentage for the Al pillar is calculated over time and shown in Figure 4-22(a-d), respectively. The general trend for the change of the energies is somehow similar to the NiTi's. However, comparing the graphs of dissipation energy in NiTi, Figure 4-20(d), with the one in Al, Figure 4-22(d), reveals that NiTi has dissipated more energy than Al at a given time. For example, at the time of 200 ps, Al has almost 65% energy dissipation, but NiTi has more than 80% of the total energy dissipated. Besides, the slope of the energy dissipation curve for NiTi is larger than Al's, showing that NiTi dissipates the energy faster than Al.

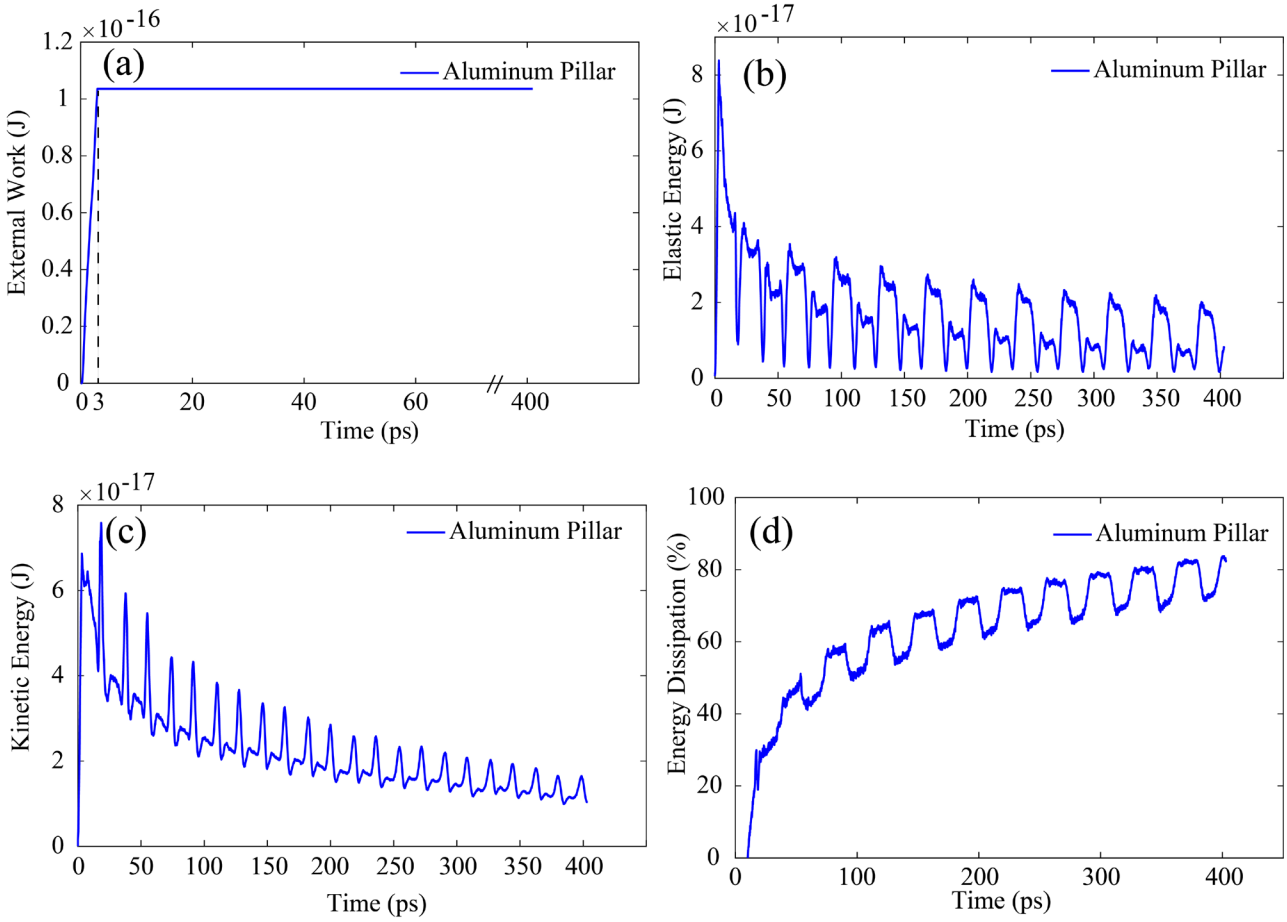

Figure 4-22. (a) Work done by applied force to the Al pillar. (b) Stored elastic energy in the Al pillar. (c) Kinetic energy in the Al pillar. (d) Total shock stress wave dissipated energy in Al pillar.

4.3.3.2 Three dimensional shock wave propagation through bulk material

Wave propagation through nano pillars and bulk materials have some similarities and some differences. In nano pillars, the wave energy is guided along one dimension and stress wave front faces same cross-section. On the other hand, for shock wave propagation through bulk materials, the wave propagates into a 3-D space where the stress wave front gets larger as the wave goes farther into the material. As a result, the maximum stress peak drops faster in the bulk materials than in the nano pillars. Figure 4-23(a) shows the maximum normal stress in the bulks of NiTi and Al over time. Comparing this graph with the graphs of Figure 4-18(b) and Figure 4-19(b) reveals that the maximum normal stress due to the shock wave loading drops faster in a 3D space than in the 1D space. Maximum shear stress inside the bulks of NiTi and Al over time is also presented in Figure 4-23(b). Similar to the normal stress, the shear stress in NiTi drops faster than in Al does.

This could be due to capability of the NiTi to dissipate energy through stress driven phase transformation.

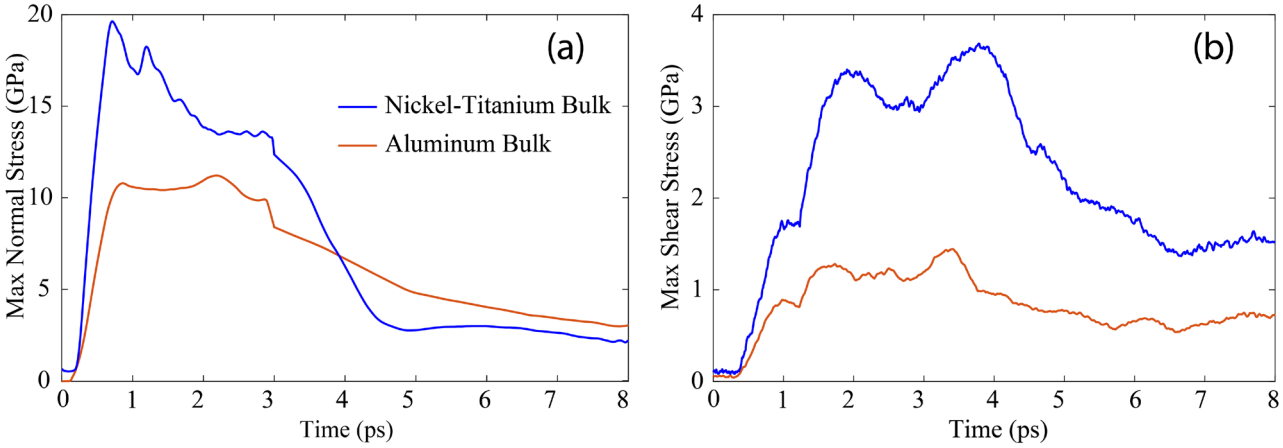

Figure 4-23. Maximum normal stress wave propagated in NiTi and al bulk systems under shock loading. (b) Maximum shear stress wave propagated in NiTi and Al bulk systems.

It is well known that the propagation speed depends on the crystal orientation [207, 224]. Therefore, due to the 3D nature of wave propagation in the bulk materials, the stress wave front will not form a full semi-sphere. Figure 4-24(a) and (b) show the normal and shear stress distribution, respectively, in NiTi and Al bulks over time. Due to the differences in crystal structure and orientation, the stress distribution is quite different in NiTi and Al structures. The normal stress propagation in Al is more concentrated towards the centerline, while it is more spread in NiTi structure. More importantly, the shear stress distribution in NiTi has a butterfly shape at the cross-section shown in Figure 4-24(b) and in Al has a cylinder shape. As discussed in [224], the shear stress propagation dictates the deformation patterns inside the bulk of material. As mentioned earlier, besides the pure elastic deformation, the deformation in NiTi is a mixture of phase transformation and plastic deformation, while it is just plastic deformation in Al structure. Inferred from Figure 4-24, although the normal and shear peak stresses drop over time, they are still high enough to propagate phase transformation and plastic deformation.

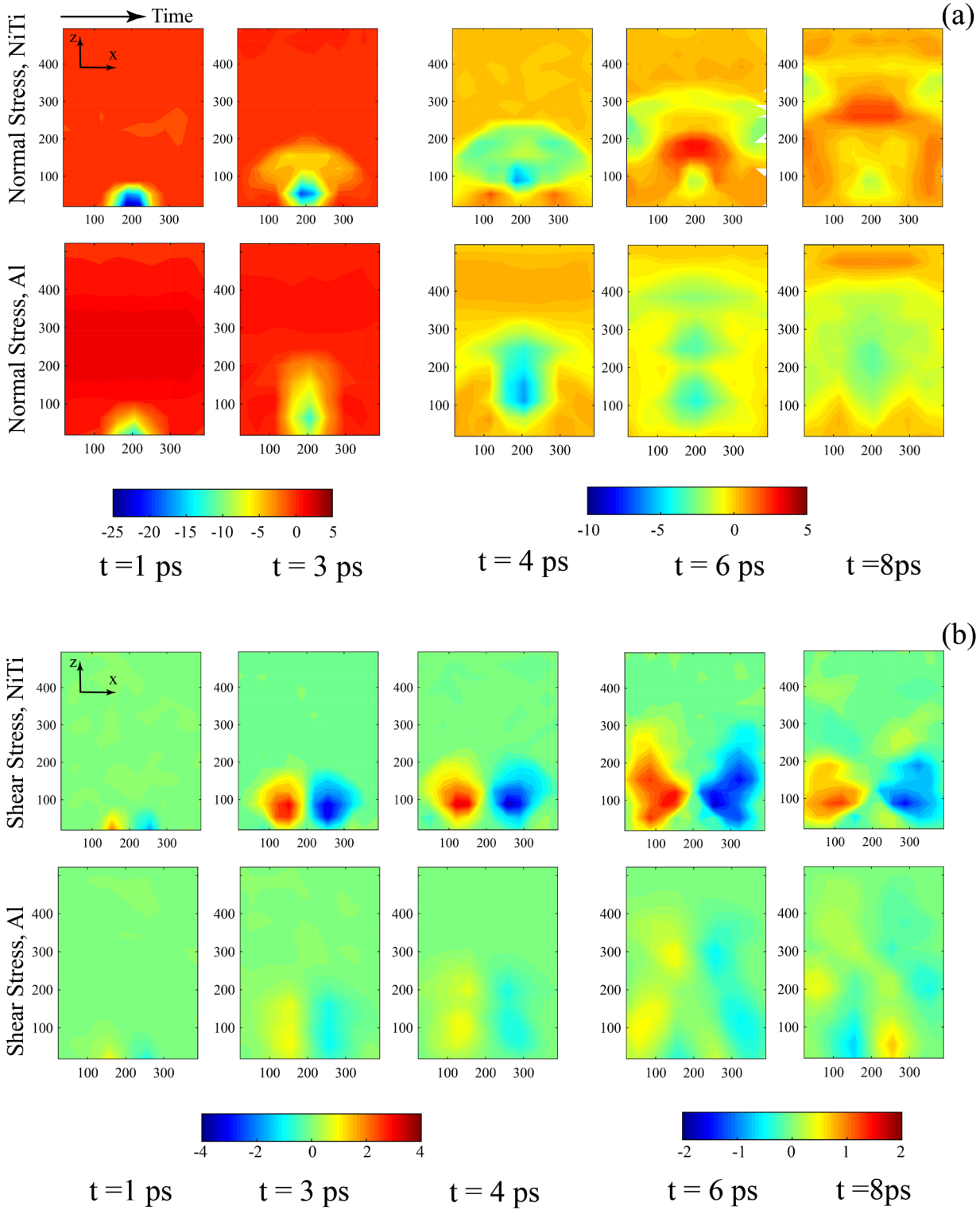

Figure 4-24. (a) Normal stress wave propagation of the NiTi and Al structures. The stress values in color bars are in GPa. (b) Shear stress wave propagation of the NiTi and Al structures. The stress values in color bars are in GPa.

Figure 4-25 shows the loading condition and deformation propagation in the NiTi bulk material. Similar to the observation in the case of the NiTi pillar, the deformation is a mixture of martensitic phase transformation and plastic deformation. Formation of B19' phase, shown in Figure 4-25(a), confirms the energy dissipation through phase transformation. As an indicator of phase transformation, von Mises shear strain was calculated where the values less than 0.11 indicate austenite phase in NiTi, and values above 0.11 indicate the regions with B19' martensite or regions with permanent plastic deformation. Figure 4-25(b) and (c) illustrate the contour plots showing von Mises shear strain taken from two perpendicular cross-section planes along the loading direction during different times through the simulation. As mentioned before, the wall piston loading is applied at the first 3 ps of the simulation and at the time of 3 ps, the loading is removed and the rest of the simulation belongs to the dynamic response of the material to the applied loading/unloading condition. Comparing the contour plots of t = 3 ps and t = 6 ps in Figure 4-25(b) and (c), it can be seen that some areas with large von Mises strain at t = 3ps (the area with green-cyan color) has lost their strain at t = 6 ps. This indicates that, once the stress is dropped in that region martensitic phase transformation is reversed. Figure 4-25(d) shows a 3D view of the deformation pattern over time showing a mixture of plastically deformed and martensitic phase transformed regions. This figure shows how this deformation is propagated through the structure, and is shrunk in some areas, over time. It is worth mentioning that comparing the deformation pattern shown in Figure 4-25(b-d) with the shear strain propagation patterns of Figure 4-24(b) for NiTi reveals that shear stress dictates the deformation pattern, both the phase transformation and the plastic deformation. This is well discussed in [224] where different crystal orientations of NiTi structure is studied.

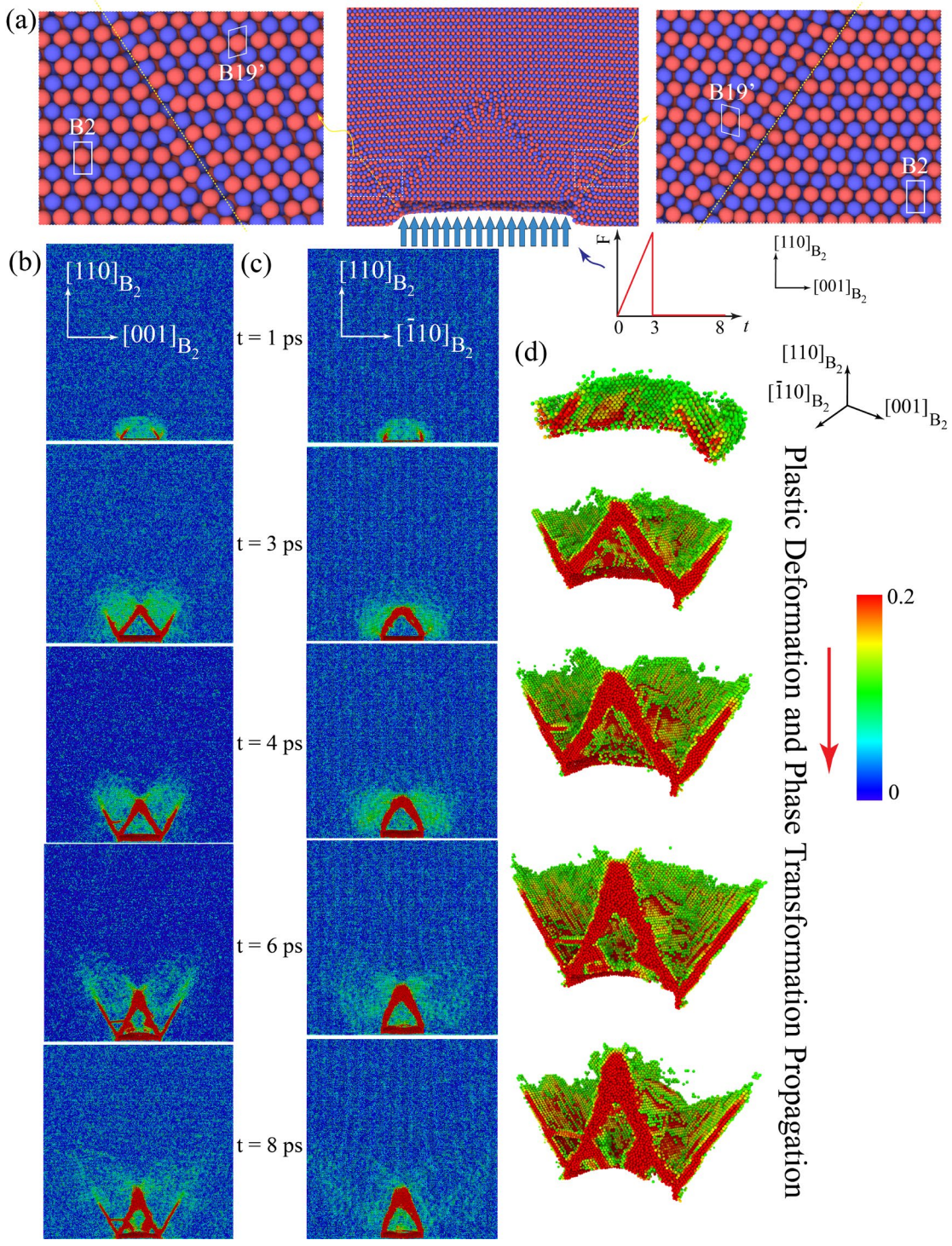

Figure 4-25. Von Mises shear strain parameter which shows phase transformation propagation and plastic deformation in NiTi bulk system under shock loading. Von Mises shear strain values 0 and 0.11 correspond to regions with austenite and martensite phases, respectively. The values between 0.11 and 0.2 show regions with combined phase transformation and plastic deformation.

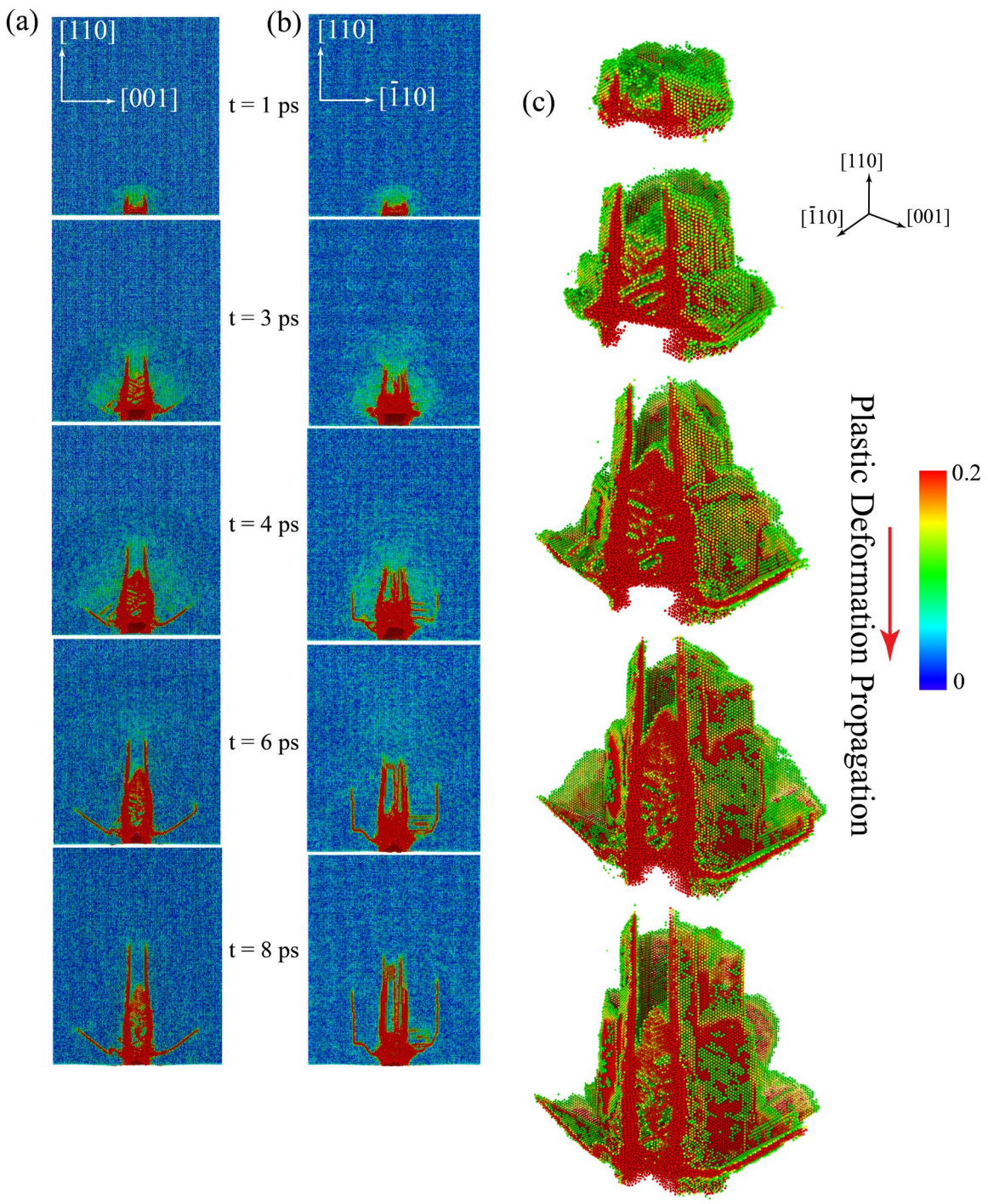

Figure 4-26. Von Mises shear strain parameter which shows plastic deformation in Al bulk system under shock loading. Von Mises shear strain values between 0.11 and 0.2 show regions with plastic deformation.

Figure 4-26 shows the deformation propagation behavior in the Al bulk structure. Figure 4-26(a) and (b) show the contour plots of von Mises shear strain at two perpendicular cross-section planes along the loading direction at different times through the simulation. It can be seen that

deformation pattern in Al is different than the pattern in NiTi. This is due to their difference in crystal structure and orientation. Another important difference in the deformation propagation behaviors in Al vs. in NiTi is that in the Al structure, the deformation is permanent, in another words purely plastic, while in NiTi structure the deformation is growing at some areas and shrinking at other areas confirming that the deformation is a mixture of plastic deformation and phase transformation. Figure 4-26(c) shows a 3D view of the deformation pattern over time. This deformed region in Al keeps growing as time goes by while the deformation in NiTi, shown in Figure 4-25(d), starts to shrink after certain time. This phenomenon reveals that plastic deformation in Al is less capable of damping the shock wave energy compared to phase transformation in NiTi. Hence, superelastic austenite NiTi alloy is a great candidate when shock wave energy attenuation and minimizing the deformation are desired.

4.3.4 Conclusions

In this study molecular dynamics simulations were utilized to study the behavior of pseudoelastic NiTi under shockwave stress loading conditions in comparison to aluminum. At the first set of simulations, nanopillars of austenite NiTi as well as Al were modeled to study one dimensional (1-D) shock wave propagation through the two different material systems. Compressive shock stress loading was applied to the system using a wall-piston method. The wave propagation and deformation mechanisms were observed to be very different in NiTi and Al. Plastic deformation and forward and reverse martensitic phase transformation were observed along the NiTi nanopillar contributing to energy dissipation, while obviously, the only energy dissipating mechanism was plastic deformation in Al pillars. The plastically deformed region in NiTi was the region close to the loading area, while in Al, the plastic deformation was propagated though the pillar. Besides, the peak stress in NiTi damped more quickly in NiTi pillar compared to in Al, revealing the capability of NiTi in shock wave energy attenuation.

The energy dissipation through phase transformation and plastic deformation were calculated and it was revealed that phase transformation mechanism dissipated larger portion of shock wave energy compared to plastic deformation. In fact, the plastic deformation happens at the initial few picoseconds of the simulation, and consecutive forward and reverse martensitic phase transformations are responsible of the energy dissipation for the rest of the simulation.

Three dimensional (3-D) shock stress wave propagation was also studied, through MD simulations of NiTi and Al bulk material systems. Same energy damping behaviors as observed in pillars were

observed in bulk material systems. 3-D nature of shock wave propagation was observed in both NiTi and Al systems where normal and shear stress propagation patterns were captured. It was observed that shear stress propagation pattern dictates the deformation patterns both for plastic deformation, in NiTi and Al, and phase transformation in NiTi system. The main difference between the deformation mechanisms in the two material systems was the reversibility of deformation in NiTi, for most of the deformed regions, as a result of reverse martensitic phase transformations. Comparing this behavior to the aluminum's, this results in the conclusion that NiTi is capable of dissipation large amount of shock wave energy and minimize the permanently deformed regions resulting in maintain the shape very close to the original structure.

Chapter five of this work includes two published papers. One work with the title of **Multiscale mechanics of the lateral pressure effect on enhancing the load transfer between polymer coated CNTs** is published in **Nanoscale journal** and the other work with the title of **Nanocrystalline nickel-graphene nanoplatelets composite: Superior mechanical properties and mechanics of properties enhancement at the atomistic level** is published in **Physical Review Materials journal**. The first author acknowledges the co-authors of these works, **Dr. Markus J. Buehler, Dr. Zhao Qin and Dr. Ayoub Yari Boroujeni**. In addition, the author acknowledges the publishers of these articles, **Royal Society of Chemistry** and **American Physical Society** for giving the right to include the articles in this dissertation which is not provided to be published commercially.

Chapter 5. Graphitic Structures as Reinforcement in NiTi Shape Memory Alloys

5.1 Multiscale Mechanics of the Lateral Pressure Effect on Enhancing the Load Transfer Between Polymer Coated CNTs

5.1.1 Overview

While individual carbon nanotubes (CNTs) are known as one of the strongest fibers ever known, even the strongest fabricated macroscale CNT yarns and fibers are still significantly weaker than individual nanotubes. The loss in mechanical properties is mainly because the deformation mechanism of CNT fibers is highly governed by the weak shear strength corresponding to sliding of nanotubes on each other. Adding polymer coating to the bundles, and twisting the CNT yarns to enhance the intertube interactions are both efficient methods to improve the mechanical properties of macroscale yarns. Here, we perform molecular dynamics (MD) simulations to unravel the unknown deformation mechanism in the intertube polymer chains and also local deformations of the CNTs at the atomistic scale. Our results show that the lateral pressure can have both beneficial and adverse effects on shear strength of polymer coated CNTs, depending on the local deformations at the atomistic scale. In chapter 5 we also introduce a bottom-up bridging strategy between a full atomistic model and a coarse-grained (CG) model. Our trained CG model is capable of incorporating the atomistic scale local deformations at the larger scale, which enables the model to accurately predict the effect of lateral pressure on larger CNT bundles and yarns. The developed multiscale CG model is implemented to study the effect of lateral pressure on the shear strength of straight polymer coated CNT yarns, and also the effect of twisting on the pull-out force of bundles in spun CNT yarns.

5.1.2 Models and Methods

Molecular dynamics simulations of polymer coated CNTs and CNT bundles are performed at two different length scales (full atomistic and coarse-grained), and the two scales are bridged together by a bottom-up approach. Both the full atomistic and CG simulations are performed using Large-scale Atomic/Molecular Massively Parallel Simulator (LAMMPS) [226]. The full atomistic framework is used to investigate the fundamental aspects of the interaction between the CNTs, coated with PMMA oligomers as used in practice to enhance the shear strength of CNTs. We particularly target studying the effect of lateral pressure on the deformation mechanisms at the

atomistic level. A bottom-up approach is then utilized to train the CG model capable of studying shear interaction between CNT bundles coated with PMMA oligomers. The dimensions of the bundles, length of the oligomers, and the density of polymer chains on the surface are identified using some recently reported experimental measurements [227]. In this approach the effect of lateral pressure is incorporated in the CG model by modifying the parameters at the mesoscale by using the atomistic scale results. Details of the bridging the two scales are given in Section 5.1.4.

5.1.2.1 Full Atomistic Model

A series of full atomistic simulations are performed using classical MD at room temperature to study the effect of lateral pressure on the shear strength of CNTs in the presence of PMMA fillers, and also to find the pressure-dependent interaction between the mesoscopic bead-spring models. The chemical and mechanical behavior of CNTs and the atoms in the PMMA are described by the ReaxFF, with a near quantum mechanical accuracy [228, 229]. Validity of implementing this force-field to study various aspects of mechanical response of CNTs and polymer coated CNTs have been extensively studied in our previous computational works [227, 230-232]. The advantage of using a reactive force-field over other possible options in this study is the capability of ReaxFF to capture possible bond braking and formations, which is more probable in our case studies due to the severe lateral loads applied to the system. Motivated by our recent experimental works [227], PMMA oligomers are modeled as chains consisting 8 repeating units [233, 234]. In the full atomistic models two (10,10)-(16,16) double-walled CNTs (DWNTs) with the length of 10 nm are considered parallel to each other, and eight chains of PMMA oligomers are covalently bonded to the outer carbon nanotubes in each DWNT (see Figure 5-1(a)). It is worth noting that the selected length for the DWNTs is remarkably smaller than the typical length of CNTs in yarns and bundles. However, as discussed in Section 5.1.3, atomistic simulations on this representative system shed light into various aspects of complicated deformation mechanisms in polymer coated CNTs subjected to a lateral pressure. Bottom-up trained CG models are used to study larger systems consisting longer CNTs. Simulations are performed under a canonical (NVT) ensemble (temperature control by a Berendsen thermostat [235]), with a time step of 0.1 fs.

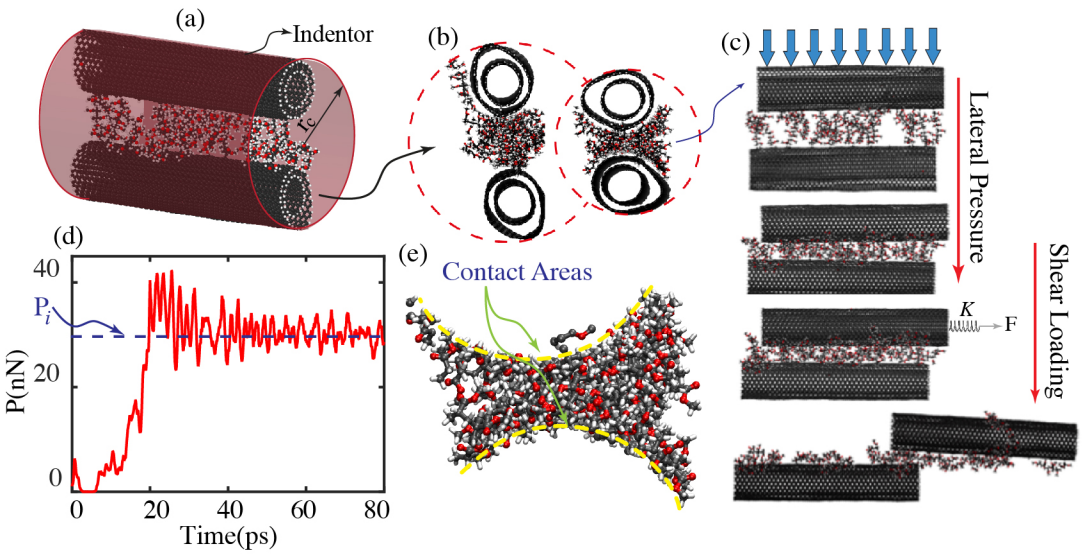

Figure 5-1. Interconnection between lateral pressure, local deformation mechanisms, and the shear strength between two parallel PMMA-coated DWNTs. (a) The system consists of two DWNTs and 16 chains of oligomers between the CNTs, eight covalently bonded to the outer surface of each DWNT. (b) A cylindrical indenter applied a lateral pressure to the DWNTs, and (c) the shear strength between the nanotubes is calculated by pulling one of the CNTs. (d) The lateral pressure is calculated using the indenter reaction force, and the shear strength is obtained for various lateral pressures (see Figure 5-2). (e) Lateral pressure affects the shear strength through atomistic scale local deformations in the polymer chains, and CNTs cross-sections (see Figure 5-4 for more details).

5.1.2.2 Coarse Grained Model

The molecular level interactions of adjacent CNTs have been extensively investigated using full atomistic methods [232, 236-240]. However, modeling bundles consisting a large number of CNTs is computationally expensive at the atomistic level, particularly for relatively long CNTs or for the case of having multiple CNTs in the bundle. The addition of an adhesive oligomer, as studied in this chapter, also adds additional computational expense to the full atomistic simulations. Hence, we select using mesoscopic bead-spring methods as a beneficial approach to simulate arrays of oligomer-coated CNTs [241-243]. This model has been proven to be a valid and efficient approach to simulate a variety of different configurations of CNT yarns and bundles, and even polymer coated CNTs [227, 231, 242, 244]. In this chapter, we implement a two-stage procedure for training the bead-spring parameters, starting with finding these parameters at zero lateral pressure on the CNTs, and then the parameters are modified to incorporate the effect of lateral pressure (see Section 5.1.4).

The CG zero-pressure parameters for the (10,10)-(16,16) DWNTs are adopted from the parameters previously reported as; equilibrium bead distance $r_0 = 10$ Å, tensile stiffness $k_t = 2000$ kcal mol^{-1}Å^{-2}, equilibrium angle $\theta_0 = 180^{\circ}$, Bending stiffness $k_\theta = 45000$ kcal mol^{-1}rad^{-2}, and dispersive parameters $\sigma = 22.63$ Å, $\varepsilon = 21.6$ kcal mol^{-1}. For more details about extracting these parameters from a full atomistic model, the reader is referred to [245]. The mentioned parameters have been implemented in a variety of mesoscale models and the accuracy of the constructed models is studied extensively in a series of previous works [227, 231, 242, 244]. The axial and bending stiffness between the repeat units in the PMMA oligomer ($C_5O_2H_8$) are adopted from Naraghi *et al.* [227]: $r_0 = 2.5$ Å, $k_t = 11.76$ kcal mol^{-1}Å^{-2}, $\theta_0 = 180^{\circ}$, $k_\theta = 23.5$ kcal mol^{-1}rad^{-2}. Several full atomistic simulations are performed to calculate the weak interactions between PMMA monomers together, and also between the DWNT beads and the monomers as: $\sigma = 4.7$ Å, $\varepsilon = 1.13$ kcal mol^{-1} for the monomer-monomer interaction and $\sigma = 12.56$ Å, $\varepsilon = 2.17$ kcal mol^{-1} for the DWNT-monomer interaction. The calculated parameters are smaller than those reported in [227], and more close to the values obtained and optimized by a MARTINI force-field [246]. The main reason for the observed differences between the calculated energy well depths at equilibrium, ε, is because we have calculated this value by separating adjacent macromolecules (monomers-monomers, and monomers-DWNTs) in three different directions and have averaged the calculated energy barriers. Our simulations show that the selected approach results in a better match between the full atomistic and CG models, particularly in the problem studied in this chapter because when the lateral force is applied to the polymer-coated CNTs, the monomers approach each other and the CNTs from different directions in space (see Figure 5-1(b, e)). More details of the CG model and the methodology of updating the weak interactions as a function of lateral pressure are given in Section 5.1.4.

5.1.3 Lateral pressure Effect on the Polymer-CNT Interaction

Applying a lateral pressure, specifically by twisting the CNT yarns, has been experimentally proven to enhance the intertube shear strength between CNTs and consequently improve the mechanical properties of manufactured yarns. In this section we implement full atomistic simulations to investigate the deformation mechanisms in both the polymer chains and CNTs at nanoscale. We also target unraveling how the lateral pressure enhances the shear strength, and particularly answer the question if there is an optimum value for the lateral pressure corresponding

to the maximum possible increase in the shear strength. Full atomistic simulations of this section, combined with the CG models in the following sections will target investigating the effect of lateral pressure in polymer-coated CNTs at different length scales.

At the atomistic level a polymer-CNT system as shown in Figure 5-1(a) is constructed. The system consists of two DWNTs and 16 chains of oligomers between the CNTs, eight covalently bonded to the outer surface of each DWNT. The system is constructed with the PMMA oligomers being parallel and close to each other, and equilibrated for 20 ps before loading. To simulate a uniform lateral pressure a cylindrical indenter is modeled around the system as shown Figure 5-1(a). The indenter's radius is reduced by time and compresses the CNTs as shown in Figure 5-1(b) from the axial view. After compressing the Polymer-CNT to a defined radius, a shear force is applied to the upper CNT while the bottom one is fixed. The pulling force is applied using steered molecular dynamics (SMD), whereby the center of mass of the group of atoms at the end of pulled tube is connected by a harmonic spring to a dummy node which is moving with a constant speed in the axial direction [247]. Some works have been reported recently on studying the effect of loading rate on the mechanical response of hydrogen-bond assemblies in proteins and biological materials [248-250]. However, compared to proteins, where the number of hydrogen bonds is extremely large, our model is less sensitive to the loading rate. For the simulations we have considered a rate of $1\mathrm{E}-6\ \mathrm{fs}^{-1}$. In order to study the feasibility of using this rate, simulations are also performed with 10 times faster and 10 times slower loading rates. The peak shear forces at these load rates are found to be within 5%, difference, so the $1\mathrm{E}-6\ \mathrm{fs}^{-1}$ rate is selected to optimize the accuracy and computational efficiency. The same rate has been also adopted in similar recently reported works (*i.e.* see Bratzel *et. al.* [231]).

The procedure of compressing and pulling is shown in Figure 5-1(c) for a representative value of lateral contraction. The reaction force of indenter is monitored during the contractions and pulling stages to calculate the average lateral pressure applied to each CNT (see Figure 5-1(d)). It is worth noting that for calculating the lateral pressure, the total force has to be divided by the contact area between two CNTs. While the length of contact area is easily found (as it is equal to the length of CNTs), the width cannot be accurately calculated, and will be changing as the force is increased. For this reason, we will report the results for force per unit length in the following sections, and the term lateral pressure will be used to indicate to this force per unit length value. The reaction

force increases during the compression until reaching the maximum value, which corresponds to the end of the compressing procedure. During the pulling procedure, the reaction force is almost constant with some minor fluctuations. The lateral force applied to each CNT, P_i, is approximated by the average of the indenter reaction force during the pulling step, as shown schematically in Figure 5-1(d).

The oligomers in the contact area between the CNTs are shown in Figure 5-1(e). Due to compression, this area changes and some of the oligomers are pulled out from the area between the CNTs. Therefore, the interaction between the oligomers and CNTs changes, and it will change the lateral shear force value.

Trajectory of the lateral shear force versus relative displacement along CNTs axis for different compressing pressures is shown in Figure 5-2. For all the cases, the lateral force reaches a maximum value, which corresponds to the shear strength, and then decreases. As shown in this figure, having a lateral pressure improves the shear strength by increasing the maximum shear force during sliding of CNTs on each other. However, increasing the lateral force above a critical value starts weakening the shear strength between CNTs. Also, the lateral pressure significantly affects the toughness. It is worth noting that the term toughness is usually used as the area under the stress-strain curves. However, as we are studying the force-displacement response of CNTs in shear loading, this term will be used for addressing the area under the force-displacement curves in the following sections of this work.

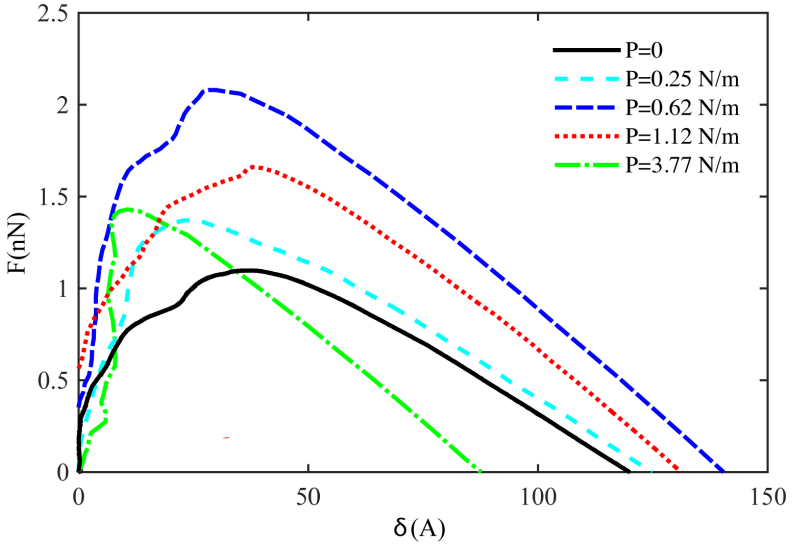

Figure 5-2. The lateral shear force versus relative displacement along CNTs axis for different lateral compressing pressures.

Variations of the maximum shear stress, and the toughness (defined as the area under the force-deflections curves) are shown in Figure 5-3. By investigating the change of both the maximum force and the energy, four different regions are distinguished as shown in Figure 5-4. In the first region (I) both the shear strength and energy increase by raising the lateral pressure up to a maximum value. This raise in the shear strength can be better understood by tracking the deformation mechanism of CNTs and polymer chains as shown in Figure 5-4. Applying the lateral pressure in this region causes the polymer chains filling the space between the two CNTs, and particularly increases the contact area between PMMA and the CNTs (also see Figure 5-1(e)).

Further increasing the lateral pressure above this critical value will start pushing the polymer chains out of the intertube region (see Figure 5-4 II), which consequently leads to a drop in the shear strength and the toughness as seen in region II in Figure 5-3. In the third region, the high lateral pressure squeezes all the polymer chains out of the intertube space, however, since the CNTs start contacting each other, the shear strength slightly increases. In this region, the toughness value is not following the shear strength, and a sharp drop is observed in the energy.

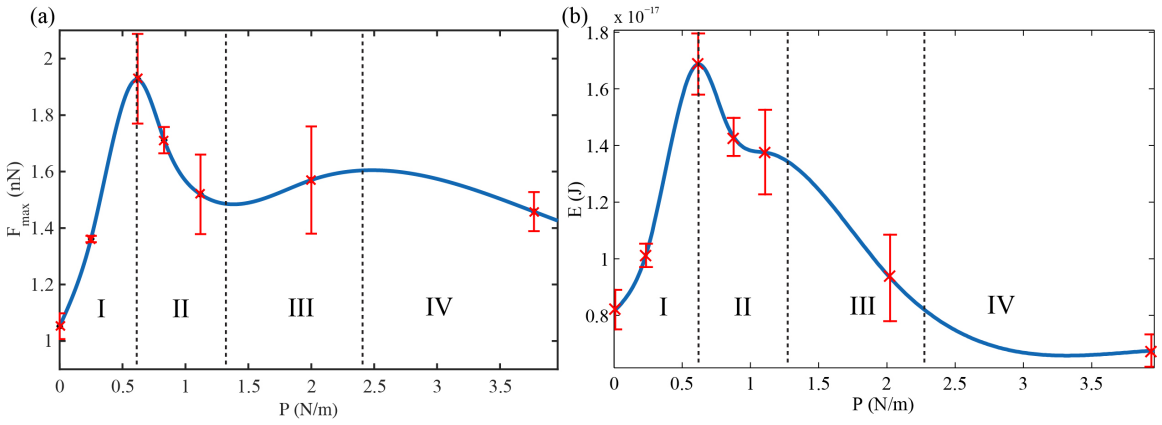

Figure 5-3. Variations of (a) the shear strength, and (b) the toughness as functions of lateral pressure. Local deformations in regions I to IV are shown in Figure 5-4. In the first region (I) both the shear strength and energy increase by raising the lateral pressure up to a maximum value, caused by increase of the interface area between CNTs and polymers. Increasing the lateral force in region II pushes the polymer chains out of the intertube regions and decreases both the shear strength and energy. Further increasing the lateral pressure (region III) is associated with a direct contact between CNTs, which makes a slight increase in the shear strength, while the energy keeps lowering. At very high lateral pressures (region IV), CNT cross-sections deform severely and both the shear strength and energy drop.

This phenomenon can be justified by the change of deformation mechanisms from the case of having polymer chains in the intertube regions (I and II), to the case at which the polymer chains

are not contributing in the shear deformation mechanisms. Further increasing the lateral force into region IV in Figure 5-3 and 4, leads both the shear strength and the energy to increase. This phenomenon is mainly governed by the excessive deformations observed in the cross-section of CNTs. At very high lateral force levels, the CNTs cross-sections buckle and this irreversible deformation mechanism is associated with a drop in the shear strength. We had previously studied such a response in pristine CNTs in detail with a similar approach, and the obtained results in region IV for the polymer-coated CNTs is consistent with those findings [232].

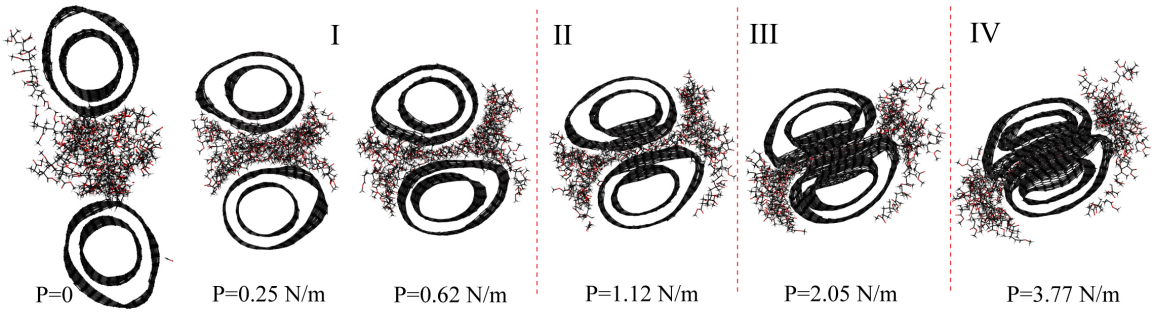

Figure 5-4. Local deformations of the CNTs and polymer chains at various levels of lateral pressure. These atomistic deformation mechanisms are directly connected to the change of shear strength and toughness as shown in Figure 5-5.

5.1.4 Bridging Mesoscale to the atomistic level

The results presented in Section 5.1.3 reveal the basic deformation mechanisms behind the complicated correlation between the lateral pressure applied to polymer-coated CNTs and the shear strength of these CNTs while sliding on each other. Implementing such a full atomistic framework is not practically possible to study large systems mainly because of the substantial increasing of the computational costs when the number of atoms in the system increases. CG modeling techniques facilitate simulating larger yarns and bundles made of several CNTs. However, by implementing a CG model several important aspects of the deformation mechanisms at the atomistic level, such as those studied in Section 5.1.3, will be missed in modeling yarns and bundles in which the polymer-coated CNTs are subjected to a lateral force (i.e. due to the twisting). In this study, we overcome this drawback and bridge the two length scales by re-training the CG model parameters as a function of the lateral pressure.

As shown in Section 5.1.3, the cross-section deformations in both the CNTs and the polymer chains filling the intertube space play a significant role on the mechanical response. As shown in Section 5.1.3, the cross-section deformations in both the CNTs and the polymer chains filling the

intertube space play a significant role on the mechanical response. As shown in Section 5.1.3, the cross-section deformations in both the CNTs and the polymer chains filling the intertube space play a significant role on the mechanical response.

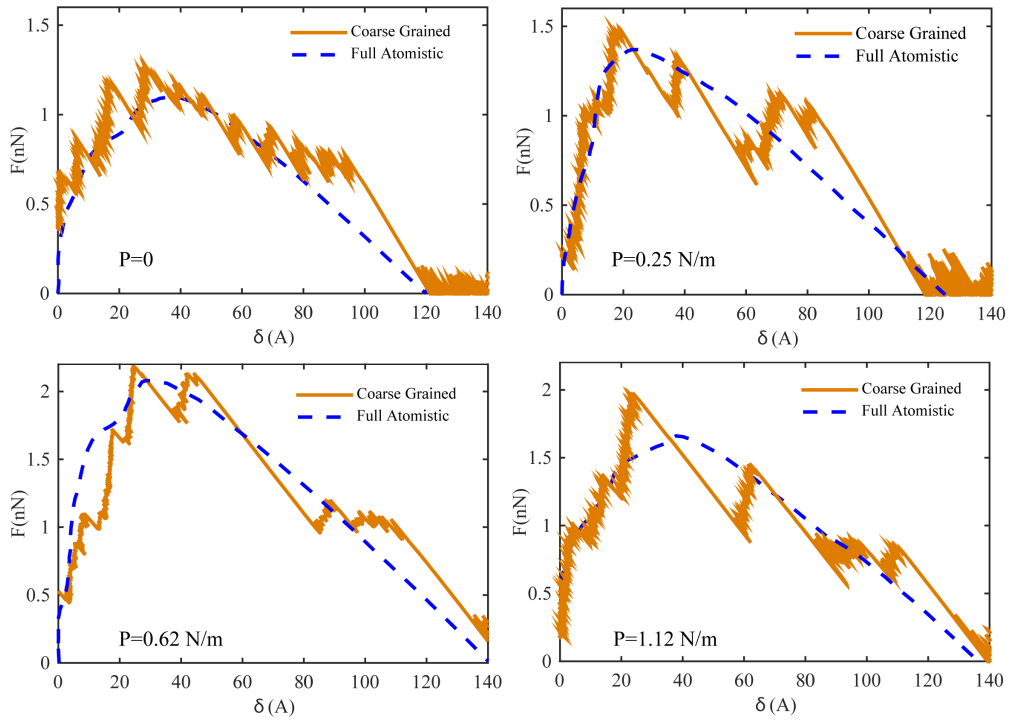

Figure 5-5. Matched force-displacement responses obtained from full atomistic simulations and the coarse-grained model for four representative lateral pressures. CG parameters are updated as a function of the lateral pressure (see text for details).

These atomistic-scale deformations will affect the CG parameters k_θ, for both the DWNT and polymer chains, and also the vdW parameters σ and ε for DWNT-DWNT, oligomer-oligomer and DWNT-oligomer interactions. In a similar approach to study the effect of twisting on the response of pristine CNT yarns, we have recently shown that selecting the dominant properties and updating them in the CG model will provide an accurate computational framework [232]. Through running sensitivity analysis and tracking the change of shear strength by varying these parameters we found the energy well depth ε for the DWNT-oligomer, and oligomer-oligomer interaction having the most significant effects on the shear strength of polymer-coated DWNTs. In order to update these parameters as a function of lateral pressure, a training set consisting the five shear loadings as studied in Section 5.1.3 is considered. The zero-pressure CG parameters are obtained with the standard method explained in Section 5.1.2.2. For each lateral pressure the

selected two CG parameters are updated to minimize the error in the force-deflection trajectories obtained by the full atomistic and CG models.

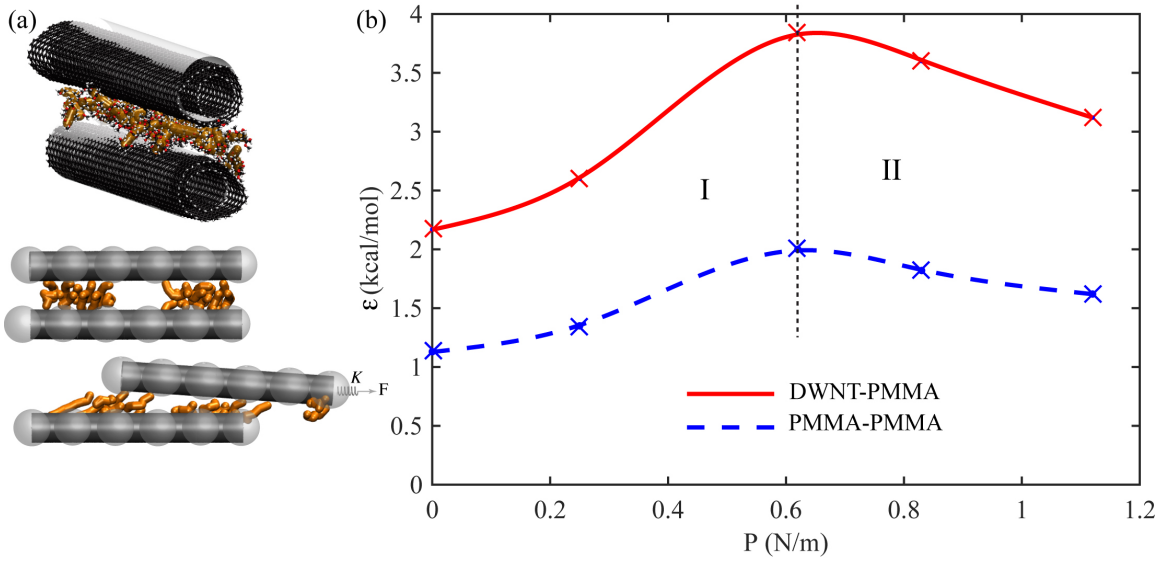

Figure 5-6. (a) A schematic of the full atomistic and CG models, and (b) calculated vdW parameters as a function of the lateral pressure. These parameters are used in the CG model in order to incorporate the effect of local deformations into the mesoscale model.

Samples of the matched force-displacement responses for four different lateral pressures are shown in Figure 5-5. While the force-deflection response obtained from full atomistic models is smooth, there are multiple fluctuations in the CG model results. This phenomenon is mainly because in the full atomistic model the contact between oligomers is distributed at several locations with a large number of atoms interacting with each other (i.e. see Figure 5-1), while in the CG model the contact is approximated by the interaction between a smaller number of beads, each representing a cluster of atoms (see Figure 5-6(a)). However, the results are in an acceptable agreement, and particularly the maximum shear force is predicted accurately in the CG model. It is worth noting that the changes in the force-displacement response at different lateral pressures originate from the local deformations at the cross-section of CNTs and the polymer chains filling the intertube space at the atomistic level. Hence, if the vdW parameters are not updated in the CG model, the force-deflection response in the CG model will be independent of the lateral pressure. The required vdW parameters for matching the full atomistic and CG models are shown in Figure 5-6. These parameters are used in the following sections to accurately study the mechanical properties, and particularly the shear strength of large polymer coated CNT bundles, and also twisted yarns made

of polymer coated CNT bundles. It is worth noting that the CG model is not trained for cases where the lateral force per unit length is larger than a critical value of P=1.2 N/m. As discussed in Section 5.1.3 and shown in Figure 5-4, for lateral forces larger than this critical value, the CNTs collapse and the cross-section undergoes a sever deformation. As we will show in the following sections, even in cases that a large lateral force is applied to bundles, the number of CNTs that share the total lateral force increases and the force per unit length on each individual CNT is not larger than this critical value.

5.1.5 Shear Strength between Polymer Coated Bundles in Presence of Lateral pressure

The question to be answered in this section is how the lateral pressure will affect the shear strength between two bundles made of several CNTs, and coated at the outer surface with the PMMA oligomers. We have recently implemented experimental and computational studies to investigate the shear strength between two PMMA coated CNT bundles as a function of the overlap length [227]. In this chapter, we implement our bottom-up trained CG framework to investigate the effect of lateral pressure on the shear strength between these bundles. It is worth noting that applying a lateral pressure to a set of two overlapped bundles is not practical in experiments. However, CNT bundles are subjected to a lateral pressure when used in yarns made of twisting several CNT bundles. Our results in this section will provide novel mechanistic insights into the deformation mechanisms involved in the loading of CNT bundles and yarns. In the next section, we will also study a twisted yarn made of PMMA coated CNT bundles.

Molecular dynamics models are constructed inspired by the polymer-coated CNT bundles used in our previous experimental work [227]. The CG model of each polymer-coated CNT bundle consists of 113 hexagonally packed tubes, and polymer crosslinks are oriented perpendicular to the bundle surface as shown in Figure 5-7(a and b). The configuration of polymer chains in this model is slightly modified compared to the previous work [227] by modeling longer chains at the intersection of two bundles, and also considering a slight penetration of polymer chains into the surface of bundles at the intersection. These modifications are consistent with the experimental observations, and also improve the match between computational and experimental results (for the case of no lateral pressure), as will be shown in the sequel. Two bundles with identical lengths (which represents the overlap length) are equilibrated on each other at 300 K for 1 ns as shown in

Figure 5-7(a). After equilibration, a cylindrical indenter compresses the bundles laterally, with a similar method used in the full atomistic models as explained in Section 5.1.3.

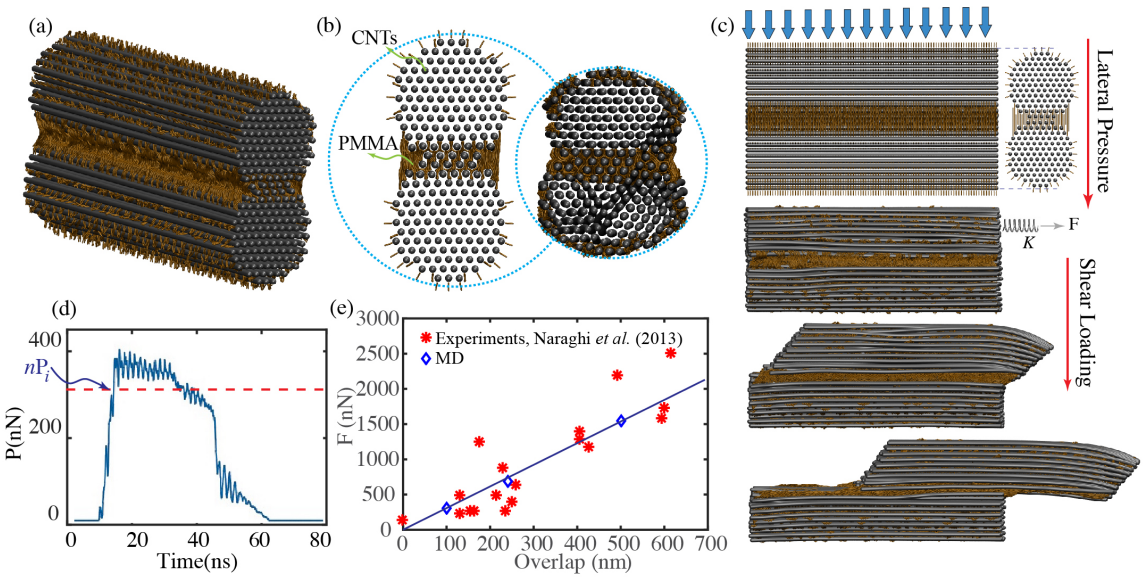

Figure 5-7. (a) Schematic of two parallel CNT bundles coated with PMMA oligomers. (b) a cylindrical indenter is used to apply a lateral pressure to the bundles, and (c) a lateral force is applied to one of the bundles to study the shear strength between the bundles in presence of various lateral pressures. (d) The total lateral pressure is calculated from the indenter force, and cross-section view (b) is used to obtain the approximate lateral pressure on each CNT. The shear strength for various lateral pressures is shown in Figure 5-7 for two overlap values, and (e) calculated zero-pressure shear strength is compared against available experimental data.

At the end of compression step, one end of the lower bundle is clamped and a pulling force is applied to the other end of the top bundle using SMD (see Figure 5-7(c)). Each simulation has been done twice. Once, the original CG parameters are used and the force deflection is recorded as shown in Figure 5-7(d). The total lateral force on the bundle is then calculated. Front view of the bundles is investigated to find the number of CNTs in contact with each other at the interface. Dividing the total lateral force by the number of CNTs in contact gives the lateral force on each CNT in the bundle. Using the results of Section 5.1.4 (see Figure 5-6) the updated CG parameters are obtained for the observed lateral pressure. A second simulation is then run for each case with the updated CG parameters, which incorporates the effect of lateral pressure deformations at the full atomistic level. In order to validate the computational model, experimental results [227] for various overlaps with no lateral pressure are used as shown in Figure 5-7(e). As shown in this figure, despite various complexities of the problem, the maximum shear force obtained from the

CG model is following the experimental results with an acceptable accuracy for the trend obtained from three representative different overlap values.

Two overlap lengths of 100 and 240 nm are selected to study the effect of lateral pressure on the shear strength of bundles. The 500 nm overlap is only considered for the case of having zero lateral pressure, and the effect of lateral force is only studied for two overlap values of 100 and 240 nm.

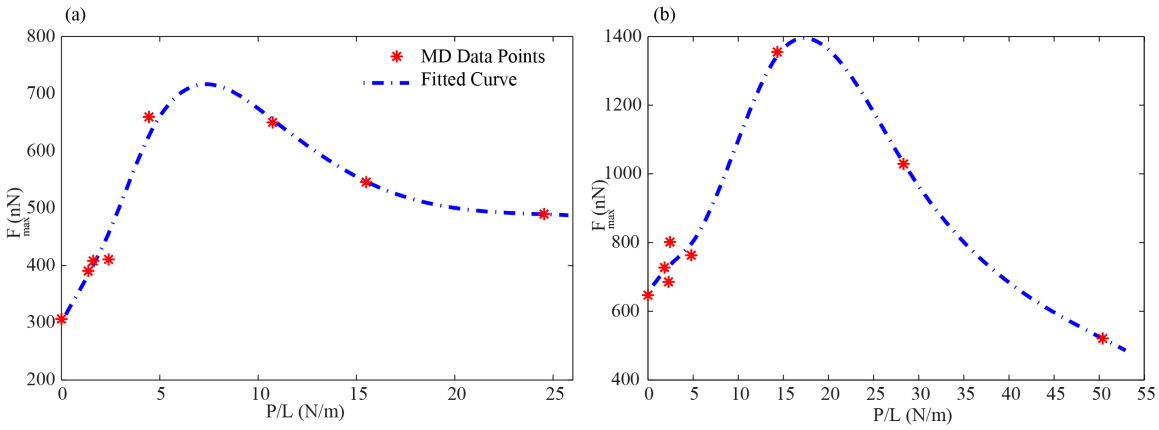

Figure 5-8. The effect of lateral pressure on the shear strength of polymer-coated CNT bundles for two overlap lengths of (a) 100 and (b) 240 nm.

This is mainly because as the length increases, the simulations become extremely time consuming, and for a common cross-section having larger lengths will not give much new fundamental understanding about the deformation mechanisms. By changing the amount of compression induced by the cylindrical indenter, different values of lateral pressure are applied to the bundles, and the shear strength is calculated as a function of lateral pressure for both the overlap lengths as shown in Figure 5-8. A similar trend, compared to the full atomistic models for two CNTs, is observed for the bundles with different overlaps. The shear strength is improved by increasing the lateral pressure up to an optimum level of pressure. Increasing the lateral pressure above this optimum value will weaken the shear strength, due to the local effects which have been observed at the atomistic scale, and are incorporated in the CG model by our scale bridging method. These simulations reveal the existence of an optimum lateral pressure for maximizing the shear strength between bundles, and the developed framework can be used as a tool to investigate an optimum configuration with improved shear strength. In practice, the lateral pressure can be applied to the adjacent bundles in a yarn of fiber made of CNTs by twisting the yarns. In the following section

we study a representative case study, to show the applicability of the developed framework in designing yarns and fibers made of polymer coated CNT bundles.

5.1.6 Pull-out Force in a Twisted Fiber

In practice, CNT bundles are used to make yarns and fibers, and it has been shown that the strength of fabricated fibers can be enhanced by twisting the fiber up to an optimum twist angle [251-253]. The improvement in the strength is directly related to the lateral pressure that is applied to the CNTs in a twisted yarn, which enhances the shear strength between the nanotubes with a similar mechanism to the cases studied in Section 5.1.5. As shown in the previous sections, the shear strength improvement in presence of a lateral pressure will be even more significant in case of having polymer coating on the surface of bundles. In this section we consider a case study to show how the atomistic-scale deformations and the shear strength enhancement between individual CNTs are related to the strength of a twisted yarn. For this purpose, we implement the bridging between the meso- and atomistic scales to study a yarn made of 19 bundles with length of 240 nm as shown in Figure 5-9. The CG model parameters are all the same as those explained in Section 5.1.5. The bundles are all coated at the surface with chains of PMMA oligomers, each containing 8 mers (See Figure 5-9(a)). Polymer-coated CNT bundles (each consists of 113 hexagonally packed tubes) are initially located in a closed pack arrangement as shown in Figure 5-9(b), and the system is equilibrated at 300 K for 1 ns. After equilibration, a cylindrical indenter compresses the bundles laterally, with a similar method used in the previous sections to guarantee the contact between adjacent bundles in the yarn (Figure 5-9(b)). The cylindrical indenter is then removed and the system is again equilibrated for 1 ns. It is worth noting that compared to the system studied in Section 5.1.5, the bundles in this twisted yarn have a lower concentration of polymer coating to reduce the computational cost (the yarn model consists approximately 2 million beads representing the CNTs and PMMA mers), while there will be no significant effect on the studied concepts.

Two identical yarns are considered, one with the initial straight yarns and one obtained by twisting the whole set of bundles around the axis as shown in Figure 5-9(c). One of the bundles at the outer surface is colored with blue in this figure to show the twisting of the yarn. In order to calculate the lateral pressure on each nanotube in the bundles we consider an approximate method based on a simplified model developed for textile fibers and yarns [254]. In this model an analytical expression is calculated for the relative stress defined as P/σ_f, where parameters σ_f and P

represent the specific stress in the fibers in a direction parallel to the fiber axis and the specific stress in the lateral direction, respectively. It is shown that the distribution of relative stress is a function of radial position r/R for different values of α in a yarn. To simplify the problem, we consider a uniform distribution for the relative stress in the cross-section by calculating the average value of this parameter from the center to the outer surface of the yarn. As an example for $\alpha = 30°$ the average value of relative stress can be approximated as 0.13 (see Figure 4-6 in [254]). By considering a stress in the fibers direction as $\sim 400\ MPa$, the specific stress and force in lateral direction between two bundles in the yarn would be $\sim 52\ MPa$ and $\sim 162.25\ N$, respectively. For the considered yarn in this section with a length of 240 nm the force per unit length is approximately 0.67 N/m.

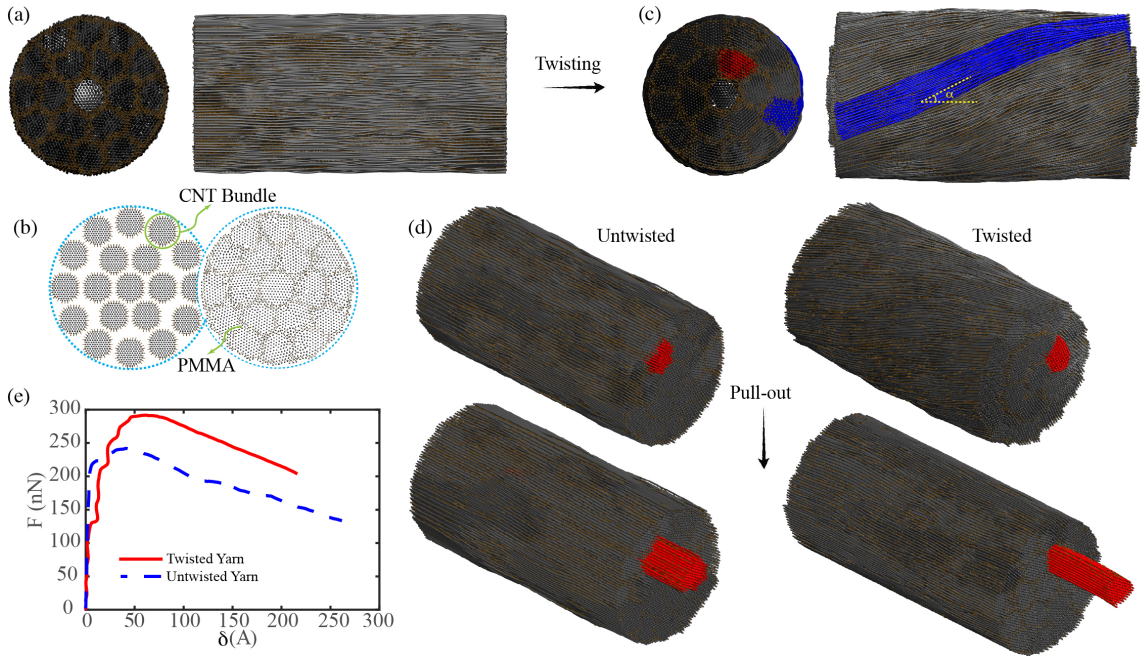

Figure 5-9. A twisted yarn made of polymer coated bundles to calculate the pull-out force in presence of the lateral pressure caused by the twisting in the yarn. (a) The untwisted yarn is made by closed packing 19 polymer coated bundles with length of 240 nm, (b) using a cylindrical indenter to help the polymer chains interact with each other, and equilibrating the system after releasing the indenter. (c) The yarn is then twisted (one of the bundles in the outer layer is shown with blue), and (d) one of the bundles in the middle layer (shown with red color) is pulled out from both the twisted and untwisted yarns. The CG parameters are updated as a function of lateral pressure caused by the twisting (see text for details). (e) Comparison of the pull-out force shows an approximately 25% improvement in the force by twisting the yarn.

The calculated approximate lateral force per unit length is used to calculate the updated vdW parameters (see Figure 5-6). The untwisted yarn is simulated with the original vdW parameters, and the updated parameters are assigned to the twisted yarn. A pull-out test is simulated in both cases to study the effect of twisting on the shear strength between bundles in the yarn. One of the bundles is selected (shown with red color in Figure 5-9(d)), one end of all the other bundles is clamped and a pulling force is applied to the other end of the selected bundle using steered molecular dynamics. As shown in Figure 5-9(e), twisting the yarn increases the shear strength or the maximum of the pull-out force by ~ 25% (the simulations are very time consuming because of the large system which is studied, and the loading is stopped after finding the maximum shear stress). It is worth noting that a significant part of this increase in the shear strength is particularly caused by the atomistic scale deformations and increase of the contact area between the polymer and CNTs, which is incorporated in the system by updating the vdW parameters. If these parameters are not updated and the system is solved for both the twisted and untwisted yarns, simulations will show a very small change in the shear strength which is unrealistic. This framework can be used to investigate an optimum twisting angle for yarns and fibers, depending on the manufacturing parameters.

5.1.7 Conclusions

In this investigation the effect of lateral pressure on the shear strength of polymer coated carbon nanotubes (CNTs) is studied. Our molecular dynamics (MD) simulations shed light into the deformation mechanisms in both the polymer chains and CNTs, and reveal the complex correlation between the shear strength and the lateral pressure on each CNT. It has been shown that while increasing the lateral pressure enhances the shear strength between CNTs due to increasing the contact area between the polymers and nanotubes, there is a specific lateral pressure at which increasing the lateral pressure above that value will weaken the shear strength. This loss in the shear strength is shown to be interconnected with the local deformations of CNTs at the atomistic scale.

A bottom-up bridging methodology is developed to train the mesoscale model using the MD simulations, while the atomistic scales local deformations in the polymer chains and CNT cross-sections are also transferred into the larger scale by adjusting the vdW interactions in the CG model as a function of the applied lateral pressure to each CNT. This bottom-up multiscale approach is

used to study the effect of lateral pressure on the shear strength of straight polymer coated CNT bundles in presence of a lateral pressure on the bundle. The framework is also implemented to investigate how twisting a CNT yarn can affect the pull-out force of a bundle from a spun yarn, offering new avenues for materials design.

5.2 A Nanocrystalline Nickel-Graphene Nanoplatelets Composite: Superior Mechanical Properties and Mechanics of Properties Enhancement at the Atomistic Level

5.2.1 Overview

A relatively easy-to-fabricate nanolayered metal composite with superior mechanical properties is introduced. The matrix is a nanocrystalline nickel in which the grain size is engineered to optimize the strength, and monolayer particles of graphene are embedded into the matrix as reinforcing interlayers. Atomistic-scale deformation mechanisms, and mechanics of hindering the dislocations propagation by graphene nanoplatelets with different configurations in the nanocrystalline metallic matrix are investigated by molecular dynamics simulations. Molecular dynamics findings are utilized to engineer the nanostructure of metal matrix composite. Nanocrystalline nickel-graphene nanolayered systems with optimum mechanical properties are identified, and fabricated with a novel and cost-efficient method. The nanostructure of the fabricated composites is examined via electron microscopy, and their mechanical performance is inspected via nanoindentation tests. The experimental results show that a nickel graphene nanolayered system with 14% areal coverage of graphene particles at the interlayers has improved the hardness of the nanocrystalline nickel by almost 40%.

5.2.2 Materials and Methods

5.2.2.1 Computational Modeling

A series of molecular dynamics (MD) simulations are performed to investigate the effects of various designs on the mechanical performance of nickel-graphene composites. An accurate modified embedded atom method (MEAM) potential for nickel-graphene, developed by Uddin *et al.* [255], is used in this chapter. In the MEAM potential, the total energy of the system is given as:

$$E = \sum_i \left[F_i(\bar{\rho}_i) + \frac{1}{2} \sum_{j(\neq i)} S_{ij} \varphi_{ij}(R_{ij}) \right], \quad (5\text{-}1)$$

where F_i , S_{ij} and $\varphi_{ij}(R_{ij})$ are embedding function for an atom i, screening function and the pair interaction between atoms i and j which are separated by a distance R_{ij}, respectively. Parameter $\bar{\rho}_i$ is the electron background density. The electron background density at each site is computed by combining several partial electron-density terms for various angular contributions with weight factors $t^{(h)}(h = 0 - 3)$. Each partial electron density is a function of atomic configuration and atomic electron density. The atomic electron densities $\rho^{\alpha(h)}(h = 0 - 3)$ are given in the form:

$$\rho^{\alpha(h)}(R) = \rho_0 \exp\left[-\beta^{(h)} \left(\frac{R}{r_c} - 1 \right) \right], \quad (5\text{-}2)$$

where ρ_0 and $\beta^{(h)}$ are the atomic electron-density scaling factor and the decay length, respectively, and both are adjustable parameters. r_c is the nearest-neighbor (NN) distance in the equilibrium reference structure. The coefficients of this potential for nickel-graphene system are calculated and reported by Uddin *et al.* [255].

All the molecular dynamics simulations in chapter 5 are performed at the finite temperature $T = 300\ K$ using time integration on Nose-Hoover style non-Hamiltonian equations of motion in isothermal-isobaric (NPT) ensembles. Large-scale atomic/molecular massively parallel simulator (LAMMPS) [167] is utilized for performing the simulations, and Ovito [168] visualization tool is used for post-processing the results of MD simulations. Two 3-D periodic cells of nickel are created in two different sizes, $500 \times 500 \times 500$ and $250 \times 250 \times 250$ Å. For each periodic cell, two types of polycrystals, possessing 10 grains and 100 grains, are created using Voronoi Tessellation algorithm [204]. As a result, two polycrystalline samples with average grain sizes of 24.8, 11.9 nm are obtained from the bigger cell seize, and two polycrystalline samples with average grain sizes of 12.4 and 5.9 nm are modeled using the smaller cell size.

The MD simulations are performed for four different embedded graphene configurations: (a) no graphene, (b) layerwise-arranged graphene particles, (c) layerwise-arranged graphene full sheets representing continuous large sheets of graphene in the matrix, and finally, (d) randomly oriented graphene particles in the grains. The graphene inserts are first embedded into the polycrystals and

then the overlapped nickel atoms are deleted. This method of incorporating the graphene particles into a polycrystalline metal will put the graphene inserts inside the nickel grains, not necessary in the grain boundaries. This assumption of graphene arrangements inside the metal grains is not far from reality, since the exceptionally low thickness of monolayer graphene would allow continuation of epitaxial [256] metal crystal growth [133, 135].

The systems are equilibrated at $T = 300\ K$ for $20\ ps$. After equilibrium, the simulation boxes are deformed in compression about 10% of their original size in z direction, which is perpendicular to the graphene planes, during $100\ ps$ and $50\ ps$ loading times. These two loading conditions represent the strain rates of 10^9 and $2 \times 10^9$1/s. For simulating the materials performance under indentation loadings, a 3-D computational cell of nickel-graphene with the size of $250 \times 250 \times 250$ Å with 10 grains is modeled and a spherical indenter with radius of 50 Å is utilized to indent the system. The system is periodic in x and y directions. After equilibration at $T = 300\ K$ for $20\ ps$, the system is compressed by the indenter in z direction for $100\ ps$ and then unloaded for $100\ ps$ while the two bottom atomic layers are fixed. More details of implementing MD to study metallic systems, and particularly tracking the structural changes in the crystal structure are reported in our recent works [95, 96, 257].

Note that the compression loading along z-direction (perpendicular to the graphene nanosheets) was chosen for the main MD simulations in favor of consistency between the numerical and experimental studies (as it is discussed in Section 5.2.2.3). However, since the material system introduced in this study is anisotropic, several MD simulations with both the tensile and compressive loadings along the three different directions are performed to clarify the contribution of graphene particles in strengthening the designed nickel nanolayered composites under various modes of deformation. MD simulations results are reported and discussed in Section 5.2.3.1 as well as in the supplementary document [258].

5.2.2.2 Composites Fabrication and Characterization

Figure 5-10 summarizes the steps towards fabricating the nickel-graphene nanolayered composites and how electron microscopy is employed to characterize the fabricated composites. As shown in the figure, circular wafers of Si <100> single crystal with diameters of 25.4 mm, by UniversityWafer Inc., are used as substrates for fabricating the nickel-graphene nanolayered composites. A PVD-250 E-beam evaporation system, by Kurt J. Lesker Co., is employed for metal

thin film depositions. As the first layer, a 20 nm thick film of titanium is deposited over the clean silicon wafers in order to improve the adhesion between the material and the substrates. Then, a 150 nm thick layer of nickel is deposited over the titanium coated silicon wafers at 2.0 Å/s deposition rate under 5.0×10^{-6} Torr pressure. The deposition rate is monitored *in-situ* by a crystal thickness monitor mounted inside the PVD-250 chamber. After nickel deposition, the silicon wafers are taken out of the E-beam evaporation chamber in order to start the graphene layer insertion procedure.

The graphene layer insertion procedure is performed via spin-coating of aquatic dispersions of graphene flakes over nickel coated wafers. The aquatic solutions contained four different concentrations of graphene flakes; 0.025, 0.050, 0.075, and 0.100 wt.% graphene in water. The desired concentrations are obtained from adding deionized (DI) water in a 1.0 wt.% research grade graphene water dispersion, by US Research Nanomaterials Inc. According to the specifications by the vendor, the graphene nanoplatelets possessed 0.55-1.2 nm thickness, which corresponds to mono and double layer graphene, and 1-12 μm diameter. The graphene dimensions are confirmed later with electron microscopy. The spin-coating procedure is performed at 2000 rpm speed for 40 s. As a result of spin-coating the various graphene concentrations various coating configurations of graphene flakes over the nickel metal deposited samples are obtained.

After this procedure, the graphene coated samples are put back in the E-beam evaporation chamber to deposit another layer of 150 nm thick nickel over the samples. The graphene and nickel deposition cycles are repeated three times more in order to obtain the designed nickel-graphene nanolayered composites. At the end of the sample preparation procedure, the samples possess 5 layers of 150 nm thick nickel metal. Between each two neighbor nickel layers, a thin layer of graphene particles is embedded. The samples are labeled as R (reference), D (dilute), M (medium), H (high), and SH (super high) representing the corresponding contained graphene dispersion concentrations. In other words, the samples named D, M, H, and SH undergo the spin-coatings of graphene dispersion concentrations of 0.025, 0.050, 0.075, and 0.100 wt.%, respectively, and the R sample do not have any graphene layer.

A LEO (Zeiss) 1550 field-emission scanning electron microscope (FE-SEM) is used to examine the quality of the graphene coatings over the nickel layers. The same FE-SEM system is used to see the cross-section of the nanolayered composites to confirm the uniformity of the nickel layers

and probe their crystallinity. The coated silicon wafers are freeze-fractured using liquid nitrogen in order to prepare their cross-section for the electron microscopy. TEM samples are also prepared and a JOEL 2100 transmission electron microscope (TEM) is employed to study the crystalline structure of the nickel layers. Selected area diffraction patterns (SADP) are obtained to confirm and quantify the crystallinity of the nanolayered nickel samples.

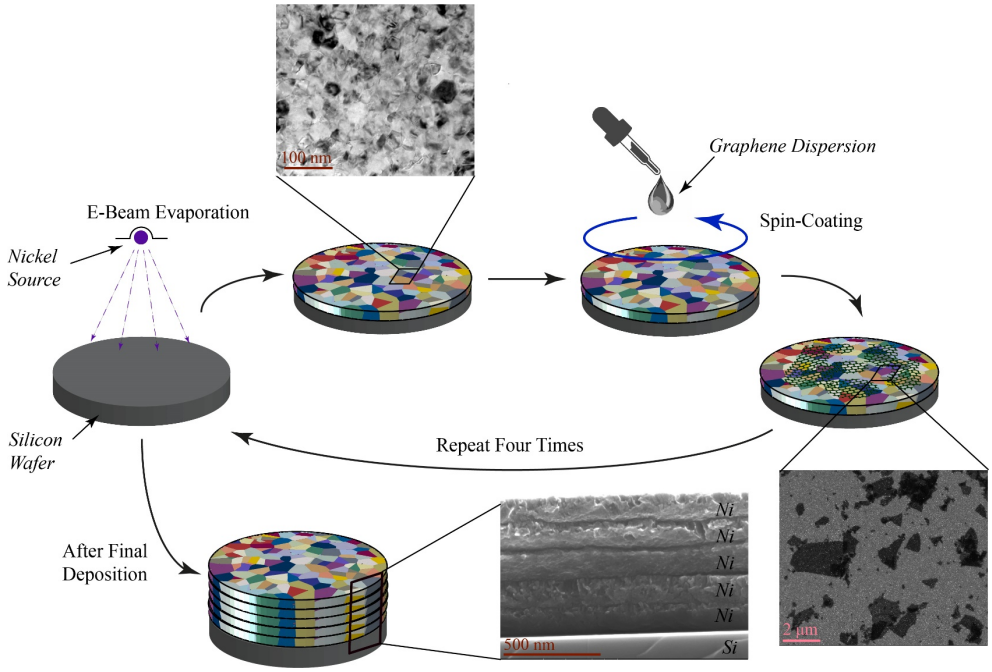

Figure 5-10. Schematic sketch of the nickel-graphene nanolayered composites fabrication. E-beam evaporation is used to deposit the first nickel layer on the silicon substrate. Graphene particles dispersion in water is spin-coated over the nickel layers. The whole process is repeated four times to achieve 5-layered nickel-graphene composite nanolaminates. Scanning electron microscopy is used to investigate the quality of the graphene particles spread over nickel layers, as well as the cross-section of the fabricated composites. Transmission electron microscopy is used to evaluate the crystallinity of the nickel layers.

5.2.2.3 Nanoindentations

A NanoTest®, by Micromaterials Inc., is used to perform nanoindentation tests on the fabricated nickel-graphene nanolayered composites in order to study the effect of different graphene particles at the interlayers on the elastic modulus and hardness of the composites. The load-controlled nanoindentation tests are performed using a diamond Berkovich indenter tip at three maximum load levels of 5.0, 10.0, and 20.0 mN. Nine indentations are done per each load case under fixed 20 s loading, 5.0 s dwell period at maximum load, and 20 s unloading times. The load-depth data is recorded during the nanoindentation tests and the data is corrected for thermal drift using a 30 s

dwell period at 10% maximum load. The data is analyzed using Oliver-Pharr method [259, 260] to obtain the hardness and reduced modulus of the nickel-graphene composites.

5.2.3 Results and Discussion

5.2.3.1 Computational Results

5.2.3.1.1 Strengthening Mechanisms and Grain Size Effect

Compressive stress-strain curves, for the atomistic simulation models under compressive loadings at 10^9 1/s strain rate, are shown in Figure 5-11 for four different average grain sizes. Figure 5-11 (a) shows the compressive stress-strain behavior when there is no graphene inside the polycrystalline nickel grains, while Figure 5-11(b) and (c) represent the results when graphene particles and graphene full sheets are added, respectively, as layers into the nanocrystalline nickel structures. Strength is indicated by flow stress values shown in Figure 5-11(d). The flow stress is calculated as the average of the stress values obtained from the stress-strain curves beyond the strain level of 0.07 after which the stress-strain curves for almost all the material systems exhibit a plateau-like behavior. Comparing the results of nickel nanocrystals with no graphene, it can be seen that as the average grain size decreases from 24.8 to 11.9 nm, the flow stress increases, and as the grain size decreases further to 5.9 nm, the flow stress drops. These results are in agreement with the reported values in the literature [143-146]. This phenomenon is due to different deformation mechanisms in nanocrystalline metals, where at coarser grain sizes (>12 nm) plastic deformation is mostly governed by dislocations nucleation and growth through the grains, representing the so called Hall-Petch effect, while at finer grain sizes (<12 nm) the role of the atomic sliding at the grain boundaries in the plastic deformation gets more highlighted, illustrating a reverse Hall-Petch effect. Since the simulations start at a dislocation-free situation, for coarse-grained nanocrystal systems, high stress is needed to nucleate dislocations inside the grains. However, as dislocations start to move inside the grains, due to the large grain sizes, significant plastic deformation occurs and stress is released to some extent. That is the reason for the compressive stress-strain curves of the coarse-grained models to demonstrate an overshot peak [147].

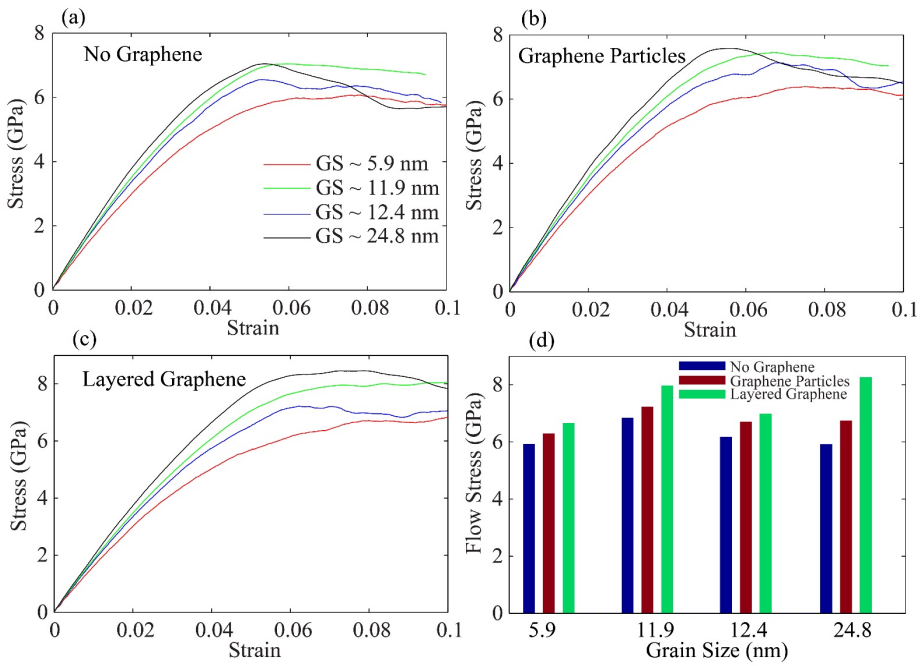

Figure 5-11. Compressive stress-strain response of the nanocrystalline nickel layered systems with different average grain sizes (GS) under compression loading at the strain rate of 10^9 1/s for the systems with (a) no graphene, (b) graphene particles, and (c) layered graphene full sheets. (d) Flow stress obtained from the stress-strain curves at different average grain sizes of the nanocrystals. It is evident that the pure nanocrystalline nickels with the average grain size of ~12nm possess the optimum grain size to have the highest flow stress under compressive loads. Both the graphene particles and graphene full sheet interlayers have strengthening effects on the nanocrystalline nickels with different average grain sizes.

It is well stablished in the literature that, nanocrystalline metals reach a maximum strength at an average grain size in which the Hall-Petch deformation regime transfers to the reverse Hall-Petch regime [147]. For nickel nanocrystals, this cross-over which is corresponding to the maximum possible strength, occurs around 10-12 nm average grain size [148], which is evident from the results of Figure 5-11. However, when graphene layers are added into the nickel nanocrystalline structure, the strength of the nanocrystals improves even further. This improvement in the strength is achieved at all the grain sizes reinforced with both the layered graphene full sheets and the nickel particles interlayers.

Inferred from the results of Figure 5-11(d), the improvement in flow stress via adding the layered graphene sheets is more pronounced in the coarse-grained structures where ~40% improvement was obtained. The mechanism behind this significant improvement can be observed in Figure 5-12. As shown in the top row in Figure 5-12, as the applied strain goes beyond 0.055, the nucleated dislocations tend to grow through the grains up to the point that they are hindered by the grain

boundaries. However, at the presence of graphene interlayers (second row of Figure 5-12), the growing dislocation loops are almost fully trapped by graphene sheets at earlier stages of their propagation. This mechanism limits the plastic deformation explaining the significant strengthening effect of layered graphene sheets. Similar trend is observed in the nickel nanocrystals reinforced with layers of graphene particles (third row of Figure 5-12).

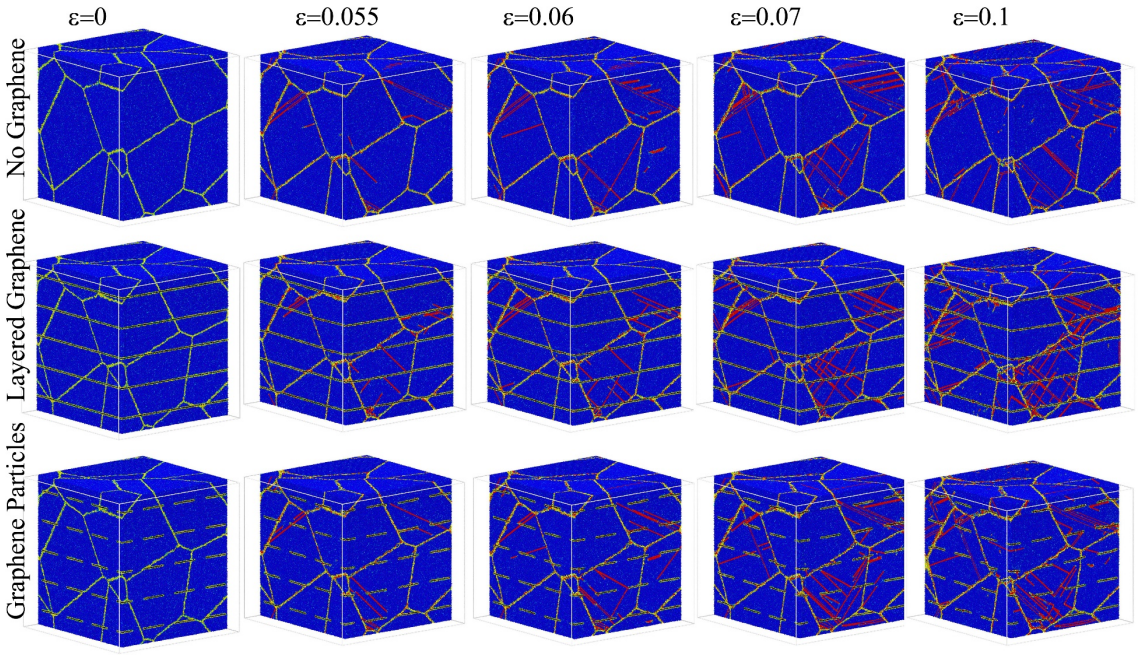

Figure 5-12. Deformation steps of nanocrystalline nickels with average grain size of 24.8 nm reinforced with no-graphene (first row), layered graphene sheets (second row), and graphene particles (third row) interlayers under compression strain loading up to 0.10. The dislocations travel through the grain as the strain increases unless they are stopped by grain boundaries (in the first row), layered graphene (second row), and graphene particles (third row).

Taking a closer look at a cross-sectional cut from the graphene reinforced nanocrystals, provided in Figure 5-13, reveals the interaction between graphene layers and dislocation motions. As shown in Figure 5-13(a) and (c), the dislocations, grown inside the grains on top and below the graphene layer, are fully stopped when they met graphene.

However, in the presence of graphene particles, shown in Figure 5-13(b) and (d), some dislocations are fully, and some partially, hindered by the graphene flakes. These dislocation motion stoppage mechanisms have caused the compressive stress-strain response of the nanocrystal systems to delay the onset of yielding (Figure 5-13(d)), resulting in exhibiting higher flow stress. Therefore, as quantitatively shown in Figure 5-11(d), 14% and 40% improvements in the strength of the nickel

nanocrystal with an average grain size of 24.8 nm were obtained via reinforcing with layered graphene sheets and graphene particles, respectively.

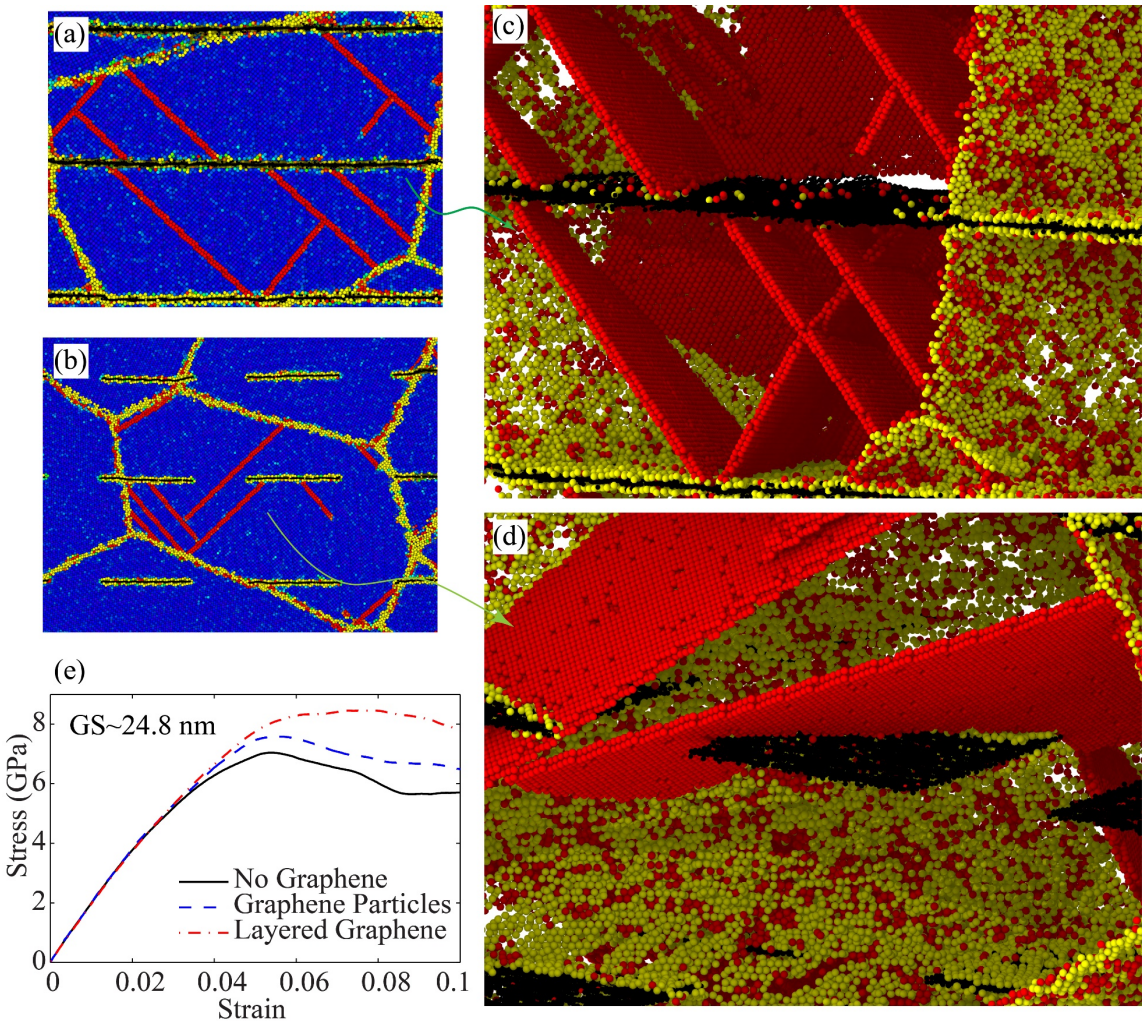

Figure 5-13. Strengthening mechanism in the nanocrystalline nickels with average grain size of 24.8 nm reinforced with (a and c) layered graphene sheets and (b and d) graphene particles. It is shown that how dislocations motions are fully stopped by graphene sheets and partially stopped by graphene particles. (e) Comparative compressive stress-strain curves of the systems reinforced differently. It is evident that graphene interlayers have raised the flow stress.

In case of nanocrystals with finer average grain sizes (e.g. 11.9 nm) similar strengthening effects can be observed when the reinforcing graphene interlayers are added into the systems. Figure 5-14 shows these nanocrystals under compressive loading, revealing how the deformation mechanisms set as compressive strain increases.

In the case of nanocrystalline nickels with the average grain size of 11.9 nm, the governing plastic deformation mechanism is a mixture of Hall-Petch and reverse Hall-Petch effect. Hence, compared

to the coarse-grained systems shown in Figure 5-12 and Figure 5-13, the reinforcing graphenes, embedded into the fine-grained systems of Figure 5-14, act slightly different in strengthening the system. Figure 5-15 shows a magnified view of cross-sectional cuts from the graphene reinforced nickel nanocrystalline systems under high compressive strain. Similar to the systems with coarser grain size, growing dislocations are trapped by graphene sheets and particles.

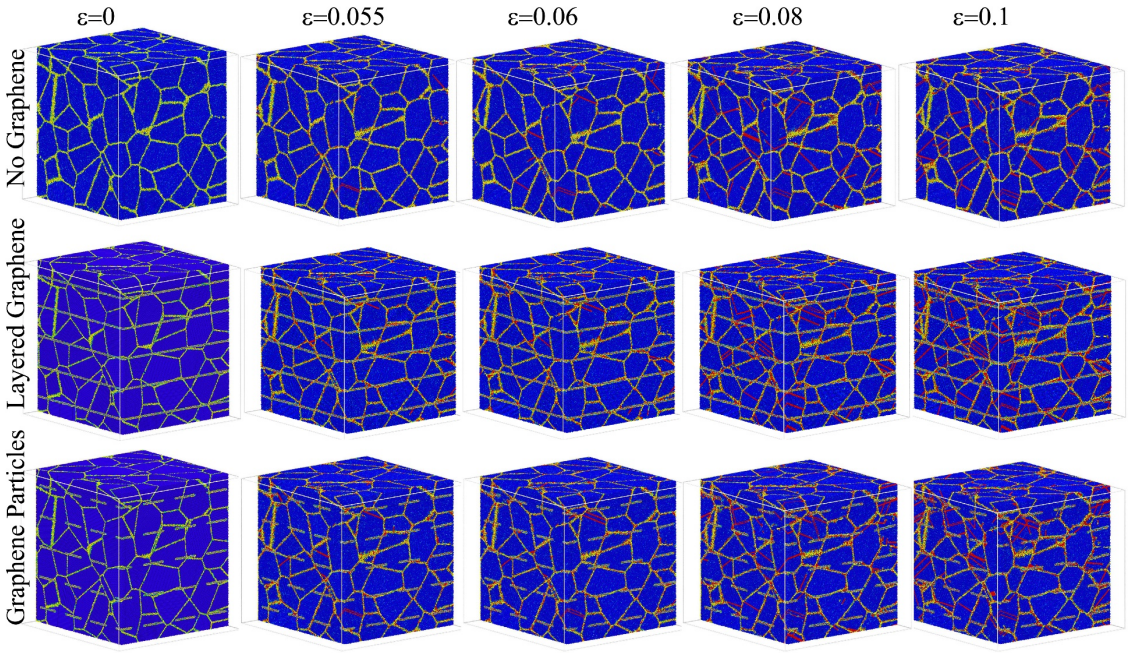

Figure 5-14. Deformation steps of nanocrystalline nickels with average grain size of 11.9 nm reinforced with no-graphene (first row), layered graphene sheets (second row), and graphene particles (third row) interlayers under compression strain loading up to 0.10. The dislocations travel through the grain as the strain increases unless they are stopped by grain boundaries (in the first row), layered graphene (second row), and graphene particles (third row).

Furthermore, since atomic sliding at the grain boundaries is another plastic deformation mechanism at nanocrystals of this grain size, it can be seen that dislocation buildups due to atomic sliding at grain boundaries are stopped by graphene layers. Particularly, in Figure 5-15(b) graphene particles are deformed slightly to prevent the atoms at the grain boundaries from sliding. Comparing the systems with the graphene particles and layered graphene sheets, the latter system has a greater chance to contribute to the strengthening mechanism. Therefore, in the compressive stress-strain curves illustrated in Figure 5-15(e), the system with the layered graphene exhibits higher flow stress than the system with graphene particles. However, the graphene particles were also successful to fully or partially block the dislocation growth.

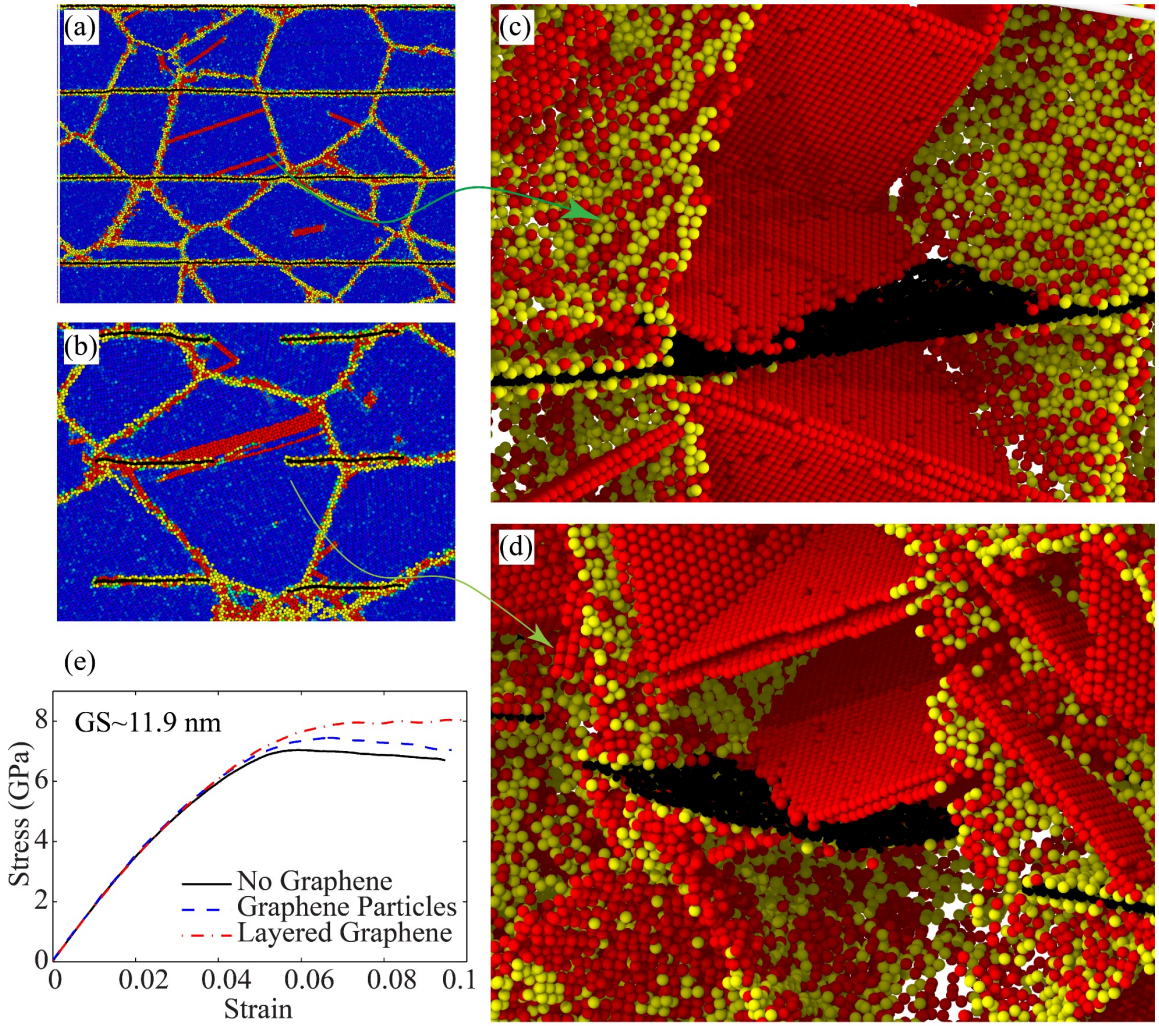

Figure 5-15. Strengthening mechanism in the nickel nanocrystals with average grain size of 11.9 nm reinforced with (a and c) layered graphene sheets and (b and d) graphene particles. It is shown that how dislocations motions are fully stopped by graphene sheets and partially stopped by graphene particles. Additionally, dislocation buildups at the grain boundaries due to atomic sliding are stopped by the graphene inserts. (e) Comparative compressive stress-strain curves of the systems reinforced differently showing graphene interlayers successfully increase the flow stress of the nanocrystalline nickel.

5.2.3.1.2 Strengthening effects of graphene particles under other modes of deformation

As mentioned in Section 5.2.2.1, two more series of MD simulations are performed on the material systems with the average grain size of 12.4 nm, which in the first one, the tensile strain, and in the second one, compressive strain is applied along the three principal directions. The tensile and compressive stress-strain curves are shown respectively in Figures S1 and S2 of the supplementary document [258] for the models with and without layered graphene particle reinforcements. The

tensile and compressive flow stress values for each stress-strain curve are calculated and presented in the bar chart of Figure 5-24 [258]. For all the loading modes and directions, the nanocrystalline nickel shows improvements in the flow stress due to existence of graphene particle interlayers. This strength improvement can be attributed to the dislocation blocking capabilities of the graphene particles explained in Section 5.2.3.1.2.

Figure5-25 illustrates a comparison between the stress-strain response of the material systems in tension and compression [258]. For both the systems with and without graphene reinforcements, the compressive strength is higher than tensile strength. This tension compression asymmetry has been reported in the literature for nanocrystalline metals [261, 262]. This is due to the fact that in the nanocrystalline metals, dislocations emission is more difficult to occur under the existence of compressive stress than under tensile stress [261, 262]. However, the existence of the interlayer graphene nanosheets has increased the strength both in tension and compression.

5.2.3.1.3 Loading Rate Effect

In addition to the aforementioned atomistic simulations performed at 10^9 1/s strain rate, a series of simulations are also performed at 2×10^9 1/s strain rate, in order to study the effect of loading rate on the strengthening mechanisms of graphene interlayers.

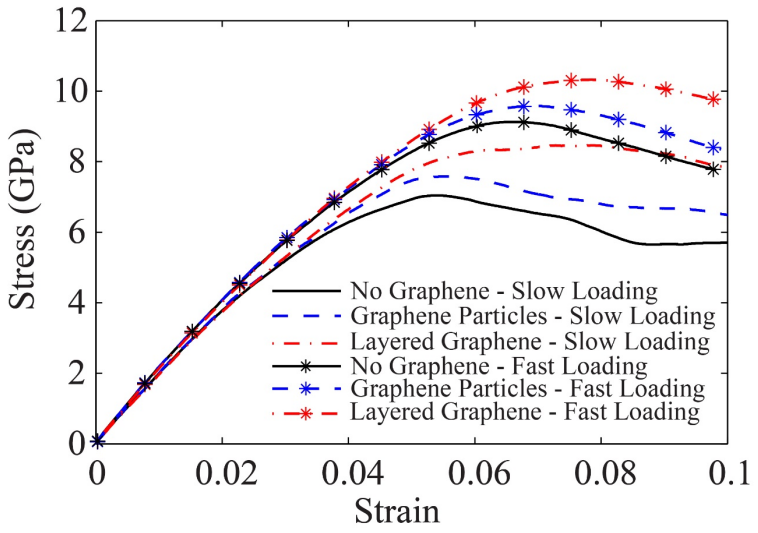

Figure 5-16. Compressive stress-strain behavior of the nickel crystalline systems reinforced with no graphene, graphene particles, and layered graphene sheets under slow loadings at the strain rate of 10^9 1/s and faster loading at of 2×10^9 1/s strain rate. The curves for the higher strain rate loading illustrate overshoots. However, these overshoots are followed by drops in stress level. Regardless of strain rate, the graphene interlayers successfully increase the flow stress at nanocrystalline nickel composites.

Figure 5-16 shows the compressive stress-strain curves for the system with average grain size of 24.8 nm with different configurations of graphene interlayers at the two abovementioned strain rates. As well-stablished in the literature [147], when the strain rate increases, higher stress is needed to be built up to nucleate dislocations from the grain boundary sources, and as strain increases further, significant plastic deformations and therefore a drop in the stress level appears due to growing the dislocation inside the grains. This phenomenon is more evident in coarser-grained polycrystals. Therefore, a jump in the stress-strain curves associated with a distinctive peak can be seen for the systems with no graphene interlayers. However, at the lower strain rate, the existence of graphene interlayers, especially the layered graphene sheets, stops the nucleated dislocations from growing, resulting in maintaining the stress level. Hence, the reinforcing capabilities of the graphene interlayers are more significant at lower strain rates.

5.2.3.1.4 Random Orientation of Graphene Dispersion

As discussed in the previous sections, when the graphene sheets or particles are distributed layerwise and perpendicular to the loading direction inside a nickel nanocrystalline systems, significant improvements in the strength of the nickel nanocrystals can be achieved. A series of simulations are also performed to examine the effect of nickel particle inserts, as they are randomly oriented inside the nickel nanocrystals, on their mechanical strength. Although fabricating such a configuration is practically very difficult, our simulations will show the efficiency of the system if graphene particles are randomly arranged inside the grains. Figure 5-17(a) presents the compressive stress-strain curves of atomistic models with two different average grain sizes, with and without randomly oriented nickel particles, under the fast loading condition along z-direction. It can be seen that almost no improvement in the strength of the nanocrystalline systems is evident. The compressive stress-strain curves of the same material system with the loading along x- and y-directions are also presented in Figure5-26 [258]. The role of graphene inserts in the deformation mechanism is shown in Figure 5-17(b-e) and Figure5-27 [258]. Similar to the graphene interlayers in the previous simulations, the graphene particles have successfully blocked some dislocations from propagating (Figure 5-17(e) and Figure5-27 (c, e and f)). However, some dislocations have initiated from the tip of the graphene inserts (Figure 5-17(d) and Figure5-27(a)). In nanocrystalline metals, since the grain sizes are too small, there is no enough space for dislocations to initiate and grow inside the grains [147].

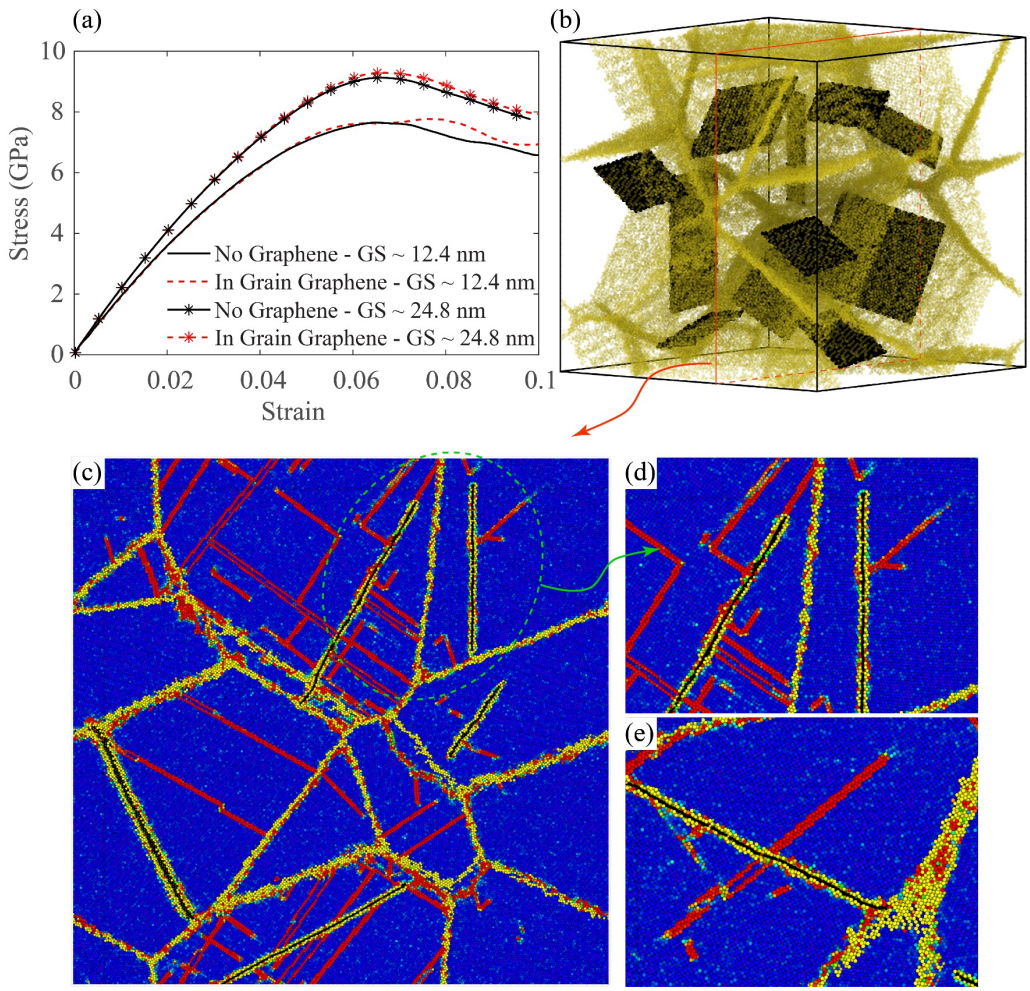

Figure 5-17. Performance of the nanocrystalline nickel samples with two different average grain sizes reinforced with randomly oriented graphene particles under fast loading rate. (a) Compressive stress-strain response. (b) Graphene arrangement inside a nickel nanocrystal. (c) Cross-sectional cut showing graphene/dislocation interactions. (d) Graphene particles with dislocations initiated at their tip. (e) A graphene particle that has stopped dislocations motion. Inferred from the stress-strain curves, the deteriorating and strengthening effects of randomly oriented graphene particles cancel out each other.

Furthermore, the MD simulations start from a defect-free grains condition [147]. Therefore, dislocations tend to initiate at the regions where a discontinuity in the crystalline structure exists; i.e. from the grain boundaries or from the tip of the graphene inserts. When the graphene inserts are arranged in a layerwise order inside the nanocrystalline matrix, a dislocation initiated at the tip of a graphene nanosheet has a relatively high chance to be blocked by the graphene nanosheets placed in the next interlayer region. In contrary, the material system reinforced with randomly oriented graphene nanosheets does not optimally benefit from this capability. Therefore, the layerwise arrangement of the graphene particles inside the material system plays a key role in

strengthening the material. In the case of randomly oriented graphene reinforcements, the dislocation initiating and dislocation blocking contributions of the graphene particles have cancelled out one another's effect on the strength of the system resulting in no significant change in the compressive stress-strain behavior.

5.2.3.1.5 Nanoindentation

In order to study the effects of reinforcing graphene interlayers under more complicated loading situations a series of atomistic models are developed to simulate the response of graphene reinforced systems to a nanoindentation loading. Comparing the simulations with real-life indentation loadings, the simulations loading rate is much higher. However, it is shown in the literature [139, 263] that for the average grain size of 4.9 to 12.1 nm and indentation depth of around 2.7 nm, the nanoindentation simulations are in a good qualitative agreement with experimental results. Therefore, satisfying these conditions, our study is qualitatively valid.

Our simulated nanocrystalline nickel systems are only reinforced with graphene particles, not full sheets of graphene. However, various areal fractions of particles are introduced into the models, as low, medium and high densities. The developed atomistic models, under indentation loadings, are shown in Figure 5-18(a-c). Figure 5-18(a), which is the system with no graphene particles, shows how a high density of dislocations are developed under the indenter head and propagated through the thickness of the polycrystal. Low density of graphene particles, in Figure 5-18(b), however, has partially blocked the dislocations. In contrast, the model with high density of graphene particles in Figure 5-18(c) shows the effect of graphene particles to block the attack of dislocations to the lower layers of nickel nanocrystal. This is the reason that in the load-depth curves of Figure 5-18(d), the nickel-graphene systems with medium and high graphene particle contents shows higher required loads for indentation to a given depth.

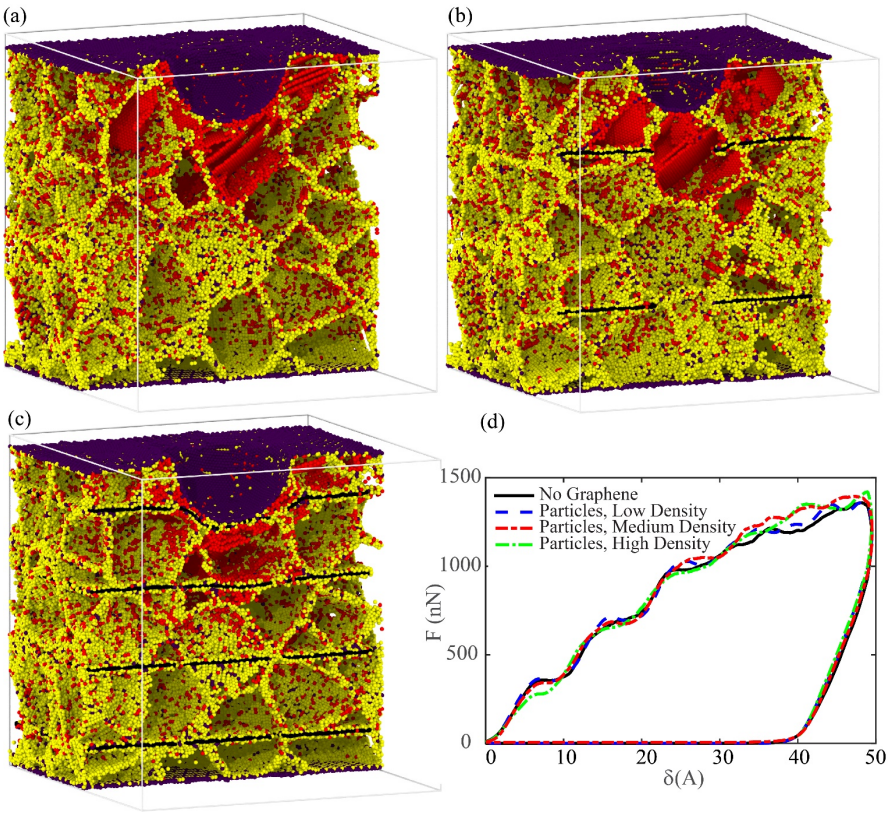

Figure 5-18. Nickel nanocrystals reinforced with (a) no graphene, (b) low and (c) high areal coverage of graphene particles under indentation loadings. (d) Load-depth curves of the nanoindentation simulations showing that the simulation with medium and high densities of graphene interlayers, on average, require higher levels of indentation force at a certain penetration depth.

5.2.3.2 Experimental Results

As previously discussed, nickel-graphene nanolayered composites inspired by the results molecular dynamics simulations are tried to be fabricated. The fabricated composites possess various areal coverages of monolayer graphene particles at their interlayers. The composites undergo nanoindentation loadings to determine an optimum areal coverage of graphene particles able to strengthen the nanocrystalline nickels at a high level.

5.2.3.2.1 Graphene interlayers

The nickel films covered with different concentrations of graphene dispersions are studied under FE-SEM, shown in Figure 5-19, to examine their graphene coverage. As shown in Figure 5-19, as graphene concentration increases, the areal coverage over the nickel layers increases. The FE-SEM micrographs, taken from different zones and with different magnifications, are analyzed using an image processing tool called, ImageJ, to quantify the areal coverage of graphene particles in the interlayer regions. As the result, D, M, H, and SH sample configurations demonstrated

13.7±0.59%, 22.2±1.00%, 26.2±1.89%, and 34.3±0.44% graphene areal coverage, respectively, in their interlayer regions. However, with increase in the graphene concentration, more agglomerated graphene flakes remain on the nickel surface. These agglomerates in the interlayer regions potentially provide unwanted discontinuity in the nanolayered composites structures which can limit the capability of the graphene layer in interlocking the dislocations growth inside the structure. However, when the nanolayered composites are under loading conditions and dislocations grow in a metal layer, wider areal coverage of graphene flakes increases the desired chance of dislocations being stopped.

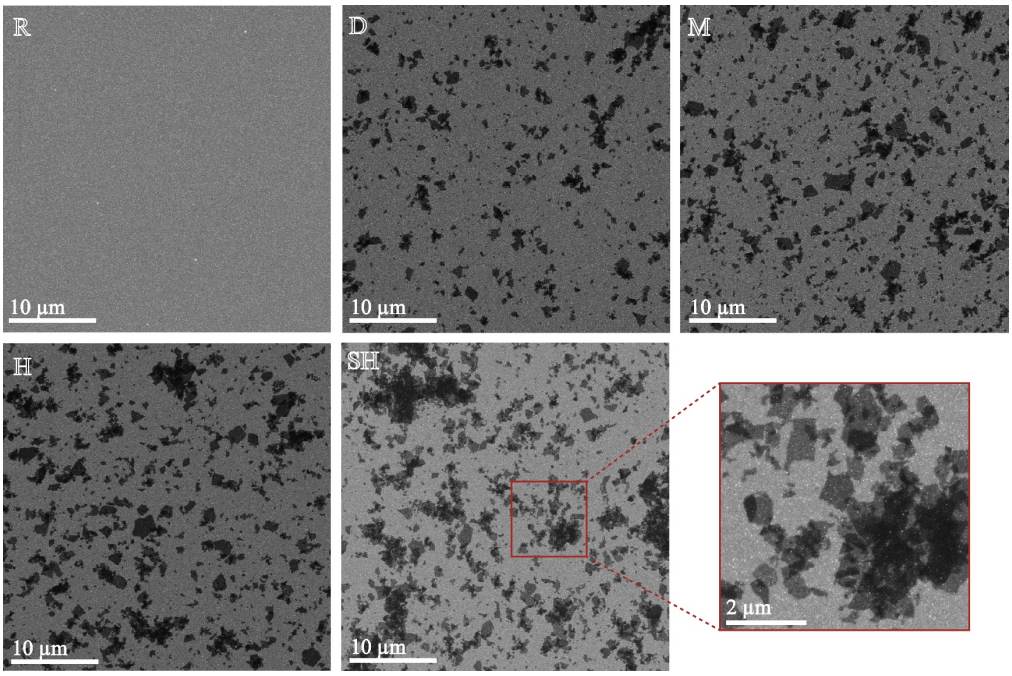

Figure 5-19. The nickel films covered with different concentrations of graphene dispersion. D, M, H, and SH are undergone the spin-coatings of graphene dispersion concentrations of 0.025, 0.050, 0.075, and 0.100 wt.%, respectively, and the R sample did not have any graphene layer. Graphene agglomerates can be observed as graphene content in the dispersion increases, as shown in the magnified picture.

5.2.3.2.2 Nickel layers

The crystalline structure of the nanolayered nickel composites is shown in the micrographs of Figure 5-20. Bright field TEM images of a deposited nickel layers, shown in Figure 5-20(a and b), confirms that the nickel layers possess a polycrystalline structure with grains diameters of ranging from few nanometers up to 40 nm. The average grain size of the nanocrystalline structure is measured to be 18.3 nm, which is close to the optimum grain size corresponding to the strongest

nickel nanocrystalline structure (~12 nm). The selected area diffraction pattern (SADP), shown in Figure 5-20(c), exhibited three complete shining rings revealing that the grown nano-grains have no preferred crystal orientations. Circle Hough transform (CHT) analysis of the SADP is performed to calculate the interplanar spacing (d-spacing) associated with the distinct circles. It is revealed that the calculated interplanar lattice spacings correspond to the ones known for FCC nickel.

The layered structure of the designed nanolayered composites is shown in the cross-sectional SEM image of Figure 5-20(d). The magnified inset illustrates the crystalline structure from the side view. The nickel nanosized grains can be observed in this picture. The grain sizes detected in this SEM micrograph is similar to the ones in the TEM images of Figure 5-11(a).

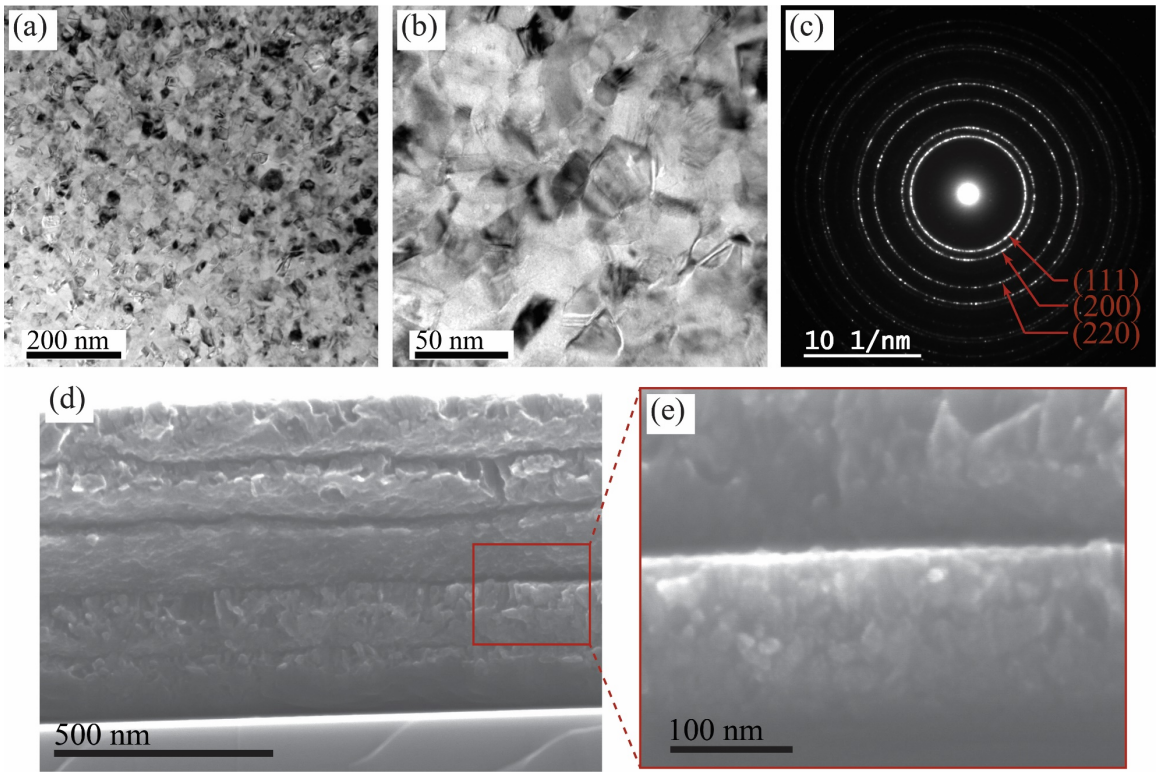

Figure 5-20. Transmission electron microscopy (TEM) images of nickel thin layers show at different magnifications in (a) and (b). The grain size is ranging from few nanometers up to 40 nm with an average size of 18.3 nm. (c) Selected area diffraction patterns (SADP) revealing the nanocrystalline structure of the nickel layers corresponding to FCC nickel structure with no preferred crystal orientation. (d) and (e) Cross-sectional scanning electron microscopy (SEM) images of the nickel nanolayered composites at two different magnifications.

5.2.3.2.3 Nanoindentation

The representative load-depth curves of the load-controlled performed nanoindentation tests are plotted in Figure 5-21(a), (b) and (c) for maximum indentation loads of 5.0, 10.0, and 20.0 mN, respectively. Strengthening effect of graphene particles at the interlayers can be seen for the nickel-graphene systems with low graphene content (Dilute), for which at a given input load, the nickel-graphene system has undergone less penetration depth. In contrary, the nickel-graphene systems with the highest graphene particle contents (Super High), underwent deeper penetration. From the load-depth curves for all the individual indentations, average hardness and reduced moduli of the samples are obtained and shown in Figure 5-21(d) and (e) respectively. For almost all the load cases, the nickel-graphene systems with dilute, medium and high contents of graphene particle interlayers exhibit improvements in hardness. Particularly, 39% improvement in the hardness of nanocrystalline nickel is observed for the dilute sample at the maximum load of 10.0 mN.

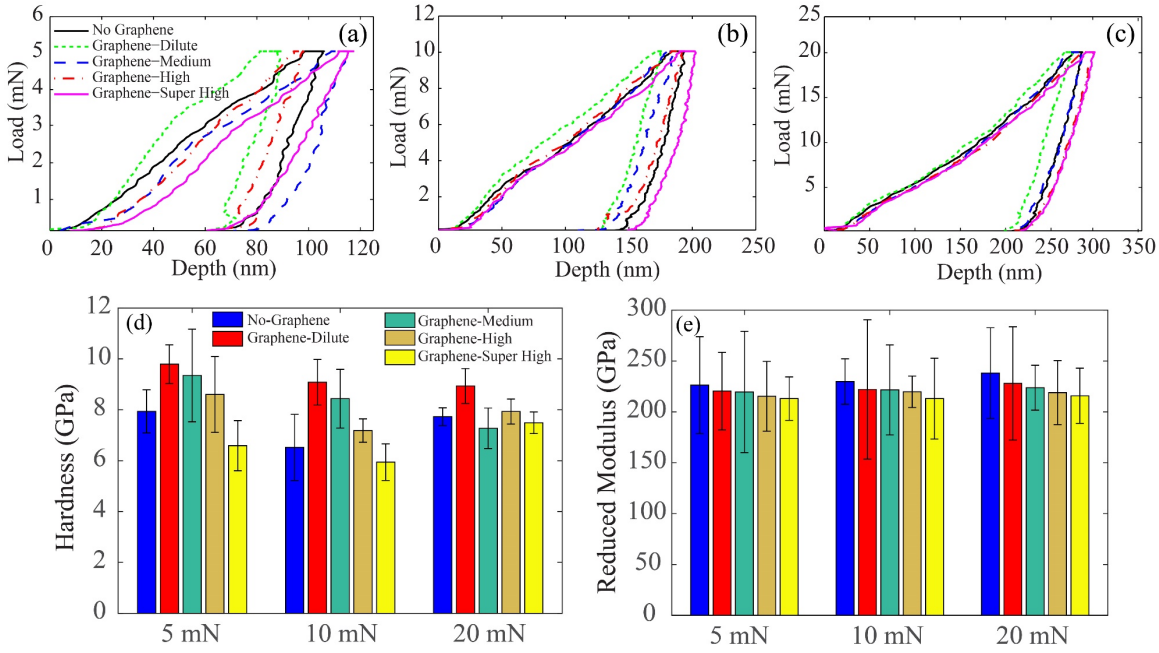

Figure 5-21. The representative load-depth curves of the load-controlled performed nanoindentation tests for maximum indentation loads of 5.0 mN (a), 10.0 mN (b), and 20.0 mN (c). Average of the obtained results; (d) hardness, and (e) reduced modulus. The nickel-graphene nanolayered composite with ~13.7% areal coverage of graphene particles at the interlayers is the optimum configuration with the highest improvements in the hardness.

The capability of the graphene particle interlayers in blocking the dislocations inside the nickel grains, as observed in the numerical simulations, can be the main reason for the hardening effects observed in the experiments. However, for the super high content of graphene particles, an evident

drop in hardness can be observed. This can be due to the existence of graphene agglomerates in the interlayer regions shown in Figure 5-19. In summary, the high concentration of graphene particles in the solution used in fabricating this specific sample configuration is the reason behind decrement in hardness.

The reduced modulus is calculated using a curve fitting at the unloading part of the load-depth curves. Taking the standard deviation into account, no significant change was observed in the reduced modulus of the nickel-graphene nanolayered composites. Retaining the elastic modulus confirms that this method of integrating the graphene nanosheets has not changed the interatomic bonding in the nickel nanocrystalline structure [264].

5.2.4 Conclusions

In the present work, we introduced a new nickel-graphene nanolayered composite system in which instead of reinforcing large individual graphene sheets in the interlayer area, monolayer graphene flakes are spread inside the interlayers. In this composite only a fraction of the interlayer area (13%-30%) is covered. This graphene-metal nanolayered composite system is relatively easy and cost-effective to fabricate in large scales. At the first steps of this study, a systematic investigation on the effect of various graphene reinforcement configurations on the nickel-graphene systems performance is performed by utilizing a series of atomistic simulations. The molecular dynamics simulations of various nanocrystalline nickel-graphene systems are performed, for the first time, for a polycrystalline system under both compression and nanoindentation loadings to reveal the effects of metal average grain size, simulation cell size, graphene reinforcements' configuration, and loading rate. It is revealed that at a certain average grain size range (~12 nm) the nanocrystalline nickel illustrates a maximum strength. This is due to the fact that plastic deformation mechanism transfers from a Hall-Petch regime, governed by dislocation growth inside the grains, into a reverse Hall-Petch regime, governed by atomic sliding at the grain boundaries. Our atomistic simulations were successfully able to capture this transfer in the deformation mechanisms. It is also revealed that graphene full sheets and particles can effectively hinder dislocations growth and atomic sliding, fully or partially, resulting in strengthening the material system under compression. However, when graphene particles were randomly oriented inside the polycrystalline nickel, no meaningful change in the strength was observed. Moreover, the molecular dynamics simulations of nanoindentation loadings confirmed the role of graphene

particle interlayers in hardening of material system via hindering the dislocation growth through the metal grains. Inspired by the results of the atomistic simulations, the best applicable nickel-graphene nanolayered systems (with an average grain size of 18.3 nm which is very close to the optimum grain size corresponding to the maximum strength of nickel polycrystals) are identified and fabricated. The fabricated nickel-graphene nanolayered composites are mechanically characterized with nanoindentation experiments to quantify their hardness. The experimental results show that a nickel graphene nanolayered system, with only 14% areal coverage of graphene particles at the interlayer, has improved the hardness of the nanocrystalline nickel by almost 40%. As the result of this investigation, it is confirmed that the introduced material system benefits from both the nanocrystallinity of the metal as well as the strengthening effects of the graphene interlayers.

5.2.5 Supplementary Document

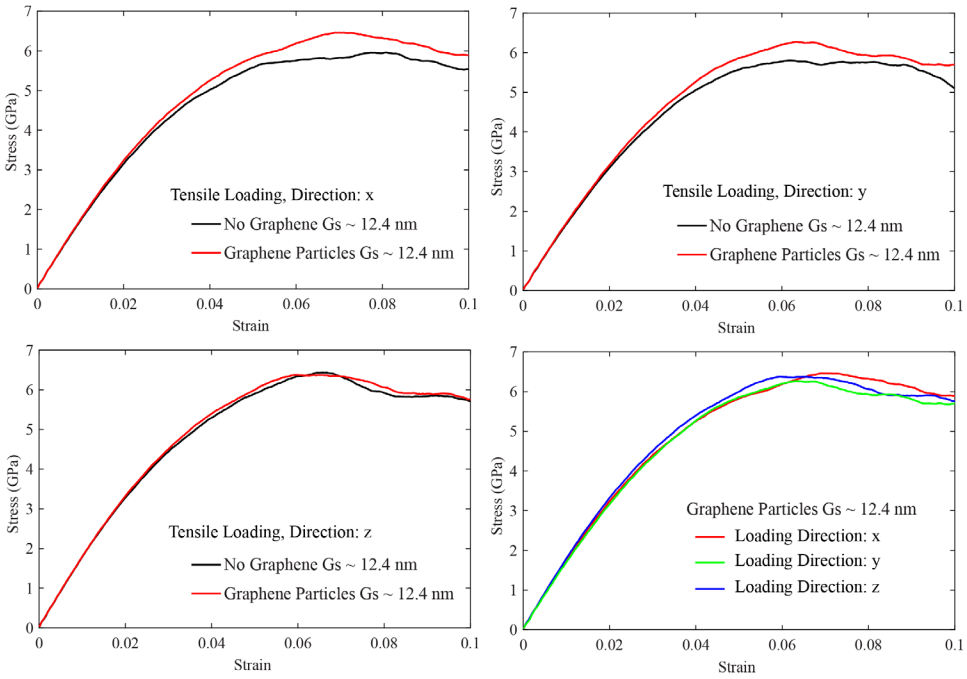

Figure 5-22. Tensile stress-strain response of the nanocrystalline nickel layered system with average grain size of 12.4 nm reinforced with graphene particles under different loading directions. x- and y-directions are in the graphenes' plane, and z-direction is perpendicular to the graphenes' plane.

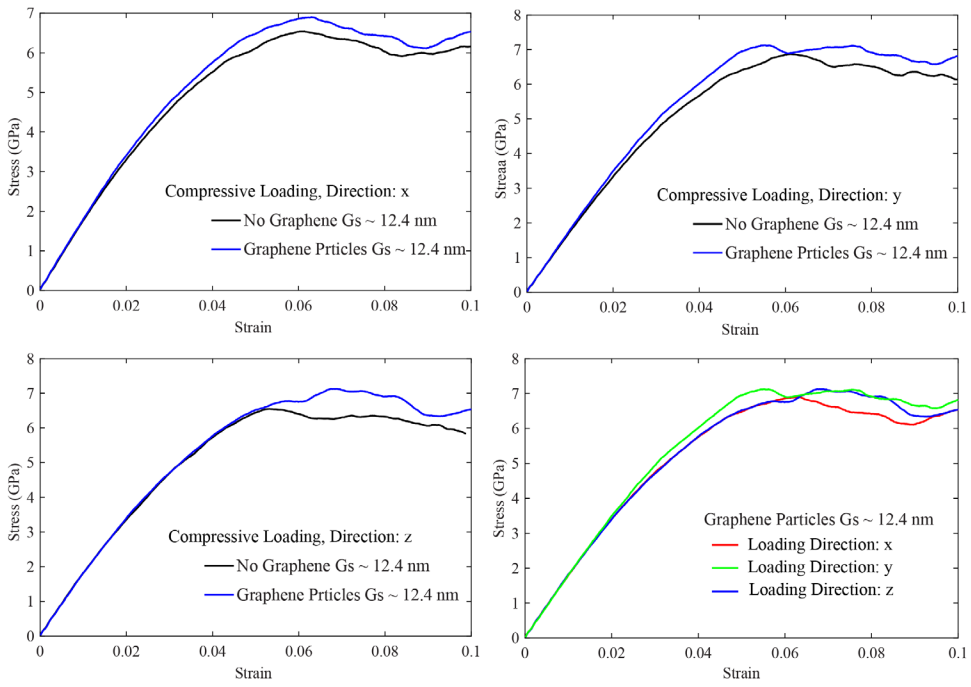

Figure 5-23. Compressive stress-strain response of the nanocrystalline nickel layered system with average grain size of 12.4 nm reinforced with graphene particles under different loading directions. x- and y-directions are in the graphenes' plane, and z-direction is perpendicular to the graphenes' plane.

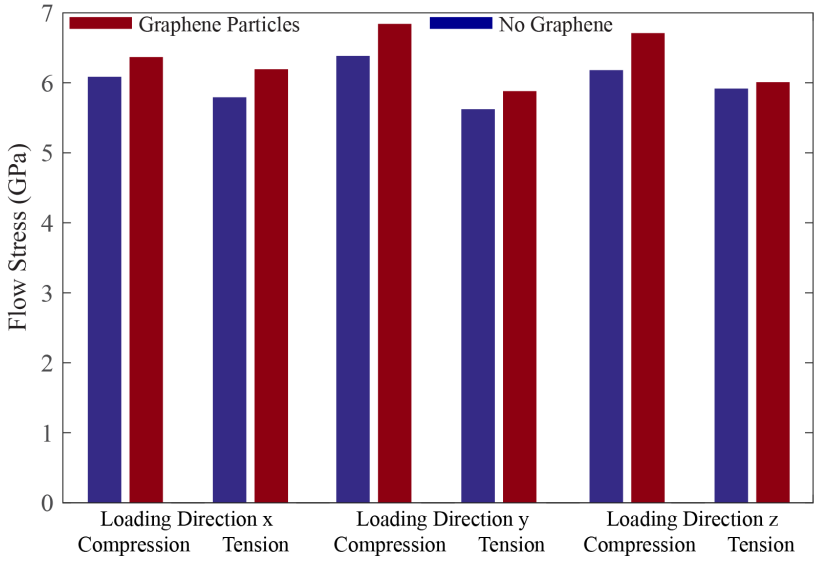

Figure 5-24. Flow stress obtained from the stress-strain curves of the nanocrystalline nickel layered systems with average grain size of 12.4 nm reinforced with graphene particles under different loading directions. x- and y-directions are in the graphenes' plane, and z-direction is perpendicular to the graphenes' plane.

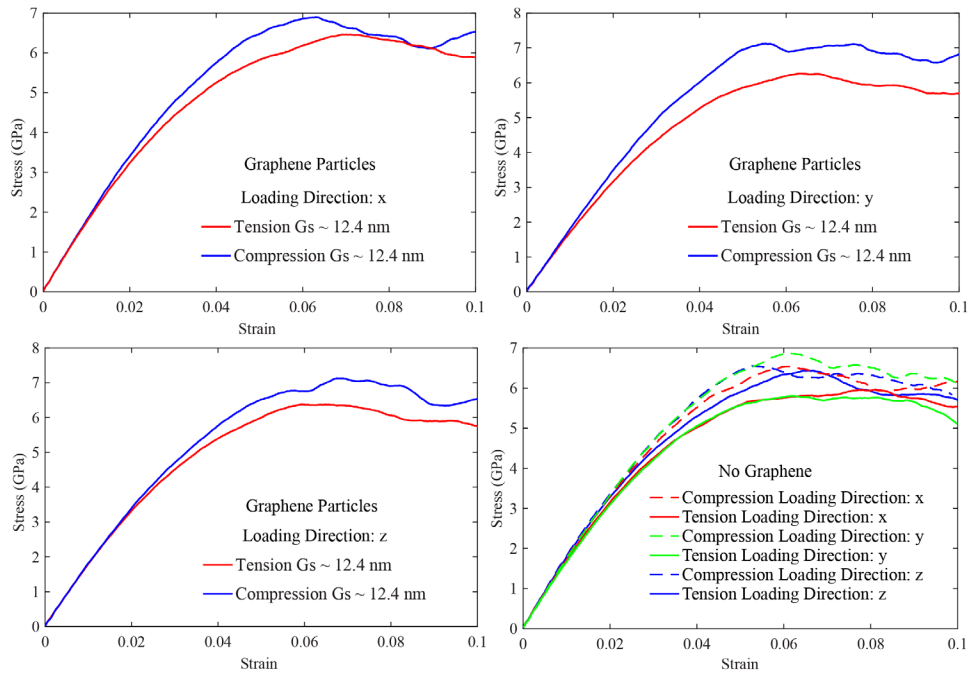

Figure5-25. Comparison between the tensile and compressive stress-strain response of the nanocrystalline nickel layered systems with average grain size of 12.4 nm reinforced with graphene particles under different loading directions. x- and y-directions are in the graphenes' plane, and z-direction is perpendicular to the graphenes' plane.

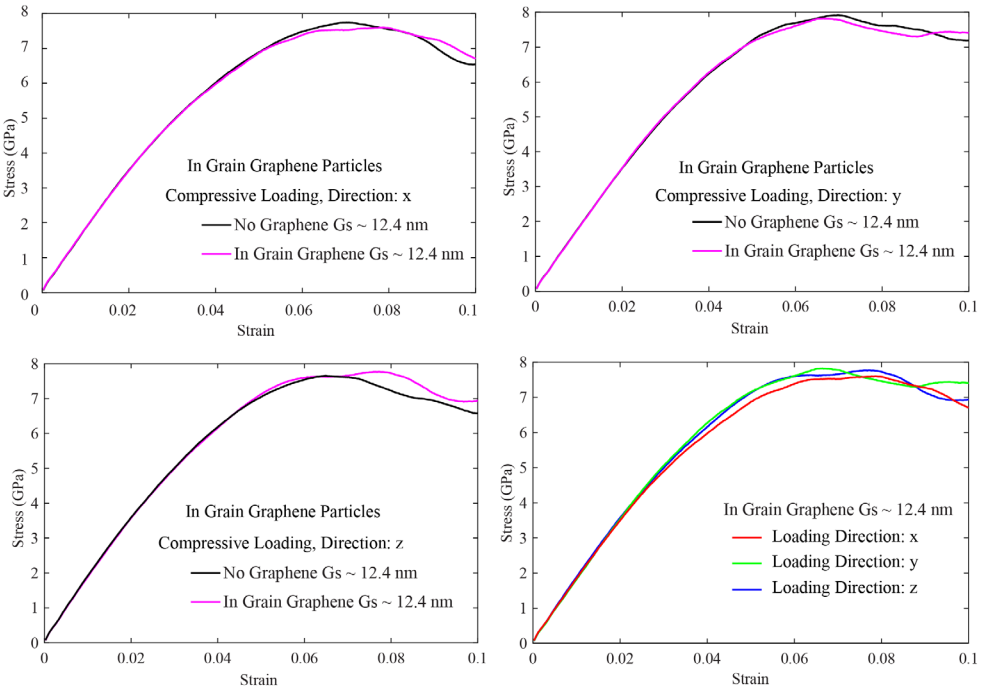

Figure5-26. Compressive stress-strain response of the nanocrystalline nickel reinforced with randomly oriented graphene particles under loadings in three different directions x, y and z.

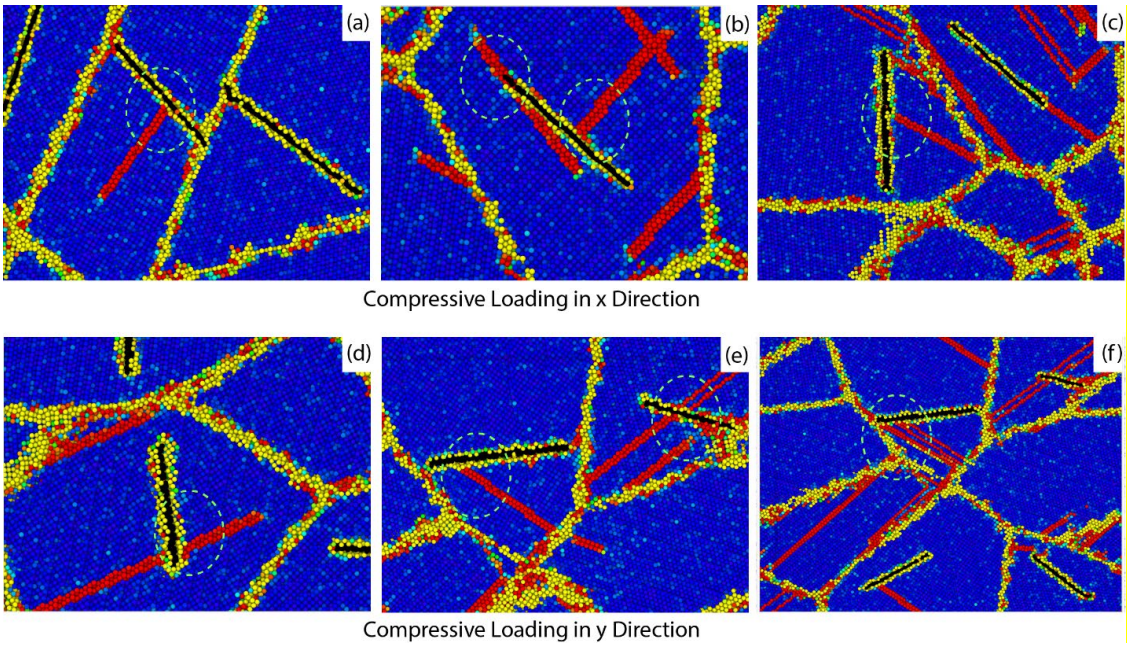

Figure5-27. Randomly arranged graphene particles inside a nickel nanocrystal under compressive loading in both x and y directions. (a) Graphene particles with dislocations initiated at graphene nickel interface. (b) Graphene particles with dislocations initiated at graphene tips and graphene nickel interface. (c) A graphene particle that has stopped dislocations motion. (d) Graphene particles with dislocations initiated at graphene tips. (e, f) A graphene particle that has stopped dislocations motion.

5.3 A Nanocrystalline NiTi-Graphene Composite: Mechanics of Properties Enhancement at the Atomistic Level

5.3.1 Overview

NiTi alloys possess two stable lattice structures at different stress or temperature conditions due to their two unique properties, the shape memory effect and the pseudoelastic response. These properties enable them to change their crystallographic structure between austenite and martensite phase in response to either mechanical or thermal loadings. The hysteretic pseudoelastic response of NiTi alloys [97, 100, 101] provides an ideal energy dissipation and damping capabilities for these alloys and make them a superior candidate to be used in passive control devices [210-212] to damp the energy in high-strain-rate and shock loading conditions [102]. As it was discussed in the previous sections, NiTi alloys show interesting behavior under shock wave loading condition. It was revealed that the dissipated energy is due to both plastic deformation and phase transformation and the small portion of the energy dissipation is due to plastic deformation. Since, the plastic deformation is an undesired phenomenon and in order to prevent the propagation of the plastic deformation in the NiTi alloys under loading, graphene nanoplatelets (GNPs) are used to

make a metal matrix composites (MMCs) which is capable of interlocking dislocations and preventing the propagation of plastic deformations. Carbon based nanomaterials, such as graphene GNPs or graphene nanosheets (GNSs) have outstanding mechanical strength and stiffness. Beside, great mechanical properties of GNSs, their unique 2D geometry has encouraged their application in a recently new type of metal matrix composites, metal nanolayered composites [135]. Metal nanolayered composites with high density interlayers have been shown to be capable of interlocking dislocations [265]. In our recent work [265], we performed molecular dynamics simulations of various nanocrystalline nickel-graphene systems, for a polycrystalline system under compression loadings to reveal the effect of graphene reinforcements on the mechanical properties. We revealed that graphene full sheets and particles both can effectively hinder dislocations growth and atomic sliding, fully or partially, resulting in strengthening the material system. Hence, using GNPs as a reinforcement in material systems are preferred since it is more cost-effective. In this work, we study the effect of adding GNPs to polycrystalline NiTi alloys on mechanical properties. Moreover, the interaction of the graphene particles with plastic deformation propagation in NiTi alloys are studied at the atomistic scale.

5.3.2 Materials and Methods

A series of molecular dynamics (MD) simulations are performed to investigate the effects of adding graphene particles on the mechanical properties of polycrystalline NiTi alloys. In order to define the interaction between Ni and Ti atoms, the many body interatomic potential, which was originally developed by Lai *et al.* [203] and subsequently improved by Zhong *et al.* [93] are used. The details of the potential function and the corresponding parameters are explained in Section 3.2.1. The coefficients for this potential have been calculated and reported by Zhong *et al.* [93] for cut-off radius $r_c = 4.2$ Å. In order to define the interaction between C atoms, CH.airebo potential is used. Moreover, LJ parameters 0.125 eV, 2.05 Å and 0.327 eV, 2.1 Å are used to define the interaction between Ni-C and Ti-C atoms, respectively.

In the present work the hybrid pair-style of eam and airebo potentials and lj parameters are used and Large-scale atomic/molecular massively parallel simulator (LAMMPS) [167] are utilized for performing the simulations, and Ovito [168] visualization tool is used for post-processing the results of MD simulations. The polycrystalline cells are created using Vorronoi Tessellation algorithm [204]. The four different periodic computational cells with the average size of $500 \times$

500×500 Å and the average grain sizes of 10.5 13.5, 23 and 27.5 nm are considered. Using these computational cells, two sets of MD simulations are performed. One set of simulations includes the four polycrystalline NiTi structures and the second set contains the four polycrystalline NiTi-graphene composites made by adding the graphene particles in to the polycrystalline NiTi alloys.

5.3.3 Results and Discussion

Figure 5-28 shows the stress-strain behavior of the pure nanocrystalline NiTi and graphene particle reinforced nanocrystalline NiTi systems under compression loadings. As mentioned earlier, the nanocrystalline systems have four different average grain sizes of 10.5, 13.5, 23, and 27.5 nm whose stress-strain curves are shown in Figure 5-28 (a) to (d), respectively. The materials are loaded up to the strain of 0.15 at 7.5×10^8 1/s strain rate. It can be seen that at the early stage of loading less than 0.02, the curves show a linear elastic behavior expected from austenite NiTi. As the strain increases, the material systems show the martensitic phase transformation behavior. Beyond certain strain level, the stress drops, showing the failure of the material as a result of plastic deformation. The maximum stress level is referred to as strength. Beyond this strain level at the bulk material failure, the material shows a flow behavior indicating the propagation of plastic deformations throughout the NiTi structure. Inferred from the curves of Figure 5-28, the presence of graphene particles increases the strength of NiTi nanocrystals for all system with different average grain sizes. Besides, graphene particles did not change the overall shape of the strain-stress curves confirming the fact that this arrangement of graphene reinforcements do not have any effect on the phase transformation capabilities of nanocrystalline NiTi. This is more evident at the curves of Figure 5-28(c) and (d) for the coarser grain sizes (23 and 27.5 nm), where the curves of the pure NiTi and NiTi-graphene systems coincide up to the strain level of 0.06. However, for the fine grain sizes of 10.5 and 13.5, the stress level for the graphene reinforced systems gets a little bit higher than the pure NiTi systems after the initial linear portion. This could be due to the difference in the deformation regimes at finer vs. coarser grain size NiTi systems, which will be discussed in the coming sections.

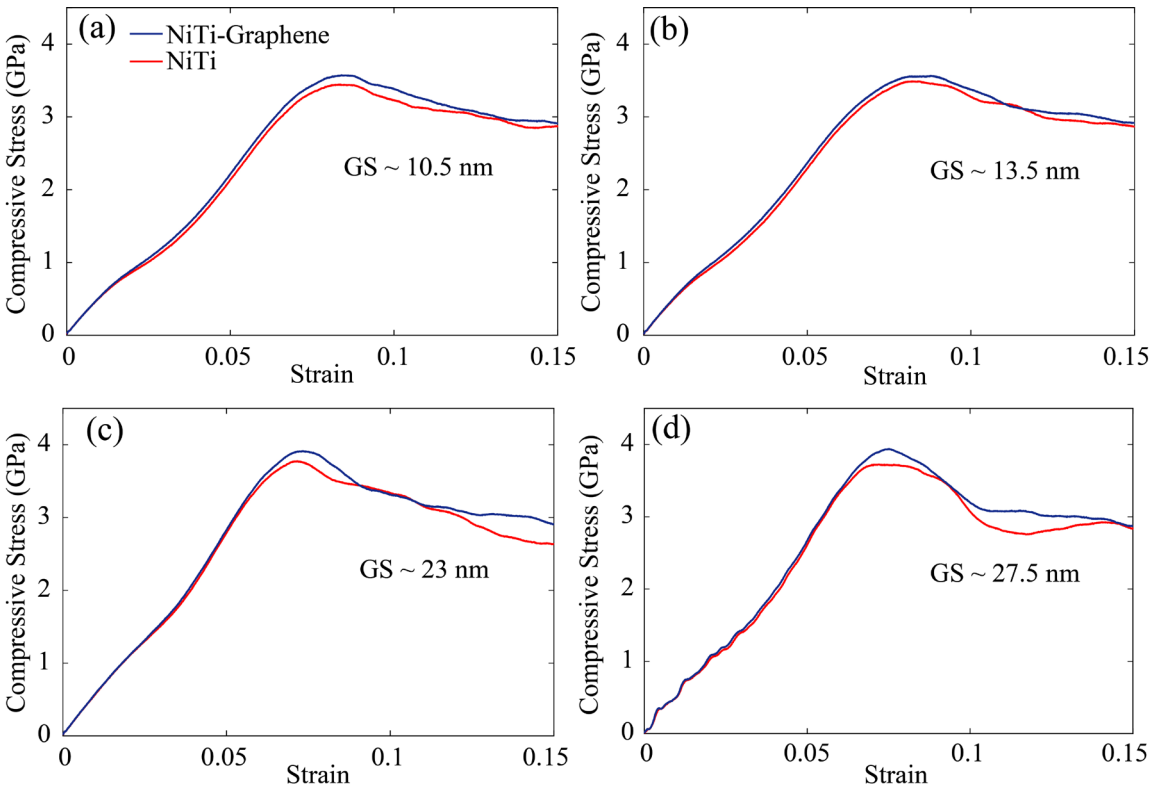

Figure 5-28. Compressive stress-strain responses of the nanocrystalline NiTi and NiTi-graphene systems under compression loading at the strain rate of 7.5 $\times 10^8$ 1/s for grain sizes of (a) GS ~ 10.5 nm, (b) GS ~ 13.5 nm, (c) 23 nm and GS ~ 27.5 nm.

Figure 5-29 shows the maximum stress that different material systems withstand, i.e. strength. As discussed in [147, 265] for polycrystalline metals, it is well stablished that as the average grain size gets smaller, the material gets stronger. This phenomenon, which is called Hall-Petch effect, is due to the plastic deformation regime controlled by dislocations' propagation inside the grains. In this mechanism, a dislocation initiated due to defects inside a grain, propagates through the grain until dislocation reaches the grain boundary and stops. The larger the grain, the longer the distance a dislocation could travel before it is trapped at the grain boundary, and therefore, the material experiences more plastic deformation. Hence, the polycrystalline with larger grain sizes show lower strength. The Hall-Petch effect is valid as long as plastic deformation mechanism is governed by the dislocation propagation inside the grains. However, at very fine grain sizes (usually less than 20 nm), the plastic deformation propagation is different, where due to the high volume ratio of grain boundary regions, the governing plastic deformation is atomic slip at the grain boundaries. For this regime of plastic deformation, as the average grain size goes smaller, the volume ratio of the grain boundaries gets higher and therefore, the material experiences more

plastic deformation, resulting in lower strength. This effect is called inverse Hall-Petch. As a result of these plastic deformation mechanisms, there exists an average grain size for every polycrystalline metal in which it shows a maximum strength. Inferred from our simulations and the results shown in Figure 5-29, the nanocrystalline NiTi with the average grain size of 20 nm is stronger compared to the other nanocrystals with the other grain sizes. At this range of grain size, the plastic deformation regime is a mixture of both the Hall-Petch and inverse Hall-Petch regimes. Via reinforcing the nanocrystalline NiTi with graphene particles, the strength is improved for both the Hall-Petch regime (GS > 20nm) and inverse Hall-Petch regime (GS < 20 nm). However, this strengthening effect is more pronounced at coarser grain sizes. This could be due to the excellent capability of the graphene particles in blocking the dislocations inside the grains. The interesting observation from these results is that using the graphene particles, the strength has been improved beyond the maximum possible strength for NiTi.

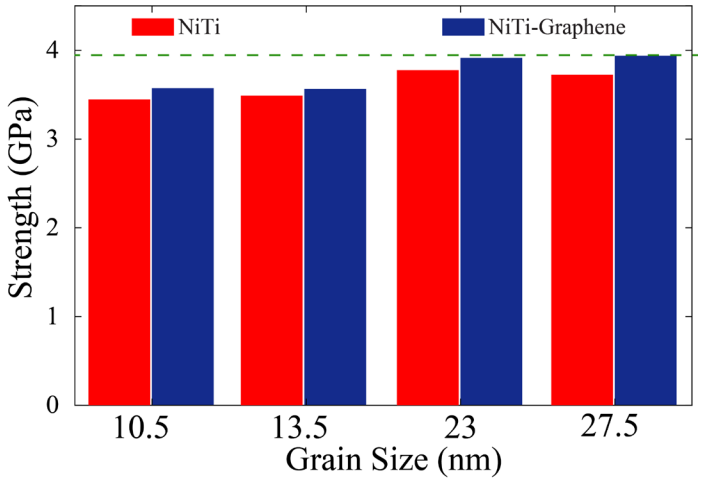

Figure 5-29. Comparison of the strength of the nanocrystalline NiTi and nanocrystalline NiTi-graphene composite with average grain sizes of 10.5, 13.5, 23 and 27.5 nm.

The same strengthening effect of graphene particles is observed at the flow stress of NiTi structures, shown in Figure 5-30. Flow stress is calculated as the average stress after the maximum stress is passed. At this stage, the plastic deformations propagate severely through the structure and the existence of graphene particles would stop and deflect them, resulting in maintaining the higher stress level. The graphene particles show strengthening effects on the nanocrystalline NiTi at all the average grain sizes.

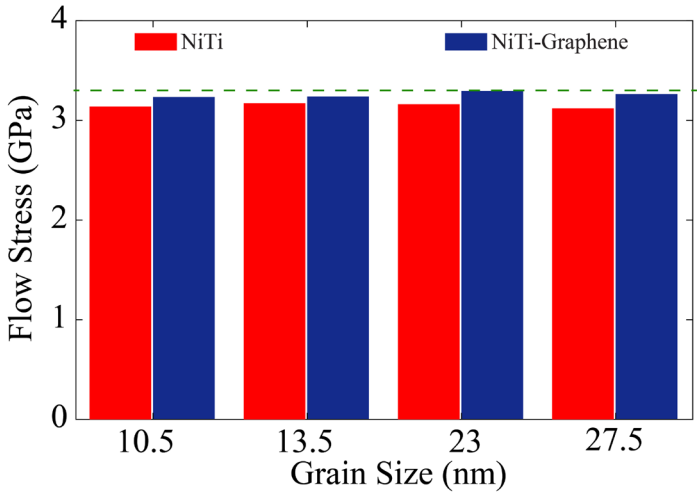

Figure 5-30. Comparison of flow stress in the nanocrystalline NiTi and nanocrystalline NiTi reinforced with graphene particles for different grain sizes of 10.5, 13.5, 23 and 27.5 nm.

Figure 5-31, shows the graphene particles' contribution in the shear strain propagation, i.e. plastic deformation, in the NiTi nanocrystalline structures with different average grain sizes. The left column in Figure 5-31 shows the grain structures, exposing the boundaries. The middle column shows the shear strain distribution at the NiTi structures under compressive loading at $\varepsilon = 0.10$, and the right column shows the same thing at graphene particles reinforced NiTi structures. Comparing the shear strain distribution at the pure NiTi structure with different grain sizes (the middle column of Figure 5-31) it can be seen that for the fine grain sizes (a, and b), the high shear strain is mostly at the grain boundaries, and for the coarser grain sizes (c, and d), the high shear strain representing the plastic deformation can be seen at the dislocations propagating inside the grains. This is the difference between the inverse Hall-Petch, and Hall-Petch plastic deformation regimes. Comparing the shear strain distribution in the pure with the reinforced NiTi systems with the GS of 10.5nm (Figure 5-31(a)) reveals that, the graphene particles located on the grain boundaries has hindered the shear strain on the boundaries. This strengthening mechanism prevents atomic slip at the grain boundaries, which is dominant at the inverse Hall-Petch regime. However, at the Hall-Petch regime where the dislocation propagation inside the grains is dominant, the graphene particles block the dislocation from propagation, fully or partially. This can be seen in Figure 5-31(d) corresponding to the NiTi nanocrystalline structure with average grain size of 27.5 nm.

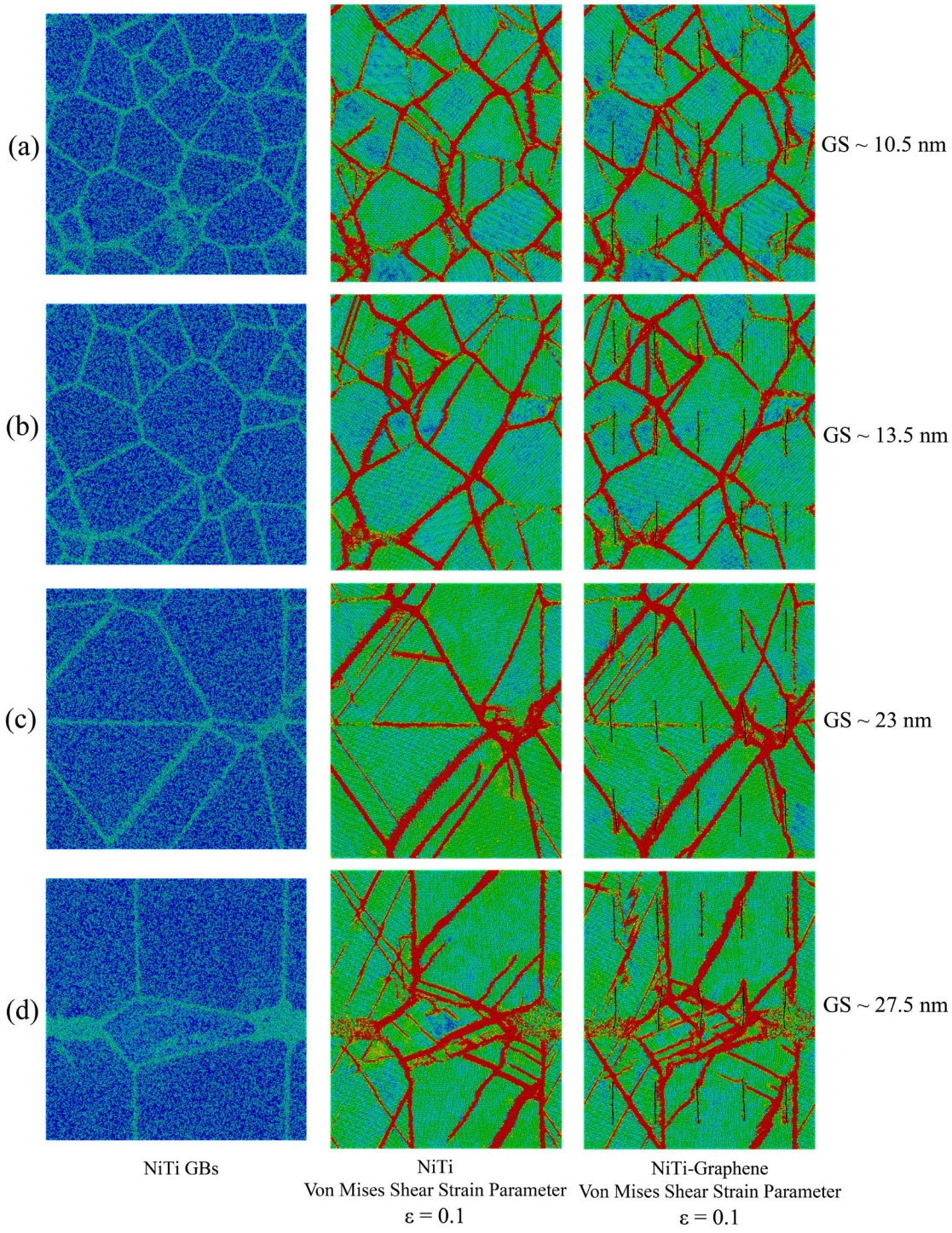

Figure 5-31. Plastic deformations propagation blockage in the nanocrystalline NiTi-graphene with average grain sizes of 10.5, 13.5, 23 and 27.5 nm.

The evolution of shear strain distribution in nanocrystalline NiTi with average grain size of 10.5 nm is shown in Figure 5-32.

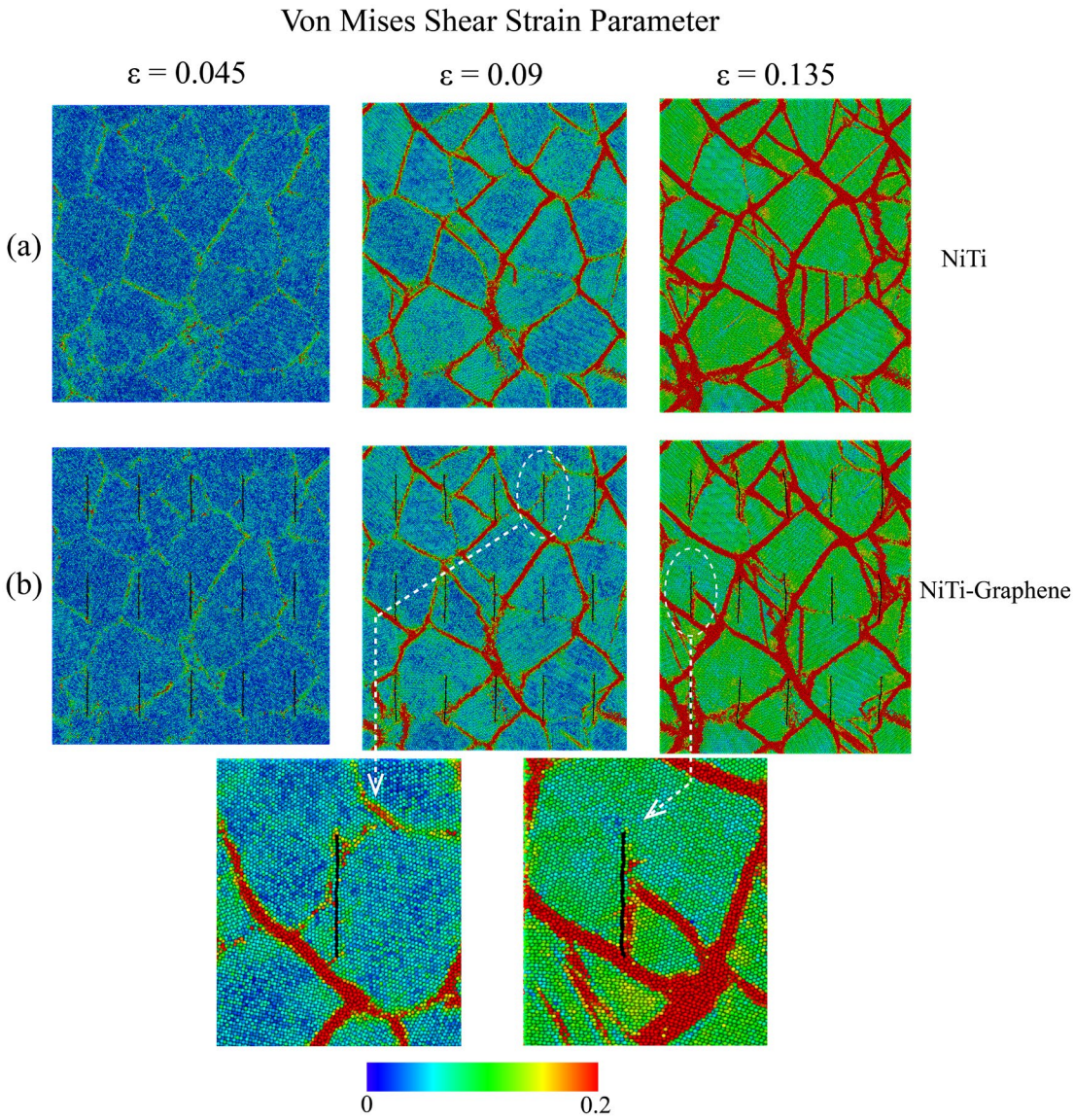

Figure 5-32. Strengthening mechanism in the NiTi nanocrystals with average grain size of 10.5 nm reinforced with graphene particles. Von Mises shear strain parameter shows that how dislocations motions are fully stopped by graphene particles. Additionally, atomic layers slidings are stopped by the graphene particles at grain boundaries.

The pure and graphene reinforced NiTi are sown in Figure 5-32(a) and (b) respectively. It can be seen that at the early stage of loading ($\varepsilon = 0.045$) the shear strain develops mostly at the grain boundaries. It would be worth mentioning that at the MD simulations, since the grains are modeled defect free, the plastic deformation should initiate at grain boundaries. In reality also, for very fine crystals, since the grain boundaries hold high volume ratio of the total structure, the plastic deformation occurs mostly at the grain boundaries. However, when a graphene particle is placed at a grain boundary, development of shear strain and plastic deformation is delayed by that

graphene particle at that boundary. For example, shown in the middle column of Figure 5-32(b), the magnified graphene particle has stopped the high shear strain at the grain boundary, while in the graphene-less structure with the same average strain, shown in the middle column of Figure 5-32(a), the same grain boundary has developed high shear strain. The shear strain developed at the grain boundaries would trigger the defects inside the grains.

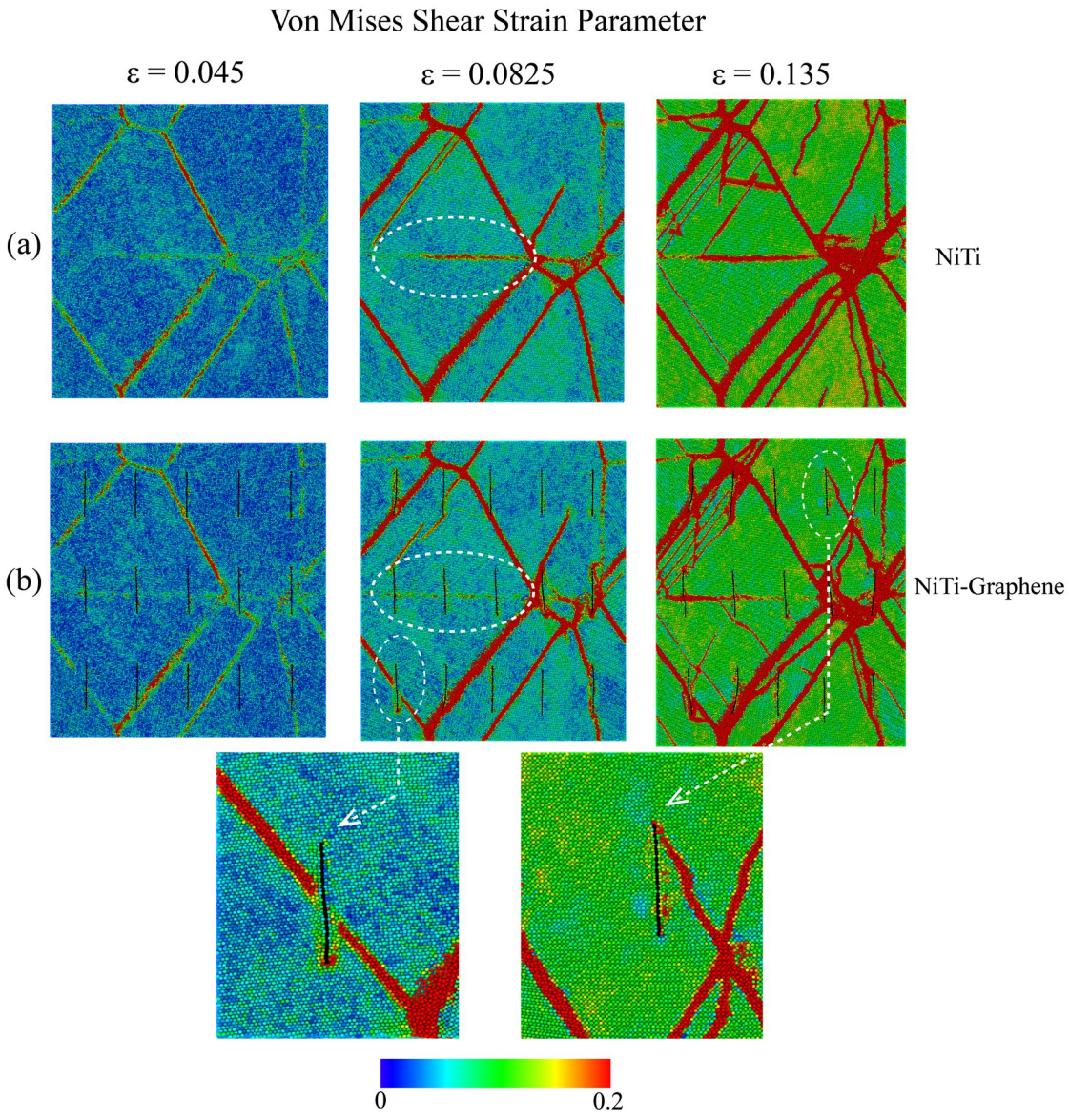

Figure 5-33. Strengthening mechanism in the NiTi nanocrystals with average grain size of 23 nm reinforced with graphene particles. It is shown that how dislocations motions are fully stopped by graphene particles. Additionally, atomic layers slidings are stopped by the graphene particles at grain boundaries.

As the loading increases, this defects propagate inside the grains as dislocations and eventually stop at the front grain boundary. At the existence of graphene particles inside a grain, the dislocations propagation could be blocked by them. For example, Figure 5-32(b) shows how a graphene particle has blocked a propagating dislocation at $\varepsilon = 0.135$. The capability of the graphene particles to hinder the plastic deformation mostly at the grain boundaries is the main strengthening mechanism at the inverse Hall-Petch regime.

The plastic deformation progression in NiTi structure with the average grain size 23 nm is shown in Figure 5-33. As also seen in the finer grain sizes, the shear strain initially grows faster at the grain boundaries than inside the grains. Comparing the NiTi and NiTi-graphene systems at $\varepsilon = 0.0825$, the shear strain at the grain boundary in the middle of the figure in NiTi system does not exist in the NiTi-graphene system. It reveals that existence of graphene delays increasing the shear at the grain boundaries. Another example is shown in the magnified picture of the graphene particle in Figure 5-33(b) at $\varepsilon = 0.0825$. An example of the capability of the graphene particles at hindering the dislocation propagation is shown in Figure 5-33(b) at $\varepsilon = 0.135$. However, the contribution of graphene particles in the plastic deformation propagation could be complicated. For example, dislocations could trigger at the edges of the graphene particles too, which could be deteriorating the strength. However, the resultant contribution of graphene particles strengthens the NiTi structure.

5.3.4 Conclusions

In the present work, we introduced a NiTi-graphene composite system in which graphene particles are spread inside the material. The molecular dynamics simulations of nanocrystalline NiTi-graphene composites with four average grain sizes of 10.5, 13.5, 23 and 27.5 nm are performed under compression loading to reveal the effect of average grain sizes and graphene reinforcements on the mechanical properties. The simulations revealed that at the average grain size of 20 nm, the nanocrystalline NiTi illustrates a maximum strength. This is due to the fact that plastic deformation mechanism transfers from a Hall-Petch regime, governed by dislocation growth inside the grains, into a reverse Hall-Petch regime, governed by atomic sliding at the grain boundaries. Our atomistic simulations were successfully able to capture this transfer in the deformation mechanisms. It is also revealed that graphene particles can effectively hinder dislocations growth and atomic sliding, fully or partially, resulting in strengthening the material system under compression.

5.4 Interaction of Graphene Particles and Shock Stress Wave in NiTi-Graphene Composite

5.4.1 Overview

In Section 4.2, the energy dissipation and the phase transformation caused by the stress wave propagation in single crystal NiTi were studied and the effects of lattice orientations on shock stress wave propagation in three different oriented single crystalline NiTi alloys were investigated. Moreover, the effect of microstructures such as grain sizes and grain boundaries on the shock stress wave propagation and phase transformation propagation in polycrystalline NiTi were studied. In addition, in order to compare the dynamic behavior of NiTi alloys with an ordinary metal like Al, a series of MD simulations were performed. The dynamic response and 1D and 3D stress wave propagations of the two material systems under shock loading were investigated. As an important achievement, the dissipated energy due to plastic deformation and phase transformation were calculated for both materials. It was discussed that, the small portion of the dissipated energy of NiTi alloys are due to plastic deformation. In this section and in order to reduce the amount of energy dissipation due to plastic deformation in NiTi alloys, we propose a new nanocrystalline NiTi-graphene composite which is capable of blocking the dislocations and plastic deformations. In the current work, the interaction of graphene particle and shock stress wave in single crystalline NiTi-graphene composites under shock wave loading are investigated through molecular dynamics method. Therefore, three different arrangements of the graphene particles are considered and added to the NiTi single crystals. The three NiTi-graphene composites are subjected to the shock loading and the results are compared to the behavior of the single crystal NiTi under shock loading.

5.4.2 Materials and Methods

A series of molecular dynamics (MD) simulations are performed to investigate the interaction of graphene particles and shock stress wave in single crystalline NiTi alloys under shock loading. In order to define the interaction between Ni and Ti atoms, the many body interatomic potential, which was originally developed by Lai *et al.* [203] and subsequently improved by Zhong *et al.* [93] are used. The details of the potential function and the corresponding parameters are explained in Section 3.2.1. The interaction between C atoms is defined by CH.airebo potential and the LJ parameters of Ni-C and Ti-C atoms are considered as 0.125 eV, 2.05 Å and 0.327 eV, 2.1 Å, respectively. Therefore, in the present work the hybrid pair-style of eam and airebo potentials and

lj parameters along with Large-scale atomic/molecular massively parallel simulator (LAMMPS) [167] are utilized for performing the simulations, and Ovito [168] visualization tool is used for post-processing the results of MD simulations. The 3D computational cells, periodic in x and y directions with the average size of $500 \times 500 \times 500$ Å and three different arrangements of graphene particles are considered. Hence, two sets of MD simulations are performed. One set of simulations includes the three single crystalline NiTi structures and the second set contains the three single crystalline NiTi-graphene composites. The corresponding results will be discussed in details in the next section.

5.4.3 Results and Discussions

As mentioned in the previous section, one NiTi single crystal and three different configurations of NiTi single crystal reinforced with graphene particles are modelled. Figure 5-34 shows the above mentioned configurations, as well as shock stress loading applied on the material systems. The pure NiTi structure is shown in Figure 5-34(a), and the NiTi-graphene arrangement A, which has five layers of single graphene particles in the middle of the NiTi structure, is shown in Figure 5-34(b). The NiTi-graphene arrangement B, which has 5 layers of 3 by 3 graphene particles perpendicular to the loading direction, is illustrated in Figure 5-34(c), and NiTi-graphene arrangement C, which has 5 layers of 3 by 3 graphene particles parallel to the loading direction, is shown in Figure 5-34(d). The loading condition is such that a linear force is applied the middle section of the models for 3 ps and then the force is suddenly removed, applying an unloading shock wave to the systems. This loading condition is similar to [224] and the purpose of different NiTi-graphene configurations is to investigate the effect of graphene on the different aspects of shock load propagation through NiTi pseudoelastic material, as well as the stress distribution, phase transformation and plastic deformation.

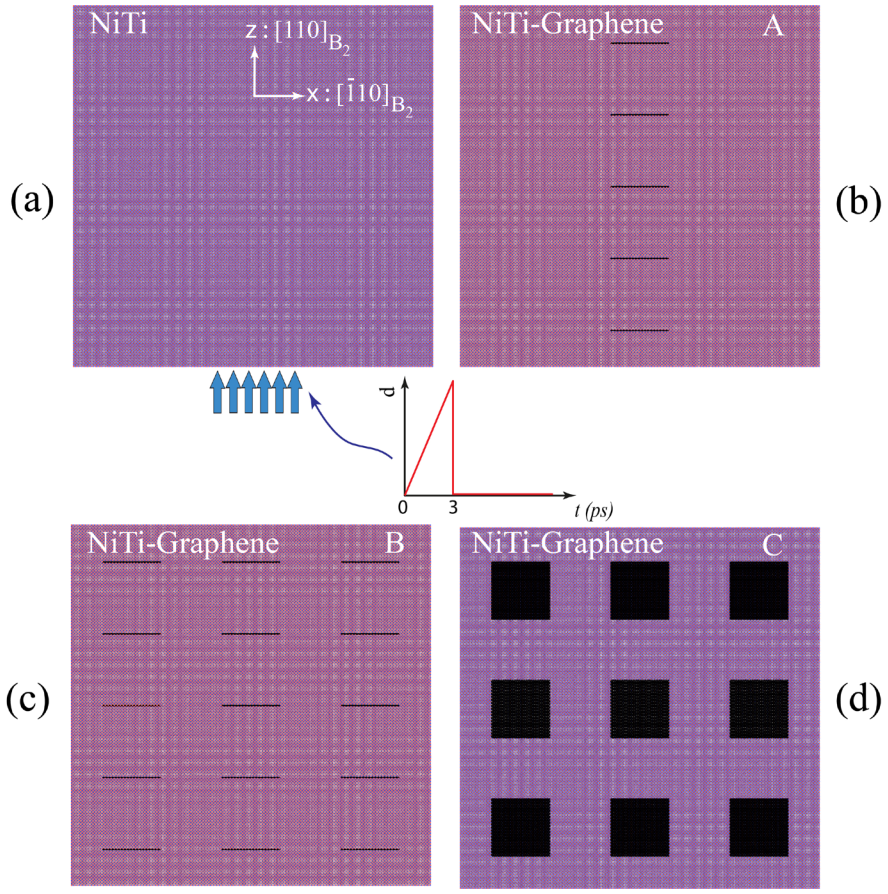

Figure 5-34. (a) Schematic of NiTi single crystal under shock wave loading. (b) NiTi-Graphene structure with graphene arrangement A. five layers of graphene particles are added to the NiTi alloy on at the center of the crystal structure. (b) NiTi-Graphene system with graphene arrangement B. Fifteen graphene particles are on x-z plane and this arrangement are repeated two more times on y direction. (c) NiTi-Graphene system with graphene arrangement C. nine graphene particles on x-z plane and this arrangement is repeated four more times on y direction.

Figure 5-35 illustrates the compressive normal stress propagation over time, along the loading direction across a middle cylinder (with radius 5 nm) for the simulated material systems. Figure 5-35(a-d) respectively corresponds to the pure NiTi, NiTi-graphene arrangement A, NiTi-graphene arrangement B, NiTi-graphene arrangement C. The general behavior of normal stress propagation in a single crystal NiTi is well-explained in [224]. As discussed, a shock wave loading in NiTi produces two distinct peaks propagating at different speeds. As shown in Figure 5-35(a), the right peak which travels faster is the elastic wave and the left peak is the inelastic wave, i.e. a mixture of plastic deformation and phase transformation. At time between 0 and 3 ps, the loading is applied and right after t = 3 ps the load is removed and the unloading elastic wave starts to propagate. Comparing the material systems, the interference of graphene particles in the traveling waves can

be observed. For example for the NiTi system, at t = 4 ps, the elastic peak is at ~ 250 Å, while for NiTi-graphene arrangements A and B, the peak is at ~ 220 Å. The reason is that for a wave to travel that far into the NiTi-graphene systems, it should pass two graphene particles laid in front of the wave and therefore, this delays the wave propagation. In addition, the compressive elastic wave reflection from the graphene particles produces a tensile elastic wave traveling backwards. This tensile elastic wave neutralizes the inelastic wave to some extent. This is the reason that the phase transformation wave fronts in NiTi-graphene A and B have lower peaks than in the pure NiTi system. Interestingly, the elastic wave speed in the NiTi-graphene arrangement C is same as in the NiTi system. This is due to the specific arrangement of graphene particles where no graphene particles are laying perpendicular to the loading direction. An interesting observation in the normal stress distribution of NiTi-graphene C system is that the peaks are not as distinctive as the other systems. This could be due to fact that the nature of the wave propagation is in 3D and the graphene particles parallel to the loading direction reflect the wave back into the middle section of the cell. These multiple reflections from multiple graphene sheets around the middle section smoothens the normal stress distribution curves.

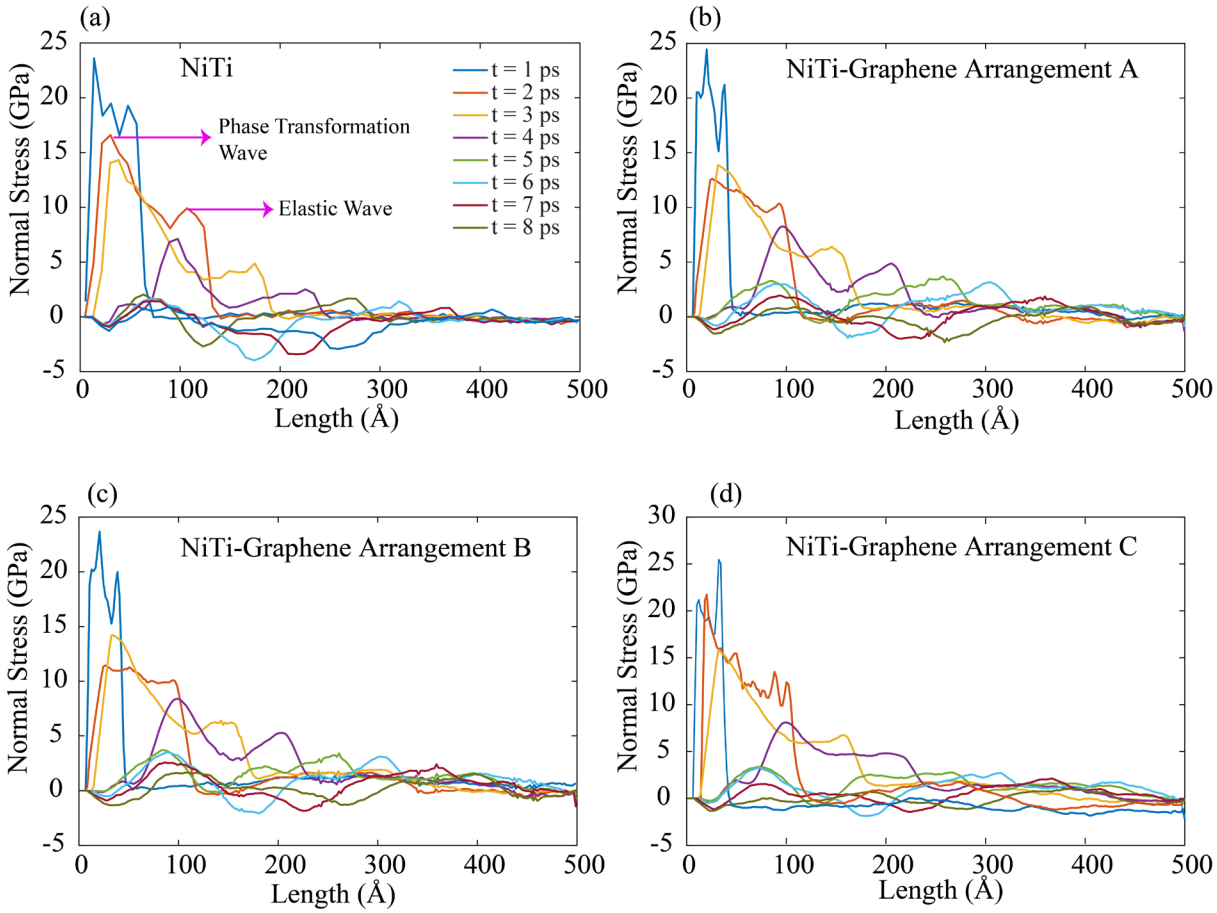

Figure 5-35. (a-d) Normal stress wave propagation during loading and propagation time for NiTi and NiTi-Graphene systems with three different arrangements of graphene.

Figure 5-36 shows 2D contour plots of normal shock stress wave propagation through the material systems. As mentioned earlier, the first 3 ps belongs to the loading portion of the simulation, and the rest belong to the unloading and wave propagation. It can be seen that for the pure NiTi system, during the loading, e.g. t = 2 ps, the wave front has traveled farther compare to the rest of the material systems. The reason is the resistance of the graphene particles against the traveling wave. During the wave propagation stage, which is t > 3 ps, peak stress is somehow accumulated at the vicinity of the graphene particles. This is due to the extra stiffness that graphene particles bring to the NiTi matrix. The existence of graphene particles has caused the stress distribution to be less uniform throughout the material, compared to the pure NiTi. This phenomenon is more evident at t = 4 ps, where the dark blue spots can be observed around the graphene particles. These high stress regions at graphene particles indicates the resistance of graphene particles against strain and deformation.

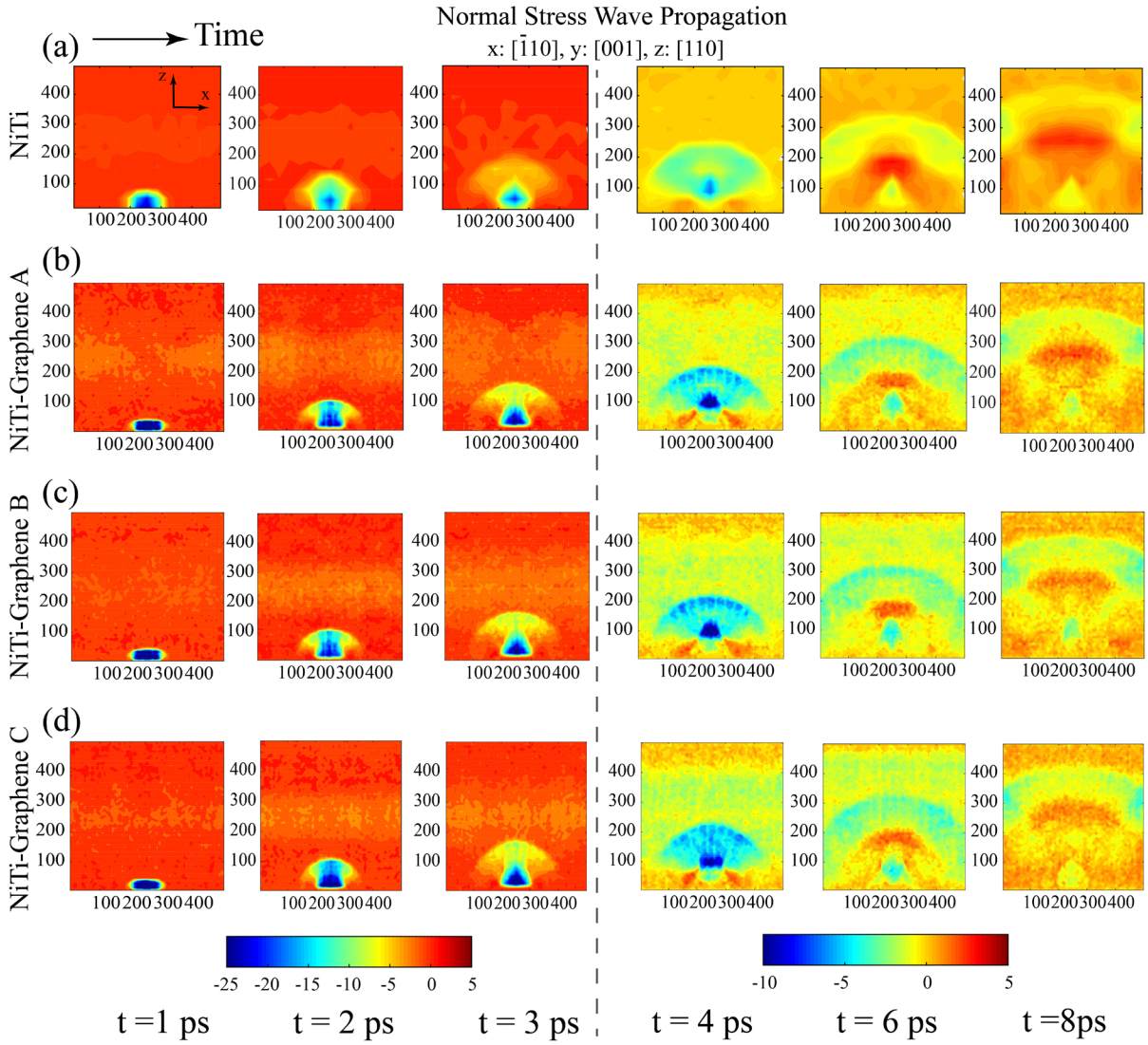

Figure 5-36. Normal stress wave propagation of NiTi single crystal and NiTi-Graphene composites for shock direction aligned with [110]. (a) Stress wave propagation in NiTi single crystal. (b) Stress wave propagation in NiTi-Graphene A. (c) Stress wave propagation in NiTi-Graphene B. (d) Stress wave propagation in NiTi-Graphene C. The stress values in color bars are in GPa.

Figure 5-37 shows the shear stress propagation through the pure NiTi as well as NiTi-graphene systems. As discussed in [224], the shear stress initiates around a circular edge, representing the edges of the piston by which the shock loading is applied. The shear stress is the driving stress for both the plastic deformation and the phase transformation. Since generally, if the shear stress along the slip planes goes beyond certain value it would plastically deform the material. Furthermore, if the shear stress, on the phase transformation preferred plane, goes beyond certain level, martensitic phase transformation occurs in an austenite NiTi. Therefore, the shear stress distribution somehow dictates the plastic deformation and phase transformation propagation distribution. Comparing the

contour plots of Figure 5-37(b-d) to Figure 5-37(a) we can see that due to the existence of graphene particles the smoothness of the stress distribution is been compromised. Although almost no difference between the stress distributions of NiTi-graphene systems of arrangement A and B (Figure 5-37(b and c)) can be observed, NiTi-graphene arrangement C has trapped the propagation of shear strain. This could be due to the special arrangement of graphene particles for this configuration where they are laid parallel to the loading direction trying to guide the wave to stay in the middle.

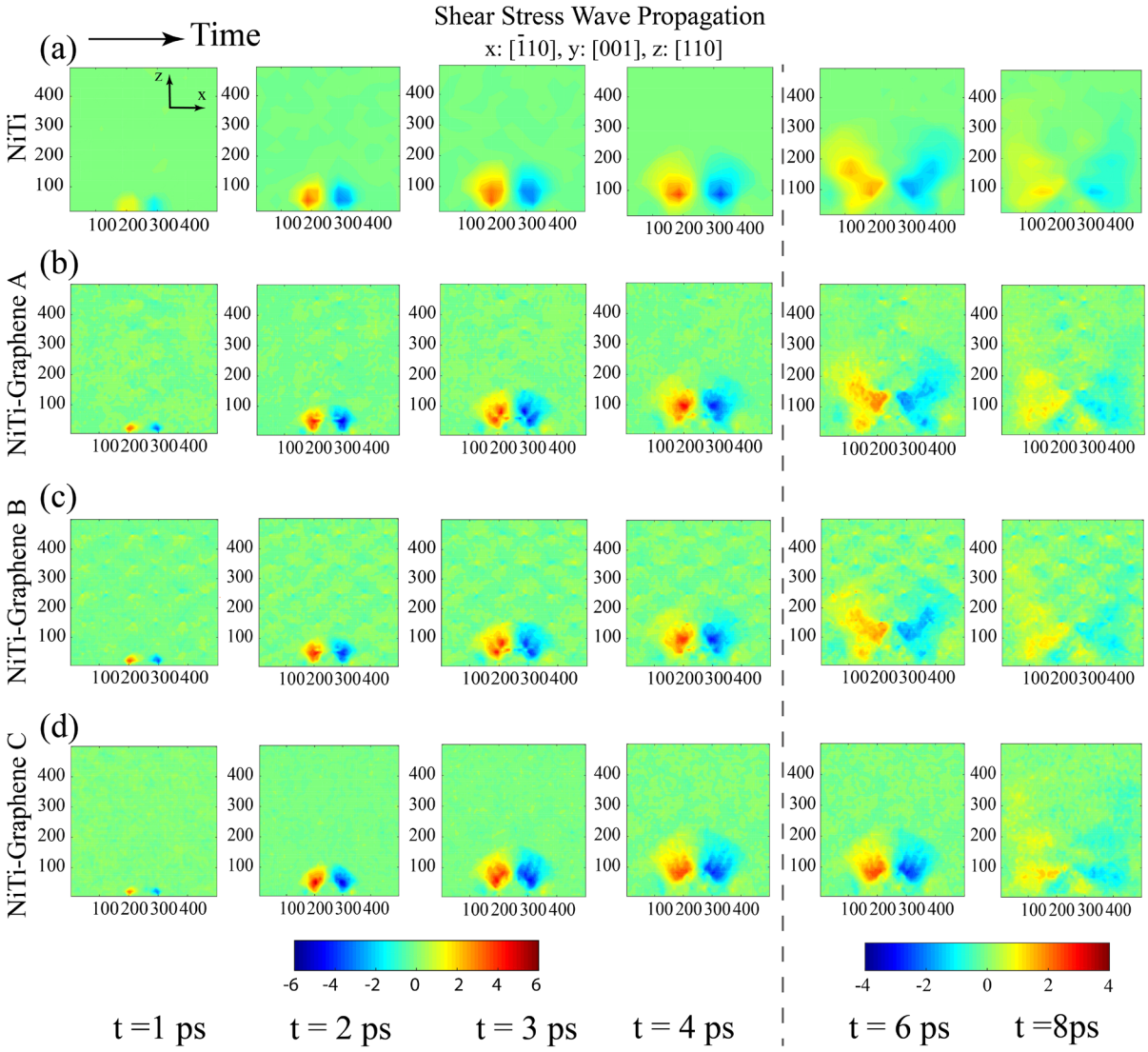

Figure 5-37. Shear stress wave propagation of NiTi single crystal and NiTi-Graphene composites for shock direction aligned with [110]. (a) Stress wave propagation in NiTi single crystal. (b) Stress wave propagation in NiTi-Graphene A. (c) Stress wave propagation in NiTi-Graphene B. (d) Stress wave propagation in NiTi-Graphene C. The stress values in color bars are in GPa.

The shear shock stress distributions of Figure 5-37 gives a preview of what to expect for deformation propagation through the material systems.

Figure 5-38(a-d) show the propagation of shear strain, presented as Von Mises shear strain parameter, inside the pure NiTi, NiTi-graphene arrangements A, B, and C, respectively. The Von Mises shear strain parameter indicates the plastic deformation and phase transformation in the NiTi systems. Comparing the contour plots of NiTi with the NiTi-graphene arrangements A and B, it can be clearly seen that graphene particles have limited the inelastic deformation travel distance inside the NiTi matrix. The deformed region in NiTi-graphene systems of A and B are smaller compared to pure NiTi deformed region. This shows the capability of the graphene particles to resist against plastic deformation. Although the distance that the plastic deformation has travelled along the z-direction is almost the same for NiTi and NiTi-graphene A and B systems, the effect of graphene particles on the wings of the deformed region is undeniable. Besides, the light blue colored regions, indicating the phase transformation, disappear faster in the graphene reinforced systems compared to the reference system. This shows that the stress level is lower in those regions allowing for reverse martensitic phase transformation. Another observation is the insignificant difference between the performances of arrangements A and B in blocking the inelastic deformations. However, the NiTi-graphene arrangement C performs differently. The graphene particles are placed parallel to the loading direction and therefore the graphene particles tend to guide the plastic deformation to stay in the middle region. For example, the left wing of the deformed region is fully recovered at t = 8 ps after it interacts with the graphene particle on the left side. Besides, along the z-direction, the middle graphene particle is loaded parallel to its plane and it resists the deformation by buckling. As a result of this deformation in the middle graphene particle, the inelastic deformation along the z-direction is almost cut in half, compared to the pure NiTi system.

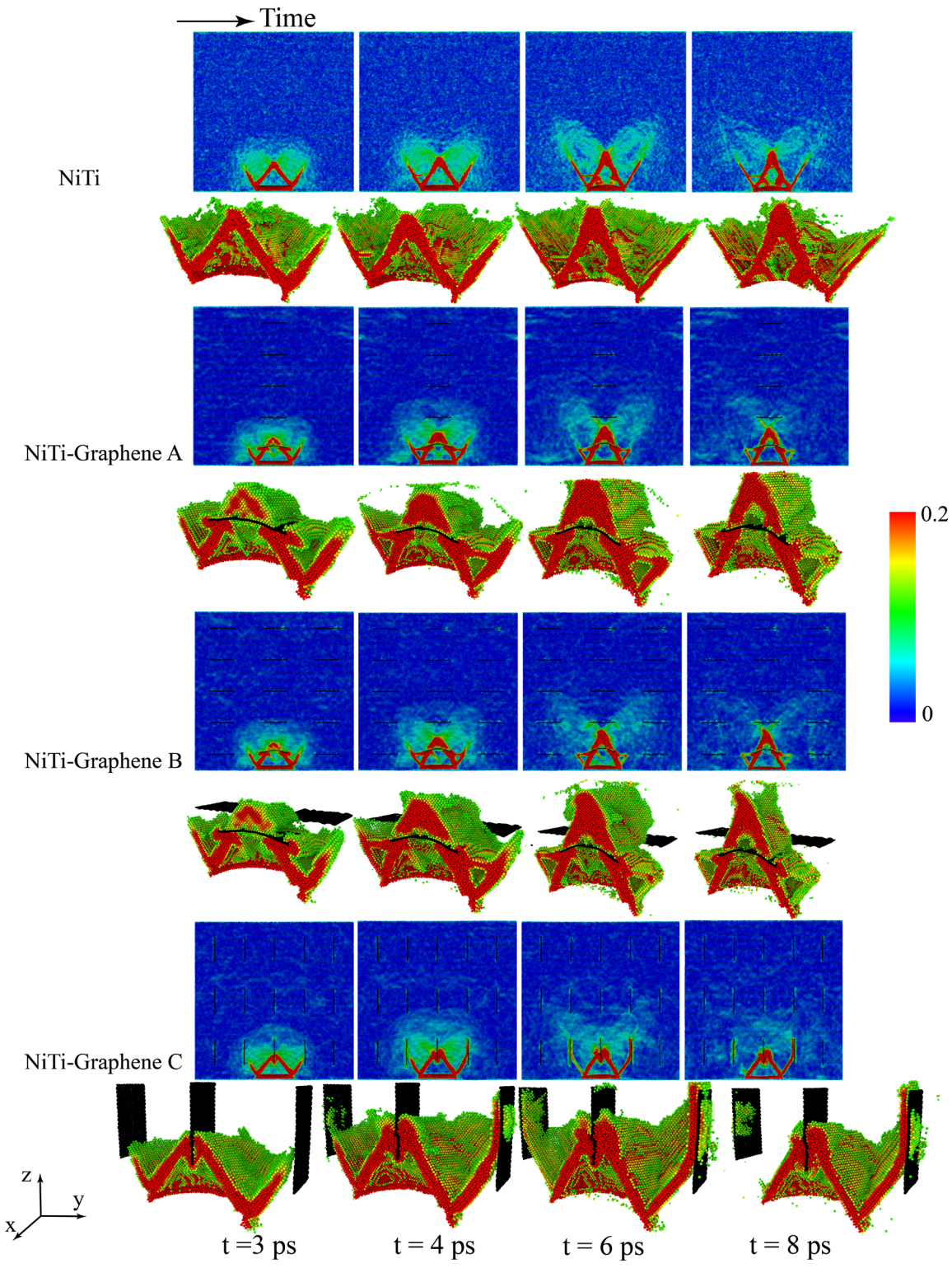

Figure 5-38. Von Mises shear strain parameter which shows plastic deformation and phase transformation propagation in NiTi and NiTi-Graphene systems during shock loading.

In conclusion to the observed performance of the graphene particle reinforcements inside the NiTi matrix, it can be seen that although the same shock stress is applied to the systems, the graphene particles absorb the shock stress energy and limit the plastic deformation into a confined region. In fact, at the early stages of the loading, they transfer the shock wave energy into internal energy, which appears as high stress at graphene particles.

Figure 5-39 shows the maximum normal and shear stress recorded in the material systems (including the graphene particles). As mentioned earlier, the maximum stress recorded in the structures belong to the graphene reinforced systems, and specifically at the graphene particles. It is worth mentioning that however the stress values at graphene particles are high, due to the outstanding strength graphene, they do not fail and help reinforcing the NiTi matrix.

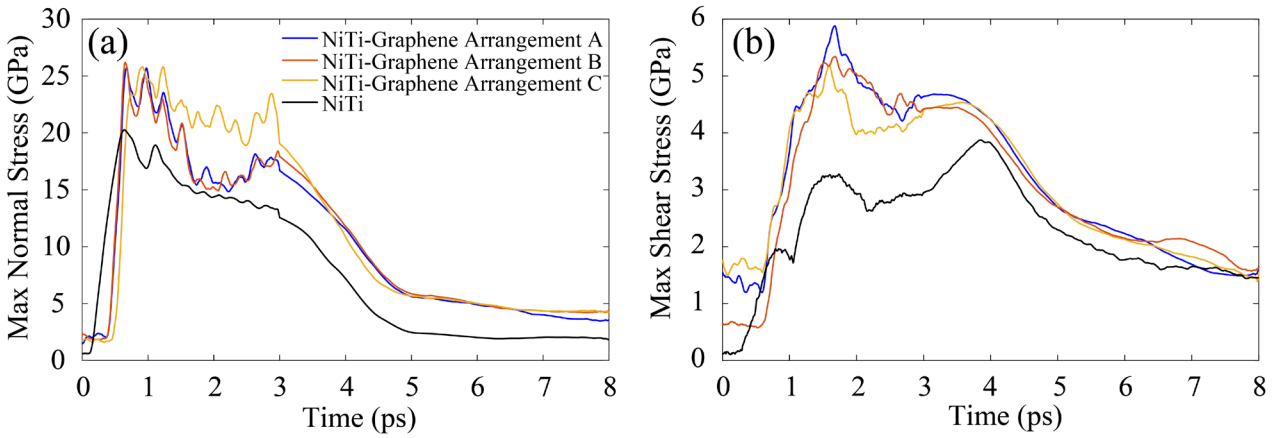

Figure 5-39. (a) Maximum of normal stress wave during loading and propagation time for NiTi and NiTi-Graphene systems. (b) Maximum of shear stress wave during loading and propagation time for NiTi and NiTi-Graphene systems.

5.4.4 Conclusions

In this work, one NiTi single crystal and three different configurations of single crystalline NiTi-graphene composites are modelled. The three configurations of NiTi-graphene composites are: A, which has five layers of single graphene particles in the middle of the NiTi structure, B, which contains 5 layers of 3 by 3 graphene particles perpendicular to the loading direction, and C, which has 5 layers of 3 by 3 graphene particles parallel to the loading direction. The results of MD simulations show that graphene particles have restricted the inelastic deformation inside the NiTi matrix. The plastically deformed region in NiTi-graphene systems of A and B are smaller compared to pure NiTi. This shows the capability of the graphene particles to limit the plastic deformation propagation. In addition, in the NiTi-graphene arrangement C, where the graphene

particles are placed parallel to the loading direction, the graphene particles tend to guide the plastic deformation to stay in the middle region. Although the same shock stress is applied to the four different systems, the graphene particles absorb the shock stress energy and limit the plastic deformation into a confined region.

Chapter 6. NiTi-Nb Composite as a Superelastic and High Hysteresis Material

6.1 Overview

As mentioned previously, NiTi shape memory alloys have received increasing attention in the recent years, due to their two unique properties, shape memory effect and superelasticity. Also, it has been discovered that NiTi alloys possess a high damping capability due to the martensitic phase transformation or twinning-detwinning transformation, which make these alloys a superior candidate for using as damping materials in different engineering fields. But possessing low yield strength is a problem associated with NiTi alloys which can limit their applications. Therefore, it becomes an urgent task to develop a new NiTi based alloy which has both a high yield strength and a high damping capacity appropriate for working in different mechanical and thermal loading conditions. In this study, it is shown that Nb is a superior candidate to make a NiTi based composite due to the compatibility between its microstructure and NiTi's [163, 164] . In addition, it is illustrated that NiTi-Nb is a perfect composite with a high damping capability and yield strength. In this regard, NiTi-Nb composite is investigated at the atomistic scale using molecular dynamics methods for the first time.

6.2 Materials and Methods

A series of molecular dynamics simulations are performed for three different periodic computational cells with the average size of 600×600×500 Å to simulate the NiTi, Nb and NiTi-Nb single crystalline structures. The orientation of the single crystal structures is: x: $[1\bar{1}0]$, y: $[110]$ and z: $[001]$. In order to define the interaction between Ni, Ti and Nb atoms, an accurate EAM potential is developed by MultiSMArt group. This potential is built by combining these two potentials: NiTi potential by [165] and NiTiNb potential by [266]. This EAM potential along with large-scale atomic/molecular massively parallel simulator (LAMMPS) [167] are utilized for performing the simulations, and Ovito [168] visualization tool is used for post-processing the results of MD simulations. In order to investigate the superelasticity and the shape memory effect of NiTi-Nb composite (25% Nb and 75%NiTi), two different loading conditions are considered. After creating the single crystalline structures, the structural energy is minimized using conjugate gradient method. Then, in the composite structure with austenitic NiTi, thermal equilibrium is applied to the system using time integration on Nose-Hoover style non-Hamiltonian equations of

motion in isothermal-isobaric (npt) ensembles to set the temperature at T = 350 K. After the equilibrium, the structure is loaded (under tension) and unloaded at 6×10^{-4} 1/s strain rate. While in the NiTi-Nb composite with the martensitic NiTi alloy, after applying the same thermal equilibrium, the temperature of the system is set at T = 500 K, then the structure is cooled down and the temperature is set at T=100 K. In the next step, the structure is loaded (under tension) and unloaded at 6×10^{-4} 1/s strain rate and finally, the structure is heated up to T=500 K. the results of the MD simulations for NiTi, Nb and NiTi-Nb composite are shown and discussed in the following sections.

6.3 Results and Discussions

6.3.1 Superelastic NiTi-Nb composite

As mentioned in the previous section, for the first step of the study, a series of MD simulations are performed to evaluate the behavior of pure superelastic NiTi, pure Nb, and NiTi/Nb composites under tension loading. Figure 6-1 shows the stress-strain behavior of the material systems under tension loading. It can be seen that Nb shows an initial linear behavior before strains around 0.05 and then starts to deviate from linearity, which is due to the start of local plastic deformations. On the other hand, NiTi behaves differently. After the initial linear response, which corresponds to the elastic deformation of austenite NiTi, the NiTi starts to undergo martensitic phase transformation locally starting at the strain around 0.015 up to the point where it is fully transformed to martensite NiTi. The plateau in the middle the stress-strain curve is the indicator of phase transformation region. The NiTi-Nb composite system however, shows a mixture of the pure NiTi and the pure Nb responses. The initial response of the composite system is linear with a stiffness between austenite NiTi and Nb. This response stays almost linear up to the strain of around 0.02. As the strain increases the stress-strain response shows a plateau, indicating the appearance of phase transformations in the NiTi. The high stiffness of Nb is responsible for delaying the start of martensitic phase transformation. The slope of the stress-strain curve starts to increase at higher strain levels, indicating that the martensite NiTi shares the major portion of NiTi content of the composite.

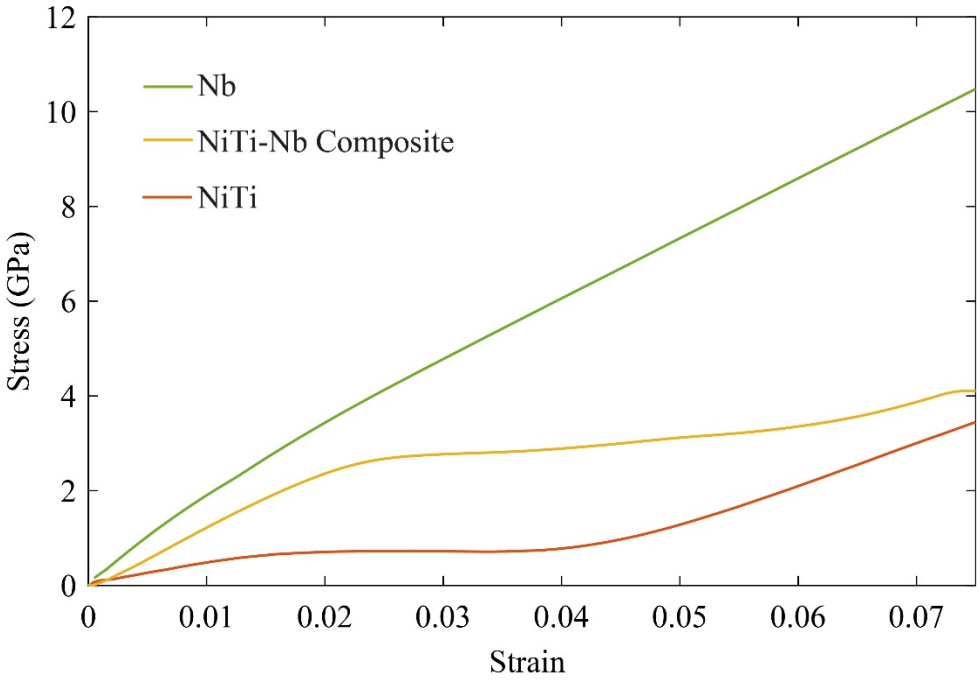

Figure 6-1. Stress-strain behavior of Nb, NiTi and NiTi-Nb composites under tension loading.

The extraordinary behavior of NiTi-Nb composite is revealed when the load is removed from the material system. Figure 6-2 shows the stress-strain behavior of pure austenite NiTi, pure Nb, and austenite NiTi-Nb composite material systems under a full loading-unloading cycle, up to 0.075 strain. The NiTi fully recovers from the applied strain, illustrating a hysteresis loop showing the absorbed energy due to forward and reverse martensitic phase transformations. The pure Nb however cannot recover from the applied strain. In fact, around 0.03 permanent plastic strain resides in Nb while stress goes back to zero. However, the austenite NiTi-Nb composite system recovers fully from 0.75 strain, showing a pseudoelastic behavior with a large hysteresis loop. This behavior was observed experimentally in [163, 164]. The mechanism behind this phenomenon is that NiTi matrix starts to undergo martensitic phase transformation and when the phase transformation Leuder bands reach the vicinity of Nb, the lattice strain in Nb increases significantly above the average applied strain [164]. Although this strain is well beyond the elastic strain capacity of Nb, after unloading when the martensitic phase transformation is reversed, this strain recovers and no permanent deformation remains in Nb. In other words, Nb shows a superelastic behavior when it is laminated in between the NiTi matrix. As a result of this mechanism, the NiTi-Nb composite represents a superelastic material system with a large hysteresis loop.

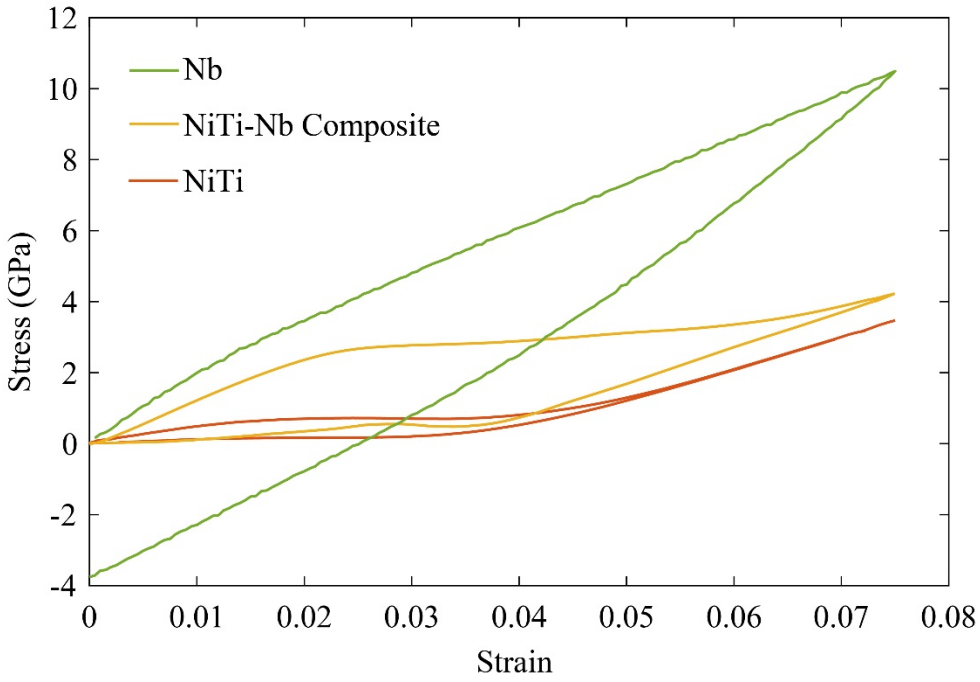

Figure 6-2. Stress-strain hysteresis behavior of Nb, NiTi and NiTi-Nb composite.

6.3.2 Shape memory NiTi-Nb composites

The next series of simulations investigates the behavior of shape memory NiTi-Nb composites under a full mechanical and thermal cycle. Figure 6-3 shows the stress-strain response of pure shape memory NiTi and NiTi-Nb material systems. As mentioned in the methods section, the material systems are initially stabilized at 500 K to make sure that the NiTi structure is fully austenitic. Then, the temperature is dropped down to 100 K, which is well below the martensite finish temperature to establish a fully shape memory NiTi in both the pure NiTi and NiTi-Nb composite material systems. Afterwards, the material systems are loaded in tension up to the strain of 0.075 and subsequently, unloaded to a stress free state. As the final step in the simulations, the temperature is again raised to 500 K. Figure 6-3 shows the mechanical response of the systems to illustrate their hysteresis loops. As shown in the figure, the pure NiTi shows an initially linear response, which corresponds to a pure elastic deformation of twinned martensite, up to the strain around 0.007 where the material system locally undergoes reorientation of martensitic structure, i.e. detwinning. During the formation of detwinned martensite, the stress value remains almost constant up to the point that NiTi structure is saturated by detwinned structure. Beyond this point,

the stress increases showing the elastic response of detwinned martensite. During the unloading step however, NiTi remains in the detwinned martensite phase. This is the reason that the unloading portion is almost completely linear and the material has a residual strain at the stress free state. In order to bring the material to the original shape, the structure is heated up to the austenite finish temperature and as a result, the residual strain disappears and the hysteresis loop almost closes. Similar behavior is observed in the stress-strain curve of NiTi-Nb composite material system. The high stiffness of Nb however, delays the start of detwinning process and heightens the stress level of the material system. As a result of this effect, the hysteresis loop of NiTi-Nb is significantly larger than pure NiTi.

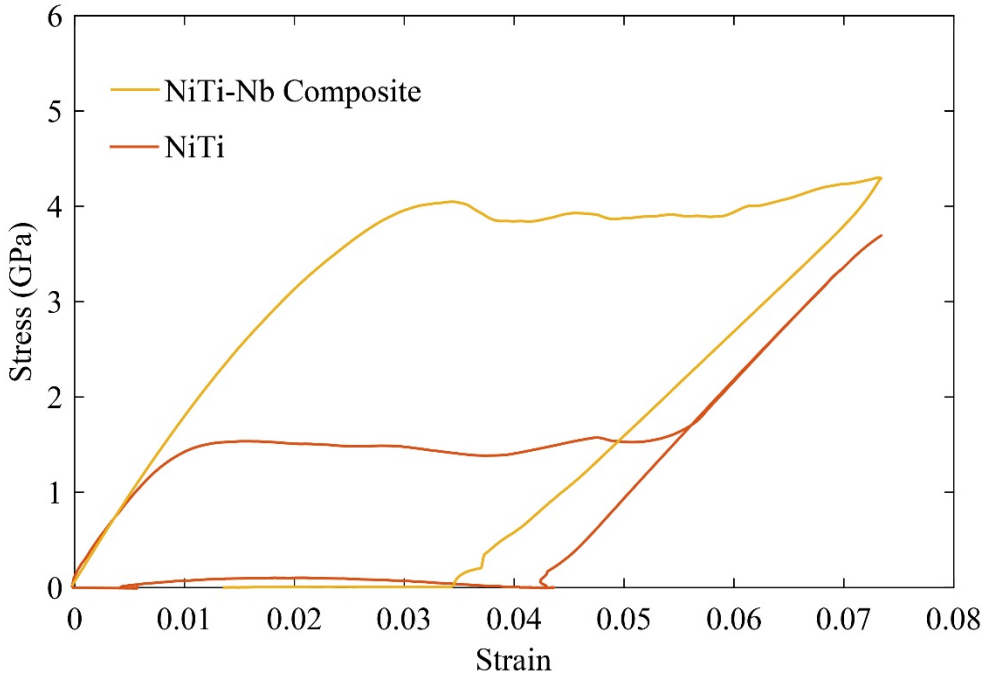

Figure 6-3. Shape memory effect of NiTi and NiTi-Nb composites.

Figure 6-4 shows the temperature-stress-strain response of the NiTi-Nb system under thermal and mechanical loading. The consecutive steps at the simulation are shown as points A to F, respectively. The shear strain conditions of the material system at different loading steps are shown in the contour plots of Figure 6-4. The material system is stabilized at a stress free condition at 500 K, represented as point A. In this temperature, the NiTi is at austenite phase. The arrangement of Ni and Ti atoms confirms the material phase to be austenite. The temperature drop to 100 K causes the NiTi to show a martensitic phase transformation. Twinned martensite can be observed in the

NiTi structure of point B. Closely located twin boundaries shows the twinned martensite structure. The material is loaded in tension afterwards, to reach to the point C where detwinned martensite starts to form locally. At point D, the NiTi is almost saturated with detwinned martensite. Comparing the magnified image of point D to the one of point B confirms the reorientation of martensite NiTi to decrease the number of twin boundaries. One important material structure change in point D is the appearance of plastic deformation in the form of dislocation propagation inside the NiTi structure, shown as the high shear stress lines which are red areas in the contour plot. The material structure in point E is basically same as in point D, except some elastic strain is recovered. The material structure after heating, shown as point F is transferred back to austenite. However, the strain is not fully back to zero because of permanent plastic deformations happened during the mechanical loading. The magnified image of point F shows how NiTi crystalline structure is defected. The purple atoms of Ni are arranged along the arrow, but two atoms are replaced by the pink atoms of Ti representing dislocation inside the NiTi material system.

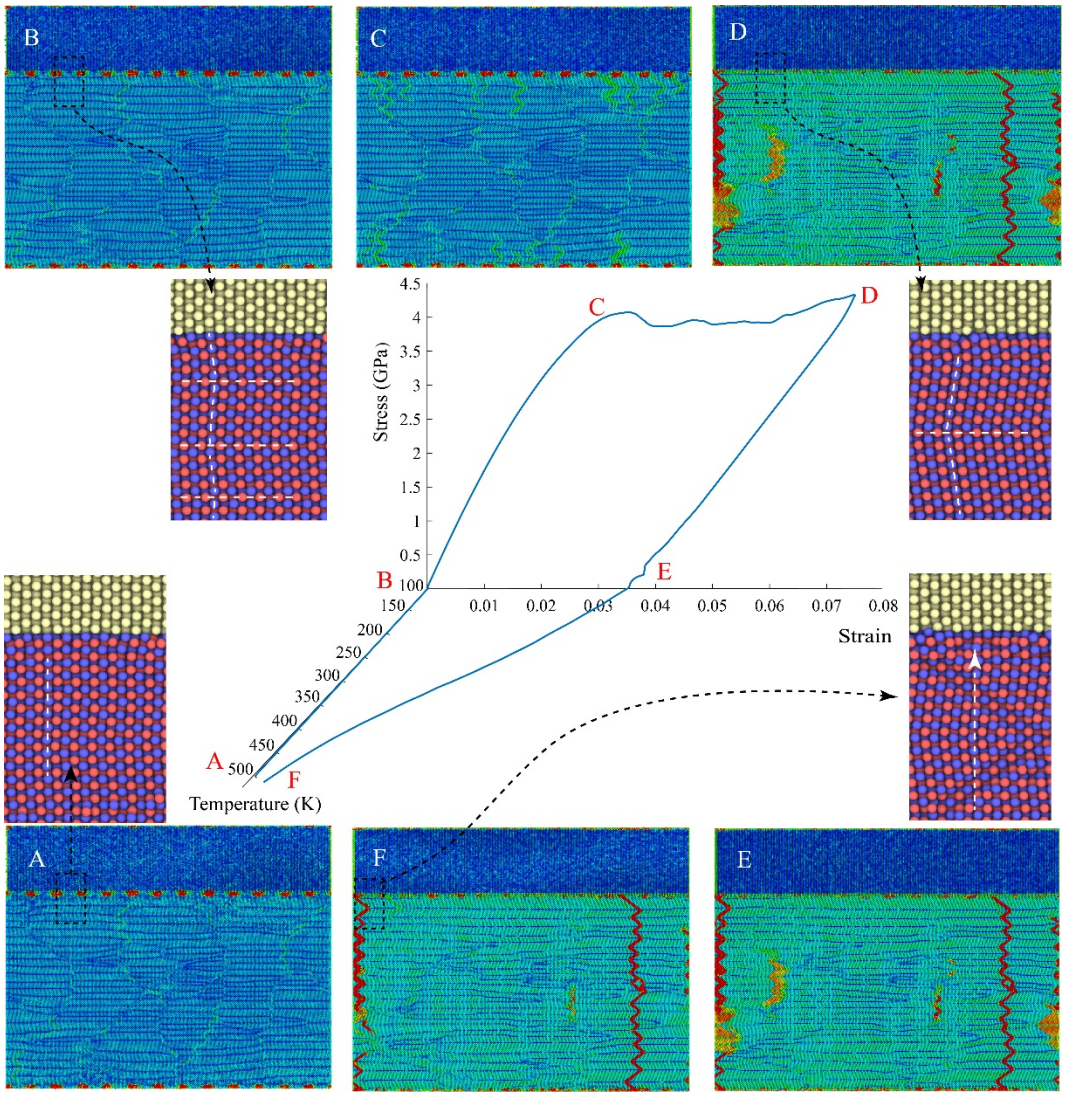

Figure 6-4. Stress-strain-temperature behavior of NiTi-Nb composites.

6.4 Conclusions

In this study, NiTi-Nb composite material systems are simulated using molecular dynamics, in order to investigate their mechanical response at the atomistic level. The first series of simulations investigates the response of superelastic NiTi-Nb composite system in comparison to the pure superelastic NiTi and pure Nb. The material systems underwent a cycle of loading/unloading up to the strain of 0.075. The pure Nb showed a high tensile modulus, but after unloading, a large permanent plastic strain remained in the Nb structure. Pure NiTi structure however underwent a full forward and inverse martensitic phase transformation cycle and the strain was fully recovered. Superelastic NiTi-Nb composite material system on the other hand, not only recovered from the

high applied strain of 0.075, but also showed a very large hysteresis loop, multiple times of the pure superelastic NiTi's. The shape memory NiTi-Nb was also studies in the next set of the MD simulations. Comparing the response of pure shape memory NiTi to the shape memory NiTi-Nb composite response, it was revealed that the composite system shows a similar behavior as the pure NiTi in addition to a very large hysteresis loop. However, slight plastic deformations were observed in the NiTi matrix.

In conclusion, for both the superelastic and the shape memory regimes of the NiTi matrix, the existence of Nb as a reinforcement enables the material system to show a very high hysteresis response with the capability of recovering large deformations. This outstanding performance of this material system makes it a great candidate for vibration attenuation and energy dissipations applications.

Chapter 7. Conclusions and Contributions

7.1 Conclusions

In chapter 2, molecular dynamics (MD) simulations and density functional theory (DFT) calculations were utilized to investigate the energy and structure of symmetric and asymmetric tilt grain boundaries (GBs) in austenite NiTi shape memory alloys. The grain boundaries excess energies were calculated as a function of the inclination and misorientation angles. The structural units at the grain boundary were identified and the correlation between the structure and grain boundary energy was studied. It was shown that the Read-Shokley model can predict the energy of low angle tilt grain boundaries in NiTi with an acceptable accuracy by considering appropriate dislocation core radii at different orientations. Two representative symmetric GBs were studied by DFT calculations. The MD results were validated against DFT, and the electron charge density distribution at the grain boundaries were compared with the bulk material to study the bonding strengths at the grain boundaries.

In chapter 3, MD simulations were utilized to study the defects in austenite NiTi alloys. Three different potentials, two EAM with different cutoff radii and one 2NN MEAM, were selected and the accuracy of each potential was investigated by studying the stacking fault energies, and also the energy, structure and stress distribution of edge dislocation in austenite NiTi. A high-energy dislocation was also considered and the dislocation dissociation was modeled with the MD simulations. In each case, the results of each potential were compared against the elasticity theory and the density functional theory calculations at the atomistic level. Our results shed light into some unknown aspects of defects in austenite NiTi, which will benefit studying the origins of unrecoverable strains accumulated in NiTi during cyclic loading, and also help us better understand the grain boundaries in SMAs. Through our results, it was shown that although none of the selected potentials were particularly trained for studying defects in NiTi, they were accurate in predicting defect-related properties, although for some properties, one of the potentials might be preferred and more precise compared to the others.

In the first section of chapter 4, the unique property of SMAs in dissipating the energy of shock loadings was investigated using complementary experimental and computational frameworks. An experimental setup was designed and implemented for generating spark-generated collapsing

bubbles near a plate surface under water and producing a water jet; where the jet leaded to a shock loading applied to the geometric center of the plate. Two different composite plates were considered in the experiments; one made by bonding a NiTi thin layer to an aluminum plate and another one with bonding an aluminum thin layer, with the same length, width and thickness, to a separate but identical aluminum plate. These two composites were subjected to almost identical cavitation-induced shock loads and their responses were compared. The effects of energy dissipation through the phase transformation in NiTi-bonded plate on damping the transverse deflections and in-plane strains were investigated. A high-speed camera, a hydrophone, a laser Doppler vibrometer and multiple strain gauges were used to characterize the generated bubbles and the mechanical response of plates. The experimental results clearly showed that the NiTi coating layer, even for the thickness of the order of one-tenth of the base structure, can effectively damp the stress shock waves in the structure. Using a set of finite element computational simulations, it is shown that if the incident shock wave is strong enough to cause global vibrations in the structure, the phase transformations originated from the deflections of the structure can also contribute to the energy dissipation and damp the response of the structure. The results provide us a better fundamental understanding about the observed excellent erosion resistance of NiTi alloys and the efficiency of using a thin layer coating of NiTi on various structures to improve their cavitation resistance in different applications.

In this second section of chapter 4, the energy dissipation and the phase transformation caused by the stress wave propagation in single crystal and polycrystalline austenite NiTi alloys under shock wave loadings were investigated. MD simulations were utilized as a superior method to study the effect of microstructures such as lattice orientations, grain sizes and grain boundaries on the patterns of stress wave and phase transformation initiation and propagation at the atomistic level in NiTi alloys. A criterion based on equivalent shear strains was used to detect the inelastic deformation in the NiTi structures. This parameter was used to detect the regions with martensitic phase transformation and plastic deformation. Regions with phase transformation and plastic deformation in the structures were distinguished by implementing two proposed methods. It is expected to observe the dissipated energy in NiTi structures being caused by both phase transformation and plastic deformation.

In the last section of chapter 4, MD simulations were utilized to study the behavior of pseudoelastic NiTi under shockwave stress loading conditions in comparison to aluminum. At the first set of simulations, nanopillars of austenite NiTi as well as Al were modeled to study one dimensional (1-D) shock wave propagation through the two different material systems. The wave propagation and deformation mechanisms were observed to be very different in NiTi and Al. Plastic deformation and forward and reverse martensitic phase transformation were observed along the NiTi nanopillar contributing to energy dissipation, while obviously, the only energy dissipating mechanism was plastic deformation in Al pillars. The plastically deformed region in NiTi was the region close to the loading area, while in Al, the plastic deformation was propagated though the pillar. Besides, the peak stress in NiTi damped more quickly in NiTi pillar compared to in Al, revealing the capability of NiTi in shock wave energy attenuation. The energy dissipation through phase transformation and plastic deformation were calculated and it was revealed that phase transformation mechanism dissipated larger portion of shock wave energy compared to plastic deformation. In fact, the plastic deformation happens at the initial few picoseconds of the simulation, and consecutive forward and reverse martensitic phase transformations are responsible for the energy dissipation for the rest of the simulation duration. Three dimensional (3-D) shock stress wave propagation was also studied, through MD simulations of NiTi and Al bulk material systems. Same energy damping behaviors as observed in pillars were observed in bulk material systems. 3-D nature of shock wave propagation was observed in both NiTi and Al systems where normal and shear stress propagation patterns were captured. It was observed that shear stress propagation pattern dictates the deformation patterns both for plastic deformation, in NiTi and Al, and phase transformation in NiTi system. The main difference between the deformation mechanisms in the two material systems was the reversibility of deformation in NiTi, for most of the deformed regions, as a result of reverse martensitic phase transformations. Comparing this behavior to the aluminum's, results in a conclusion that NiTi is capable of dissipation large amount of shock wave energy and minimize the permanently deformed regions resulting in maintaining the shape very close to the original structure.

In the first section of chapter 5, the effect of lateral pressure on the shear strength of polymer coated carbon nanotubes (CNTs) is studied. Our MD simulations shed light into the deformation mechanisms in both the polymer chains and CNTs, and reveal the complex correlation between the shear strength and the lateral pressure on each CNT. It has been shown that while increasing

the lateral pressure enhances the shear strength between CNTs due to increasing the contact area between the polymers and nanotubes, there is a specific lateral pressure at which increasing the lateral pressure above that value will weaken the shear strength. This loss in the shear strength was shown to be interconnected with the local deformations of CNTs at the atomistic scale. A bottom-up bridging methodology was developed to train the mesoscale model using the MD simulations, while the atomistic scales local deformations in the polymer chains and CNT cross-sections were also transferred into the larger scale by adjusting the vdW interactions in the CG model as a function of the applied lateral pressure to each CNT. This bottom-up multiscale approach was used to study the effect of lateral pressure on the shear strength of straight polymer coated CNT bundles in the presence of a lateral pressure on the bundle. The framework was also implemented to investigate how twisting a CNT yarn can affect the pull-out force of a bundle from a spun yarn, offering new avenues for materials design.

In the second section of chapter 5, we introduced a new nickel-graphene nanolayered composite system in which instead of reinforcing large individual graphene sheets in the interlayer area, monolayer graphene flakes are spread inside the interlayers. In this composite only a fraction of the interlayer area (13%-30%) is covered. This graphene-metal nanolayered composite system is relatively easy and cost-effective to fabricate in large scales. At the first steps of this study, a systematic investigation on the effect of various graphene reinforcement configurations on the nickel-graphene systems performance was performed by utilizing a series of atomistic simulations. The molecular dynamics simulations of various nanocrystalline nickel-graphene systems were performed, for the first time, for a polycrystalline system under both compression and nanoindentation loadings to reveal the effects of metal average grain size, simulation cell size, graphene reinforcements' configuration, and loading rate. It was revealed that at a certain average grain size range (~12 nm) the nanocrystalline nickel illustrates a maximum strength. This is due to the fact that plastic deformation mechanism transfers from a Hall-Petch regime, governed by dislocation growth inside the grains, into a reverse Hall-Petch regime, governed by atomic sliding at the grain boundaries. Our atomistic simulations were successfully able to capture this transfer in the deformation mechanisms. It is also revealed that graphene full sheets and particles can effectively hinder dislocations growth and atomic sliding, fully or partially, resulting in strengthening the material system under compression. However, when graphene particles were randomly oriented inside the polycrystalline nickel, no meaningful change in the strength was

observed. Moreover, the molecular dynamics simulations of nanoindentation loadings confirmed the role of graphene particle interlayers in hardening of material system via hindering the dislocation growth through the metal grains. Inspired by the results of the atomistic simulations, the best applicable nickel-graphene nanolayered systems (with an average grain size of 18.3 nm which is very close to the optimum grain size corresponding to the maximum strength of nickel polycrystals) were identified and fabricated. The fabricated nickel-graphene nanolayered composites were mechanically characterized with nanoindentation experiments to quantify their hardness. The experimental results showed that a nickel graphene nanolayered system, with only 14% areal coverage of graphene particles at the interlayer, has improved the hardness of the nanocrystalline nickel by almost 40%. As the result of this investigation, it was confirmed that the introduced material system benefits from both the nanocrystallinity of the metal as well as the strengthening effects of the graphene interlayers.

In the third section of chapter 5, we introduced a NiTi-graphene composite system in which graphene particles are spread inside the material between the layers of NiTi matrix. The molecular dynamics simulations of nanocrystalline NiTi-graphene composites with four average grain sizes of 10.5, 13.5, 23 and 27.5 nm were performed under compression loading to reveal the effect of average grain sizes and graphene reinforcements on the mechanical properties. The simulations revealed that at the certain average grain size (~ 20 nm), the nanocrystalline NiTi illustrates a maximum strength. This is due to the fact that plastic deformation mechanism transfers from a Hall-Petch regime, governed by dislocation growth inside the grains, into a reverse Hall-Petch regime, governed by atomic sliding at the grain boundaries. Our atomistic simulations were successfully able to capture this transfer in the deformation mechanisms. It was also revealed that graphene particles can effectively hinder dislocations growth and atomic sliding, fully or partially, resulting in strengthening the material system under compression.

In the last section of chapter 5, one NiTi single crystal and three different configurations of single crystalline NiTi-graphene composites were modelled and examined under shock stress wave loading. The three configurations of NiTi-graphene composites were: A, which had five layers of single graphene particles in the middle of the NiTi structure, B, which contained 5 layers of 3 by 3 graphene particles perpendicular to the loading direction, and C, which had 5 layers of 3 by 3 graphene particles parallel to the loading direction. The results of MD simulations showed that

graphene particles have restricted the inelastic deformation inside the NiTi matrix. The plastically deformed region in NiTi-graphene systems of A and B were smaller compared to pure NiTi. This showed the capability of the graphene particles to limit the plastic deformation propagation. In addition, in the NiTi-graphene arrangement C, where the graphene particles were placed parallel to the loading direction, the graphene particles tend to guide the plastic deformation to stay in the middle region. Although the same shock stress is applied to the four different systems, the graphene particles absorb the shock stress energy and limit the plastic deformation into a confined region.

In the last chapter, NiTi-Nb composite material systems were simulated using molecular dynamics, in order to investigate their mechanical response at the atomistic level. The first series of simulations investigated the response of superelastic NiTi-Nb composite system in comparison to the pure superelastic NiTi and pure Nb. The material systems underwent a cycle of loading/unloading up to the strain of 0.075. The pure Nb showed a high tensile modulus, but after unloading, a large permanent plastic strain remained in the Nb structure. Pure NiTi structure however underwent a full forward and inverse martensitic phase transformation cycle and the strain was fully recovered. Superelastic NiTi-Nb composite material system on the other hand, not only recovered from the high applied strain of 0.075, but also showed a very large hysteresis loop, multiple times larger than the pure superelastic NiTi's. The shape memory NiTi-Nb was also studied in another set of MD simulations. Comparing the response of the pure shape memory NiTi to the shape memory NiTi-Nb composite response, it was revealed that the composite system shows a similar behavior as the pure NiTi in addition to a very large hysteresis loop. However, slight plastic deformations were observed in the NiTi matrix. In conclusion, for both the superelastic and the shape memory regimes of the NiTi matrix, the existence of Nb as a reinforcement enables the material system to show a very high hysteresis response with the capability of recovering large deformations. This outstanding performance of this material system makes it a great candidate for vibration attenuation and energy dissipations applications.

7.2 Contributions

The main contributions of this dissertation can be summarized as:

- The microstructure and energy of the grain boundaries in NiTi SMAs is studied for the first time,
- Defects in the NiTi crystalline structure are investigated. Deformation mechanisms in presence of dislocations and the stacking fault energies are studied in these alloys.
- The performance of NiTi under shock wave loading and vibrations, their vibrations attenuation and energy dissipation capabilities are examined using computational modeling at the atomistic scale for the first time.
- The effect of graphitic structures, as reinforcements, on the performance of metal matrix composites under static and shock stress wave loading conditions is investigated at the atomistic scale.
- Deformation mechanisms in superelastic and shape memory NiTi-Nb composites and their outstanding mechanical properties are studied at the atomistic scale for the first time.

List of Publications

1. **F. Yazdandoost**, R. Mirzaeifar. Stress Wave and Phase Transformation Propagation at the Atomistic Scale in NiTi Shape Memory Alloys Subjected to Shock Loadings, *Shape Memory and Superelasticity*. 2018. In Press, https://doi.org/10.1007/s40830-018-0189-5.
2. O. Sadeghi, M. Bakhtiari-Nejad, **F. Yazdandoost**, S. Shahab, R. Mirzaeifar. Dissipation of Cavitation-Induced Shock Waves Energy through Phase Transformation in NiTi Alloys. *International Journal of Mechanical Sciences*. 2018. 137, 304-314.
3. **F. Yazdandoost**, A. Y. Boroujeni, R. Mirzaeifar. A Nanocrystalline Nickel-Graphene Nanoplatelets Composite: Superior Mechanical Properties and Mechanics of Properties Enhancement at the Atomistic Level. *Physical Review Materials*. 2017. 1, 076001.
4. **F. Yazdandoost**, R. Mirzaeifar. Z. Qin, M. J. Buehler. Multiscale Mechanics of the Lateral Pressure Effect on Enhancing the Load Transfer Between Polymer Coated CNTs. *Nanoscale*. 2017. 9, 5565-5576.
5. **F. Yazdandoost**, R. Mirzaeifar. Generalized Stacking Fault Energy and Dislocation properties in NiTi Shape Memory Alloys. *Journal of Alloys and Compounds*. 2017. 709, 72-81.
6. **F. Yazdandoost**, R. Mirzaeifar. Tilt Grain Boundaries Energy and Structure in NiTi Alloys. *Computational Materials Science*. 2017. 131, 108-119.

References

1. Cui, J., et al., *Combinatorial search of thermoelastic shape-memory alloys with extremely small hysteresis width.* Nature materials, 2006. **5**(4): p. 286-290.
2. Hartl, D.J. and D.C. Lagoudas, *Aerospace applications of shape memory alloys.* Proceedings of the Institution of Mechanical Engineers, Part G: Journal of Aerospace Engineering, 2007. **221**(4): p. 535 - 552.
3. Sun, L., et al., *Stimulus-responsive shape memory materials: a review.* Materials & Design, 2012. **33**: p. 577-640.
4. Ueland, S.M. and C.A. Schuh, *Grain boundary and triple junction constraints during martensitic transformation in shape memory alloys.* Journal of Applied Physics, 2013. **114**(5): p. 053503.
5. Manchuraju, S., et al., *Pseudoelastic deformation and size effects during in situ transmission electron microscopy tensile testing of NiTi.* Acta Materialia, 2012. **60**(6): p. 2770-2777.
6. Ezaz, T., et al., *Plastic deformation of NiTi shape memory alloys.* Acta Materialia, 2013. **61**(1): p. 67-78.
7. Kröger, A., et al., *In situ transmission electron microscopy-investigations on the strain-induced B19'-phase in NiTi shape memory alloys structured by focused ion beam.* Materials Science and Engineering: A, 2006. **438**: p. 513-516.
8. Gall, K., et al., *Effect of microstructure on the fatigue of hot-rolled and cold-drawn NiTi shape memory alloys.* Materials Science and Engineering: A, 2008. **486**(1): p. 389-403.
9. Tschopp, M. and D. McDowell, *Structures and energies of Σ 3 asymmetric tilt grain boundaries in copper and aluminium.* Philosophical Magazine, 2007. **87**(22): p. 3147-3173.
10. Watanabe, T., *An approach to grain boundary design for strong and ductile polycrystals.* Res Mechanica, 1984. **11**(1): p. 47-84.
11. Palumbo, G., et al., *Grain boundary design and control for intergranular stress-corrosion resistance.* Scripta Metallurgica et Materialia, 1991. **25**(8): p. 1775-1780.
12. Watanabe, T., *The impact of grain boundary character distribution on fracture in polycrystals.* Materials Science and Engineering: A, 1994. **176**(1): p. 39-49.
13. Watanabe, T., et al., *Structure-dependent grain boundary deformation and fracture at high temperatures.* Materials Science and Engineering: A, 2005. **410**: p. 140-147.
14. Randle, V., *Twinning-related grain boundary engineering.* Acta materialia, 2004. **52**(14): p. 4067-4081.
15. Tschopp, M. and D. McDowell, *Asymmetric tilt grain boundary structure and energy in copper and aluminium.* Philosophical Magazine, 2007. **87**(25): p. 3871-3892.
16. Wolf, U., et al., *The influence of grain boundary inclination on the structure and energy of σ= 3 grain boundaries in copper.* Philosophical Magazine A, 1992. **66**(6): p. 991-1016.
17. Miyamoto, H., K. Ikeuchi, and T. Mimaki, *The role of grain boundary plane orientation on intergranular corrosion of symmetric and asymmetric [110] tilt grain boundaries in directionally solidified pure copper.* Scripta materialia, 2004. **50**(12): p. 1417-1421.
18. Randle, V., *'Special'boundaries and grain boundary plane engineering.* Scripta materialia, 2006. **54**(6): p. 1011-1015.
19. Blewitt, T., R. Coltman, and J. Redman, *Low-Temperature Deformation of Copper Single Crystals.* Journal of Applied Physics, 1957. **28**(6): p. 651-660.
20. Siegel, D.J., *Generalized stacking fault energies, ductilities, and twinnabilities of Ni and selected Ni alloys.* Applied Physics Letters, 2005. **87**(12): p. 121901-121901.
21. Morawiec, A., *Method to calculate the grain boundary energy distribution over the space of macroscopic boundary parameters from the geometry of triple junctions.* Acta materialia, 2000. **48**(13): p. 3525-3532.

22. Saylor, D.M., A. Morawiec, and G.S. Rohrer, *Distribution and energies of grain boundaries in magnesia as a function of five degrees of freedom.* Journal of the American Ceramic Society, 2002. **85**(12): p. 3081-3083.
23. Dillon, S.J. and G.S. Rohrer, *Characterization of the Grain-Boundary Character and Energy Distributions of Yttria Using Automated Serial Sectioning and EBSD in the FIB.* Journal of the American Ceramic Society, 2009. **92**(7): p. 1580-1585.
24. Li, J., S.J. Dillon, and G.S. Rohrer, *Relative grain boundary area and energy distributions in nickel.* Acta Materialia, 2009. **57**(14): p. 4304-4311.
25. Rohrer, G., et al., *Deriving grain boundary character distributions and relative grain boundary energies from three-dimensional EBSD data.* Materials Science and Technology, 2010. **26**(6): p. 661-669.
26. Beladi, H. and G.S. Rohrer, *The relative grain boundary area and energy distributions in a ferritic steel determined from three-dimensional electron backscatter diffraction maps.* Acta materialia, 2013. **61**(4): p. 1404-1412.
27. Beladi, H., N.T. Nuhfer, and G.S. Rohrer, *The five-parameter grain boundary character and energy distributions of a fully austenitic high-manganese steel using three dimensional data.* Acta materialia, 2014. **70**: p. 281-289.
28. Holm, E.A., et al., *Validating computed grain boundary energies in fcc metals using the grain boundary character distribution.* Acta Materialia, 2011. **59**(13): p. 5250-5256.
29. Rohrer, G.S., et al., *Comparing calculated and measured grain boundary energies in nickel.* Acta Materialia, 2010. **58**(15): p. 5063-5069.
30. Holm, E.A., D.L. Olmsted, and S.M. Foiles, *Comparing grain boundary energies in face-centered cubic metals: Al, Au, Cu and Ni.* Scripta Materialia, 2010. **63**(9): p. 905-908.
31. Olmsted, D.L., S.M. Foiles, and E.A. Holm, *Survey of computed grain boundary properties in face-centered cubic metals: I. Grain boundary energy.* Acta Materialia, 2009. **57**(13): p. 3694-3703.
32. Ogata, S., J. Li, and S. Yip, *Energy landscape of deformation twinning in bcc and fcc metals.* Physical Review B, 2005. **71**(22): p. 224102.
33. Yesilleten, D. and T. Arias, *Atomic-level physics of grain boundaries in bcc molybdenum.* Physical Review B, 2001. **64**(17): p. 174101.
34. Wolf, D., *Structure and energy of general grain boundaries in bcc metals.* Journal of applied physics, 1991. **69**(1): p. 185-196.
35. Wolf, D., *Correlation between the energy and structure of grain boundaries in bcc metals I. Symmetrical boundaries on the (110) and (100) planes.* Philosophical Magazine B, 1989. **59**(6): p. 667-680.
36. Wolf, D., *Correlation between the energy and structure of grain boundaries in bcc metals. II. Symmetrical tilt boundaries.* Philosophical Magazine A, 1990. **62**(4): p. 447-464.
37. Tschopp, M.A., et al., *Probing grain boundary sink strength at the nanoscale: Energetics and length scales of vacancy and interstitial absorption by grain boundaries in α-Fe.* Physical Review B, 2012. **85**(6): p. 064108.
38. Kröger, A., et al., *Direct transmission electron microscopy observations of martensitic transformations in Ni-rich NiTi single crystals during in situ cooling and straining.* Materials Science and Engineering: A, 2008. **481**: p. 452-456.
39. Xie, Z., Y. Liu, and J. Van Humbeeck, *Microstructure of NiTi shape memory alloy due to tension–compression cyclic deformation.* Acta Materialia, 1998. **46**(6): p. 1989-2000.
40. Zhong, Y., K. Gall, and T. Zhu, *Atomistic characterization of pseudoelasticity and shape memory in NiTi nanopillars.* Acta Materialia, 2012. **60**(18): p. 6301-6311.
41. Huang, X.Y., G.J. Ackland, and K.M. Rabe, *Crystal structures and shape-memory behaviour of NiTi.* Nature Materials, 2003. **2**(5): p. 307-311.
42. Knowles, K., *A high-resolution electron microscope study of nickel-titanium martensite.* Philosophical Magazine A, 1982. **45**(3): p. 357-370.

43. Xie*, Z. and Y. Liu, *HRTEM study of⟨011⟩type II twin in NiTi shape memory alloy.* Philosophical Magazine, 2004. **84**(32): p. 3497-3507.
44. Buchheit, T.E. and J.A. Wert, *Modeling the effects of stress state and crystal orientation on the stress-induced transformation of NiTi single crystals.* Metallurgical and Materials Transactions A-physical Metallurgy and Materials Science, 1994. **25**: p. 2383-2389.
45. Buehler, W.J., J. Gilfrich, and R. Wiley, *Effect of low-temperature phase changes on the mechanical properties of alloys near composition TiNi.* Journal of applied physics, 1963. **34**(5): p. 1475-1477.
46. Suresh, K.S., et al., *Interrelation of grain boundary microstructure and texture in a hot rolled Ni-rich NiTi alloy.* Scripta Materialia, 2012. **66**(8): p. 602-605.
47. Luo, J., et al., *Crystallographic mechanisms of fracture in a textured polycrystalline TiNi shape memory alloy.* Journal of Applied Physics, 2007. **102**(4): p. 043526.
48. Dlouhy, A., J. Khalil-Allafi, and G. Eggeler, *Multiple-step martensitic transformations in Ni-rich NiTi alloys--an in-situ transmission electron microscopy investigation.* Philosophical Magazine, 2003. **83**(3): p. 339-363.
49. Ahadi, A. and Q. Sun, *Stress hysteresis and temperature dependence of phase transition stress in nanostructured NiTi—Effects of grain size.* Applied Physics Letters, 2013. **103**(2): p. 021902.
50. Ahadi, A. and Q. Sun, *Effects of grain size on the rate-dependent thermomechanical responses of nanostructured superelastic NiTi.* Acta Materialia, 2014. **76**: p. 186-197.
51. Brinson, L.C., I. Schmidt, and R. Lammering, *Stress-induced transformation behavior of a polycrystalline NiTi shape memory alloy: micro and macromechanical investigations via in situ optical microscopy.* Journal of the Mechanics and Physics of Solids, 2004. **52**(7): p. 1549-1571.
52. Ueland, S.M., Y. Chen, and C.A. Schuh, *Oligocrystalline shape memory alloys.* Advanced Functional Materials, 2012. **22**(10): p. 2094-2099.
53. Bhattacharya, S.K., et al., *Ab initio study of symmetrical tilt grain boundaries in bcc Fe: structural units, magnetic moments, interfacial bonding, local energy and local stress.* Journal of Physics: Condensed Matter, 2013. **25**(13): p. 135004.
54. Marinopoulos, A., *First-principles study of hydrogen configurations at the core of a high-angle grain boundary in cubic yttria-stabilized zirconia.* Journal of Physics: Condensed Matter, 2013. **26**(2): p. 025502.
55. Uberuaga, B.P., et al., *Point defect? grain boundary interactions in MgO: an atomistic study.* Journal of Physics: Condensed Matter, 2013. **25**(35): p. 355001.
56. Zhang, Y., et al., *Molecular dynamics simulations of He bubble nucleation at grain boundaries.* Journal of Physics: Condensed Matter, 2012. **24**(30): p. 305005.
57. Voyiadjis, G.Z. and M. Yaghoobi, *Role of grain boundary on the sources of size effects.* Computational Materials Science, 2016. **117**: p. 315-329.
58. Xu, J., et al., *Assessment of the CSL and SU models for bcc-Fe grain boundaries from first principles.* Computational Materials Science, 2016. **122**: p. 22-29.
59. Yu, W., S. Shen, and Q. Liu, *Energetics of point defect interacting with bi-crystal Σ3 copper grain boundaries.* Computational Materials Science, 2016. **118**: p. 47-55.
60. Zhang, L., C. Lu, and K. Tieu, *A review on atomistic simulation of grain boundary behaviors in face-centered cubic metals.* Computational Materials Science, 2016. **118**: p. 180-191.
61. Lim, T.J. and D.L. McDowell, *Cyclic thermomechanical behavior of a polycrystalline pseudoelastic shape memory alloy.* Journal of the Mechanics and Physics of Solids, 2002. **50**(3): p. 651-676.
62. Miyazaki, S., et al., *Effect of cyclic deformation on the pseudoelasticity characteristics of Ti-Ni alloys.* Metallurgical Transactions A, 1986. **17**(1): p. 115-120.
63. Sehitoglu, H., et al., *Cyclic deformation behavior of single crystal NiTi.* Materials Science and Engineering: A, 2001. **314**(1–2): p. 67-74.
64. Liu, Y. and G.S. Tan, *Effect of deformation by stress-induced martensitic transformation on the transformation behaviour of NiTi.* Intermetallics, 2000. **8**(1): p. 67-75.

65. Shi, X.B., et al., *Grain size effect on stress hysteresis of nanocrystalline NiTi alloys.* Journal of Alloys and Compounds, 2016. **688, Part B**: p. 62-68.
66. Li, H.X., et al., *An in situ TEM study of the size effect on the thermally induced martensitic transformation in nanoscale NiTi shape memory alloy.* Journal of Alloys and Compounds, 2014. **588**: p. 337-342.
67. Hull, D. and D.J. Bacon, *Introduction to dislocations*. 2001: Butterworth-Heinemann.
68. Li, S., et al., *Dislocation Core Structure and Peierls Stress of B2-Based AlSc in {110} Plane.* Journal of Electronic Materials: p. 1-9.
69. Simon, T., et al., *On the multiplication of dislocations during martensitic transformations in NiTi shape memory alloys.* Acta Materialia, 2010. **58**(5): p. 1850-1860.
70. Schroll, R., V. Vitek, and P. Gumbsch, *Core properties and motion of dislocations in NiAl.* Acta materialia, 1998. **46**(3): p. 903-918.
71. Crimp, M., S. Tonn, and Y. Zhang, *Dislocation core structures in B2 NiAl alloys.* Materials Science and Engineering: A, 1993. **170**(1): p. 95-102.
72. Mills, M., R. Srinivasan, and M.S. Daw, *Observations and modelling of a〈011〉 dislocations in NiAl at intermediate temperatures.* Philosophical Magazine A, 1998. **77**(3): p. 801-823.
73. Brown, J., et al., *The mechanics of slip transition at intermediate temperatures in< 001>-oriented NiAl single crystals II. A metastable state for α< 111>{110} dislocations in NiAl and its role in their decomposition.* Philosophical Magazine A, 2000. **80**(12): p. 2855-2870.
74. Vailhe, C. and D. Farkas, *Shear faults and dislocation core structure simulations in B2 FeAl.* Acta materialia, 1997. **45**(11): p. 4463-4473.
75. Paidar, V. and M. Čák, *Three types of dislocation core structure in B2 alloys.* Intermetallics, 2016. **73**: p. 21-25.
76. Vailhe, C. and D. Farkas, *Trends in dislocation core structures and mechanical behavior in B2 aluminides*. 1995, Materials Research Society, Pittsburgh, PA (United States).
77. Soleymani, M., M. Parsa, and H. Mirzadeh, *Molecular dynamics simulation of stress field around edge dislocations in aluminum.* Computational Materials Science, 2014. **84**: p. 83-96.
78. Delville, R., et al., *Transmission electron microscopy investigation of dislocation slip during superelastic cycling of Ni–Ti wires.* International Journal of Plasticity, 2011. **27**(2): p. 282-297.
79. Moitra, A., S.-G. Kim, and M. Horstemeyer, *Solute effect on the< a+ c> dislocation nucleation mechanism in magnesium.* Acta Materialia, 2014. **75**: p. 106-112.
80. Wang, J., H. Sehitoglu, and H. Maier, *Dislocation slip stress prediction in shape memory alloys.* International Journal of Plasticity, 2014. **54**: p. 247-266.
81. Zimmerman, J.A., H. Gao, and F.F. Abraham, *Generalized stacking fault energies for embedded atom FCC metals.* Modelling and Simulation in Materials Science and Engineering, 2000. **8**(2): p. 103.
82. Yan, J.-A., C.-Y. Wang, and S.-Y. Wang, *Generalized-stacking-fault energy and dislocation properties in bcc Fe: A first-principles study.* Physical Review B, 2004. **70**(17): p. 174105.
83. Li, W., et al., *Generalized stacking fault energies of alloys.* Journal of Physics: Condensed Matter, 2014. **26**(26): p. 265005.
84. Pei, Z., et al., *Ab initio and atomistic study of generalized stacking fault energies in Mg and Mg–Y alloys.* New Journal of Physics, 2013. **15**(4): p. 043020.
85. Van Swygenhoven, H., P.M. Derlet, and A.G. Froseth, *Stacking fault energies and slip in nanocrystalline metals.* Nat Mater, 2004. **3**(6): p. 399-403.
86. Farkas, D., et al., *Embedded atom calculations of unstable stacking fault energies and surface energies in intermetallics.* Journal of materials research, 1997. **12**(01): p. 93-99.
87. Eichler, H. and B. Pegel, *Intrinsic Stacking Faults on {112} Planes in the BCC Lattice.* physica status solidi (b), 1969. **35**(1): p. 333-338.
88. Heino, P., et al., *Stacking-fault energy of copper from molecular-dynamics simulations.* Physical Review B, 1999. **60**(21): p. 14625.

89. Mutter, D. and P. Nielaba, *Simulation of structural phase transitions in NiTi.* Physical Review B, 2010. **82**(22): p. 224201.
90. Mutter, D. and P. Nielaba, *Simulation of the thermally induced austenitic phase transition in NiTi nanoparticles.* The European Physical Journal B, 2011. **84**(1): p. 109-113.
91. Ko, W.-S., et al., *Atomic scale processes of phase transformations in nanocrystalline NiTi shape-memory alloys.* Acta Materialia, 2017. **123**: p. 90-101.
92. Mutter, D. and P. Nielaba, *Simulation of the shape memory effect in a NiTi nano model system.* Journal of Alloys and Compounds, 2013. **577**: p. S83-S87.
93. Zhong, Y., K. Gall, and T. Zhu, *Atomistic study of nanotwins in NiTi shape memory alloys.* Journal of Applied Physics, 2011. **110**(3): p. -.
94. Wu, C.-D., P.-H. Sung, and T.-H. Fang, *Study of deformation and shape recovery of NiTi nanowires under torsion.* Journal of molecular modeling, 2013. **19**(4): p. 1883-1890.
95. Mirzaeifar, R., et al., *Structural transformations in NiTi shape memory alloy nanowires.* Journal of Applied Physics, 2014. **115**(19): p. 194307.
96. Yazdandoost, F. and R. Mirzaeifar, *Tilt grain boundaries energy and structure in NiTi alloys.* Computational Materials Science, 2017. **131**: p. 108-119.
97. Chowdhury, P., et al., *Molecular Dynamics Modeling of NiTi Superelasticity in Presence of Nanoprecipitates.* International Journal of Plasticity, 2016.
98. Chowdhury, P., G. Ren, and H. Sehitoglu, *NiTi superelasticity via atomistic simulations.* Philosophical Magazine Letters, 2015: p. 1-13.
99. Ren, G. and H. Sehitoglu, *Interatomic potential for the NiTi alloy and its application.* Computational Materials Science, 2016. **123**: p. 19-25.
100. Mirzaeifar, R., R. DesRoches, and A. Yavari, *A combined analytical, numerical, and experimental study of shape-memory-alloy helical springs.* International Journal of Solids and Structures, 2011. **48**(3-4): p. 611-624.
101. Sehitoglu, H., et al. *Hysteresis in NiTi alloys*. in *Journal de Physique IV (Proceedings)*. 2004. EDP sciences.
102. Nemat-Nasser, S., et al., *High strain-rate, small strain response of a NiTi shape-memory alloy.* Journal of Engineering Materials and Technology, 2005. **127**(1): p. 83-89.
103. Yuan, F. and X. Wu, *Shock response of nanotwinned copper from large-scale molecular dynamics simulations.* Physical Review B, 2012. **86**(13): p. 134108.
104. Arman, B., et al., *Dynamic response of Cu 46 Zr 54 metallic glass to high-strain-rate shock loading: Plasticity, spall, and atomic-level structures.* Physical Review B, 2010. **81**(14): p. 144201.
105. Bringa, E., et al., *Shock deformation of face-centred-cubic metals on subnanosecond timescales.* Nature materials, 2006. **5**(10): p. 805-809.
106. Zhao, F., et al., *Shock-induced melting of honeycomb-shaped Cu nanofoams: Effects of porosity.* Journal of Applied Physics, 2015. **118**(3): p. 035904.
107. Yin, Q., X. Wu, and C. Huang, *Atomistic study on shock behaviour of NiTi shape memory alloy.* Philosophical Magazine, 2017. **97**(16): p. 1311-1333.
108. Jiang, S., T.D. Sewell, and D.L. Thompson, *Molecular Dynamics Simulations of Shock Wave Propagation through the Crystal–Melt Interface of (100)-Oriented Nitromethane.* The Journal of Physical Chemistry C, 2016. **120**(40): p. 22989-23000.
109. Kadau, K., et al., *Microscopic view of structural phase transitions induced by shock waves.* Science, 2002. **296**(5573): p. 1681-1684.
110. Luo, S.-N., et al., *Anisotropic shock response of columnar nanocrystalline Cu.* Journal of Applied Physics, 2010. **107**(12): p. 123507.
111. Luo, S.-N., et al., *Shock wave loading and spallation of copper bicrystals with asymmetric Σ 3(110) tilt grain boundaries.* Journal of Applied Physics, 2010. **108**(9): p. 093526.
112. Ma, W., W. Zhu, and F. Jing, *The shock-front structure of nanocrystalline aluminum.* Applied Physics Letters, 2010. **97**(12): p. 121903.

113. Lagoudas, D.C. and P. Popov, *Numerical studies of wave propagation in polycrystalline shape memory alloy rods.* Smart Structures and Materials 2003, 2003. **5053**: p. 294-304.
114. Treacy, M.M.J., T.W. Ebbesen, and J.M. Gibson, *Exceptionally high Young's modulus observed for individual carbon nanotubes.* Nature, 1996. **381**(6584): p. 678-680.
115. Baughman, R.H., A.A. Zakhidov, and W.A. De Heer, *Carbon nanotubes--the route toward applications.* science, 2002. **297**(5582): p. 787-792.
116. Wilder, J.W., et al., *Electronic structure of atomically resolved carbon nanotubes.* Nature, 1998. **391**(6662): p. 59-62.
117. Berber, S., Y.-K. Kwon, and D. Tománek, *Unusually high thermal conductivity of carbon nanotubes.* Physical review letters, 2000. **84**(20): p. 4613.
118. Kuzumaki, T., et al., *Processing of carbon nanotube reinforced aluminum composite.* Journal of Materials Research, 1998. **13**(09): p. 2445-2449.
119. Cha, S.I., et al., *Extraordinary strengthening effect of carbon nanotubes in metal-matrix nanocomposites processed by molecular-level mixing.* Advanced Materials, 2005. **17**(11): p. 1377-1381.
120. Kim, K.T., et al., *The Role of Interfacial Oxygen Atoms in the Enhanced Mechanical Properties of Carbon-Nanotube-Reinforced Metal Matrix Nanocomposites.* Small, 2008. **4**(11): p. 1936-1940.
121. Johannes, L.B., et al., *Survivability of single-walled carbon nanotubes during friction stir processing.* Nanotechnology, 2006. **17**(12): p. 3081.
122. Morisada, Y., et al., *MWCNTs/AZ31 surface composites fabricated by friction stir processing.* Materials science and engineering: A, 2006. **419**(1): p. 344-348.
123. Chai, G., Y. Sun, and Q. Chen, *Mechanical properties of carbon nanotube–copper nanocomposites.* Journal of Micromechanics and Microengineering, 2008. **18**(3): p. 035013.
124. Bartolucci, S.F., et al., *Graphene–aluminum nanocomposites.* Materials Science and Engineering: A, 2011. **528**(27): p. 7933-7937.
125. Jiang, L., et al., *An approach to the uniform dispersion of a high volume fraction of carbon nanotubes in aluminum powder.* Carbon, 2011. **49**(6): p. 1965-1971.
126. Wang, J., et al., *Reinforcement with graphene nanosheets in aluminum matrix composites.* Scripta Materialia, 2012. **66**(8): p. 594-597.
127. Pérez-Bustamante, R., et al., *Microstructural and hardness behavior of graphene-nanoplatelets/aluminum composites synthesized by mechanical alloying.* Journal of Alloys and Compounds, 2014. **615**: p. S578-S582.
128. Jeon, C.-H., et al., *Material properties of graphene/aluminum metal matrix composites fabricated by friction stir processing.* International journal of precision engineering and manufacturing, 2014. **15**(6): p. 1235-1239.
129. Koltsova, T.S., et al., *New hybrid copper composite materials based on carbon nanostructures.* Journal of Materials Science and Engineering B, 2012. **2**(4): p. 240-246.
130. Hwang, J., et al., *Enhanced mechanical properties of graphene/copper nanocomposites using a molecular-level mixing process.* Advanced Materials, 2013. **25**(46): p. 6724-6729.
131. Pavithra, C.L., et al., *A new electrochemical approach for the synthesis of copper-graphene nanocomposite foils with high hardness.* Scientific reports, 2014. **4**: p. 4049.
132. Tang, Y., et al., *Enhancement of the mechanical properties of graphene–copper composites with graphene–nickel hybrids.* Materials Science and Engineering: A, 2014. **599**: p. 247-254.
133. Chen, L.-Y., et al., *Novel nanoprocessing route for bulk graphene nanoplatelets reinforced metal matrix nanocomposites.* Scripta Materialia, 2012. **67**(1): p. 29-32.
134. Kuang, D., et al., *Graphene–nickel composites.* Applied Surface Science, 2013. **273**: p. 484-490.
135. Kim, Y., et al., *Strengthening effect of single-atomic-layer graphene in metal–graphene nanolayered composites.* Nature communications, 2013. **4**.
136. Hoagland, R.G., R.J. Kurtz, and C.H. Henager, *Slip resistance of interfaces and the strength of metallic multilayer composites.* Scripta materialia, 2004. **50**(6): p. 775-779.

137. Wang, J., et al., *Atomistic simulations of the shear strength and sliding mechanisms of copper–niobium interfaces.* Acta materialia, 2008. **56**(13): p. 3109-3119.
138. Wang, J., et al., *Atomistic modeling of the interaction of glide dislocations with "weak" interfaces.* Acta materialia, 2008. **56**(19): p. 5685-5693.
139. Chang, S.-W., A.K. Nair, and M.J. Buehler, *Nanoindentation study of size effects in nickel–graphene nanocomposites.* Philosophical Magazine Letters, 2013. **93**(4): p. 196-203.
140. Muller, S.E. and A.K. Nair, *Dislocation Nucleation in Nickel-Graphene Nanocomposites Under Mode I Loading.* JOM, 2016. **68**(7): p. 1909-1914.
141. Hall, E., *The deformation and ageing of mild steel: III discussion of results.* Proceedings of the Physical Society. Section B, 1951. **64**(9): p. 747.
142. Petch, N., *The cleavage strength of polycrystals.* J. Iron Steel Inst., 1953. **174**: p. 25-28.
143. Schiøtz, J., F.D. Di Tolla, and K.W. Jacobsen, *Softening of nanocrystalline metals at very small grain sizes.* Nature, 1998. **391**(6667): p. 561-563.
144. Schiøtz, J., et al., *Atomic-scale simulations of the mechanical deformation of nanocrystalline metals.* Physical Review B, 1999. **60**(17): p. 11971.
145. Van Swygenhoven, H., et al., *Competing plastic deformation mechanisms in nanophase metals.* Physical Review B, 1999. **60**(1): p. 22.
146. Van Swygenhoven, H., A. Caro, and D. Farkas, *A molecular dynamics study of polycrystalline fcc metals at the nanoscale: grain boundary structure and its influence on plastic deformation.* Materials Science and Engineering: A, 2001. **309**: p. 440-444.
147. Schiøtz, J. and K.W. Jacobsen, *A maximum in the strength of nanocrystalline copper.* Science, 2003. **301**(5638): p. 1357-1359.
148. Farkas, D. and W.A. Curtin, *Plastic deformation mechanisms in nanocrystalline columnar grain structures.* Materials Science and Engineering: A, 2005. **412**(1): p. 316-322.
149. Otsuka, K. and C.M. Wayman, *Shape memory materials*. 1999: Cambridge university press.
150. Cai, W., X. Lu, and L. Zhao, *Damping behavior of TiNi-based shape memory alloys.* Materials Science and Engineering: A, 2005. **394**(1-2): p. 78-82.
151. Wu, S. and H. Lin, *Damping characteristics of TiNi binary and ternary shape memory alloys.* Journal of alloys and compounds, 2003. **355**(1-2): p. 72-78.
152. Rajagopalan, S., et al., *Elastic modulus of shape-memory NiTi from in situ neutron diffraction during macroscopic loading, instrumented indentation, and extensometry.* Applied Physics Letters, 2005. **86**(8): p. 081901.
153. Van Humbeeck, J., *Damping capacity of thermoelastic martensite in shape memory alloys.* Journal of Alloys and Compounds, 2003. **355**(1-2): p. 58-64.
154. van der Eijk, C., J.S. Olsen, and Z. Zhang. *Applications of NiTi shape memory alloy dampers in civil structures*. in *Proceedings of the first international conference on self healing materials, Noordwijk aan Zee, Netherland Google Scholar*. 2007.
155. Duerig, T.W., K. Melton, and D. Stöckel, *Engineering aspects of shape memory alloys*. 2013: Butterworth-Heinemann.
156. Fu, X., et al., *Effects of Nb content on yield strength of NiTiNb alloys in martensite state.* Chinese Journal of Aeronautics, 2009. **22**(6): p. 658-662.
157. Cai, W., X. Meng, and L. Zhao, *Recent development of TiNi-based shape memory alloys.* Current Opinion in Solid State and Materials Science, 2005. **9**(6): p. 296-302.
158. Li, D., et al., *Lightweight NiTi shape memory alloy based composites with high damping capacity and high strength.* Journal of Alloys and Compounds, 2010. **490**(1-2): p. L15-L19.
159. Biscarini, A., et al., *Extraordinary high damping of hydrogen-doped NiTi and NiTiCu shape memory alloys.* Journal of alloys and compounds, 2003. **355**(1-2): p. 52-57.
160. Karaca, H., et al., *NiTiHf-based shape memory alloys.* Materials Science and Technology, 2014. **30**(13): p. 1530-1544.

161. Hong, S.H., et al., *Influence of Zr content on phase formation, transition and mechanical behavior of Ni-Ti-Hf-Zr high temperature shape memory alloys.* Journal of Alloys and Compounds, 2017. **692**: p. 77-85.
162. Xiao, F., et al. *A novel TiNiNb shape memory alloy with high yield strength and high damping capacity*. in *International Conference on Smart Materials and Nanotechnology in Engineering*. 2007. International Society for Optics and Photonics.
163. Liu, Z., et al., *Influence of internal stress coupling on the deformation behavior of NiTi–Nb nanowire composites.* Scripta Materialia, 2014. **77**: p. 75-78.
164. Wang, S., et al., *Locality and rapidity of the ultra-large elastic deformation of Nb nanowires in a NiTi phase-transforming matrix.* Scientific reports, 2014. **4**: p. 6753.
165. Lai, W.S. and B.X. Liu, *Lattice stability of some Ni-Ti alloy phases versus their chemical composition and disordering.* Journal of Physics: Condensed Matter, 2000. **12**(5): p. L53.
166. Yin, Q., et al., *Atomistic study of temperature and strain rate-dependent phase transformation behaviour of NiTi shape memory alloy under uniaxial compression.* Philosophical Magazine, 2015. **95**(23): p. 2491-2512.
167. Plimpton, S., *Fast Parallel Algorithms for Short-Range Molecular Dynamics.* Journal of Computational Physics, 1995. **117**(1): p. 1 - 19.
168. Stukowski, A., *Visualization and analysis of atomistic simulation data with OVITO–the Open Visualization Tool.* Modelling and Simulation in Materials Science and Engineering, 2009. **18**(1): p. 015012.
169. Giannozzi, P., et al., *QUANTUM ESPRESSO: a modular and open-source software project for quantum simulations of materials.* Journal of physics: Condensed matter, 2009. **21**(39): p. 395502.
170. Kresse, G. and D. Joubert, *From ultrasoft pseudopotentials to the projector augmented-wave method.* Physical Review B, 1999. **59**(3): p. 1758.
171. Monkhorst, H.J. and J.D. Pack, *Special points for Brillouin-zone integrations.* Physical review B, 1976. **13**(12): p. 5188.
172. Hahn, E.N., et al., *Symmetric tilt boundaries in body-centered cubic tantalum.* Scripta Materialia, 2016. **116**: p. 108-111.
173. Ratanaphan, S., et al., *Grain boundary energies in body-centered cubic metals.* Acta Materialia, 2015. **88**: p. 346-354.
174. Sangid, M.D., et al., *Energy of slip transmission and nucleation at grain boundaries.* Acta Materialia, 2011. **59**(1): p. 283-296.
175. Kexel, C., S. Schramm, and A.V. Solov'yov, *Atomistic simulation of martensite-austenite phase transition in nanoscale nickel-titanium crystals.* The European Physical Journal B, 2015. **88**(9): p. 1-8.
176. Rittner, J.D. and D.N. Seidman, *〈110〉 symmetric tilt grain-boundary structures in fcc metals with low stacking-fault energies.* Physical Review B, 1996. **54**(10): p. 6999-7015.
177. Shibuta, Y., S. Takamoto, and T. Suzuki, *A molecular dynamics study of the energy and structure of the symmetric tilt boundary of iron.* ISIJ international, 2008. **48**(11): p. 1582-1591.
178. Patoor, E., et al., *Shape memory alloys, Part I: General properties and modeling of single crystals.* Mechanics of materials, 2006. **38**(5): p. 391-429.
179. Lejcek, P., *Grain boundary segregation in metals*. Vol. 136. 2010: Springer Science & Business Media.
180. Read, W.T. and W. Shockley, *Dislocation Models of Crystal Grain Boundaries.* Physical Review, 1950. **78**(3): p. 275-289.
181. Suzuki, S. and D. Kuroiwa, *Grain-boundary energy and grain-boundary groove angles in ice.* Journal of Glaciology, 1972. **11**(62): p. 265-277.
182. Sangid, M.D., et al., *Grain boundary characterization and energetics of superalloys.* Materials Science and Engineering: A, 2010. **527**(26): p. 7115-7125.

183. DiVincenzo, D., et al., *Electronic and structural properties of a twin boundary in Si.* Physical review letters, 1986. **56**(18): p. 1925.
184. Fisher, C.A., et al., *First Principles Calculations of Grain Boundaries in LiCoO2.* 2010.
185. Elsässer, C., et al. *Ab-Initio Determination of the Atomic Structure of Symmetrical Tilt Grain Boundaries in BCC Transition Metals*. in *MRS Proceedings*. 1997. Cambridge Univ Press.
186. Ochs, T., et al., *Symmetrical tilt grain boundaries in body-centred cubic transition metals: an ab initio local-density-functional study.* Philosophical Magazine A, 2000. **80**(2): p. 351-372.
187. Wright, A.F. and S.R. Atlas, *Density-functional calculations for grain boundaries in aluminum.* Physical Review B, 1994. **50**(20): p. 15248.
188. Baskes, M.I., *Modified embedded-atom potentials for cubic materials and impurities.* Physical Review B, 1992. **46**(5): p. 2727-2742.
189. Lee, B.-J. and M.I. Baskes, *Second nearest-neighbor modified embedded-atom-method potential.* Physical Review B, 2000. **62**(13): p. 8564-8567.
190. Ko, W.-S., B. Grabowski, and J. Neugebauer, *Development and application of a Ni-Ti interatomic potential with high predictive accuracy of the martensitic phase transition.* Physical Review B, 2015. **92**(13): p. 134107.
191. Bulatov, V. and W. Cai, *Computer simulations of dislocations*. Vol. 3. 2006: Oxford University Press on Demand.
192. Cai, W., et al., *Periodic image effects in dislocation modelling.* Philosophical Magazine, 2003. **83**(5): p. 539-567.
193. Hirth, J.P. and J. Lothe, *Theory of dislocations.* 1982.
194. Shetty, M., *Dislocations and mechanical behaviour of materials*. 2013: PHI Learning Pvt. Ltd.
195. Sadeghi, O., et al., *Dissipation of Cavitation-Induced Shock Waves Energy through Phase Transformation in NiTi Alloys.* International Journal of Mechanical Sciences, 2018.
196. Qidwai, M.A. and D.C. Lagoudas, *Numerical implementation of a shape memory alloy thermomechanical constitutive model using return mapping algorithms.* International Journal for Numerical Methods in Engineering, 2000. **47**(6): p. 1123 - 1168.
197. Mirzaeifar, R., et al., *A semi-analytic analysis of shape memory alloy thick-walled cylinders under internal pressure.* Archive of Applied Mechanics, 2011. **81**(8): p. 1093-1116.
198. Mirzaeifar, R., R. DesRoches, and A. Yavari, *Exact solutions for pure torsion of shape memory alloy circular bars.* Mechanics of Materials, 2010. **42**(8): p. 797-806.
199. Mirzaeifar, R., M. Shakeri, and M. Sadighi, *Nonlinear finite element formulation for analyzing shape memory alloy cylindrical panels.* Smart Materials and Structures, 2009. **18**(3).
200. Boyd, J.G. and D.C. Lagoudas, *Thermodynamical constitutive model for shape memory materials. Part I. The monolithic shape memory alloy.* International Journal of Plasticity, 1996. **12**(6): p. 805 - 842.
201. Thamburaja, P. and L. Anand, *Polycrystalline shape-memory materials: effect of crystallographic texture.* Journal of the Mechanics and Physics of Solids, 2001. **49**(4): p. 709 - 737.
202. Jacobus, K., H. Sehitoglu, and M. Balzer, *Effect of stress state on the stress-induced martensitic transformation in polycrystalline Ni-Ti alloy.* Metallurgical and Materials Transactions A, 1996. **27**: p. 3066-3073.
203. Lai, W. and B. Liu, *Lattice stability of some Ni-Ti alloy phases versus their chemical composition and disordering.* Journal of Physics: Condensed Matter, 2000. **12**(5): p. L53.
204. Boots, B.N., *The arrangement of cells in random networks.* Metallography, 1982. **15**(1): p. 53 - 62.
205. Lagoudas, D.C., et al., *Dynamic loading of polycrystalline shape memory alloy rods.* Mechanics of Materials, 2003. **35**(7): p. 689 - 716.
206. Brill, T., et al., *Elastic properties of NiTi.* Journal of Physics: Condensed Matter, 1991. **3**(48): p. 9621.
207. Lane, C., *Wave Propagation in Anisotropic Media*, in *The Development of a 2D Ultrasonic Array Inspection for Single Crystal Turbine Blades*. 2014, Springer International Publishing: Cham. p. 13-39.

208. Shimizu, F., S. Ogata, and J. Li, *Theory of shear banding in metallic glasses and molecular dynamics calculations.* Materials transactions, 2007. **48**(11): p. 2923-2927.
209. Qin, S.-J., et al., *Symmetrical tilt grain boundary engineering of NiTi shape memory alloy: An atomistic insight.* Materials & Design, 2018. **137**: p. 361-370.
210. DesRoches, R. and B. Smith, *Shape memory alloys in seismic resistant design and retrofit: a critical review of their potential and limitations.* Journal of Earthquake Engineering, 2004. **8**: p. 415-29.
211. DesRoches, R., B. Taftali, and B.R. Ellingwood, *Seismic performance assessment of steel frames with shape memory alloy connections. Part I analysis and seismic demands.* Journal of Earthquake Engineering, 2010. **14**(4): p. 471-486.
212. DesRoches, B.A.R., *Effect of hysteretic properties of superelastic shape memory alloys on the seismic performance of structures.* Structural Control and Health Monitoring, 2007. **14**: p. 301-320.
213. Sichani, M.M. and D.E. Spearot, *A molecular dynamics study of the role of grain size and orientation on compression of nanocrystalline Cu during shock.* Computational Materials Science, 2015. **108**: p. 226-232.
214. Wang, J.J. and W.G. Guo. *Pseudo-Elastic Behavior of NiTi SMA under the Quasi-Static and the Impact Cyclic Tests*. in *Advanced Materials Research*. 2012. Trans Tech Publ.
215. Razorenov, S., et al., *Behavior of the nickel-titanium alloys with the shape memory effect under conditions of shock wave loading.* Physics of the Solid State, 2011. **53**(4): p. 824-829.
216. Chen, W.W., et al., *Compressive superelastic behavior of a NiTi shape memory alloy at strain rates of 0.001–750 s− 1.* International Journal of Solids and Structures, 2001. **38**(50-51): p. 8989-8998.
217. Niemczura, J. and K. Ravi-Chandar, *Dynamics of propagating phase boundaries in NiTi.* Journal of the Mechanics and Physics of Solids, 2006. **54**(10): p. 2136-2161.
218. Zhang, X. and Z. Tang, *Experimental study on the dynamic behavior of TiNi cantilever beams with rectangular cross-section under transversal impact.* International Journal of Impact Engineering, 2010. **37**(7): p. 813-827.
219. Bekker, A., et al., *Impact induced propagation of phase transformation in a shape memory alloy rod*, in *International Journal of Plasticity*. 2002. p. 1447 - 1479.
220. Zurbitu, J., et al., *Low-energy tensile-impact behavior of superelastic NiTi shape memory alloy wires.* Mechanics of Materials, 2009. **41**(9): p. 1050-1058.
221. Saletti, D., S. Pattofatto, and H. Zhao, *Measurement of phase transformation properties under moderate impact tensile loading in a NiTi alloy.* Mechanics of Materials, 2013. **65**: p. 1-11.
222. Zurbitu, J., et al., *Thermo-mechanical behaviour of NiTi at impact*, in *Shape Memory Alloys*. 2010, InTech.
223. Chen, Y. and D.C. Lagoudas, *Wave propagation in shape memory alloy rods under impulsive loads.* Proceedings of the Royal Society A: Mathematical, Physical and Engineering Sciences, 2005. **461**(2064): p. 3871 - 3892.
224. Yazdandoost, F. and R. Mirzaeifar, *Stress Wave and Phase Transformation Propagation at the Atomistic Scale in NiTi Shape Memory Alloys Subjected to Shock Loadings.* Shape Memory and Superelasticity, 2018: p. 1-15.
225. Mishin, Y., et al., *Interatomic potentials for monoatomic metals from experimental data and ab initio calculations.* Physical Review B, 1999. **59**(5): p. 3393.
226. Plimpton, S., *FAST PARALLEL ALGORITHMS FOR SHORT-RANGE MOLECULAR-DYNAMICS.* Journal of Computational Physics, 1995. **117**(1): p. 1-19.
227. Naraghi, M., et al., *Atomistic Investigation of Load Transfer Between DWNT Bundles "Crosslinked" by PMMA Oligomers.* Advanced Functional Materials, 2013. **23**(15): p. 1883-1892.
228. Chenoweth, K., A.C.T. van Duin, and W.A. Goddard, *ReaxFF reactive force field for molecular dynamics simulations of hydrocarbon oxidation.* Journal of Physical Chemistry A, 2008. **112**(5): p. 1040-1053.

229. Strachan, A., et al., *Thermal decomposition of RDX from reactive molecular dynamics.* Journal of Chemical Physics, 2005. **122**(5).
230. Beese, A.M., et al., *Bio-Inspired Carbon Nanotube–Polymer Composite Yarns with Hydrogen Bond-Mediated Lateral Interactions.* ACS Nano, 2013. **7**(4): p. 3434-3446.
231. Bratzel, G.H., et al., *Bioinspired noncovalently crosslinked "fuzzy" carbon nanotube bundles with superior toughness and strength.* Journal of Materials Chemistry, 2010. **20**(46): p. 10465-10474.
232. Mirzaeifar, R., Z. Qin, and M.J. Buehler, *Mesoscale mechanics of twisting carbon nanotube yarns.* Nanoscale, 2015. **7**(12): p. 5435-5445.
233. Naraghi, M., et al., *A Multiscale Study of High Performance Double-Walled Nanotube− Polymer Fibers.* ACS Nano, 2010. **4**(11): p. 6463-6476.
234. Filleter, T., et al., *Experimental-computational study of shear interactions within double-walled carbon nanotube bundles.* Nano Letters, 2012. **12**(2): p. 732-742.
235. Berendsen, H.J.C., et al., *MOLECULAR-DYNAMICS WITH COUPLING TO AN EXTERNAL BATH.* Journal of Chemical Physics, 1984. **81**(8): p. 3684-3690.
236. Chen, B., et al., *Binding energy of parallel carbon nanotubes.* Applied Physics Letters, 2003. **83**(17): p. 3570-3571.
237. Liew, K., C. Wong, and M. Tan, *Buckling properties of carbon nanotube bundles.* Applied Physics Letters, 2005. **87**(4): p. 041901.
238. Liew, K., C. Wong, and M. Tan, *Tensile and compressive properties of carbon nanotube bundles.* Acta materialia, 2006. **54**(1): p. 225-231.
239. Zhou, W., et al., *Self-folding of single-and multiwall carbon nanotubes.* Applied Physics Letters, 2007. **90**(7): p. 073107.
240. Zhu, C., Z. Xie, and K. Guo, *Formation of close-packed multi-wall carbon nanotube bundles.* Diamond and related materials, 2004. **13**(1): p. 180-183.
241. Buehler, M.J., A.C. van Duin, and W.A. Goddard III, *Multiparadigm modeling of dynamical crack propagation in silicon using a reactive force field.* Physical review letters, 2006. **96**(9): p. 095505.
242. Cranford, S., et al., *A single degree of freedom 'lollipop'model for carbon nanotube bundle formation.* Journal of the Mechanics and Physics of Solids, 2010. **58**(3): p. 409-427.
243. Cranford, S. and M.J. Buehler, *Mechanomutable carbon nanotube arrays.* International Journal of Materials and Structural Integrity, 2009. **3**(2-3): p. 161-178.
244. Cranford, S.W. and M.J. Buehler, *In silico assembly and nanomechanical characterization of carbon nanotube buckypaper.* Nanotechnology, 2010. **21**(26): p. 265706.
245. Buehler, M.J., *Mesoscale modeling of mechanics of carbon nanotubes: self-assembly, self-folding, and fracture.* Journal of Materials Research, 2006. **21**(11): p. 2855-2869.
246. Uttarwar, R.G., J. Potoff, and Y. Huang, *Study on interfacial interaction between polymer and nanoparticle in a nanocoating matrix: a martini coarse-graining method.* Industrial & Engineering Chemistry Research, 2012. **52**(1): p. 73-82.
247. Izrailev, S., et al., *Steered molecular dynamics*, in *Computational molecular dynamics: challenges, methods, ideas*. 1999, Springer. p. 39-65.
248. Keten, S. and M.J. Buehler, *Asymptotic strength limit of hydrogen-bond assemblies in proteins at vanishing pulling rates.* Physical Review Letters, 2008. **100**(19): p. 198301.
249. Ackbarow, T., et al., *Hierarchies, multiple energy barriers, and robustness govern the fracture mechanics of α-helical and β-sheet protein domains.* Proceedings of the National Academy of Sciences, 2007. **104**(42): p. 16410-16415.
250. Sotomayor, M. and K. Schulten, *Single-molecule experiments in vitro and in silico.* Science, 2007. **316**(5828): p. 1144-1148.
251. Cheng, T.-W. and W.-K. Hsu, *Winding of single-walled carbon nanotube ropes: An effective load transfer.* Applied Physics Letters, 2007. **90**(12): p. 123102.
252. Ericson, L.M., et al., *Macroscopic, neat, single-walled carbon nanotube fibers.* Science, 2004. **305**(5689): p. 1447-1450.

253. Fang, S., et al., *Structure and process-dependent properties of solid-state spun carbon nanotube yarns.* Journal of Physics: Condensed Matter, 2010. **22**(33): p. 334221.
254. Hearle, J.W., P. Grosberg, and S. Backer, *Structural mechanics of fibers, yarns, and fabrics.* 1969.
255. Uddin, J., et al., *Modified embedded atom method study of the mechanical properties of carbon nanotube reinforced nickel composites.* Physical Review B, 2010. **81**(10): p. 104103.
256. Matthews, J., *Epitaxial growth*. 2012: Elsevier.
257. Yazdandoost, F. and R. Mirzaeifar, *Generalized stacking fault energy and dislocation properties in NiTi shape memory alloys.* Journal of Alloys and Compounds, 2017. **709**: p. 72-81.
258. *See Supplemental Material at [URL will be inserted by publisher] for more studies under various loading modes.* .
259. Oliver, W.C. and G.M. Pharr, *An improved technique for determining hardness and elastic modulus using load and displacement sensing indentation experiments.* Journal of materials research, 1992. **7**(06): p. 1564-1583.
260. Oliver, W.C. and G.M. Pharr, *Measurement of hardness and elastic modulus by instrumented indentation: Advances in understanding and refinements to methodology.* Journal of materials research, 2004. **19**(01): p. 3-20.
261. Lund, A. and C. Schuh, *Strength asymmetry in nanocrystalline metals under multiaxial loading.* Acta materialia, 2005. **53**(11): p. 3193-3205.
262. Zhou, K., et al., *Molecular dynamics simulations of tension–compression asymmetry in nanocrystalline copper.* Physics Letters A, 2017. **381**(13): p. 1163-1168.
263. Mordehai, D., et al., *Nanoindentation size effect in single-crystal nanoparticles and thin films: A comparative experimental and simulation study.* Acta Materialia, 2011. **59**(6): p. 2309-2321.
264. Hao, S., et al., *A transforming metal nanocomposite with large elastic strain, low modulus, and high strength.* Science, 2013. **339**(6124): p. 1191-1194.
265. Yazdandoost, F., A.Y. Boroujeni, and R. Mirzaeifar, *Nanocrystalline nickel-graphene nanoplatelets composite: Superior mechanical properties and mechanics of properties enhancement at the atomistic level.* Physical Review Materials, 2017. **1**(7): p. 076001.
266. Li, Y., et al., *Atomic approach to the optimized compositions of Ni–Nb–Ti glassy alloys with large glass-forming ability.* RSC Advances, 2015. **5**(4): p. 3054-3062.